Author:
Hill, G. F. J

Title:
The development and application of a delamination prediction method to composite structures.

The Development and Application of a Delamination Prediction Method to Composite Structures

G. F. J. Hill

Department of Aerospace Engineering,
University of Bristol, Bristol, BS8 1TR, U.K.

December 2000

A dissertation submitted to the University of Bristol in accordance with the requirements of the degree of PhD in the Faculty of Engineering

Word Count: 35,134

Abstract

A method of predicting delamination in fibre-reinforced composite materials including several previously disregarded strength issues is presented. Thermal residual stresses, volume of stressed material, in-plane stresses and the hydrostatic stress in the polymer matrix are introduced and their influence on composite material strength discussed. These factors are then applied in a stress based method for predicting delamination which can deal with both unidirectional and general laminates. The results from a series of scaled unidirectional specimens designed to produce interlaminar tensile strength data are used to determine the strength parameters for the method.

The method is shown to be effective in predicting failure in the fill-in region of two 'T'-piece specimen designs to within 14%. The failures were dominated by tension acting between fibres in large blocks of unidirectional material which had high thermal residual stresses and tensile hydrostatic stress due to constraint from the surrounding material.

The method is also applied to a series of test pieces which used general laminates. The designs are based on sandwich panel sections and a tapered I-beam specimen. In the sandwich panel specimens, the edge closure sections were constructed using 0, 90 and $\pm 45^{o}$ plies. Delamination occurred in a region of dropped plies and curvature making all the stress components important in producing accurate predictions, which are within 16% of the failure loads in testing.

The tapered I-beam specimens were designed to delaminate in a doubly-curved laminate region of 90 and $\pm 45^{o}$ plies. The delamination predictions were within 13% of the first delamination loads found in testing.

The method produced failure predictions which were all within 16% of the failure loads of the tested specimens. It is found that the local geometry of the delamination region is critical in determining the stress levels in the specimens and therefore their strength. Variations in the manufacture of such specimens and components is therefore clearly important in establishing the delamination loads of composite structures.

Acknowledgements

Acknowledgements are made to the EPSRC and GKN/Westland Helicopters Ltd for providing financial support for this PhD. Professor Michael Wisnom is thanked for useful advice and discussions during the period of this work. Special thanks are also due to Mr. Mike Jones for preparing and testing the specimens which are analysed within this thesis.

Author's Declaration

I declare that the work contained in this dissertation was carried out in accordance with the Regulations of the University of Bristol. The work is original except where indicated by special reference in the text and no part of the dissertation has been submitted for any other degree.

Any views expressed in the dissertation are those of the author and in no way represent those of the University of Bristol.

The dissertation has not been presented to any other University for examination either in the United Kingdom or overseas.

SIGNED:  DATE: 4/5/01

Contents

Contents

List of Figures

List of Tables

Nomenclature

σ_{11}	Stress in the Fibre Direction
σ_{22}	Stress in the Transverse In-Plane Direction
σ_{33}	Stress in the Through-Thickness Direction
τ_{12}	In-Plane Shear Stress
τ_{13}	Fibre/Through-Thickness Shear Stress
τ_{23}	Transverse/Through-Thickness Shear Stress
σ_1	Maximum Principal Stress
σ_2	Middle Principal Stress
σ_3	Minimum Principal Stress
σ_R	Raghava Stress in the Matrix
R	Ratio of Compressive to Tensile Yield Stress in Resin
V	Volume of Material Under Stress - For Weibull Analysis
m	Weibull Modulus
S_0	Strength of Unit Volume of Material
σ_{UVES}	Unit Volume Equivalent Stress in the Matrix - Weibull
e	Element Number - Weibull
n	Number of Elements in Model - Weibull
σ_X	Element Local X-Direction Stress
σ_Y	Element Local Y-Direction Stress
σ_Z	Element Local Z-Direction Stress
τ_{XY}	Element Local XY-Plane Shear Stress
τ_{XZ}	Element Local XZ-Plane Shear Stress
τ_{YZ}	Element Local YZ-Plane Shear Stress
X	Strength in X-Direction (Fibre Direction)
Y	Strength in Y-Direction (Transverse In-Plane Direction)
Z	Strength in Z-Direction (Through Thickness Direction)
S	Shear Strength of Material

S_{12}	Shear Strength of Material in 1-2 Direction
S_{13}	Shear Strength of Material in 1-3 Direction
S_{23}	Shear Strength of Material in 2-3 Direction
U	Internal energy - fracture mechanics
W	External work - fracture mechanics
c	Crack length - fracture mechanics
G	Energy release rate - fracture mechanics
G_C	Fracture toughness - fracture mechanics

Subscript characters I, II, III refer to fracture mechanics Modes.

Chapter 1

Introduction

1.1 Composite Materials

A composite material is one that is composed of more than one constituent part, each providing a useful contribution to the final properties. Composite materials are not modern, man-made inventions, they were first used in nature for the construction of organic structural members such as bones and wood. They are effective in producing relatively lightweight and strong structures optimised for the application in which they are used. This makes composites interesting to structural engineers and of great importance to the aerospace industry.

In this work, we are specifically referring to modern composite materials that are usually made from continuous glass, aramid or carbon fibres in a plastic matrix, although ceramic and metal matrix materials can be used for high temperature applications. The fibres themselves are strong and stiff when pulled in tension, but are flexible and buckle easily when compressed, and so need support.

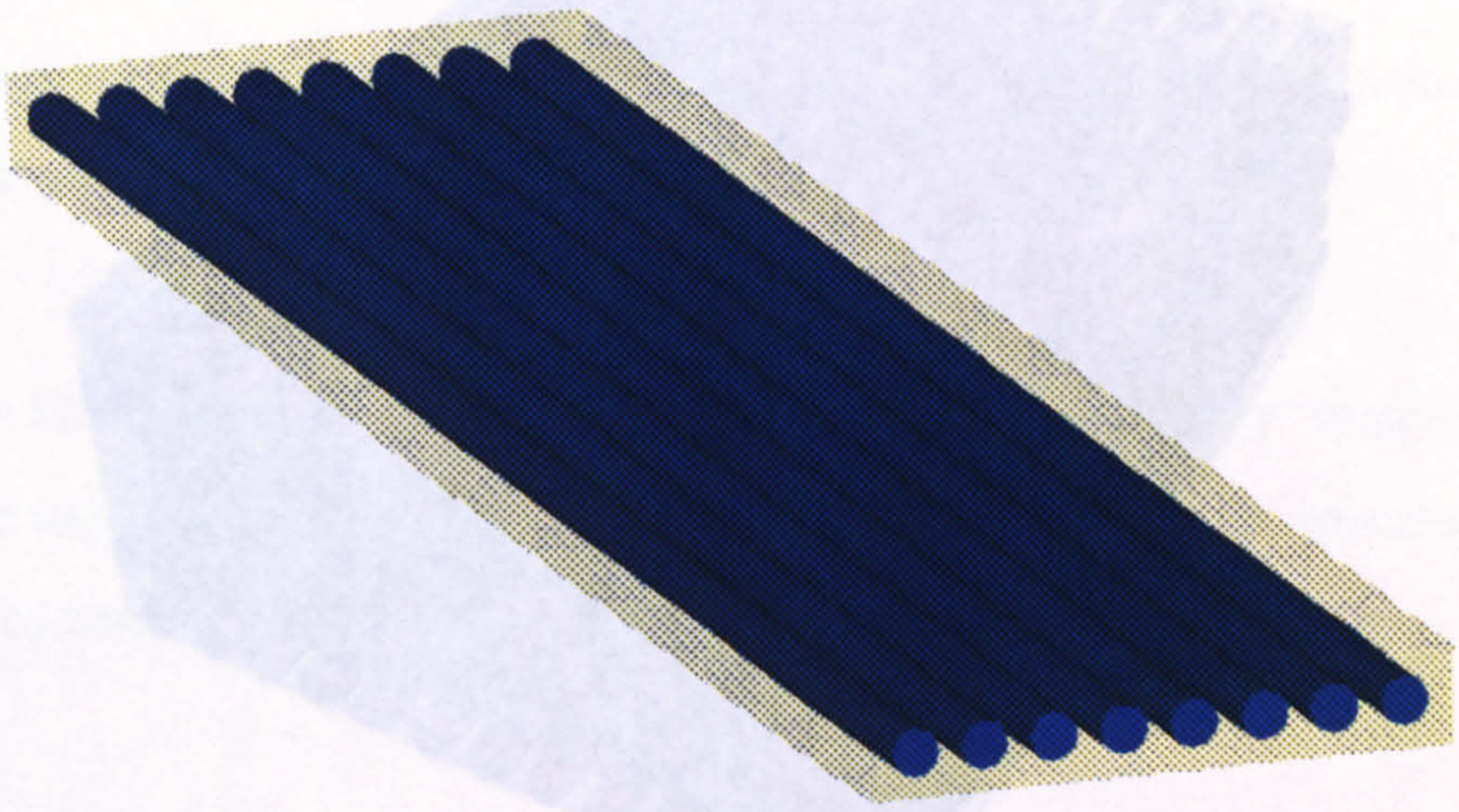

Figure 1.1: The Composite Ply - Fibres Embedded in a Matrix

This support is provided by the matrix material which holds them in place, preventing buckling and improving the compressive properties of the material. The matrix also provides the fibres with protection from the environment and supports the shear and tensile loads across the fibres. Some of the most commonly used matrix materials are epoxy resins. These are thermoset polymers which bond well with the fibres, and have good mechanical properties and resistance to chemicals.

The fundamental building block for a laminated composite structure is a ply. This is basically a flat sheet (lamina) of the composite made from the matrix material embedded with fibres aligned in a particular direction. There are normally many fibres through the thickness of one ply, but can be visualised as a single row of fibres, such as the layout shown in Figure 1.1.

A number of plies together form a laminate, and the orientation of each ply can be chosen so that the structure can meet the demands of the load applied to it and to give specific properties in different directions. The plies are bonded together by curing them under pressure at a temperature normally between 120 and 180°C in an autoclave. An idealised

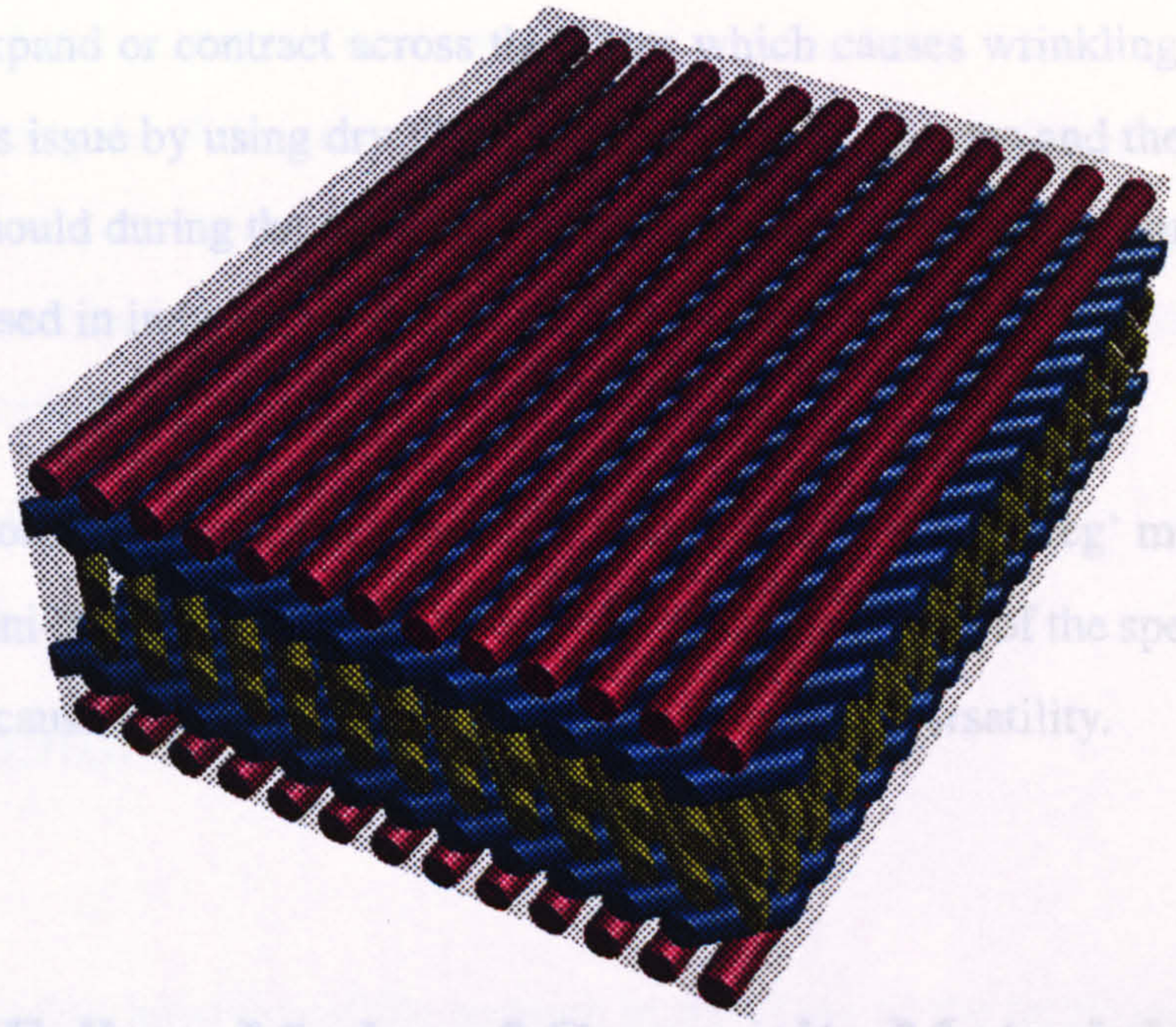

Figure 1.2: View of an Idealised Composite Laminate

example of a composite laminate is shown in Figure 1.2, where there are six plies, formed with a $[0/-45/+45]_S$ lay up.

The fibrous nature of composite materials leads to anisotropic properties for the individual plies. In the direction of the fibres, the plies are very stiff and strong, but across them, they are relatively flexible and weak. This is also true for natural composites. Wood, for example, is easily split along the grain, but is tougher across the lignin fibres. The stiffness of a carbon fibre based composite, for example, can be 140GPa in the fibre direction and 9GPa across them. This obviously introduces more complexity into the design process when composites are used in place of metals. The orthotropic nature of the material has to be taken into account, whereas with metals the isotropic properties are valid and are simpler to use.

A composite material structure made from individual plies, or from laminates, does not have to be flat as shown in Figure 1.2. Curved structures can be made by laying the plies up over forming tools that are in the shape of the required component. Problems can occur when making doubly curved structures such as a hemisphere because the individual

plies need to expand or contract across the fibres which causes wrinkling. It is possible to minimise this issue by using dry fibres in the laying up process and then injecting the resin into the mould during the cure cycle. This process is called resin transfer moulding (RTM) and is used in industry for large scale production.

This research concentrates on structures manufactured using 'pre-preg' material, consisting of plies of uni-directional material. This was used to make all of the specimens studied in this work because it is widely used in industry due to the versatility.

1.2 The Failure Modes of Composite Materials

As stated earlier, composite materials are made from fibres embedded in a supporting matrix. This gives rise to them having fibre-related and matrix-dominated failure modes. Failure of the fibre usually only happens in axial tension or compression. In tension, the fibre fails in a brittle manner at a weak point along the fibre. In compression, the failure is usually due to microbuckling. This means that bundles of fibres buckle and can fail due to the resultant bending or shear stresses. In this project, the goal is to investigate a matrix based failure mode and hence, the issue of fibre failure will not be studied.

The matrix in a composite material has a number of different failure modes, each depending upon the plane in which the crack grows. The first of these is called matrix cracking which consists of a fracture of the matrix in a plane perpendicular to the fibres. The second is called transverse splitting which consists of a fracture parallel to the fibres and perpendicular to the plane of the ply. Both of these are effectively in-plane failures of a ply, and often have little or no direct effect on the load carrying capability of a composite laminate because the in-plane loads are carried by the fibres. These types of failure were not investigated as part of this research.

The final failure mode of the matrix material is delamination. This occurs in a plane which

is between the plies, causing the laminate to split, or delaminate. This requires the matrix to be cracked along the fibres and tends to occur in the matrix rich regions between the plies. These failures can be catastrophic as any load which is carried through the thickness of a laminate has to be carried by the matrix material. This is the failure mode which was investigated during this research.

1.3 Delamination

Composite materials have incredible strength in the plane of the laminate because of the stiff and strong fibres which carry the load. Unfortunately, a laminated composite material structure will have pure matrix material between the plies. This means that any load transfer or induced stress through the thickness of the laminate has to be carried by the matrix material alone. This has a much lower strength than the fibres and fails easily. A delamination is caused when the stress levels in the matrix get too high, causing the matrix to fail and the laminate to split.

There are many situations which can lead to the generation of through-thickness stresses in the matrix. Some of these are shown in Figure 1.3.

Figure 1.3a shows a spar to skin joint made from composite material. Tensile and bending loads in the spar are transferred to the skin through the thickness of the composite material in the joint, generating interlaminar stresses. These stresses can be of a high enough magnitude to cause delamination. Interlaminar stresses can also be generated by load acting in curved laminates, seen in Figure 1.3b. The curvature of the laminate causes interlaminar tensile stresses to develop to balance the tensile forces in the plane of the plies. Interlaminar shear stresses, which also cause delamination, can be produced by loading both curved and flat laminates in the through-thickness direction.

Delamination can also be caused by dynamic events such as foreign object impact (Fig-

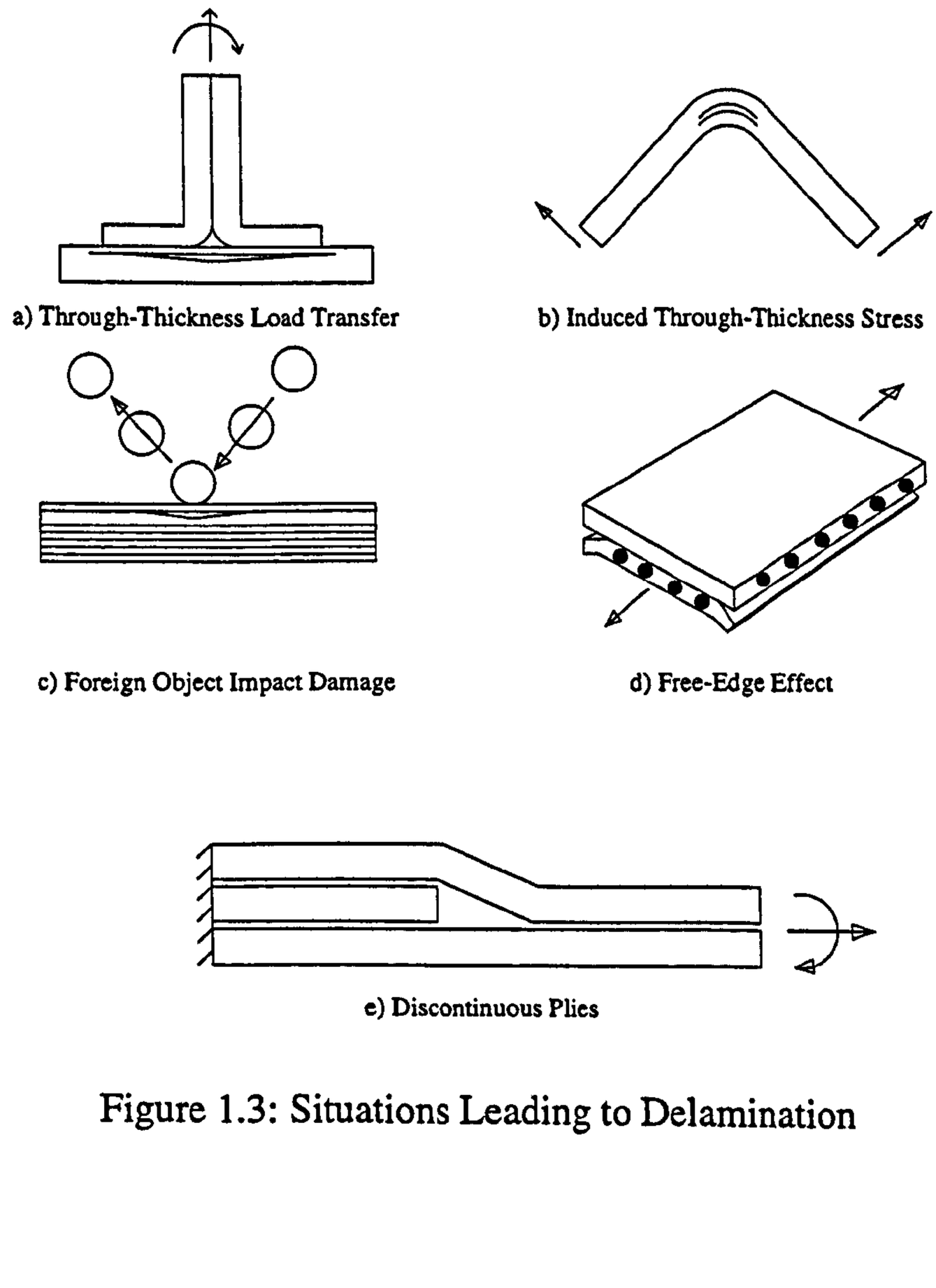

a) Through-Thickness Load Transfer

b) Induced Through-Thickness Stress

c) Foreign Object Impact Damage

d) Free-Edge Effect

e) Discontinuous Plies

Figure 1.3: Situations Leading to Delamination

ure 1.3c). This can happen when a component is in use (e.g. impact from stones or a bird-strike), or merely in maintenance (e.g. a dropped tool). The impact induces high interlaminar shear stresses in the material which delaminates. The danger is that this damage cannot always be seen on the outer surface, and even if it can, the damage inside can be many times larger and be throughout the thickness of the laminate. Ways of improving the damage tolerance [1, 2] and detection [3, 4] in composite materials are being researched widely.

Delamination can also occur at the free edges of a laminate as shown in Figure 1.3d. When a material is extended in one direction, it contracts in the perpendicular directions due to the Poisson effect. A composite ply, unlike an isotropic material, has different Poisson ratios depending upon the direction in which it is stretched. In a composite laminate, adjacent plies with different ply orientations will contract a different amount to each other. High interlaminar tensile and shear stresses can result which lead to delamination which is initiated at the free edge. Edge stresses are not only caused by the Poisson effect. They can also be generated by the interaction of the stress fields of adjacent plies.

The final example of delamination is that of a discontinuous ply as shown in Figure 1.3e. Laminates need to be tapered in thickness where the strength and stiffness requirements change. This is done by dropping plies from the lay-up which introduces discontinuities into the structure. In-plane loads or bending lead to interlaminar tension and shear around the dropped ply which can be large enough to cause delamination.

Any or all of these features can be present in a composite component, and each will contribute to the interlaminar stress field. Care should be taken in the design of any component which has these features as delamination can occur unexpectedly at low loads.

There are three modes of delamination in a composite material and these are shown in Figure 1.4. The research published so far mainly concentrates on delaminations produced in Modes I&II. It should be noted at this stage that the term 'Mode' is used to describe the fracture process itself, not the stresses producing the fracture.

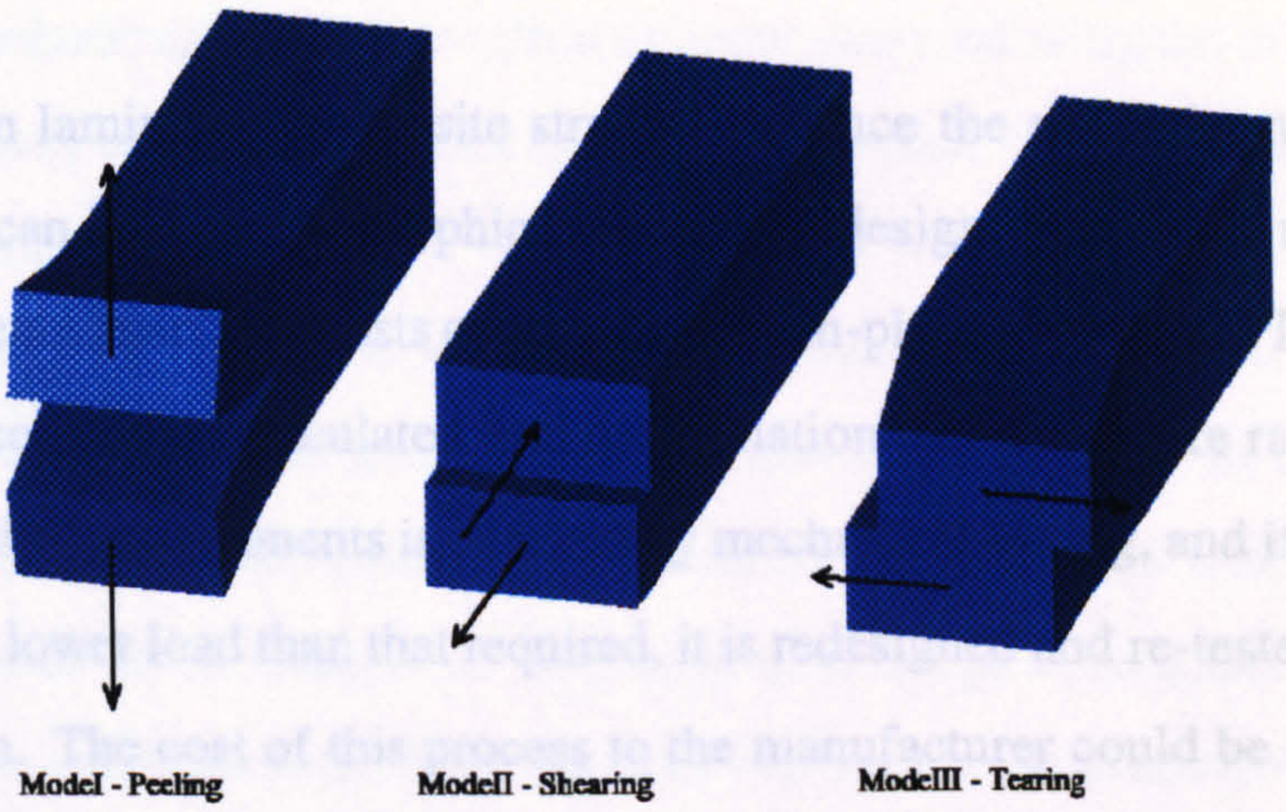

Figure 1.4: Composite Material Fracture Growth Modes

In all three of the cases shown, the fracture is produced between the plies and the Mode describes the action causing the growth. Most delaminations that occur in composite structures are a combination of these processes, mainly Modes I&II. Mode III fractures are less common in structures, but are just as important.

The consequence of any of these fracture processes occurring in a composite laminated structure can be catastrophic. Depending on the design of a component, the act of a crack initiating between the plies can lead to an unstable crack propagation which compromises the integrity of the structure. Indeed, if there is enough energy available to the process, the fracture can actually cross fibres and cut them. This would clearly cause a significant reduction in the load carrying capability of the structure. If the delamination is severe, it can actually cause a complete loss of load carrying capability, i.e. the component fails. Even if the crack is small, a different load case, such as axial compression, could then cause the structure to fail. The delamination would produce a loss in second moment of area, the stiffness to resist buckling, and catastrophic failure could occur.

1.4 Research Objective

Delaminations in laminated composite structures reduce the strength and stiffness of a component and can lead to catastrophic failure. The design process for most composite aircraft components mainly consists of assessing the in-plane ply strains. The interlaminar stresses are not commonly calculated, and delamination predictions are rarely performed. The strength of these components is checked by mechanical testing, and if the component delaminates at a lower load than that required, it is redesigned and re-tested for airworthiness certification. The cost of this process to the manufacturer could be reduced if there was a method which can consistently predict delamination.

This thesis was produced as part of research carried out at the University of Bristol. The work was sponsored by GKN Westland Helicopters, the Engineering and Physical Sciences Research Council and the Ministry of Defence. Some of the work presented within has been published in the form of technical papers [5, 6].

The objective of this research was to predict delamination in composite structures more reliably than previous methods have allowed. A number of specimen designs, based on composite aircraft structure components, were analysed and tested. Each provided a unique problem for any failure prediction technique that would be applied. The problems included constrained geometry, curved and tapered geometry and doubly curved geometry. A delamination prediction method was produced which was capable of coping with these problems.

In order to understand the complexities of the research, a literature review was carried out. This included the currently established methods which are in use for predicting failure in composite material structures. The literature review also highlights some important issues which affect the strength and behaviour of composite materials in delamination.

These issues are integrated into a delamination prediction method for unidirectional mate-

rials in Chapter 3 and expanded to deal with general laminates in Chapter 4. The strength parameters for the carbon-fibre composite material HTA/913C are found by testing a series of scaled interlaminar tensile strength specimens analysed using the proposed method. This method is then applied to a series of specimens which were designed to fail by delamination. Chapter 5 reports on 'T'-piece specimens which failed in a block of unidirectional material. The analysis of sandwich panel edge closure elements are reported on in Chapters 6 and 7. The local geometry of the delamination zones are found to be critical in producing accurate delamination predictions. The design of a tapered composite 'I'-beam is reported on in Chapter 8. This specimen design delaminated in a region of double-curvature where the full 3-D stress field was used in the prediction.

Chapter 2

Literature Review

In the previous chapter, the general properties and behaviour of fibre-reinforced composite materials were introduced. The issue of delamination was discussed, and was attributed to the lack of fibre-reinforcement through the thickness of a laminate. In this chapter, the prediction of delamination will be investigated and currently available, published, criteria discussed.

Damage in carbon fibre-reinforced composite materials occurs by two main processes, fibre breakage and matrix fracture. There are many methods of predicting failure in the composite ply as shown in a recent round-robin of composite laminate failure theories conducted by Soden and Hinton [7, 8]. These theories cover initial failure in the fibre or matrix, progression of the failure through ply damage and stiffness loss, all the way to the ultimate failure of the laminate. Most of these theories include matrix failure criteria in one form or another, and it is these which are of interest to the author. It would be possible to use any matrix failure criterion as a delamination prediction method because both the in-plane failure mode of transverse splitting and delamination are matrix-dominated failure modes.

The prediction of delamination in composite material structures generally uses stress based or energy release rate based criteria. There are other less well established methods for assessing delamination in composites such as 'J'-integrals [9] and 'Stress Intensity Factors' [10]. These are not discussed as part of this thesis.

In the previous chapter, the various failure modes of fibre- reinforced composite materials were introduced. In this work we are only concerned with the matrix failure mode of delamination. Delaminations can be caused by stresses generated by impact or by the geometry of the structure. There are a number of factors which can affect the matrix strength of polymer composites, which are reported on here. A summary of the work carried out previously using stress and energy release rate based methods is also presented.

2.1 Factors Affecting Delamination

There are a number of factors which influence the strength of composite materials. These range from manufacturing issues, such as voidage and other defects, to those encountered in use, such as impact damage and water ingress. In the course of this research, the manufacture and testing of all the specimens were carefully controlled, so impact damage and water ingress were not an issue. Manufacturing defects were minimal due to careful and consistent laying up procedures, and were generally disregarded. The factors investigated were the volume effect, the in-plane stress, thermal residual stresses and hydrostatic pressure.

2.1.1 The Volume Effect

Most materials used in engineering applications have an accepted strength, a stress above which the material will fail regardless of the size of the specimen being tested. Evidence

shows that many materials exhibit lower strengths in large specimens than those found in small specimens of the same design. Some composite materials also exhibit this effect. Not only is the matrix affected, but also the fibres which, as would be expected, fail at their weakest point first. This 'Weak link' hypothesis is the basis of a theory used in studying the effect of volume on material strength. The magnitude of the 'Volume Effect' can cause concern if results from small coupon tests are used to find a material's strength for large structures. Shivakumar [11] reported more than a 50% loss of interlaminar strength for 4 times the amount of AS4/3501-6 graphite epoxy material. This can clearly be a significant problem which needs to be addressed for all materials.

This effect has been shown by a number of other researchers for all modes of failure, including fibre breakage and delamination. Further examples of some of the work carried out include Bullock [12], O'Brien [13], and Wisnom [14]. A summary of the work performed can be found in Sutherland et.al. [15] and includes conception of the theory of size effects in brittle materials, brittle fibres and composites. Zweben [16] stated that the question of a size effect in composite materials has been around since the 1960s, and even with the current level of research into the issue, there is no definitive answer regarding its importance, as yet. This could be due to the fact that there are difficulties in testing some material systems and not all of them exhibit a volume effect.

The most commonly used method of analysing the magnitude of the volume effect is Weibull theory [17]. In Weibull theory the most significant assumption is that the material fails suddenly. This assumption means that the failure of a small section of the material is enough to trigger a large amount of damage around it, and cause potentially catastrophic failure. In the matrix of composite materials, these local brittle failures can be contained by the fibres giving rise to a progressive failure due to a series of delaminations which accumulate to produce large scale damage which eventually causes complete failure. Smaller specimens are stronger in the theory because the statistical distribution of defects within the material results in smaller specimens being less likely to have the largest, most weakening defects. The theory can be represented by Eqn. 2.1, which represents the comparison of two different volume specimens of the same material, each in a

constant stress state.

$$V_i \left(\frac{\sigma_i}{\sigma_0}\right)^m = V_{ii} \left(\frac{\sigma_{ii}}{\sigma_0}\right)^m \tag{2.1}$$

where V is the stressed volume of material, σ_0 is the strength of that material at unit volume and m is the Weibull modulus of the material. If the Weibull modulus is a positive number, it can be seen that if the volume of 'i' is larger than that of 'ii', then the stress in 'i' has to be lower for equality, and hence, failure to occur.

When the strength of a material is affected by the size of the specimen, or more specifically the volume of a material subjected to a certain stress state, then it is advisable to compare the strength of that material at a particular volume only. In this research, a unit volume ($1mm^3$) was chosen, and the strength of the material found using scaled specimens and extrapolated down to this amount. In analysis, the strength of the specimens was also extrapolated down to this amount, making the procedure consistent.

2.1.2 The Effect of In-Plane Stress on Interlaminar Strength

This has not been reported on extensively in the literature, although it can clearly be vital. Cui and Ruiz [18] is one work which clearly demonstrates a variation in the interlaminar strength of a specimen with the fibre-direction stress. It also indicates a change in failure mode as the fibre direction stress changes from tensile to compressive in the region of failure. Cui et.al.[19] showed a 15% improvement in delamination predictions of waisted tensile test specimens with the fibre direction stress taken into account compared to a simple maximum interlaminar stress criterion.

The contribution of in-plane stresses to the delamination of composite laminates is mentioned by Fenske and Vizzini[20]. Within a review of the literature, they report that 'While

the in-plane stresses have been calculated as significant, they have not been considered as playing a role in delamination.', although they do not report where this comes from. They go on to utilise the in-plane stresses at the matrix level in a delamination criterion which performs better than a criterion of a similar form, but without the in-plane contribution. Rotem [21] includes the fibre direction stress contribution to the matrix in his failure criterion because 'The matrix failure is controlled by all the stress components.'

There is evidence of delamination being influenced by the in-plane fibre direction stress and this is an important factor to include in any prediction. From this, it can be postulated that all stress components have a bearing on the failure of the matrix, especially in a 3-dimensional stress field.

2.1.3 Thermal Residual Stress

Thermal residual stresses occur where a material, or structure, does not allow the free expansion or contraction of a region in its construction. Isotropic material structures can contain significant thermal residual stresses around welds due to the large temperature gradients. Where there are no large temperature gradients the residual stresses are small because the coefficient of expansion of the material is constant in all directions.

Fibre-reinforced composite materials are not only highly anisotropic in terms of their elastic moduli, they also have very different thermal expansion coefficients in different directions. During the cool-down after cure, the resin tries to shrink because of the very large coefficient of thermal expansion. The stiff fibres have a virtually zero coefficient of thermal expansion, some even being negative, i.e. they reduce in length as the temperature increases. The fibres therefore prevent the resin from shrinking and this constraint leads to residual stresses being produced. This anisotropic expansion is of little concern in a uni-directional member as there are no restraining effects from ply to ply. It should be noted, however, that around each fibre the matrix material is in a state of hoop

tension which could influence the behaviour of the composite as a whole, for example the difference between transverse tensile and compressive strengths. In multi-directional laminates, however, adjacent plies restrain each other during the cooling process, and intralaminar residual stresses are produced. These stresses can be of the order of 25MPa in HTA/913C and are carried by the resin as well as the fibre, therefore ignoring them will lead to quantitative error in the matrix stress levels when loads are applied. When the laminate is curved, then interlaminar stresses can be produced as well, which will affect the delamination of the composite directly.

2.1.4 Hydrostatic Pressure Effect

A number of researchers (e.g.[22, 23]) have shown that polymer materials exhibit increases in stress and strain to failure with increasing compressive hydrostatic pressure. Hydrostatic pressure (or stress) is a constant level of pressure acting in all directions in a structure. The commonest way of evaluating the magnitude of this effect is to load a test coupon inside a pressurised container at different pressures.

If a composite material has a polymer as the matrix (e.g. epoxy or PEEK), then it follows that hydrostatic pressure will also change the stress and strain to failure of the composite for matrix-dominated failure modes. This has been shown for a number of resin systems with varying magnitudes. For example, 3M's Scotchply SP319, with the T300 fibre, has been tested extensively [24, 25, 26]. The in-plane shear strength for a 0° tube tested in torsion increased by 250% for a hydrostatic pressure of 4000 bar compared to the strength at 1 bar. This increase in strength indicates the possible range of the effect in a composite. Other examples from these references show a less extreme response for the matrix dominated modes. For a 90° tube of the T300/SP319 material, the strength increase was 43% at 6000 bar and the pure SP319 resin had an increase of 40% at 4000 bar [26].

An extensive review of the effects of hydrostatic pressure on the mechanical behaviour of composite materials can be found in Hoppel et.al.[27]. This covers matrix strength, yield behaviour and the effect on elastic modulus.

These strength increases are for very large pressures, but for a typical load case on a highly constrained region in a structure the hydrostatic stress can be over 50MPa (see Chapter 5). At this level, the strength decrease due to the hydrostatic stress in a specimen made from T300/SP319 could be as low as 3%, or as high as 30% depending upon the failure mode. This is a significant amount and should be included in delamination predictions on constrained material in a composite structure. It is possible for hydrostatic stress to be generated in a fibre-reinforced composite structure through lay-up effects and the geometry, anything that can cause a constraining effect on the movement of material through Poisson strain. This effect can be important in the accurate prediction of delamination in a polymer matrix composite and should be taken into account.

2.1.5 Other Effects

The issue of moisture absorption on the strength of composite materials is particularly important when the lifetime performance of these materials is taken into account. The interlaminar strength tends to decrease over time to a lower limit which is the final strength of the material. Structures should be designed to this value of strength, not the maximum possible found soon after curing as this performance is not available throughout the lifetime of the component. In this research, moisture does not affect the specimens, as all were dry and tested soon after manufacture. If moisture effects are considered important for the proposed application, then test coupons should be treated accordingly, and tested when moisture has been applied.

The fibre volume fraction can affect the interlaminar strength of composite materials. Variation in this can arise from different amounts of consolidation in the curing pro-

cess, and is therefore a manufacturing issue. Experimental data taken from deKok[28] in glass/epoxy shows that the transverse tensile strength increased from 40 to 48MPa for 46 to 64% volume fraction. The in-plane shear strength increased from 75 to 100MPa for 47 to 71% volume fraction. This magnitude of variation is significant and should not be ignored in the design process. It would be possible to include this effect in a failure criterion, but establishing the volume fraction before testing would be difficult. It is therefore suggested that the strength used for comparison with a criterion have the volume fraction with the lowest strength likely in manufacture. This should ensure conservative failure predictions.

Voidage is another manufacturing issue which can reduce the interlaminar strength of a composite material significantly [29]. As for the volume fraction, if the specimens being analysed are consistent with baseline strength specimens, then it isn't a concern and can be neglected.

The most useful factors to address in a delamination prediction criterion are those which are dependent upon the stress field, rather than the quality of manufacturing. These are the volume effect, thermal stresses, all stress components and the hydrostatic effect. The manufacturing issues are best accounted for through having baseline strength specimens which have been manufactured to a quality similar to any components being designed.

2.2 Stress Based Methods

There are many stress based criteria for predicting delamination in composite materials. They range from limiting criteria which consider only the maximum stress in one direction to interactive criteria which combine stresses in different directions with differing strengths in those directions. The delamination of a laminated fibre-reinforced material should depend upon the stresses in the matrix material because it is a matrix dependent failure mode. Where possible, it is common practice to only consider a 2-D plane of the

structure and to ignore the other stress components if they are relatively small. This is often a valid approach to take, but the other stress components are commonly ignored even when they are significant. The two stress components generally considered in a 2-D analysis are the interlaminar normal stress and the interlaminar shear stress.

It is relatively straightforward to calculate the stresses in the plies of a laminate using laminated plate theory. This analytical approach can calculate the strains and stresses of plies due to in-plane loading and out-of-plane bending. The through-thickness stresses are assumed to be zero throughout the laminate. When interlaminar stresses are required, it is common to use finite element analysis. By modelling the geometry of a component, the interaction of different materials and load cases can be assessed, and all stress components can be calculated. With the stress levels determined, delamination failure criteria can be applied. Failure is predicted to occur when the chosen criterion is satisfied.

2.2.1 Maximum Stress

The simplest forms of failure criterion are the maximum stress criteria (sometimes referred to as limiting criteria). They only work reliably when there is only one interlaminar stress component present, or dominant, in a specimen. If one of these criteria is used, then failure is predicted to occur when the stress value reaches or exceeds the strength of the material in that particular direction. There are four maximum stress criteria for delamination in polymer matrix composites in 3-dimensions:

$$\sigma_{33} \geq Z_t \qquad when \;\; \sigma_{33} > 0 \tag{2.2}$$

$$|\sigma_{33}| \geq |Z_c| \qquad when \;\; \sigma_{33} < 0 \tag{2.3}$$

$$|\tau_{13}| \geq S_{13} \tag{2.4}$$

$$|\tau_{23}| \geq S_{23} \tag{2.5}$$

where σ is the direct stress, τ is the shear stress, subscript 1 refers to the fibre direction and subscripts 2 and 3 refer to the in-plane and out-of-plane directions transverse to the fibres respectively. Z_t and Z_c are the absolute values of the through-thickness tensile and compressive strengths, respectively. The interlaminar shear strength of the material along the fibres is referred to by S_{13}, and the strength across them by S_{23}.

Puppo and Evensen [30] were early investigators of interlaminar stresses, and therefore delamination. Their main investigations were based at the free edge in flat plates and the shear stresses which build up due to mismatch in the material properties in adjacent plies. They used maximum stress criteria for failure prediction at the free edges in their early work.

These criteria are rarely useful in real structures as there is usually more than one of the stress components acting, but they are applicable to test coupons designed to assess individual material strengths. A common assumption in composite materials is transverse isotropy. This means that the transverse in-plane direct and shear properties are the same as the interlaminar direct and shear properties. Transverse properties are measured using methods such as rail-shear and tensile and compressive testing of a laminate. Generally, however, the interlaminar and transverse strengths are slightly different, due to different fibre distributions, so it is advisable to use actual through-thickness data wherever possible.

The accurate prediction of delamination in structural components is unlikely with these criteria. The other stress components, when significant, must also be included because they interact with one another (see Section 2.1.2). This leads on to criteria which consider the interaction of more than one stress component, the so-called interactive criteria.

2.2.2 Interactive Stress

When there is more than one significant interlaminar stress component at a point in a structure, it is necessary to combine the stresses in some way. There have been numerous different interaction formulae considered for delamination prediction in composites, some of which are presented here.

The most widely used interactive failure criteria for the composite as a whole are Tsai-Hill [31] (Eqn. 2.6) and Tsai-Wu [32] (Eqn. 2.7). These are shown for 2-D plane stress and predict through-thickness and fibre failure assuming zero cross-width stress. Tsai-Wu is shown in the quadratic tensor polynomial function form.

$$\left(\frac{\sigma_{11}}{X}\right)^2 - \left(\frac{\sigma_{11}\sigma_{33}}{X}\right)^2 + \left(\frac{\sigma_{33}}{Z}\right)^2 + \left(\frac{\tau_{13}}{S}\right)^2 = 1 \tag{2.6}$$

$$\left(\frac{1}{X_t} - \frac{1}{X_c}\right)\sigma_{11} + \left(\frac{1}{Z_t} - \frac{1}{Z_c}\right)\sigma_{33} + \left(\frac{\sigma_{11}^2}{X_t X_c}\right) + \left(\frac{\sigma_{33}^2}{Z_t Z_c}\right) + F_{13}\sigma_{11}\sigma_{33} + \left(\frac{\tau_{13}^2}{S^2}\right) = 1 \tag{2.7}$$

In Eqn2.6, X and Z refer to the tensile strengths of the material in the fibre and the inter-laminar directions. In Eqn2.7, X_t and X_c are the absolute values of the fibre-direction tensile and compressive strengths. The value of F_{13} is the interaction term for the fibre/through-thickness directions. A number of values have been proposed for its value, but ideally a biaxial test should be carried out, and with the biaxial tensile strength of P, it takes the form of:

$$F_{13} = \frac{\left(1 - P\left(\left(\frac{1}{X_t} - \frac{1}{X_c}\right) + \left(\frac{1}{Z_t} - \frac{1}{Z_c}\right)\right) - P^2\left(\frac{1}{X_t X_c} + \frac{1}{Z_t Z_c}\right)\right)}{2P^2} \tag{2.8}$$

These criteria have been altered to be used as delamination prediction criteria by con-

sidering them in the interlaminar direction instead of in-plane. The interaction term in the Tsai-Wu could partially account for hydrostatic effects. Thermal stresses can be accounted for, as in all criteria, by applying a thermal load in the load case. The effectiveness of Eqn. 2.6 is shown in Appendix B.

Of the interactive stress-based criteria for matrix-related failure modes, the most general ones are isotropic material related. Perhaps the most widely known is the von Mises yield criterion. This was originally proposed for use with metals, but has been used to model progressive failure in the rich epoxy resin layer between glass plies by Vizzini and Lee [33] and is reported on later. The criterion predicts yielding, or failure (as in the case of this reference), when inequality 2.9 is satisfied:

$$(\sigma_1 - \sigma_2)^2 + (\sigma_2 - \sigma_3)^2 + (\sigma_3 - \sigma_1)^2 \geq 2\sigma_Y^{t2} \tag{2.9}$$

where σ_1 , σ_2 & σ_3 are the principal stresses in the matrix and σ_Y^t is the yield strength in uniaxial tension. It should be noted that the polymer matrix of composite materials has been known to behave non-linearly when loaded in shear almost as long as composite materials have existed, e.g. Waddoups [34].

Failure prediction approaches that can use results taken directly from the homogeneous composite model are more commonly used than von Mises because of their relative ease of use. Hashin [35] proposed a number of criteria for in-plane matrix based inter-fibre failure, IFF, in composites. The criteria did not include the fibre direction stress, which was dealt with separately as part of fibre-failure criteria. Transverse isotropy was assumed, simplifying the criteria. The strength of the matrix is generally different in tension and compression, and to cope with this the tensile and compressive failure modes were differentiated between by using the following inequalities:

When $(\sigma_{22} + \sigma_{33}) > 0$

$$\frac{(\sigma_{22} + \sigma_{33})^2}{Y_t^2} + \frac{(\tau_{23}^2 - \sigma_{22}\sigma_{33})}{S_{23}^2} + \frac{(\tau_{12}^2 + \tau_{13}^2)}{S_{12}^2} = 1 \tag{2.10}$$

When $(\sigma_{22} + \sigma_{33}) < 0$

$$\frac{\left(\left(\frac{Y_c}{2S_{23}}\right)^2 - 1\right)(\sigma_{22} + \sigma_{33})}{Y_c} + \frac{(\sigma_{22} + \sigma_{33})^2}{4S_{23}^2} + \frac{(\tau_{23}^2 - \sigma_{22}\sigma_{33})}{S_{23}^2} + \frac{(\tau_{12}^2 + \tau_{13}^2)}{S_{12}^2} = 1 \tag{2.11}$$

In Eqn2.10, Y_t refers to the in-plane tensile strength of the matrix. In Eqn2.11, Y_c refers to the absolute value of the in-plane compressive strength of the matrix. The accuracy of these equations is reported on later.

A single criterion that can predict delamination for both through-thickness tensile and compressive cases was proposed by Altus and Dorogoy [36]. They accounted for the relative tensile and compressive strengths using:

$$\frac{\sigma_{33}}{2Z_t} + \sqrt{\left(\frac{\sigma_{33}}{2Z_t}\right)^2 + \left(\frac{\tau}{S}\right)^2} = 1 \tag{2.12}$$

where $S = S_{13} = S_{23}$ and $\tau^2 = (\tau_{13}^2 + \tau_{23}^2)$. The formulation will never allow failure in pure compression, however if pure compression is acting in a material, a limiting criterion would be used instead. It was shown to give good correlation with the delamination initiation location around a hole in a composite laminate. The formulation does not include all of the stress components in the ply, but could be altered if required. Unfortunately, no useful quantitative comparisons were made, so the numerical accuracy could not be assessed.

One of the simpler forms of criterion appeared in 1988 and was proposed by Brewer and Lagace [37]. This is a quadratic interaction criterion with each part being a maximum stress criterion, and the magnitude of the components assessed (Eqn. 2.13).

$$\left(\frac{\tau_{13}}{S_{13}}\right)^2 + \left(\frac{\tau_{12}}{S_{12}}\right)^2 + \left(\frac{\sigma_{33}}{Z_t}\right)^2 + \left(\frac{\sigma_{33}}{Z_c}\right)^2 = 1 \qquad (2.13)$$

The last two terms are used interchangeably. If the interlaminar normal stress is tensile, then the fourth term is ignored, otherwise the third is neglected. It would be quite feasible to include all stress components in the composite material matrix in this criterion, by simply adding more parts in the same format. However, it is not possible to easily account for the hydrostatic stress and volume effects.

Christensen [38] proposed another type of failure criterion for the matrix failure in a composite laminate. The criterion is shown in Equation 2.14.

$$\alpha_1 k_1(\sigma_{22} + \sigma_{33}) + (1 + 2\alpha_1)\left[\frac{1}{4}(\sigma_{22} - \sigma_{33})^2 + \tau_{23}^2\right] + (\tau_{12}^2 + \tau_{13}^2) \geq k_1^2 \qquad (2.14)$$

Where $k_1 = \tau_{12}^Y = \frac{|Y_c|}{2}$ and $\alpha_1 = \frac{1}{2}\left(\frac{|Y_c|}{Y_t} - 1\right)$. The formulation would allow for the hydrostatic stress effect to be accounted for and includes all of the stress components apart from the fibre direction. No comparisons with experimental data have been found for this criterion, so the accuracy cannot be assessed.

Rotem [21] used a quadratic interaction equation based on a fatigue strength criterion originally proposed by himself and Hashin [39] to predict matrix failure in a laminate. This new criterion included the fibre direction stress as shown in Equation 2.15.

$$\left(\frac{E_M \epsilon_1}{S_M}\right)^2 + \left(\frac{\sigma_{22}}{Y_t}\right)^2 + \left(\frac{\tau_{12}}{S_{12}}\right)^2 \geq 1 \tag{2.15}$$

The first term in Eqn2.15 contains the elastic modulus of the composite material in the fibre direction (E_M) and the fibre direction strain (ϵ_1). These values, when multiplied together, produce the fibre direction stress, which can contribute to the failure of the matrix and be significant if the magnitude is large enough. The proposed method for including the fibre direction matrix stress will not necessarily provide a reasonable estimate of the stress in the matrix. The stress in the matrix can be related directly to the σ_{11} stress by the ratio of matrix elastic modulus to the composite elastic modulus. By using the fibre strain, this approach could miss out on any stress contribution due to constraint, or provide more stress due to Poisson contraction when the composite is stress free macroscopically. These are possible sources of error, although in many cases they are likely to be relatively minor in terms of the overall contribution to failure. This criterion can be easily transformed for delamination prediction including all stress components and accounting for thermal stresses. The hydrostatic stress effect is not accounted for.

Puck [40] has proposed an IFF criterion. It is based on a quadratic interaction criterion, but includes a stress interaction factor based on the failure envelope for the material being analysed. A version of the criterion modified to interlaminar failure in a plane stress domain is shown in Equation 2.16.

$$\sqrt{\left(\frac{\tau_{13}}{S_{13}}\right)^2 + \left(1 - P_F\left(\frac{Z}{S_{13}}\right)\right)^2 \left(\frac{\sigma_{33}}{Z}\right)^2} + P_F\left(\frac{\sigma_{33}}{S_{13}}\right) = 1 \tag{2.16}$$

Where P_F is the stress interaction factor taken as the negative slope of the failure envelope at $\sigma_{33} = 0$ in the σ_{33}/τ_{13} plane, and would be calculated based on a series of experiments with varying stress ratios. The hydrostatic stress effect is accounted for by the interaction factor and the empirical nature of the criterion. The other stress components which are not included here would be possible to account for, but other interaction factors would be

required. The accuracy of this criterion is shown in Appendix B.

Earlier in the chapter, four effects were presented which can have significant influence on the inter-fibre strength of composite materials. These were the volume effect, thermal residual stresses, in-plane stress and hydrostatic pressure. Several of the reported criteria include a method of compensating for the hydrostatic stress effect.

The most critical aspect of the strength of the matrix is probably the volume effect. This has not been applied widely to failure criteria which are currently available in the literature, one example is Wisnom et.al.[41].

In most of the criteria, the full stress field is not accounted for, although most have provision to allow for this in the failure prediction if altered accordingly.

Stress based criteria such as these have their uses in many applications, although they do have limitations. Geometry such as ply drops, drilled holes and other sources of stress singularities are common weaknesses of standard stress based criteria. A method which was proposed that attempts to overcome this follows.

2.2.3 Dealing with Singularities

Where a model of a composite material has a ply drop or any other discontinuity such as a free-edge, the stress level can be singular. In a finite element model, this means that the stress increases as the element size reduces, leading to mesh dependent or indeterminate results. Taking the stress at these locations is questionable, as failure could be predicted at low loads using any standard stress based criterion, if the mesh is highly refined.

Whitney and Nuismer [42] proposed two approaches to overcome the issue of stress sin-

gularities around holes in laminates. Although they applied these methods to in-plane transverse failure they could equally be applied to delamination. The simplest was a 'point stress criterion', which assumed that failure occurred when the stress exceeded the strength of the material at some distance from the discontinuity. This distance was described as 'the distance over which the material must be critically stressed in order for there to be a sufficiently large flaw to initiate failure'.

The other approach suggested by Whitney and Nuismer was that failure is predicted when the average stress over some distance, a_0, away from the discontinuity exceeds the strength of the material:

$$\frac{1}{a_0}\int_0^{a_0}\sigma \mathrm{d}x \geq \sigma_F \tag{2.17}$$

where σ_F is the material strength and x is the distance from the edge of the discontinuity. They found that a value of $a_0 = 3.8mm$ was good for predicting failure for a range of crack lengths and hole sizes in both glass and carbon $(0/\pm 45)_S$ laminates, though it was less accurate the larger the discontinuity became. Most of the stress based criteria shown previously can be used to formulate the σ_F value in Equation 2.17.

Kim and Soni [43] modified the stress averaging technique of Whitney and Nuismer [42] to predict free-edge delamination in carbon/epoxy laminates in both axial tension and compression. They used the transverse strength and assumed transverse isotropy for the interlaminar tensile strength value. By using an averaging distance of 1 ply thickness, they predicted delamination for six different lay-ups. They achieved this with a reasonable degree of accuracy, although one case was approximately 60% unconservative. However, it should be noted that the method was consistently more accurate than using a standard stress based criterion.

Fish and Lee [44] used a heavily modified Tsai-Wu [32] criterion to predict the delam-

ination of tapered laminates. Their criterion predicted delamination when the distance averaged stresses obeyed Equation 2.18.

$$\frac{(Z_c - Z_t)}{Z_c Z_t}\sigma_{33} + \frac{\sigma_{33}^2}{Z_c Z_t} + \frac{(\tau_{23}^2 + \tau_{13}^2)}{S^2} = 1 \tag{2.18}$$

The location of the delamination was accurately predicted, but, the predicted delamination load depended heavily on the averaging distance taken from the location of the ply drop. This was due to the stress concentration caused by the discontinuous fibres. The accuracy of the stress-averaging method would therefore rely heavily on a large amount of testing to calculate the averaging distance prior to use.

The problems with using a stress based method in areas of a laminate with ply drops or free-edge delamination are clearly difficult to overcome. The stresses at singularities are infinite and cannot be used to predict delamination or further damage growth. Isotropic materials have a similar problem with crack growth in brittle materials, such as cast iron. Designers found that it was not possible to estimate how much a crack would grow, or what load would cause it to extend. There was a clear need for an approach which could get around this issue and hence energy based methods such as fracture mechanics were devised.

2.3 Fracture Mechanics Based Criteria

2.3.1 Background

Fracture mechanics based criteria usually utilise energy release rate methods to assess the amount of energy released by the growth of a crack a certain distance through a material.

This was first postulated and applied to isotropic materials (specifically glass) in 1920 by Griffith [45] and furthered by Irwin [46] who coined the phrase 'energy release rate.' This was extended to composite materials by Rybicki [47] who modified Irwin's crack closure integral.

The basis of this method comes from the assumption that energy in the body being analysed is dissipated at the crack tip when it grows. The energy release rate, G, is calculated using the expression:

$$G = \frac{dW}{dc} - \frac{dU}{dc} \tag{2.19}$$

where W is the work done on the body by external forces per unit width, U is the internal strain energy per unit width and c is the crack length. This expression can be used to evaluate the energy release rate in a crack propagation by analytical methods or through the use of a finite element model.

Finite element analysis software can, as part of the solution of a problem, calculate the total internal energy within a model. If the effect of the crack is small on the internal strain energy in a structure, the finite element analysis software may not discern a difference in the energy levels as it is a very small proportion of the overall amount. In situations like this, it is sometimes necessary to use a localised approach to assess the energy release due to the crack propagation. One method which can assess this is virtual crack closure (VCC). VCC is mainly used in situations where the interaction of the delamination Modes is important, and the separate energy components are required.

The process of virtual crack closure involves the modelling of a structure which includes the likely path for fracture initiation and propagation. The model is constructed such that there are two parts to the model in the case of a single crack. Stiff springs or MPCs are then inserted into the model along the crack path which provide the necessary forces

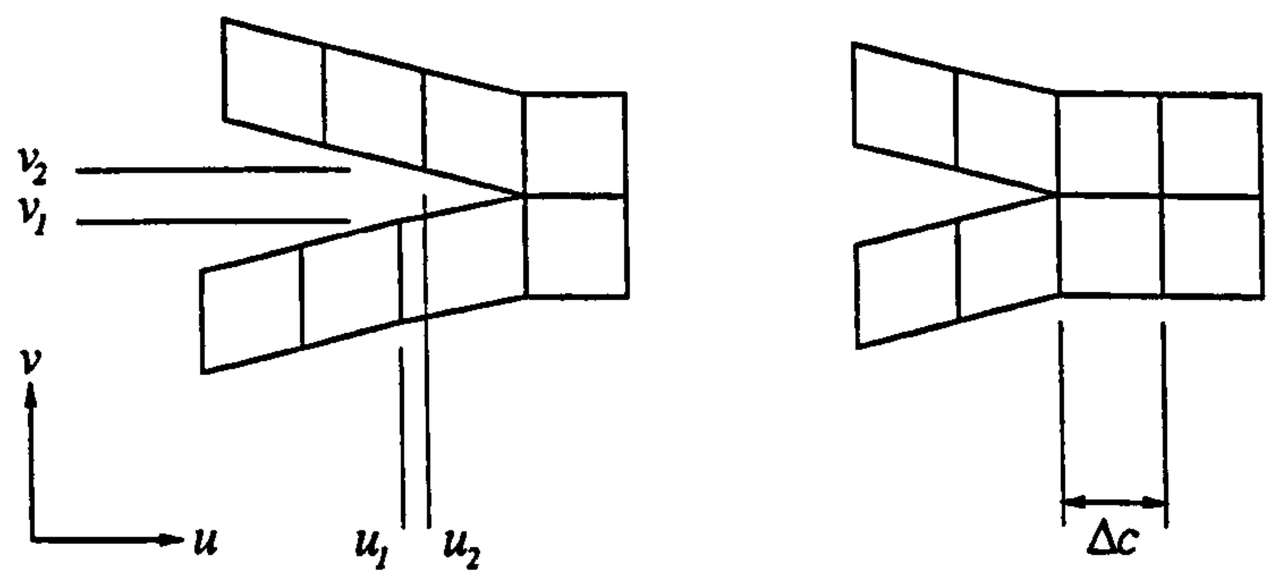

Figure 2.1: Schematic of Virtual Crack Closure Method

and, when removed, displacements required to establish the amount of work applied to close the virtual crack. The interlaminar tension and shear energy release rates (G_I and G_{II}) are calculated using the vertical and horizontal forces (F_C and T_C) at the crack tip between nodes 1 and 2 (see Figure 2.1) before crack growth. The energy release rates are calculated using Equations 2.20 and 2.21. The assumption for using the crack closure integral is that by extending the crack a small amount, *dc*, the energy absorbed in the process is equal to the work required to close the crack by the same amount. The corresponding displacements after crack growth (horizontal, u and vertical, v) are also required in Equations 2.20 and 2.21 to evaluate the components of energy release rate for a constant applied load.

$$G_I = \frac{F_C(v_1 - v_2)}{2\Delta c} \tag{2.20}$$

$$G_{II} = \frac{T_C(u_1 - u_2)}{2\Delta c} \tag{2.21}$$

$$G_{III} = 0 \tag{2.22}$$

The sum of these values is equal to the total energy release rate for the body under the modelled loading conditions with crack length, c.

One good example of the application of energy methods is Johnson [48] where a number of protagonists were asked to estimate the energy release rate in a cracked-lap-shear (CLS) specimen with prescribed dimensions and various crack lengths. This specimen is supposed to produce delaminations in Modes I and II in varying proportions. In this case, the lap and strap were made from aluminium, but the method is still applicable to composite material components and delamination. The models varied from 2-dimensional linear geometric finite element analyses to 3-dimensional, with some purely analytical methods. It was found that the 2-D non-linear methods were the most consistent, but the 3-D analysis showed important G_{III} values at the free edges and varying G_I & G_{II} values across the width. These results indicate a concern with the reliability of the CLS specimen for establishing the effect of mode ratio in a material. Many of the interactive energy release rate criteria from the next section were correlated using the CLS specimen, throwing some doubt on to their validity.

2.3.2 Energy Release Rate Failure Criteria

The 'strength' of a material with respect to crack growth is referred to as the fracture toughness. It is, to a certain extent, equivalent to the strength of a material, but is based on the energy required to form or grow a crack, rather than the limiting stress. In a manner comparable to the maximum stress criteria, if the fracture growth is in one pure mode, then it should be reasonable to predict crack growth using Equation 2.23.

$$G \geq G_C \tag{2.23}$$

where G_C is the fracture toughness value of the dominant mode. This equation is also

valid for crack growth in isotropic materials.

Composite materials tend to exhibit significantly different crack propagation mechanisms in different fracture modes. This can lead to very different values of fracture toughness for Modes I, II and III. Mixed-mode delamination growth has not been observed to follow a single propagation law, with various criteria being used by investigators to fit their test data. The simplest form is shown in Equation 2.24.

$$G_T = G_I + G_{II} \geq G_C \tag{2.24}$$

This equation, however, may only describe delamination growth for materials with G_{IC} equal to G_{IIC}. Despite this, Rybicki et.al. [49] and O'Brien [50] have used this equation to predict mixed-mode delamination growth at the free edge of laminates. In both cases, the predictions were accurate to within 5%.

Most composite materials have significantly different G_{IC} and G_{IIC} values due to the variation in fracture morphology. In general, the fracture surface of a Mode II crack is much larger than a Mode I crack for the same debond area and hence, G_{IIC} is much greater. Due to the differences in fracture toughness, a more appropriate criterion is considered as being:

$$\left(\frac{G_I}{G_{IC}}\right)^m + \left(\frac{G_{II}}{G_{IIC}}\right)^n \geq 1 \tag{2.25}$$

It should be noted at this point that the reliability of the use of these criteria revolves around the accuracy of the fracture toughness values. It has been shown by many researchers that the fracture toughness is affected by the ply orientations at the fracture surface. Examples include Nicholls and Gallagher [51] and Robinson and Song [52].

Jurf and Pipes [53] showed that m=n=1 gave good correlation with their test data for mixed mode delamination growth in a graphite/epoxy composite (AS1/3501-6). Rhee [54] also showed good agreement for carbon/PEEK materials for m=n=1. However, Law [55] used Equation 2.25 with m=0.5 and n=1 to fit test data for free edge delamination behaviour in $(\pm 25/90)_S$ laminates. Hwu [56] showed m=1.25 and n=1.5 for glass/epoxy. From these examples, it is shown that there is no consistent set of values for m and n for all materials or lay-ups. This means that after testing pure mode specimens to get the G_{IC}, G_{IIC} and G_{IIIC} values, further testing to evaluate the interaction terms must be carried out.

There are further failure criteria to be found in the literature, but none has been found to be reliable in a wide range of materials. A comprehensive list can be found in the work by Greenhalgh et.al.[57].

Many of the previously mentioned delamination failure criteria have been applied to more complex specimens than strength coupons. Some of this work is reported on in the next section.

2.4 Application to Specimens

Predicting the delamination of a composite material component is a very different proposition to correlating a failure criterion using test coupons. Actual components tend to have more complex stress fields and load distributions, and such analyses can assess the accuracy of criteria more effectively. Some of the examples in the literature are shown in this section.

Hashin[35] applied Equations 2.10 & 2.11 to the transverse in-plane failure of glass/epoxy

off-axis specimens loaded in tension. A number of fibre angles were tested, the 30, 45 and 60° specimen's failures were predicted within 10% error. The 15° specimens failed at loads around 20% lower than that predicted with considerable scatter. The prediction was consistently unconservative and became more inaccurate as the fibre stress levels increased. As previously stated, this indicates that the matrix dominated failure is probably affected significantly by the fibre direction stress which was not included in the applied criteria.

Vizzini and Lee [33] used finite element analysis to investigate several different laminates with internal ply drops. They used the von Mises criterion (Equation 2.9) in the modelled resin pockets and resin-rich layers between the composite plies. Application of a progressive damage modelling technique led them to deduce that the resin pocket failed before delamination occurred. From this damaged model, the initiation and propagation of delaminations in the various specimens could be predicted. Quantitative predictions were not feasible because the resin layer stresses depended heavily upon the resin layer thickness. This could indicate significant problems with the whole process of delamination prediction due to manufacturing variation. If the stress levels vary with resin layer thickness, then there is variation in component strength and predicting delamination becomes more difficult.

Zhou and Sun [58] applied the distance averaging method using Equation 2.26, a quadratic interaction criterion, to evaluate the equivalent stress. The free edge delamination of various laminates and lay-ups were predicted.

$$\left(\frac{\sigma_3}{Z_t}\right)^2 + \left(\frac{\tau_{23}}{S}\right)^2 + \left(\frac{\tau_{13}}{S}\right)^2 \geq 1 \tag{2.26}$$

They used a distance averaging value, a_0, of the thickness of 2 plies to achieve accurate predictions of edge delaminations. Errors of no more than 5% were reported for a number of laminates that suffered edge delamination due to applied longitudinal tension. This shows that the distance averaging technique can be accurate once correlated for a specific

material.

When a structure contains a stress singularity, it is considered better to use a fracture mechanics based approach [19]. The main problem with applying fracture mechanics to a failure prediction is that it is difficult to work out where to initiate the crack and grow it if there are a number of possible locations for the fracture. By initially using a stress based method to assess the most likely location of fracture, it becomes more feasible to perform fracture mechanics and therefore predict the failure. This approach was proposed by Minguet and O'Brien [59]. They used the maximum stress criterion to determine the location and initiation load of matrix cracking in a carbon/epoxy skin-stringer in four-point bending. Using an energy release rate approach based on a fracture initiating in that area of the specimen, they managed to achieve good agreement with the experimental results.

Theotokoglou and Moan [60] carried out an experimental investigation on the strength of composite sandwich panel T-joints. These structures are used in ship construction at hull-bulkhead intersections. The thickness and size of the attachment laps in the joint were varied in order to improve the strength. Failure correlation was carried out using finite element analysis, delamination in the glass-fibre composite material being predicted using independent maximum stress criteria for tension and shear. Failure in the foam core material was predicted using von Mises (Eqn. 2.9). Correlation was not achieved accurately because the authors believed that the only specimen analysed did not have a 'proper glue filling'. This would have affected the failure load and mode leading to inaccuracy. This indicates that modelling a component in order to predict failure will require accurate geometry which represents the load path within the structure.

Analysis of a series of composite hat stringer specimens by Li et.al. [61] have been performed using energy based methods. The equation using the mixed-mode ratio $\left(\frac{G_{II}}{G_T}\right)$, the fracture energy in Mode II divided by the total for all modes G_T, for predictions is shown in Equation 2.27.

$$G_C = M_0 + M_1\left(\frac{G_{II}}{G_T}\right) + M_2\left(\frac{G_{II}}{G_T}\right)^2 + M_3\left(\frac{G_{II}}{G_T}\right)^3 \tag{2.27}$$

The fitting parameters (M_0, M_1, M_2 & M_3) were calculated from a series of tests using double cantilever beam, end-notched flexure and mixed-mode bending specimens. These gave a range of fracture toughness values for pure Mode I to pure Mode II. The specimens were tested in a pull-off mode and failed by delamination at dropped plies in the flange region. The geometry of each specimen differed slightly in this region which affected the stress distributions, and hence the energy available for delamination. Each specimen was modelled separately, giving rise to all predictions being within 10%. The importance of the local geometry in the accuracy of delamination predictions is highlighted along with a concern over manufacturing variability.

2.5 Discussion

The stress based failure prediction methods tend to only be useful in cases where there are no stress singularities present. There is no consistently successful method, and the designer's choice of criterion depends upon the failure mode being analysed and personal choice. When stress singularities are not present in a structure, it is considered better to use a stress based approach, rather than a fracture mechanics method, to predict failure [19].

One stress based method which can be used to predict delamination at singularities is Whitney-Nuismer. The examples given for Whitney and Nuismer's distance averaging technique did not have a consistent a_0 (the characteristic distance) value for different failure modes in a material and different lay-ups. This method therefore requires a series of tests to be carried out on each failure mode before it can be used. This makes the method undesirable, unless a large amount of testing is not an issue, and other techniques should be considered, i.e. energy methods.

A number of matrix strength issues have been identified which affect the interlaminar strength of laminated composite materials. These are the volume effect, thermal residual stresses due to curing, the in-plane stresses within the matrix and the hydrostatic effect in polymers. These 'stress' factors have, in the past, been largely disregarded in delamination prediction criteria. Depending upon the situation, each can provide more than a 10% difference in the failure prediction. It is apparent that they could all make a useful contribution to a delamination prediction criterion.

The most significant of these factors is probably the volume effect. Many laminated composite materials exhibit a lower strength for large volumes of material when compared to small volumes. The importance of this in improving the accuracy of a delamination prediction was shown by Wisnom et.al.[62]. The failure of two croquet hoop specimen types were analysed using finite element methods. They showed that varying amounts of interlaminar tension and shear stress were in the curved sections of the specimens. By using an interactive stress criterion which did not account for the volume effect, the predicted failure loads were about 25% conservative. When the loaded volumes were taken into account for both the interlaminar tensile and shear stress, the predictions came to within 11% of the experimental results. This level of improvement indicates that stressed volume is a significant factor which should be taken into account when predicting delamination.

Predicting delamination accurately, whether using stress or energy based methods, requires precise modelling of the specimen geometry in order to correctly represent the load path. Individual specimens can be represented in this manner, but mass produced components would have some variation in their geometry. This makes it impossible to predict the failure of every component, but the strength of the weakest component could be predicted if the worst case of the variation was applied to the model.

There is no totally effective method of predicting delamination in composites. This is mainly due to the fact that stress based methods can only be used in areas where stress singularities are not present, and fracture-mechanics based criteria can only be used reliably at a point where a strong singularity is present. It was seen that the stress based meth-

ods were generally less accurate in their failure predictions than the fracture-mechanics criteria in their applications. It was concluded that there was a need for an accurate and reliable stress-based criterion for predicting delamination.

Chapter 3

A Stress Based Delamination Prediction Method

3.1 Introduction

The previous chapter reviewed some of the many failure prediction criteria available for use in cases of delamination. It was concluded that for cases where there are no stress-singularities, it is best to use a stress based method. There are few criteria currently available which are reliable and accurate for a wide range of cases including uni-directional and cross-ply laminates. The present chapter introduces the theory behind a new stress based delamination prediction method for unidirectional and general laminates which compensates for the volume effect, in-plane stresses and the hydrostatic pressure effect.

In the past, most fibre-reinforced composite materials have been used in applications with modest thicknesses to carry what are effectively in-plane loads. The testing and design of composites has therefore concentrated on in-plane properties and the prediction of ply failure. More recently, however, the use of composites has been extended to thicker

lay-ups, where the through-thickness behaviour needs to be understood. This is particularly important where the interlaminar strength has a controlling influence on the overall strength of the component.

The proposed method was developed to include a number of factors which affect the strength of polymer materials. The method was designed to predict the first delamination in various specimen designs based on the interlaminar tensile strength of a simple test coupon. The delaminations of the specimens are all assumed to occur in the matrix and be tensile. It therefore assumes that the microscopic stress-field around the fibres is consistent between the strength specimens and the analysed structures.

3.2 Factors Affecting Delamination

In the previous chapter, a number of factors which can influence the failure of the matrix material in a composite were introduced. The factors ranged from manufacturing issues, such as voidage and other defects, to those encountered in use, such as impact damage and water ingress. In the course of this research, the manufacture and testing of all the specimens were carefully controlled, so impact damage and water ingress could be ignored. Manufacturing defects were minimal due to careful and consistent laying up procedures, and were generally disregarded. The factors investigated were the volume effect, the in-plane stress, thermal residual stresses and hydrostatic pressure.

The volume effect has previously been shown to have a significant effect on the strength of a laminated composite component. It is possible to take account of this by applying Weibull theory which is a statistical method assuming distributed flaws in the material. It would be straightforward for a designer to consider the size of a component and use strength values based on the volume of material of which it is comprised. This would be a conservative approach because it is the stressed volume of material which is critical in the failure, not the overall volume of the component. This can be calculated in a finite

element analysis by considering each element of the model in turn, using the element stress and volume in the calculation.

It has been shown that all the stresses in the matrix material contribute to the failure of the matrix material. This fact can be taken into account relatively easily using finite element analysis because it can provide all stress components which are available in the analysis domain.

The thermal residual stresses due to curing are significant in multi-directional laminates. As all stress components contribute to matrix failure, then the thermal stresses should be calculated for inclusion in the failure prediction. This is relatively straightforward to achieve in finite element analysis.

The hydrostatic stress affects the strength of polymer materials. It is therefore reasonable that composite materials with polymer matrix materials behave similarly. This factor should be taken into account before predicting delamination from the stress levels in a component with a high degree of constraint.

These factors have, in the past, been largely disregarded in delamination prediction criteria. Depending upon the situation, they can provide as much as a 10% difference in the failure prediction, and as much as 25% for the volume effect. It is apparent that they could all make a useful contribution to a delamination prediction. In the next section, they are combined into a process which predicts delamination.

The assumptions made to simplify the implementation were as follows:

- The elastic moduli and thermal expansion coefficients of the materials do not change with temperature, i.e. the material behaviour is linear.
- The complete stress field in the matrix is the dominant contributor to the delamination of composite materials.

- The microscopic stress field in the matrix around the fibres is ignored and is not significantly different in the various failure modes.
- The hydrostatic stress affects the polymer resin failure as indicated by Raghava's equation.
- The volume effect has a significant effect on the strength of the matrix material, which can be represented by a linear, two parameter, Weibull model.

3.3 The Procedure

The procedure to predict interlaminar failure in a uni-directional specimen is described in this section. The factors affecting delamination strength are analysed and then a procedure formulated in two main parts, the generation and analysis of the model, and the calculation of the effective stress acting in the matrix of the composite. The method is then correlated for use by using the results from a series of scaled interlaminar tensile strength specimens.

3.3.1 Modelling Routine

The basic approach is to model the structure using finite element analysis, in 2-D or 3-D as necessary to represent the stress field accurately. Two load cases have to be applied, a thermal cure cool down cycle with a low mechanical load, then the same thermal case with a high mechanical load. The stresses from each of these cases are post-processed to remove the fibre contribution, then these effective matrix stresses are applied to the equations themselves. The details of this process follow.

The basic flow chart for the modelling process is shown in Figure 3.1. The volume effect is accounted for by calculating the 'Unit Volume Equivalent Stress' (UVES) for the matrix material throughout the structure. The UVES is a value which is calculated using

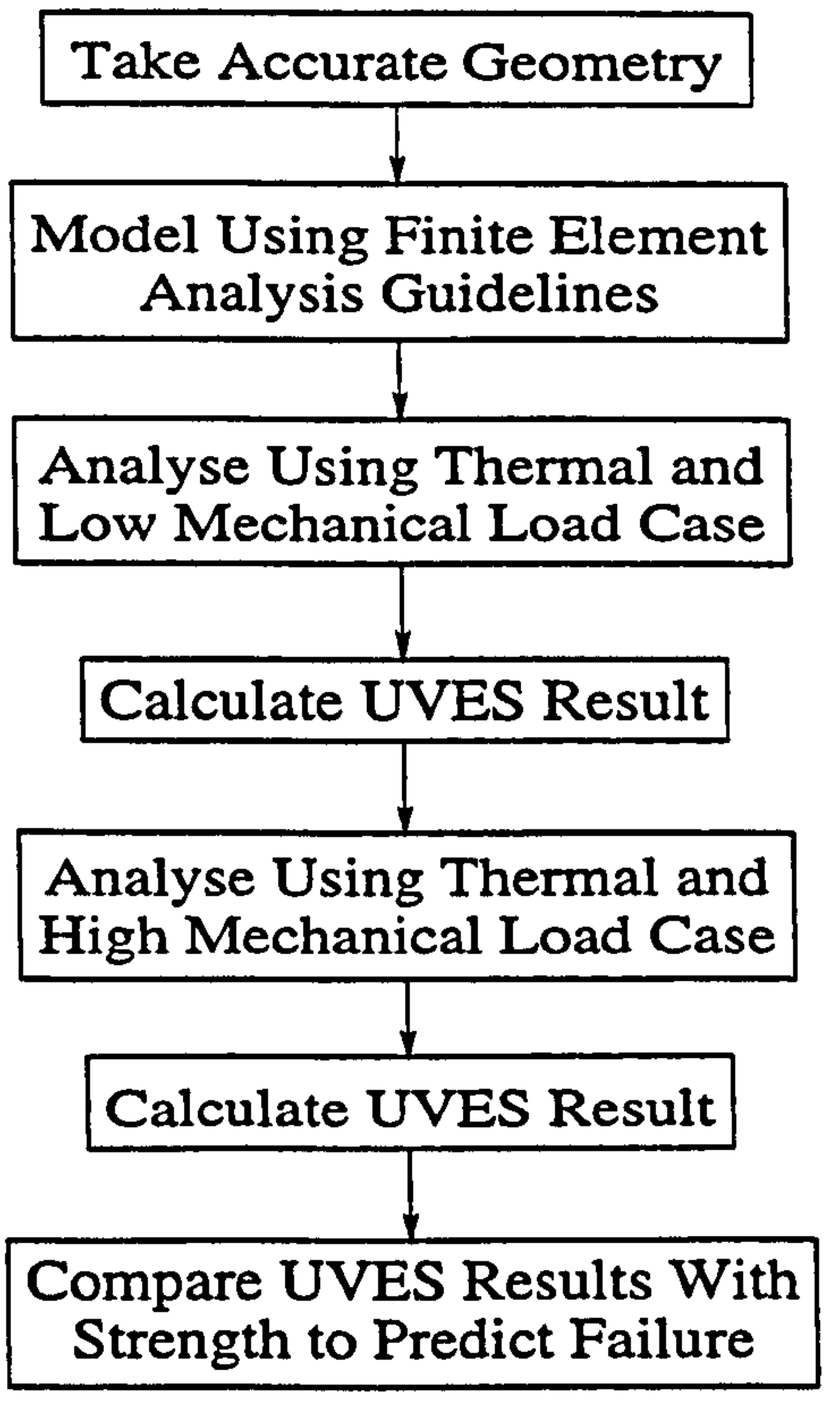

Figure 3.1: The Modelling Routine Algorithm

the volume of an element and the element centroidal stress and is explained in the next section. For elements with the same stress, a larger element contributes more to the UVES value as it has a larger stressed volume and, from the volume effect theory, is more likely to fail. This is critical in calculating the predicted failure load of the specimen accurately.

The FE model should be created in an analysis domain which is detailed enough to produce enough of the stress field to allow accurate predictions. If a 3-D stress-field is required, then a 3-D model should be created. It is important to accurately measure the specimen, especially in regions of curvature before creating the finite element model. The dimensions of a specimen and the local ply geometry can have a significant effect on the stress-field [33]. Variation in the stress field of the model to that of the specimen can lead to inaccurate predictions. From the author's experience in using this method, there are some guidelines to follow when producing the FE mesh:

- Aim for a minimum of 1x8-noded 2-D parabolic element per each block of plies with a particular orientation angle, e.g. 1 element for two 0^o plies, or for a single 90^o ply.

- Having more than 2 elements per ply will not generally give more accurate results.
- It is generally acceptable to use averaged ±45° properties in elements where a +45 and a -45° ply are present.
- Ensure that all elements in the delamination area are well shaped, i.e. keep quadrilateral elements as square as possible.
- In regions of curvature, ensure there is a minimum of 1 element per every 5° of curvature.

The assignment of material properties and orientations to the elements is relatively simple using a pre-processor. It is important that the values of the properties and the orientations are accurate because these will also affect the stress field.

With the mesh completed, the analyses can be carried out. The first of these should be with the thermal load case, starting from the cure temperature and going down to room temperature, and an applied mechanical load lower than the expected failure. The UVES result is assessed for that case in the most critical elements, and the next load case can then be applied. This case includes the thermal load case and a mechanical load higher than the expected failure load, and of a similar magnitude. Once again, the UVES result is calculated for all of the elements in the region of high interlaminar stresses.

The prediction of delamination in composite structures using finite element analysis generally requires some sort of post-processing to evaluate the failure load. This new approach requires post-processing to produce a prediction, as the magnitude of the volume effect is more easily evaluated after the finite element analysis has been completed. The volume effect is accounted for by calculating the UVES for the matrix material throughout the structure. The UVES is then compared to the strength found from interlaminar tensile strength coupons. The interlaminar tensile strength specimens used for this research are analysed later in this chapter.

The predicted failure load is now calculated from these two results. As a linear Weibull distribution is being applied, it is valid to use linear interpolation to the unit volume

strength value, provided that the stress field has not changed significantly between the two load cases. This would not be an issue if the thermal residual stresses were not included in the analyses because the linear analyses would produce the same stress field, but with different magnitudes. If the applied mechanical load doubles, then the stress field due to this applied load doubles along with the UVES result.

The thermal residual stresses can affect the stress distribution when the magnitude is large enough, which is the case with many composite material components. This can result in a slightly non-linear increase in the UVES with increasing load. Any inaccuracy in the assumption of using linear interpolation is made insignificant by using two mechanical load cases close to, and either side, of the predicted failure load. The mechanical load cases dominate the stress field to a point where the non-linearity in the UVES results is low. Also, the linear interpolation will be slightly conservative compared to a non-linear interpolation (using more data points), which is preferable in failure prediction.

3.3.2 UVES Routine

The most important routine for this method has been designated as the 'Unit Volume Equivalent Stress' (UVES) routine. It is applied to every region within a finite element mesh where delamination is considered to be a risk. This can be done using the results at integration points or the centroids of the relevant elements. A simple algorithm for this routine is shown in Figure 3.2.

Once the stress-field has been established, the fibre direction stress in each element must be factored down to that of the pure matrix material. This should be performed by taking σ_{11}, multiplying by the matrix modulus and dividing by the fibre direction modulus of the composite. This will produce the stress in the fibre direction within the matrix more accurately than by using the fibre direction strain and multiplying by the matrix modulus. This is because the stress in the matrix, as in any material, will depend upon all of the

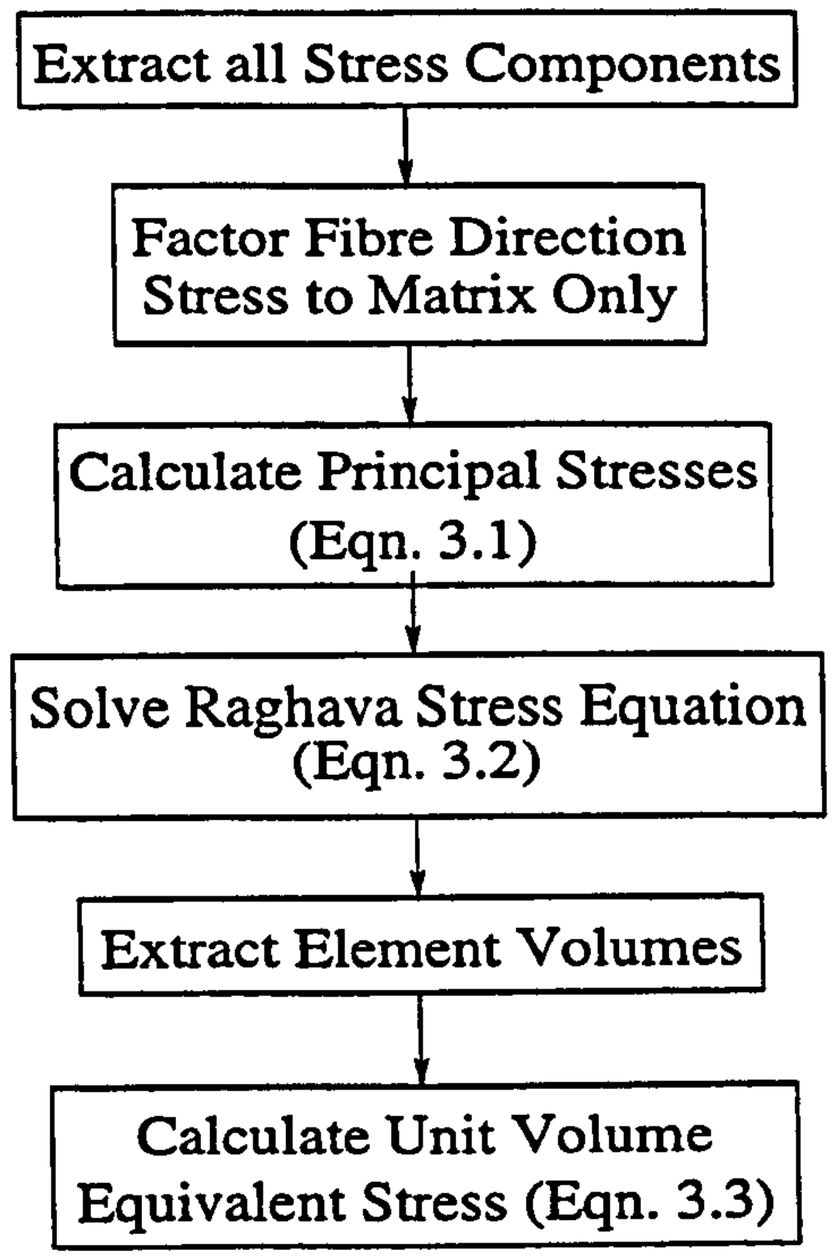

Figure 3.2: The UVES Routine Algorithm

strains acting, not just the fibre-direction strain.

It is feasible to take the stress-field within the matrix of a composite and use that to predict whether delamination will take place. By using all of the stress components, the effect of in-plane stress on the out-of-plane behaviour through stress interaction can be accounted for. What is predicted by this is matrix damage in the composite, not just delamination, therefore care must be taken to investigate the stress-field in the region of predicted failure. Delamination is only one possible matrix failure mode, transverse in-plane failure could also be a possibility. To confirm that the failure mode is delamination, the transverse in-plane stresses should be investigated and compared to the interlaminar stresses. If the interlaminar stresses are larger, then the failure mode is more likely to be delamination.

With the matrix stress-field realised, the principal stresses must be formed so they can be applied later to Raghava's equation [63]. This is done by solving a cubic equation (3.1) taken from Roark [64]. The three solutions for σ, when put in order from highest positive to lowest, are known as the maximum, middle and minimum principal stresses and are designated as σ_1, σ_2 & σ_3.

$$\sigma^3 - \sigma^2(\sigma_{11} + \sigma_{22} + \sigma_{33}) + \sigma\left(\sigma_{11}\sigma_{22} + \sigma_{22}\sigma_{33} + \sigma_{11}\sigma_{33} - \tau_{12}^2 - \tau_{13}^2 - \tau_{23}^2\right)$$
$$-\left(\sigma_{11}\sigma_{22}\sigma_{33} + 2\tau_{12}\tau_{13}\tau_{23} - \sigma_{11}\tau_{23}^2 - \sigma_{22}\tau_{13}^2 - \sigma_{33}\tau_{12}^2\right) = 0 \tag{3.1}$$

In modern composite materials, the matrix material is often a polymer and in the case of this research, it is a 913C epoxy resin. Polymers usually exhibit different compressive and tensile yield strengths and the hydrostatic stress also affects the yielding process. Raghava [63] proposed a yield criterion that has been shown to work well with polymers, taking account of the hydrostatic stress issue.

The matrix stresses, now formed as the independent principal stresses, are combined taking account of the hydrostatic stress effect using Raghava's equation. It is shown below (Eqn. 3.2) in a slightly re-organised form using the ratio of compressive to tensile yield stress (R). The resin used in this research was part of the HTA/913C pre-preg system from Hexcel [65]. The value of the yield stress ratio was not available for this resin system, so an assumed value of 1.3 was used. This value was taken from an average of that for epoxy resins in the literature [66], which have a range of around 1.2 to 1.4. The highest positive solution of σ_R (the Raghava stress) should be taken to be used later.

$$(\sigma_1 - \sigma_2)^2 + (\sigma_2 - \sigma_3)^2 + (\sigma_3 - \sigma_1)^2 + 2(\sigma_1 + \sigma_2 + \sigma_3)(R-1)\sigma_R \geq 2R\sigma_R^2 \tag{3.2}$$

Each element in the model represents part of the volume of a specimen or component. The area (2-D) or volume (3-D) of each element must be converted to produce the volume to which the element corresponds. These values are then applied to the volume effect equation (Eqn. 3.3) for every element in the region of interest. This includes parts of the component which are curved or experience through-thickness loading as these have the highest interlaminar stresses and are, therefore, most critical in establishing a delamination prediction. This equation can be formed by taking a standard Weibull equation (e.g. Eqn. 2.1) and summing for the elements in a varying interlaminar stress field in a model.

$$\sigma_{UVES} = \left(\sum_{e=1}^{n} V_e \sigma_{R_e}^m \right)^{\frac{1}{m}} \tag{3.3}$$

The number of elements, n, used in this equation is the choice of the user, and is the number of elements with significant interlaminar stresses. Elements around the loading point in the model should be avoided because they can cause false indications of delaminations due to singular stresses, especially when loads are applied to a single node. Including elements with low interlaminar stresses does not affect the delamination significantly, so using all the elements in the model is acceptable. The 'volume' of each element, V_e, is produced by the finite element analysis software as an output request, and needs to be factored to a value equivalent to the specimens being analysed. For example, a unit thickness 2-D half model of a component of width 20mm needs to have the element volumes multiplied by 40 to represent the structural volume. The Raghava stress for each element, σ_{R_e}, is that calculated using Eqn. 3.2. The Weibull modulus value, m, is that calculated for the interlaminar strength coupons, and is calculated for the HTA/913C matrix later in this Chapter.

Using this process, the 'Unit Volume Equivalent Stress' can be calculated for a model at a particular load case. This method needs to be applied at least twice to the model to account for thermal residual stresses and enables interpolation to different applied loads.

3.4 Material Strength Data

The interlaminar tensile strength data due to the volume effect is described by two values. Firstly, the strength for a unit volume of composite material, and secondly, the Weibull modulus which governs the sensitivity of the matrix to the volume effect. These values were calculated for the HTA/913C composite system from test results on a series of specimens.

The volume effect is shown by using a series of scaled tests, with an order of magnitude difference in volume between each specimen size. This can be done using any interlaminar tensile strength specimen. In this research a curved beam in bending was used. This specimen was previously analysed in 3-D by Wisnom for glass/epoxy [67]. This 'Humpback Bridge' (HBB) specimen was tested and analysed in 3-D using Wisnom's method to establish material strength data for the HTA/913C material used in this research.

These results are conditional on the quality of the material and manufacture. The interlaminar strength of composite material is greatly reduced by voidage [68] & [69]. The specimens were manufactured in a consistent manner, and should have had a similar material quality to one another. The values of interlaminar strength are therefore only valid for predicting delamination of similar quality specimens.

3.4.1 The Humpback Bridge Specimen

3.4.1.1 Introduction

This specimen was designed as a relatively simple way of testing the interlaminar tensile strength of composite materials. It also provides a simple way of scaling the specimens to establish the effect of volume on the material strength in interlaminar tension.

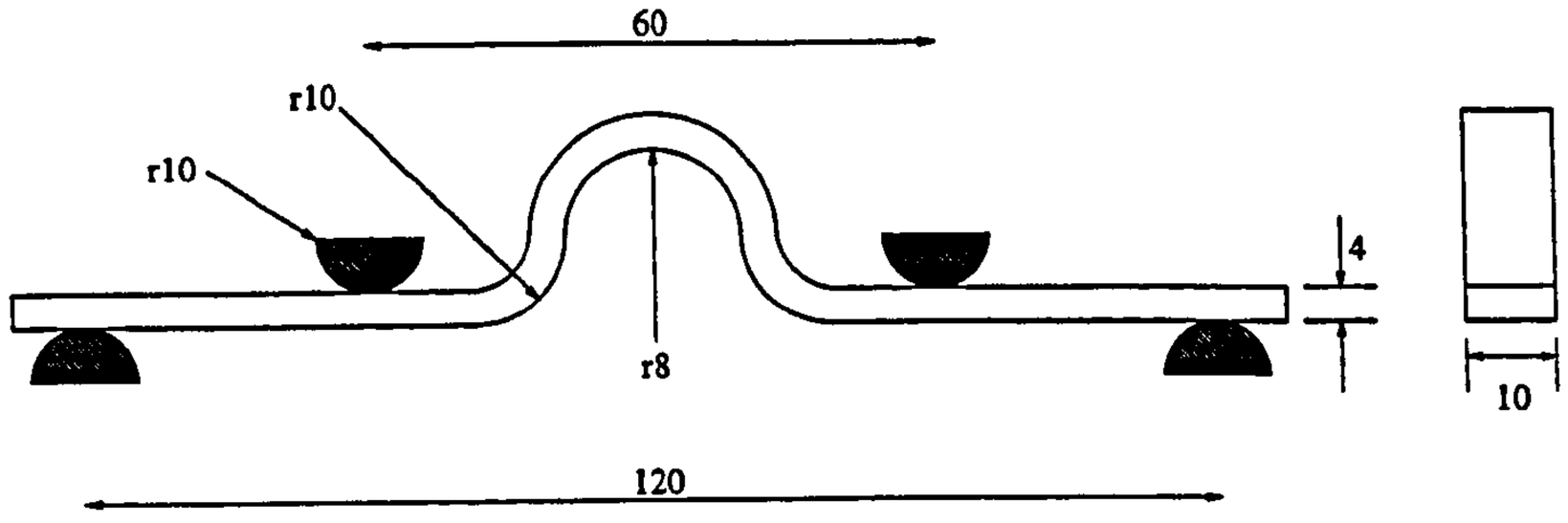

All dimensions in mm

Figure 3.3: Medium Humpback Bridge Specimen Dimensions

A schematic of the specimen with the loading nose locations is shown in Figure 3.3. The dimensions are shown for a medium sized specimen. In order to calculate the effect of stressed volume on the strength of the material, it was necessary to perform a series of scaled tests on the specimen. The dimensions for a small specimen were half the magnitude of those shown, and a large specimen had double the dimensions. The roller dimensions were also scaled in this way, the roller diameter for the medium-sized specimens was 20mm. The finite element analysis slice model mesh is shown in Fig.3.4.

3.4.1.2 Testing

A number of specimens were laid up in plates over tooling shaped to the relevant dimensions for each specimen size. 16, 32 and 64 plies for the small, medium and large specimens respectively. All specimen sizes were cured according to the manufacturer's instructions (Hexcel [65]), the 32 and 64-ply specimens requiring a dwell period. After curing, each specimen was cut from the cured plates using a diamond saw. The dimensions of each specimen were carefully measured to establish mean dimensions for analysis purposes. The full dimensions are recorded in Appendix A along with all test results.

Specimens were tested on an Instron 1341 test machine under displacement control. The displacement rates were scaled with specimen size, ensuring a consistent strain rate for all the specimens. The medium-sized specimen rate was 1.05mm/min. The mean max-

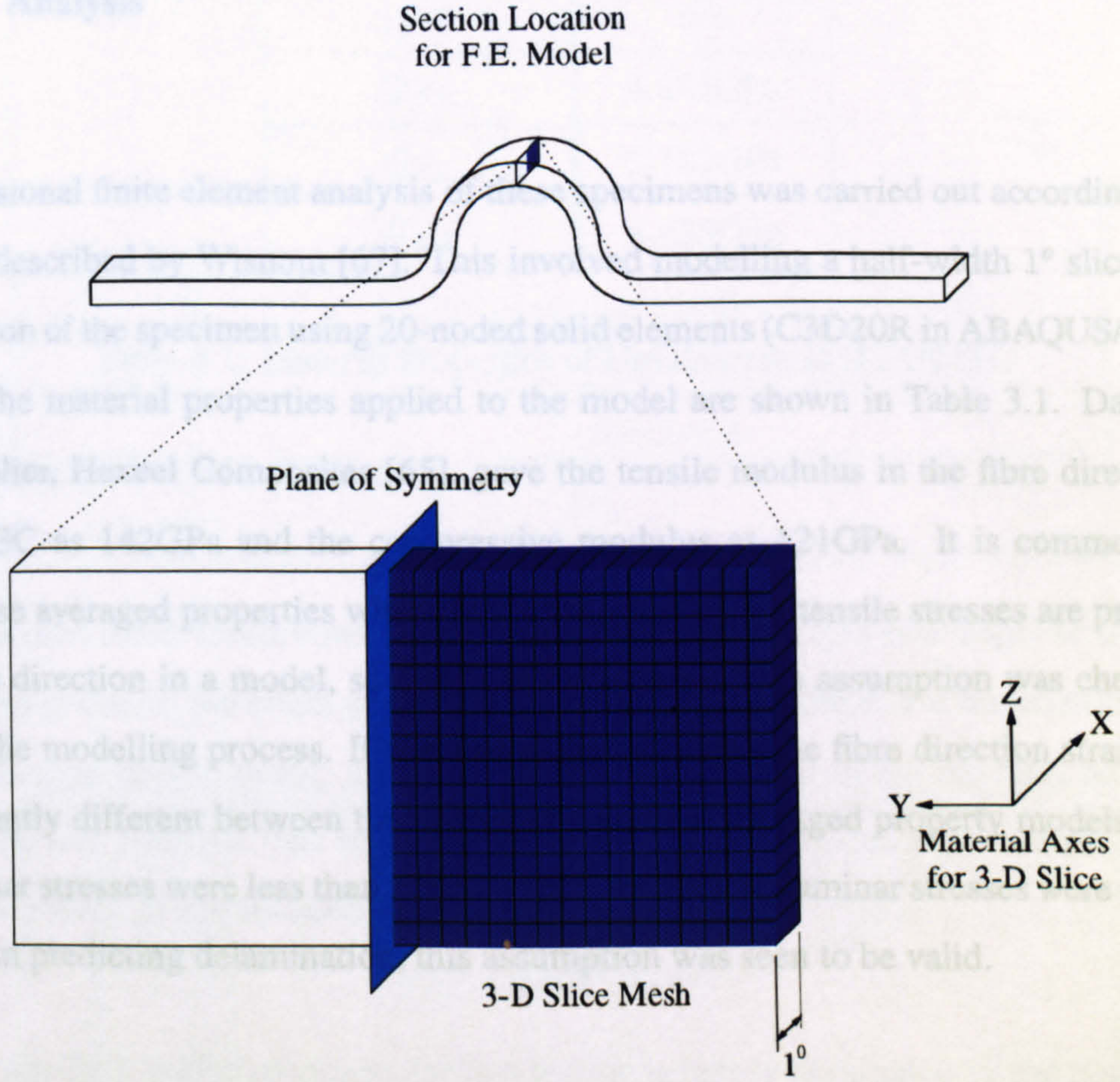

Figure 3.4: Humpback Bridge F.E. Mesh

imum load reached in all tests was that used as the failure load in analysis. All failures were sudden and brittle in the form of a delamination, generally occurring just below the centreline of the section. Analysis showed that this was at the neutral axis of the curved structure, and the peak interlaminar stress point.

3.4.1.3 Analysis

3-dimensional finite element analysis of these specimens was carried out according to the method described by Wisnom [67]. This involved modelling a half-width 1° slice of the test section of the specimen using 20-noded solid elements (C3D20R in ABAQUS/Standard [70].) The material properties applied to the model are shown in Table 3.1. Data from the supplier, Hexcel Composites [65], gave the tensile modulus in the fibre direction of HTA/913C as 142GPa and the compressive modulus as 121GPa. It is common practice to use averaged properties where both compressive and tensile stresses are present in the fibre direction in a model, so 131.5GPa was used. This assumption was checked as part of the modelling process. It was found that although the fibre direction strains were significantly different between the bi-modular and the averaged property models, the interlaminar stresses were less than 1% different. As the interlaminar stresses were the most critical in predicting delamination, this assumption was seen to be valid.

Each face of the slice model had to be constrained to behave in a manner equivalent to the rest of the specimen being present for a case of pure bending. This was achieved by using multi-point constraint equations on each of the nodes on the cut faces of the slice. The load was applied as a couple which produced the same bending moment as that applied by the four-point bending rig at the mean failure load of the specimens.

The following results were produced from the medium-sized specimen model. The interlaminar tensile stress is the most critical stress component in an interlaminar tensile strength specimen. This is shown in Figure 3.5 on an exaggeratedly deformed mesh. It is viewed along the specimen looking at half of the cross-section with the centre-line of the

Material Property	HTA/913C 0°
E_X	131.5GPa
E_Y	9.2GPa
E_Z	9.2GPa
ν_{XY}	0.3
ν_{YZ}	0.45
ν_{XZ}	0.3
G_{XY}	4.875GPa
G_{YZ}	3.103GPa
G_{XZ}	4.875GPa

Table 3.1: Material Properties of Unidirectional HTA/913C

specimen on the left side of the mesh.

The deformed mesh bends downwards at the right-hand end (the free-edge) of the specimen. This is due to the effect of anti-clastic curvature, and there is a resultant reduction in interlaminar tensile stress. The mean peak stress reached in the medium sized HBB specimens was 106MPa. The interlaminar tensile stress at the free edge was around 20% lower as a result of the anti-clastic curvature.

In the humpback bridge specimen, the test section is highly dominated by the interlaminar tensile stress, but it does contain other stress components. The next largest inter-fibre stresses act in the transverse direction and are shown in Figure 3.6.

The magnitude of these stresses are significant in the region of highest interlaminar tensile stress, and should therefore be taken into account in assessing the matrix failure. The transverse stress is caused by the anti-clastic curvature, or rather the resistance of the curved laminate to submit to anti-clastic bending. The free edge cannot resist and therefore does bend, and hence there are no significant transverse stresses. The anti-clastic bending also gives rise to interlaminar shear stresses in the plane of the cross-section

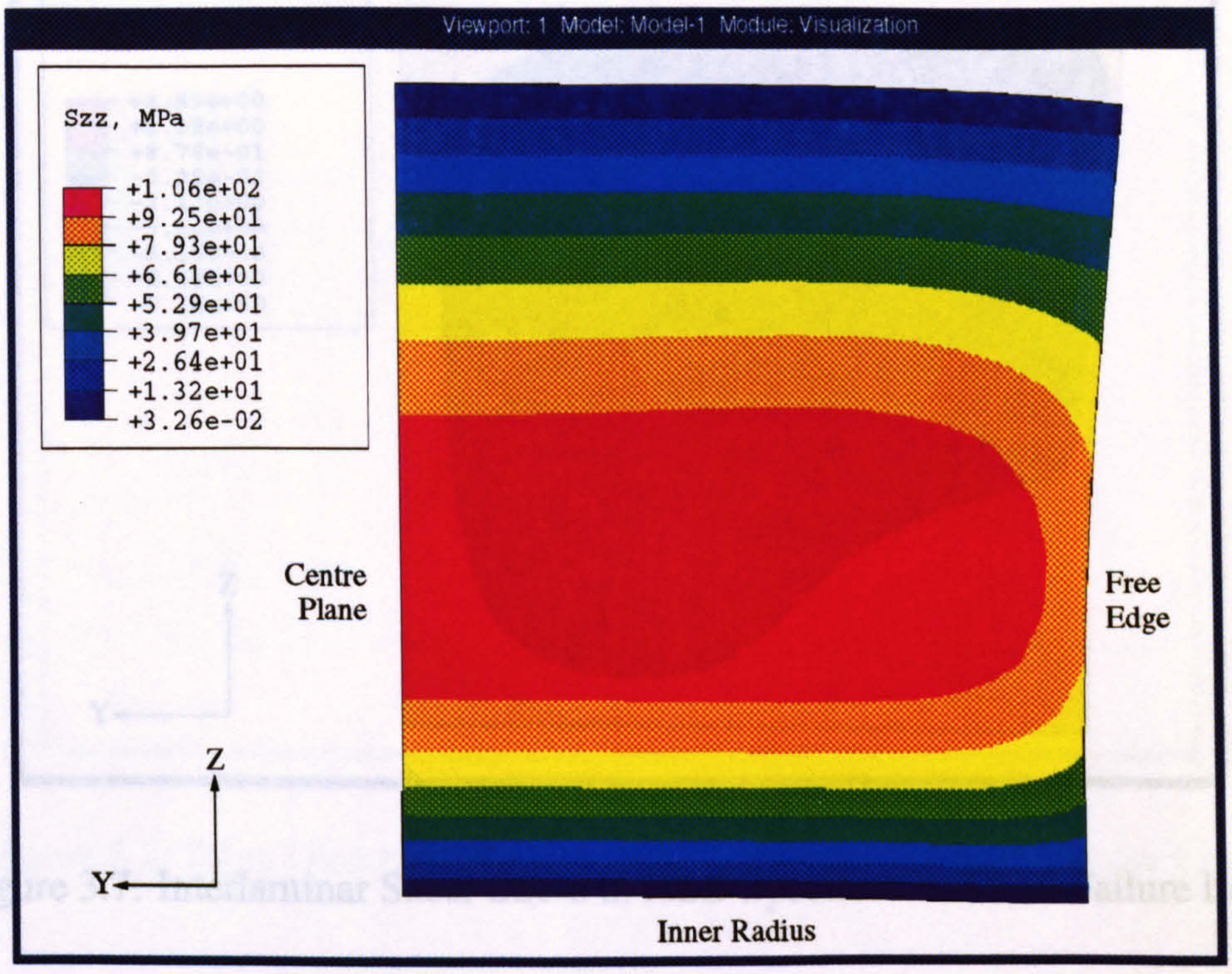

Figure 3.5: Interlaminar Tensile Stress in HBB Specimen at Mean Failure Load

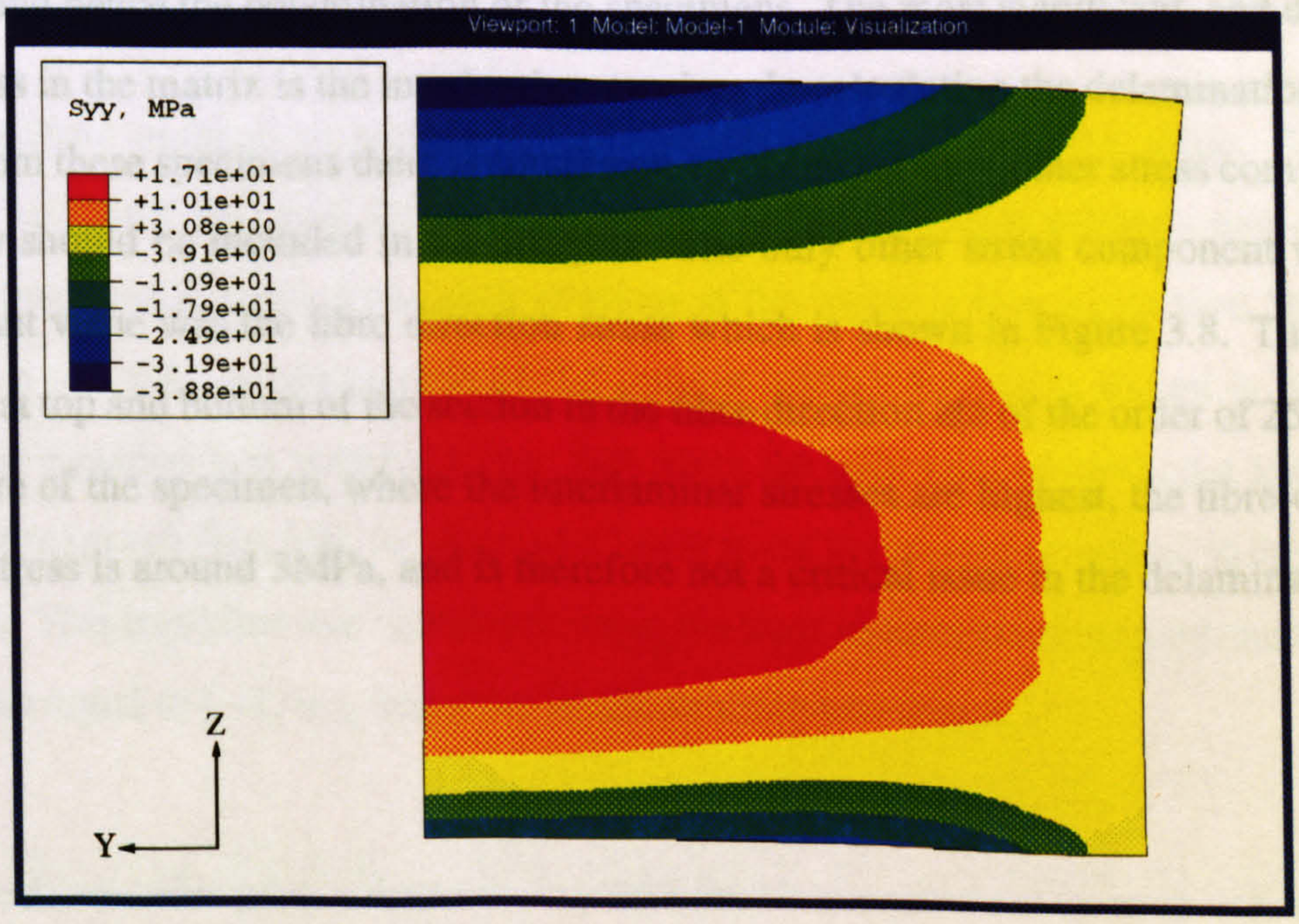

Figure 3.6: Transverse Stress in HBB Specimen at Mean Failure Load

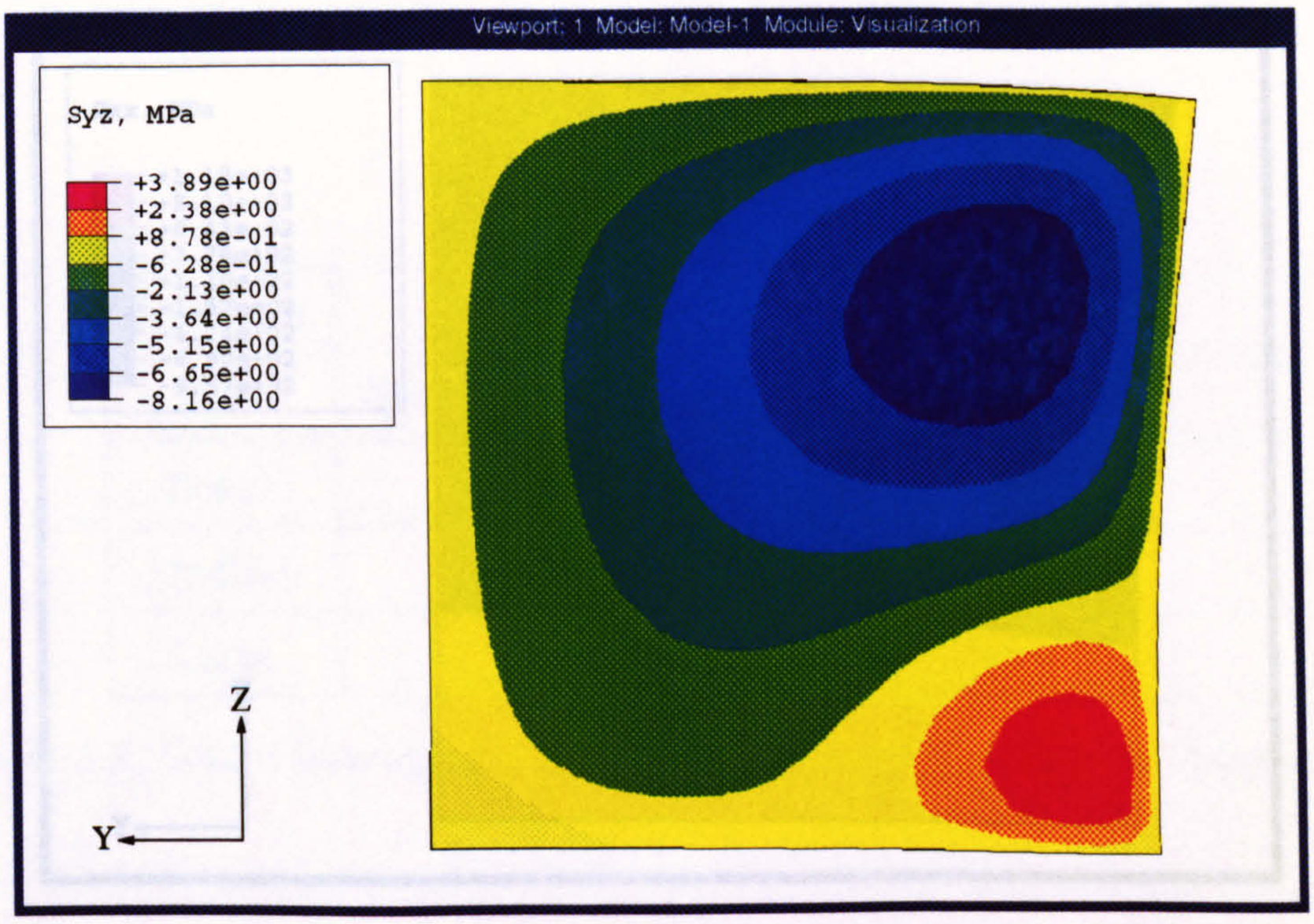

Figure 3.7: Interlaminar Shear Stress in HBB Specimen at Mean Failure Load

which are shown in Figure 3.7.

All of the stresses in the test section of the HBB specimen contribute to the failure of the matrix, and hence the delamination of the specimens. The most significant, and dominating, stress in the matrix is the interlaminar tension. In calculating the delamination failure stress from these specimens there is significant contribution from other stress components, and they should be included in the analysis. The only other stress component with any significant value was the fibre direction stress which is shown in Figure 3.8. The matrix stresses at top and bottom of the section in the fibre direction are of the order of 25MPa. In the centre of the specimen, where the interlaminar stresses are highest, the fibre-direction matrix stress is around 3MPa, and is therefore not a critical issue in the delamination.

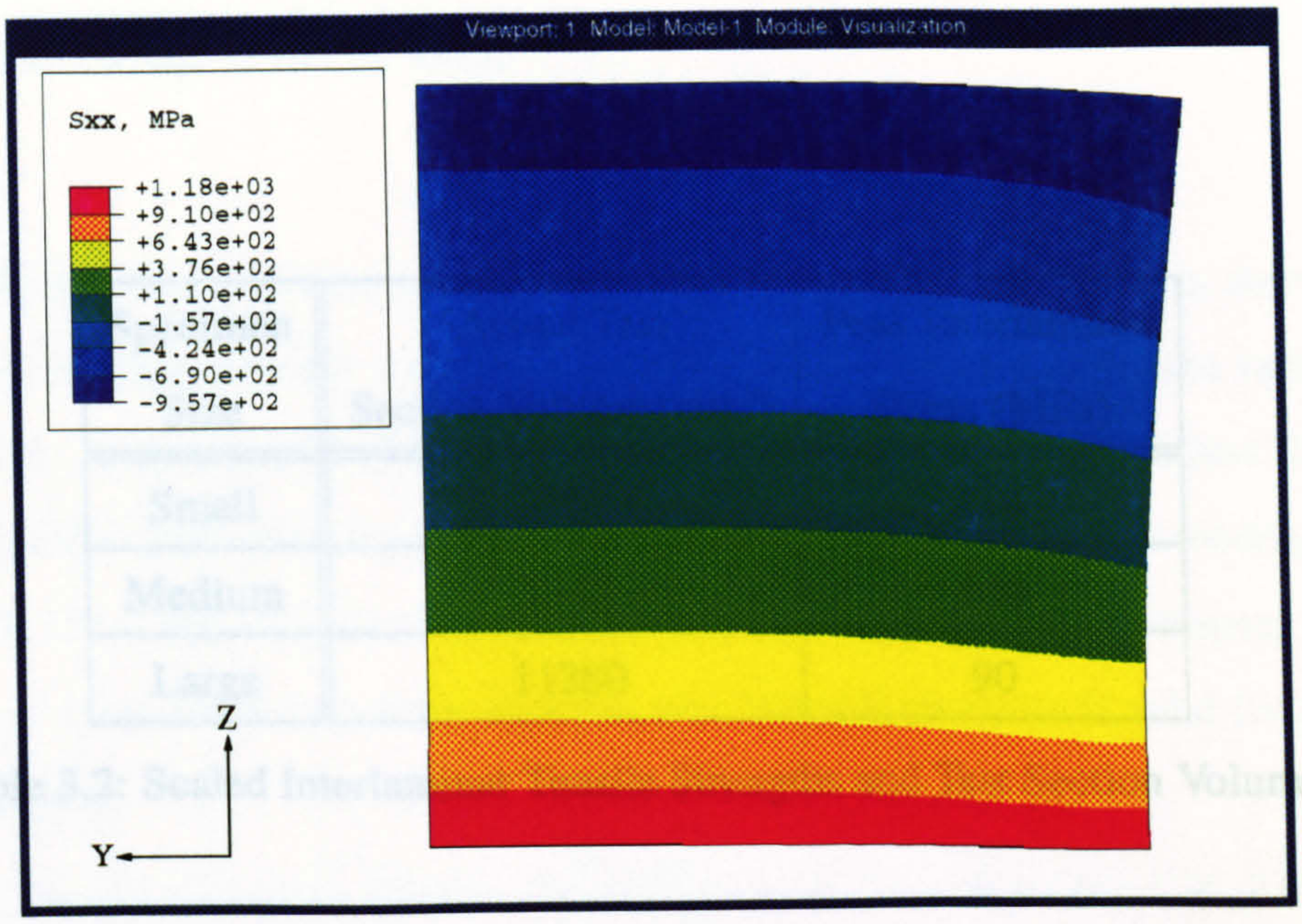

Figure 3.8: Fibre Direction Stress in HBB Specimen at Mean Failure Load

3.4.2 Application of the Procedure

3.4.2.1 The Initial Weibull Modulus Value

The procedure outlined in section 3.3 requires the Weibull modulus value. This was initially estimated by using the three specimen size test section volumes and the peak interlaminar tensile stress from each analysis at the mean failure loads (see Table 3.2) plotted on a graph. A formulation of the volume effect equation is shown in Eqn. 2.1. From this equation it is possible to see that when the data were plotted on a log(stress)-log(volume) graph (Fig.3.9), the slope of a linear trend line would be related to the Weibull modulus. This trend line was calculated using the least squares error method and the slope of the line equal to $(-1/m)$, hence an initial m value was found.

The linear trend line gave a slope of -0.0553 which is equivalent to an m value of 18.1. With the initial Weibull modulus value evaluated, the 3-D slice model stress levels could be calculated and a unit volume matrix strength (S_0) value found for the HTA/913C material.

Specimen Size	Actual Test Section Volume (mm^3)	Peak Interlaminar Stress (MPa)
Small	157	114
Medium	1332	106
Large	11280	90

Table 3.2: Scaled Interlaminar Tensile Strengths and Test Section Volumes

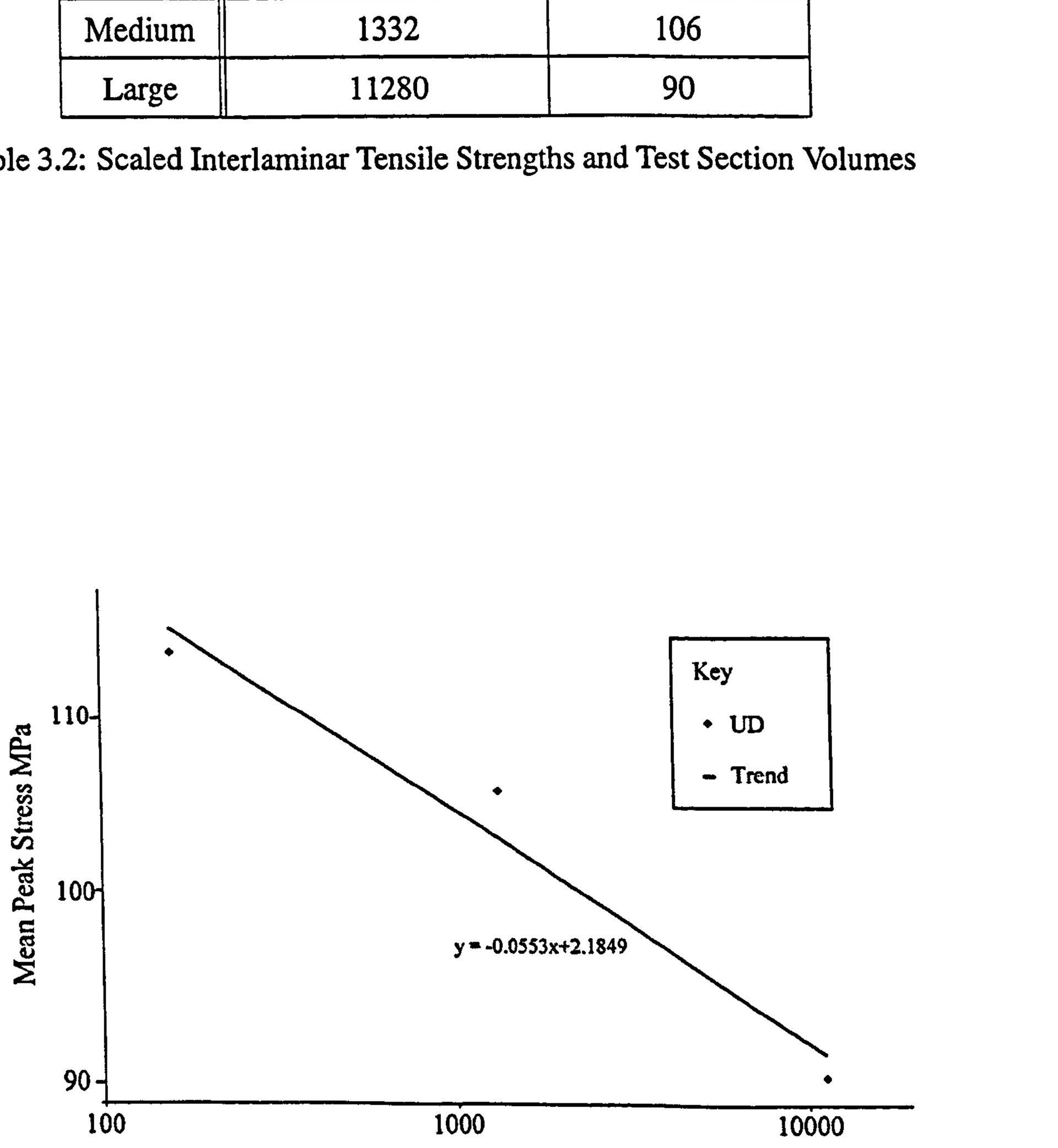

Figure 3.9: Interlaminar Tensile Stress at Failure vs. Specimen Volume

3.4.2.2 Calculation of the S_0 Value

The UVES procedure was then applied to all three of the HBB slice models. Results from the centroid of each element were used to calculate the stress component values using equation 3.3. A spreadsheet (Microsoft Excel 97 [71]) was used to process the results from each model. The unit volume equivalent stress values from the three models, in MPa, were 131.2, 136.8 and 130.5 for the small, medium and large specimens respectively. The similarity of these results confirms that the trial Weibull modulus is valid for use in all further analyses.

It was prudent for a conservative value for S_0 to be chosen, so 130.5MPa was selected. This will be applied to a specimen which suffered a delamination failure in a region of uni-directional plies in Chapter 5. Before this, however, the method will be automated to reduce user time and to allow general laminates to be used.

Chapter 4

Extension of the Method to General Laminates

4.1 Introduction

In the previous chapter, a stress based method of predicting delamination was described and applied to a series of scaled interlaminar tensile strength coupons. From this it was possible to evaluate the size effect and calculate the Unit Volume Equivalent Strength of the HTA/913C material. In this chapter, the method will be extended to cope with any angle of ply and resin pockets. After this, the interlaminar tensile strength of non-UD material will be studied in order to check the validity of the technique.

4.2 User Defined Material Behaviour

In order to allow the method to cope with angle-plies and allow the Raghava stress to be calculated automatically, it was necessary to introduce 'User Material' behaviour for use within ABAQUS. The main reason for producing the user defined material behaviour code was so that the post-processing task could be simplified. In order for this to be carried out, standard orthotropic elastic material behaviour had to be included as part of the routine. This code was written in Fortran77 [72] and replaced the built-in orthotropic material code which provides the material stiffness matrix and stress information for each integration point in a finite element model. It had to be able to deal with ply angles for multi-directional laminates and different material moduli for regions of pure resin and other materials. It was also necessary for the code to be used in 2-D and 3-D models which results in different information requirements for ABAQUS. The main purpose of the code is to calculate the overall Raghava stress within the matrix ready for post-processing with the element volume for the unit volume equivalent stress calculation and delamination prediction. This post-processing task has also been coded in Fortran77, and is described later.

4.2.1 User Material Code

The user material code is used by ABAQUS to calculate stress increments and total stresses for each increment in a loading step. The code is also required to produce the stiffness matrix (referred to as the Jacobian) for the material at the particular integration point of the element currently being dealt with. In order for the code to be able to deal with different materials, ABAQUS can send useful information included in the .INP file to the user code, such as the ply stiffness and ply angle. The user code calculates all stress components for the analysis using the strains. It also evaluates the Raghava stress for the matrix material which is sent back to ABAQUS as a state dependent variable.

4.2.1.1 Orthotropic Elastic Material Behaviour

At the ply level, the orthotropic material behaviour is generally represented in composite materials by the $[Q]$ matrix [73]. In this example, all six stress-strain components and the complete matrix are shown in Equation 4.1. The stresses and strains are taken orthogonally to the fibre direction, subscript 1 referring to the fibre direction, 2 to the transverse in-plane and 3 to the interlaminar.

$$\begin{pmatrix} \sigma_{11} \\ \sigma_{22} \\ \sigma_{33} \\ \tau_{23} \\ \tau_{13} \\ \tau_{12} \end{pmatrix} = \begin{pmatrix} Q_{11} & Q_{12} & Q_{13} & 0 & 0 & 0 \\ Q_{12} & Q_{22} & Q_{23} & 0 & 0 & 0 \\ Q_{13} & Q_{23} & Q_{33} & 0 & 0 & 0 \\ 0 & 0 & 0 & Q_{44} & 0 & 0 \\ 0 & 0 & 0 & 0 & Q_{55} & 0 \\ 0 & 0 & 0 & 0 & 0 & Q_{66} \end{pmatrix} \begin{pmatrix} \epsilon_{11} \\ \epsilon_{22} \\ \epsilon_{33} \\ \gamma_{23} \\ \gamma_{13} \\ \gamma_{12} \end{pmatrix}$$

Where

$$Q_{11} = E_{11}(1-\nu_{23}\nu_{32})/\Delta$$

$$Q_{12} = (\nu_{21}+\nu_{31}\nu_{23})E_{11}/\Delta$$

$$Q_{13} = (\nu_{31}+\nu_{21}\nu_{32})E_{11}/\Delta$$

$$Q_{22} = E_{22}(1-\nu_{31}\nu_{13})/\Delta$$

$$Q_{23} = (\nu_{32}+\nu_{12}\nu_{31})E_{22}/\Delta$$

$$Q_{33} = E_{33}(1-\nu_{12}\nu_{21})/\Delta$$

$$Q_{44} = G_{23}$$

$$Q_{55} = G_{13}$$

$$Q_{66} = G_{12}$$

$$\Delta = 1-\nu_{12}\nu_{21}-\nu_{23}\nu_{32}-\nu_{13}\nu_{31}-2\nu_{21}\nu_{32}\nu_{13}$$

(4.1)

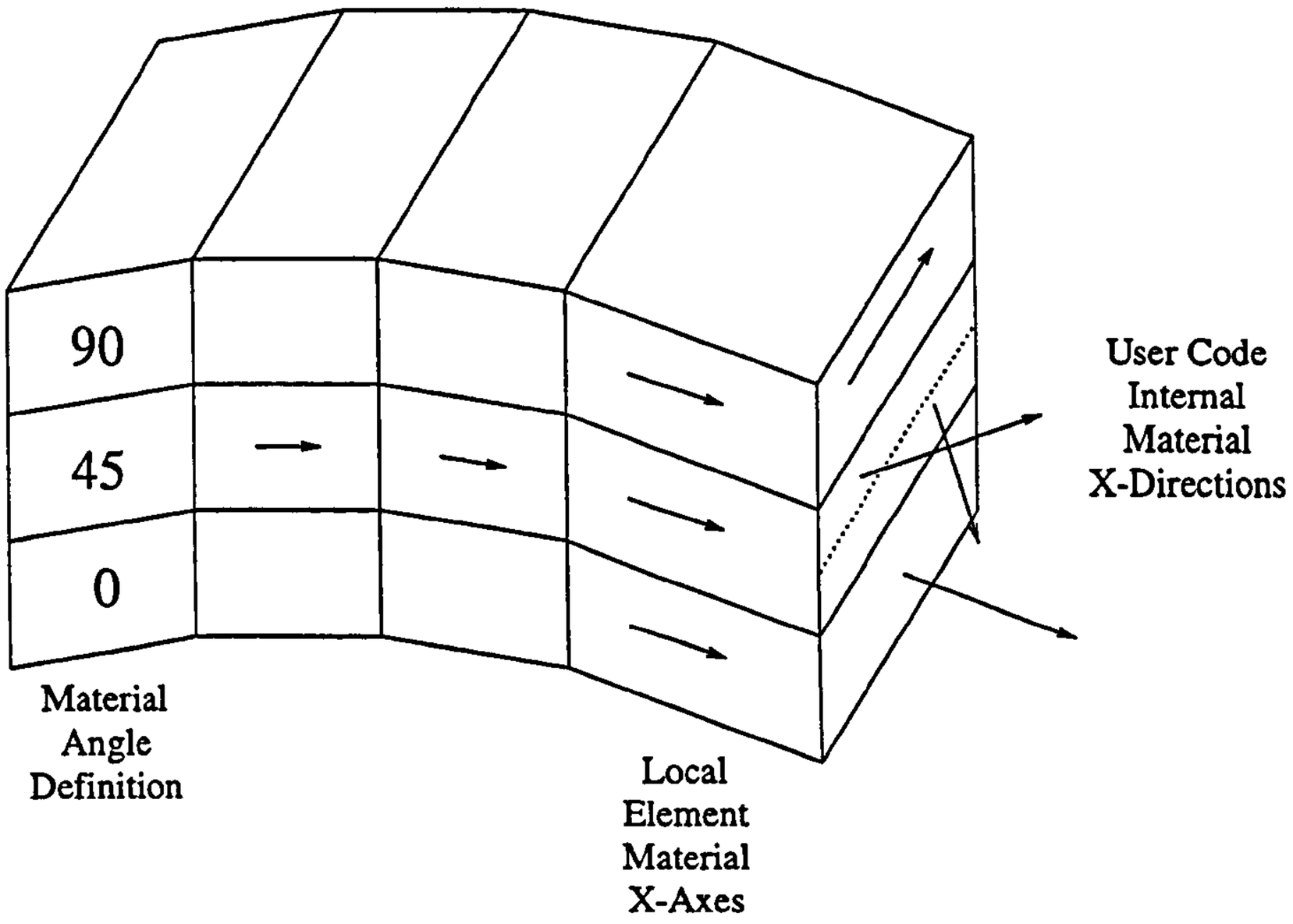

Figure 4.1: Ply Orientation for User Coded Material Properties

Although the ply behaviour is a required part of the code, and standard composite material notation could be used, it was also necessary to consider the requirements of ABAQUS. In a 2-dimensional plane strain case, the element axes are the X and Y, with Z being through the thickness of the element. These axes are different to those of the composite ply, so care had to be taken in order for the theory to produce the required information correctly. Also, the ply orientation had to be dealt with by the user code (see Figure 4.1), introducing further complexity.

The calculation of the element-level Jacobian and the stress increments in a 2-D plane strain case are governed by Equation 4.2. It can be seen that the 2 and 3 subscripts refer to the standard composite ply directions, and for a 0° ply are in the element Z and Y directions respectively. The ply angle rotation operation is also part of the $[\overline{Q}]$, with the ply angle being defined by θ. The ply angle is usually considered as an angular rotation about the ply Z-axis, and the theory available in the literature covers this extensively. As this user developed code had to rotate the ply angle about the element's Y-axis, the standard theory had to be modified so that the stress and strain calculations would be correct.

$$\begin{pmatrix} \sigma_{XX} \\ \sigma_{YY} \\ \sigma_{ZZ} \\ \tau_{XY} \end{pmatrix} = \begin{pmatrix} \overline{Q}_{11} & \overline{Q}_{13} & \overline{Q}_{12} & 0 \\ \overline{Q}_{13} & \overline{Q}_{33} & \overline{Q}_{23} & 0 \\ \overline{Q}_{12} & \overline{Q}_{23} & \overline{Q}_{22} & 0 \\ 0 & 0 & 0 & \overline{Q}_{55} \end{pmatrix} \begin{pmatrix} \epsilon_{XX} \\ \epsilon_{YY} \\ \epsilon_{ZZ} \\ \gamma_{XY} \end{pmatrix}$$

Where

$\theta = Ply\ Angle$

$$\overline{Q}_{11} = Q_{11}\cos^4\theta + 2(Q_{12}+2Q_{66})\cos^2\theta\sin^2\theta + Q_{22}\sin^4\theta$$

$$\overline{Q}_{12} = (Q_{11}+Q_{22}-4Q_{66})\cos^2\theta\sin^2\theta + Q_{12}(\cos^4\theta+\sin^4\theta)$$

$$\overline{Q}_{13} = Q_{13}\cos^2\theta + Q_{23}\sin^2\theta$$

$$\overline{Q}_{22} = Q_{11}\sin^4\theta + 2(Q_{12}+2Q_{66})\cos^2\theta\sin^2\theta + Q_{22}\cos^4\theta$$

$$\overline{Q}_{23} = Q_{13}\sin^2\theta + Q_{23}\cos^2\theta$$

$$\overline{Q}_{33} = Q_{33}$$

$$\overline{Q}_{55} = Q_{55}\cos^2\theta + Q_{44}\sin^2\theta$$

(4.2)

In situations where there are pairs of $\pm 45^o$ plies together in an element, the material properties are averaged. This means that the twist/extension/shear couplings are assumed to be relatively insignificant in the generation of interlaminar stresses in a 2-dimensional plane strain model. This is reasonable because the plane strain assumption for the model does not allow extension-twist or extension-shear coupling to occur.

Another area of material behaviour which was important to establish was the method of dealing with regions of pure resin material, or resin pockets. These occur wherever plies are dropped from within a laminated composite material structure. The method is required to calculate the effective matrix stress in the fibre-direction of the ply, and does

so by using the ratio of matrix elastic modulus to the composite ply elastic modulus. This information is included in the definition of the material along with the fibre angle and elastic moduli. If the material is pure resin, a value of 1 is used for the ratio, and the modulus data for the matrix material without fibres is given to the relevant elements.

By treating the pure matrix regions in this way, the matrix strength is assumed to be the same as the composite in delamination. The strength of the pure 913 epoxy resin was not found in the literature, nor was it reported by the manufacturer. An assumption regarding the strength of the resin had to be made, and by simply assuming the same parameters as for the resin when in the composite, a solution was found.

4.2.1.2 Coding

The 2-D plane strain user material code was written in Fortran77 [72] and is included in Appendix C. There are two main parts to the routine, the first providing the interface between the user defined code and ABAQUS, handling the data transfer between the two. This information was supplied by HKS[70] in the user manuals for ABAQUS. The ABAQUS software communicates with the code and sends the total and incremental strain for the current increment of the analysis along with the material data from the input file.

The next portion of the user code calculates the $[Q]$ values for the local ply level Jacobian. These are then used to calculate the $[\overline{Q}]$ values for the plane strain element Jacobian. The element level stress increments and totals are then calculated for the current time increment. These are sent back to ABAQUS at the end of the routine.

The local ply stresses also need to be calculated, and to start this process, the 4 total local ply strains are calculated. Then the total ply stresses are calculated using the $[Q]$ values. At this point, the principal stresses should be calculated, but before this can happen, the

fibre direction stress must be factored down to that of the matrix alone. To ensure that the shear stress is in the correct plane for the principal stress calculation, it is necessary to exchange the interlaminar and transverse stresses because the element and material local axes are in different directions. If this swap operation is not performed, then the subroutine to calculate the principal stresses will do so incorrectly. This does not affect the behaviour of the elements because the stiffness matrix and stresses have already been calculated and are not altered.

The 'SPRINC' subroutine calculates the principal stresses and is supplied by HKS as part of ABAQUS. Now that the principal stresses are calculated, the Raghava stress can be calculated ready for output at the end of the routine as a state dependent variable. ABAQUS sends this value to the results file with the element area when requested in the input file. The information in the results file can be processed using another Fortran77 routine.

4.2.2 Post-Processing Code

The results file (.fil) contains any requested output information sent to it from the analysis, from stress and strain values to the reaction forces at particular nodes. In the case of these analyses, the areas and Raghava stress values for every element integration point or centroid are sent to the file for post-processing. A separate Fortran code takes these values and produces the overall Weibull unit volume equivalent stress for each load case analysed using Eqn. 3.3. The code is reproduced in Appendix D.

The first part of the code accesses the results file and pulls the contents of this file into an array. These values include the areas for each integration point or centroid, Raghava stress, step number and element numbers for each step in the analysis. Once formatted in the array, the data is easily processed incrementally.

The next part of the code requests the volume factor to be entered manually. This value is the ratio of the volume of the specimen compared to volume of the model. This has to be entered manually as it can vary from model to model.

The final part of the code contains a loop which cycles through all of the elements in turn adding the Weibull values together to produce the total Weibull value. The unit volume equivalent stress for that step and load case is then calculated using Eqn. 3.3. The step and UVES values are then output to the screen for the user. The load for predicted failure can then be calculated by linear interpolation between the relevant results.

The process of calculating the unit volume equivalent stress could have also been included as part of the ABAQUS analysis. This would have involved much of the same code, but it would have been within a user subroutine called 'URDFIL' which is accessed internally by ABAQUS during analysis. The decision to use an external method was largely because of the need to enter different volume ratios for different models. The author felt that an external method would be more convenient in the long run.

4.2.3 Application to Specimens/Models

With the delamination failure prediction code established, it needs to interface with ABAQUS in order to be useful. This is a relatively straightforward process whereby the normal material definition within the input file is replaced with references to the user material code. This includes the number of state dependent variables, the material data and ply angle. Part of an example input file with the critical lines highlighted is supplied in Appendix E.

The elements in the area of interest have the USER material assigned to them. ABAQUS requires the material properties, ply angle and ratio of matrix to fibre direction modulus to be entered here. The USER code calculates the necessary stress values for ABAQUS to be able to output it for graphical post-processing, and also outputs the Raghava stress

and element areas to the results file for post-processing using the UVES custom Fortran code.

4.3 Non-UD Interlaminar Strength

4.3.1 Specimen

In Chapter 3, the interlaminar tensile strength of uni-directional material was assessed. The method proposed in this thesis was intended to predict delamination between plies in general, and not just 0^o plies. In order to appraise the method's effectiveness in predicting delamination in a multi-directional laminate, it was applied to an HBB specimen with a $[0_2/\pm 45]_{4S}$ lay-up.

This specimen had the same basic dimensions as the medium sized uni-directional HBB specimen, only with double the width. The width increase was applied to limit the edge effect issue, which often affects composite materials, and increase the central constant stress state region. The specimens were loaded in 4-point bending as before, and the mean applied load at failure used to carry out the analysis. A summary of the results is included in Appendix A.

4.3.2 Analysis

4.3.2.1 Stress Due to Bending

The specimen was modelled in the same way as the UD specimens, the slice model technique providing a reasonable approximation to the displacement field of the section of

Property	Magnitude
α_1	$2.2\text{x}10^{-8}$
α_2	$2.7\text{x}10^{-5}$
α_3	$2.7\text{x}10^{-5}$

Table 4.1: Thermal Expansion Coefficient Values

heterogeneous material. The material properties were the same as those used previously, the $\pm 45^{\circ}$ properties being calculated by the user-defined code. In contrast to the unidirectional HBB specimens, these specimens required thermal expansion coefficient data because of the non-UD lay-up. This information could not be found in the literature and could not be provided by the supplier, Hexcel. As a result of this, the data from another carbon-fibre material was used, T300/924 [74]. The expansion properties of the matrix are the most important in generating the expansion coefficients of the composite. The use of another resin system's expansion coefficients is not ideal; however, the order of magnitude of these values do not change between different materials. Results from the analyses performed using these values would be improved by using accurate data, but it was not available. The expansion coefficients used are quoted in Table 4.1.

The mean applied bending moment at failure in the Non-UD specimens was equivalent to 52875Nmm. The interlaminar tensile stress (Figure 4.2) has a lower magnitude when compared to the 32-ply medium sized UD specimens. They had a mean peak stress of 106MPa at failure, whereas these specimens show a mean peak stress of only 98MPa. This difference is discussed later.

The transverse stresses are shown in Figure 4.3. In this case, it is evident that the highest magnitude stresses are in the ± 45 plies, and can be explained by Poisson effects. The 45° plies have very high Poisson ratios and want to expand across the width at the top of the curved beam where it is in compression. The curvature of the beam restrains the material in the centre, and so compressive stresses develop. The material is free to expand at the edge, and the stresses reduce as the edge is approached. In the 0° plies, the transverse stresses are about the same magnitude as those in the UD specimens, and will contribute

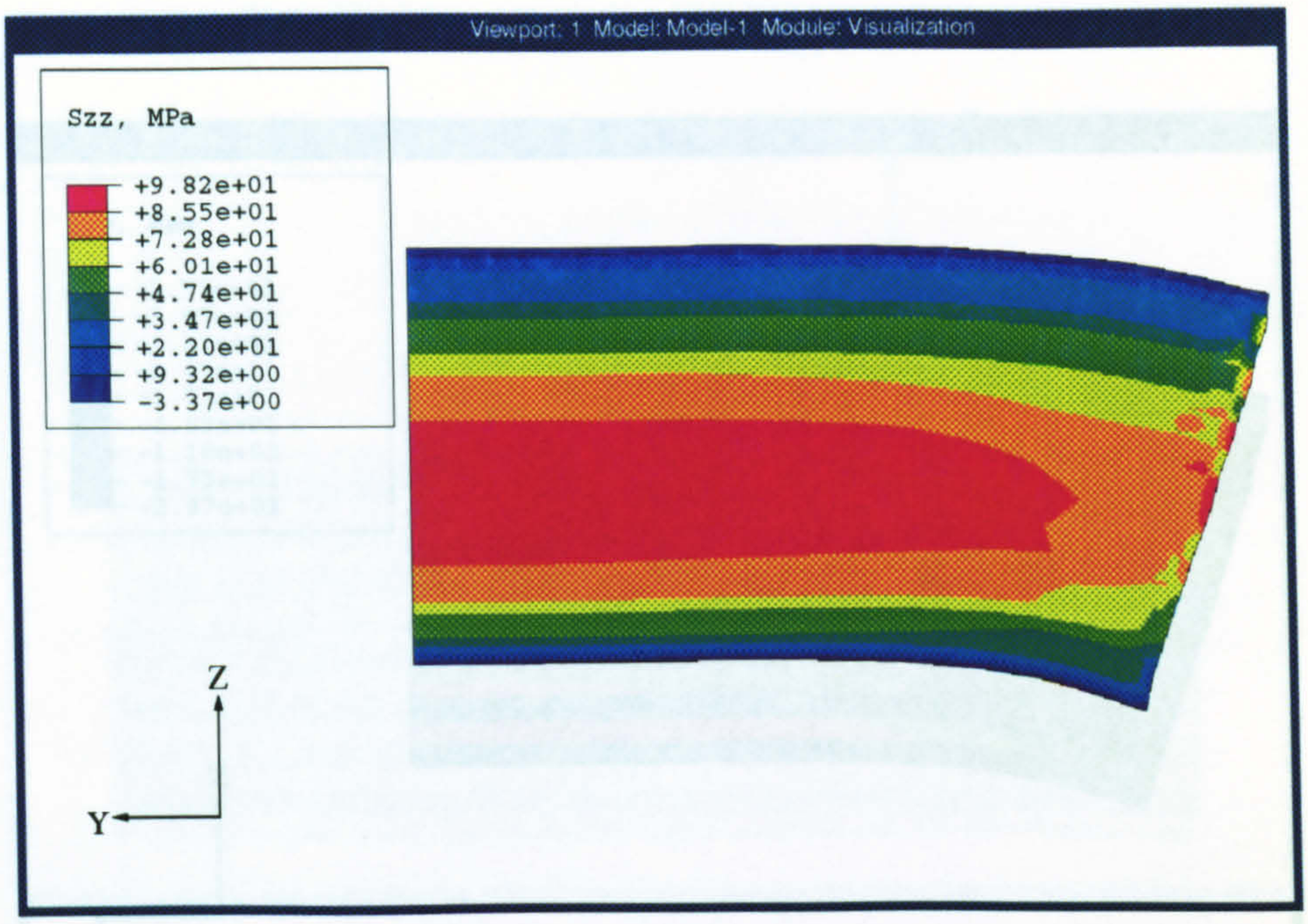

Figure 4.2: Interlaminar Tensile Stress in Non-UD HBB Specimen

to the failure of the matrix in the central interlaminar failure region.

The transverse interlaminar shear stresses (Figure 4.4) are over three times larger than in the UD case. The peak shear stress is in the region of the highest interlaminar tensile stresses, so they will contribute to the overall stress state in the resin.

4.3.2.2 Thermal Residual Stress

The UD HBB specimens had no ply level thermal residual stresses due to curing because all the plies had the same expansion coefficients in each direction. The non-UD specimens did have residual stresses. The 0^o and $\pm 45^o$ plies have different expansion coefficients, and the cure cycle cooling leads to stress in the plane of the plies. The interlaminar stresses were of a very low magnitude away from the free edge (of the order of 10^{-2} MPa) and are not shown here. The thermal stresses therefore do not contribute to the interlaminar stress field, but they do to the intralaminar stresses. As delamination is a matrix failure mode, the matrix stresses are critical in failure, and so thermal stresses will contribute to failure.

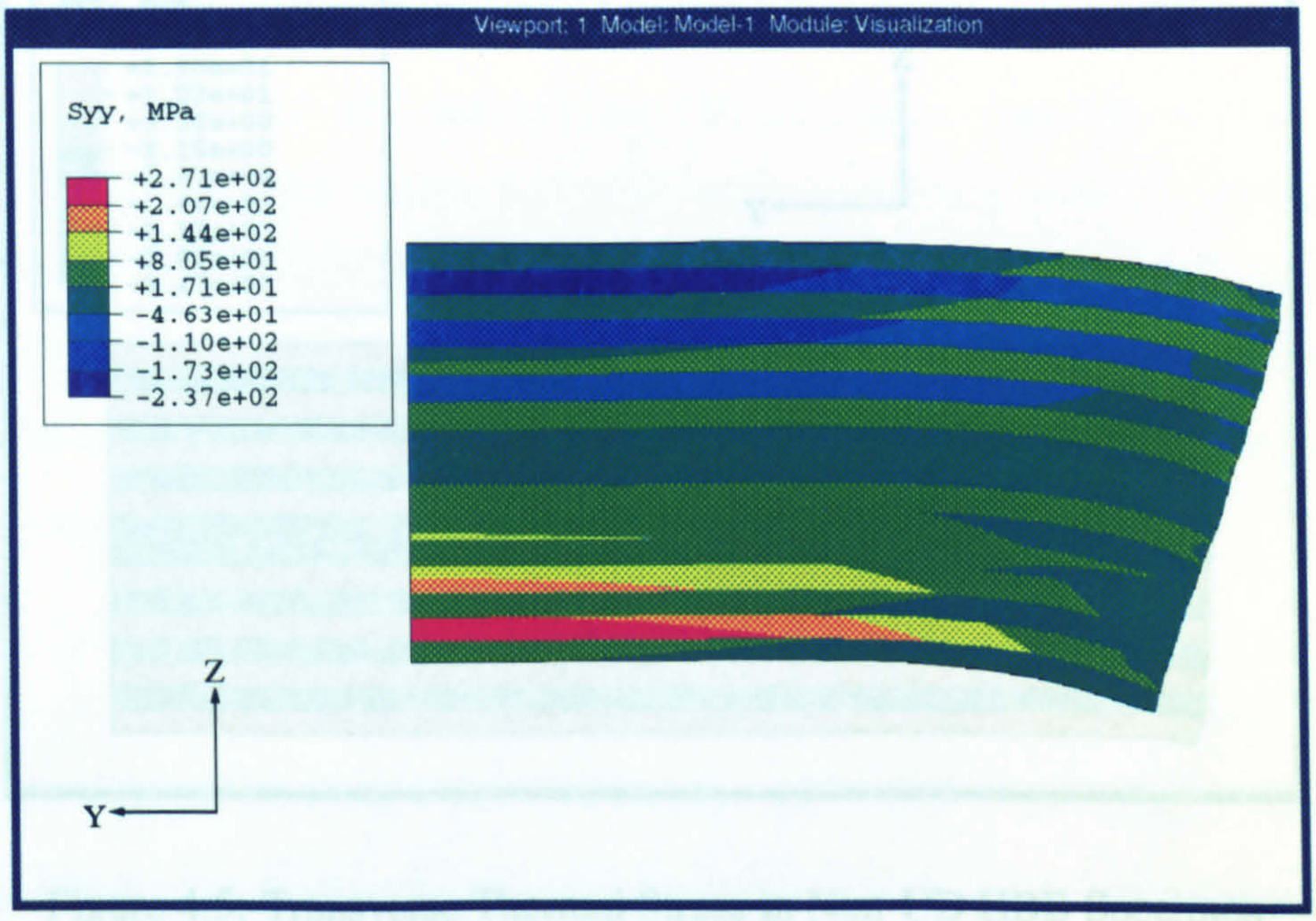

Figure 4.3: Transverse Stress in Non-UD HBB Specimen

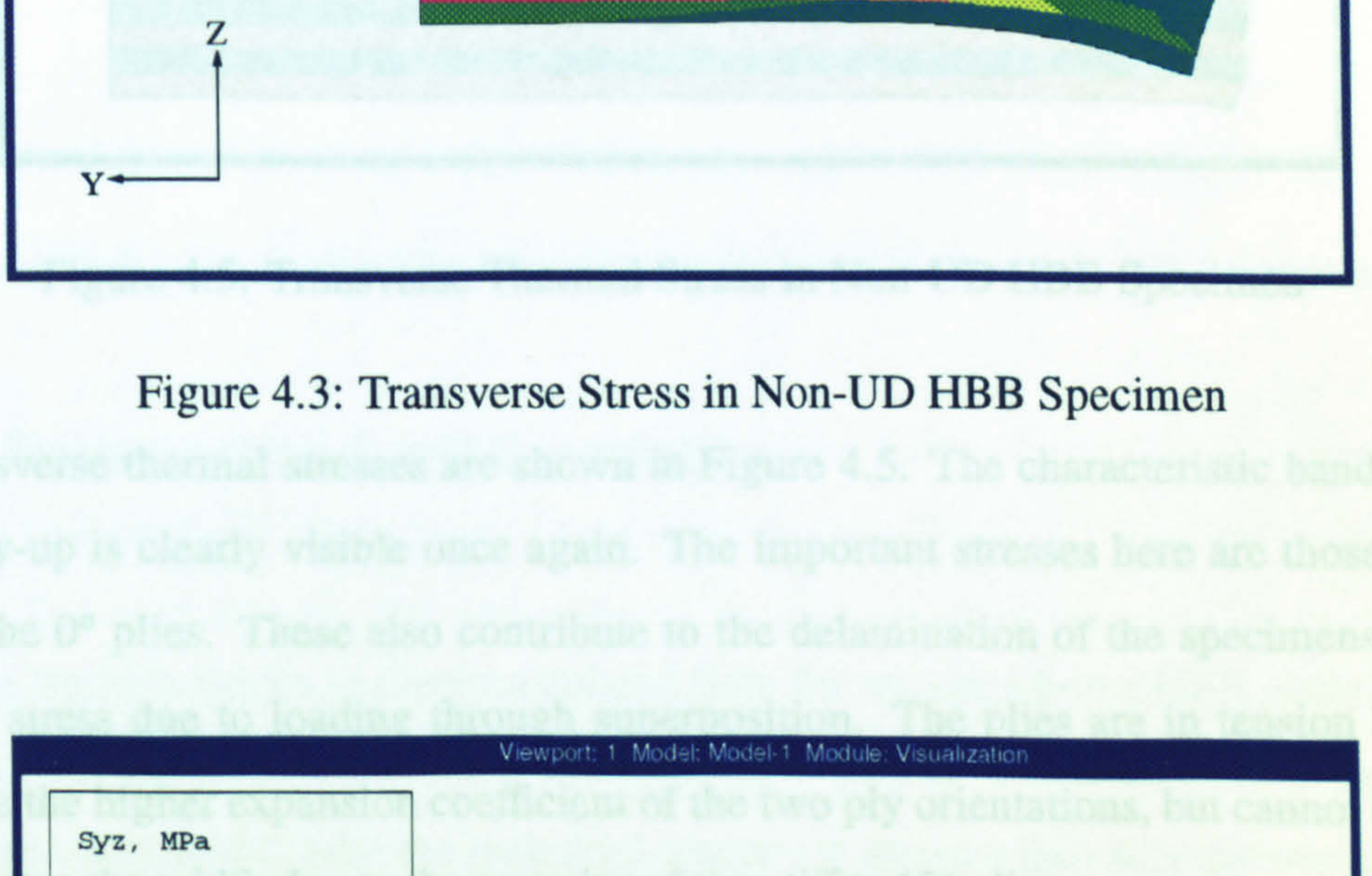

Figure 4.4: Transverse Interlaminar Shear Stress in Non-UD HBB Specimen

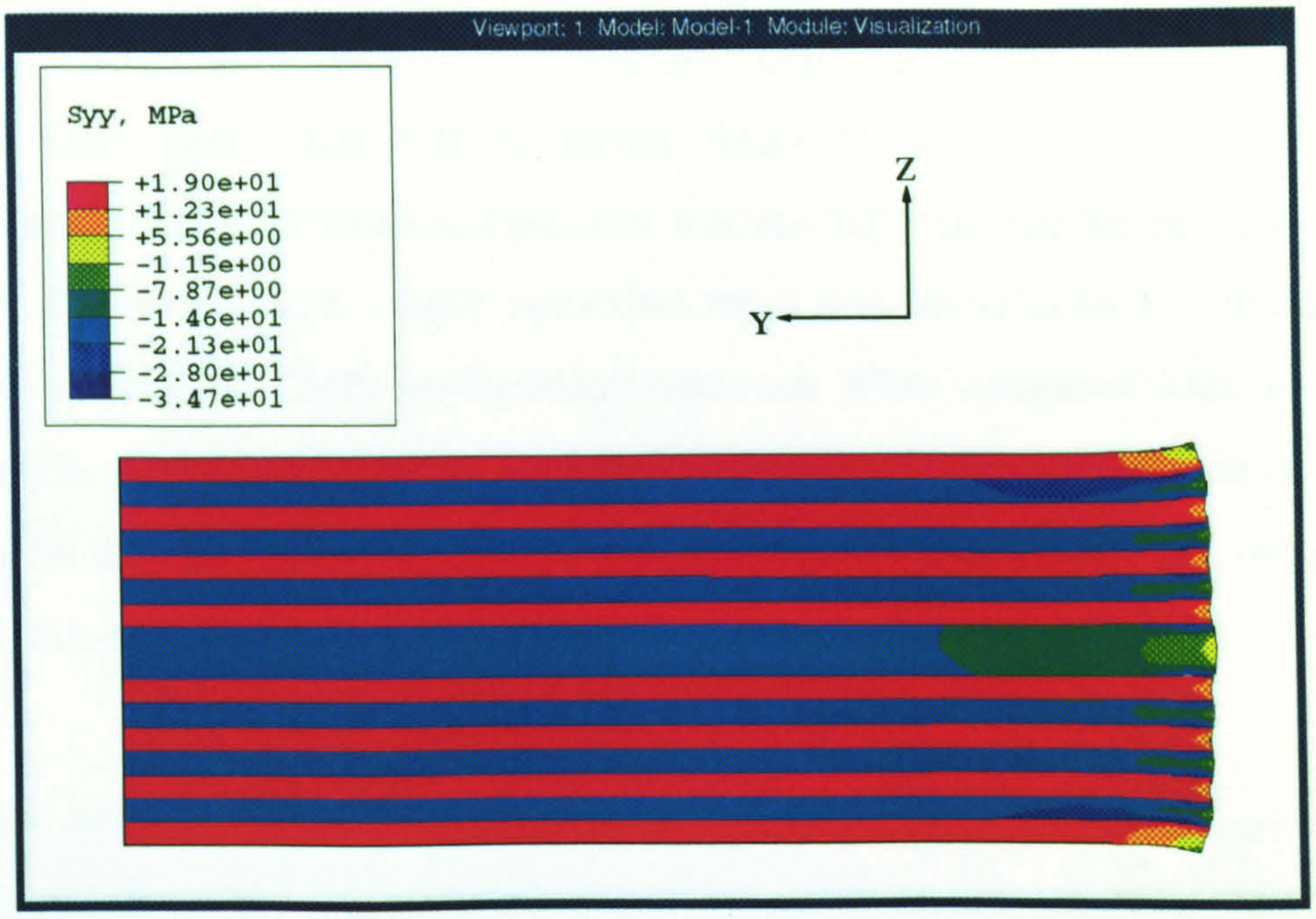

Figure 4.5: Transverse Thermal Stress in Non-UD HBB Specimen

The transverse thermal stresses are shown in Figure 4.5. The characteristic banding due to the lay-up is clearly visible once again. The important stresses here are those in red, seen in the 0^o plies. These also contribute to the delamination of the specimens, acting with the stress due to loading through superposition. The plies are in tension because they have the higher expansion coefficient of the two ply orientations, but cannot contract freely across the width due to the restraint of the stiffer 45^o plies.

The longitudinal stress levels due to thermal effects are shown in Figure 4.6. The stresses are fairly low in the 0^o plies, especially considering the stiff fibre direction. The delamination process is matrix stress dominated, the matrix carried less than 1MPa and will contribute little to the failure in this case. The 45^o plies matrix stress magnitude is only around 4MPa, which is negligible when compared to the through-thickness stresses, so they are not important in this case, but will be included nevertheless.

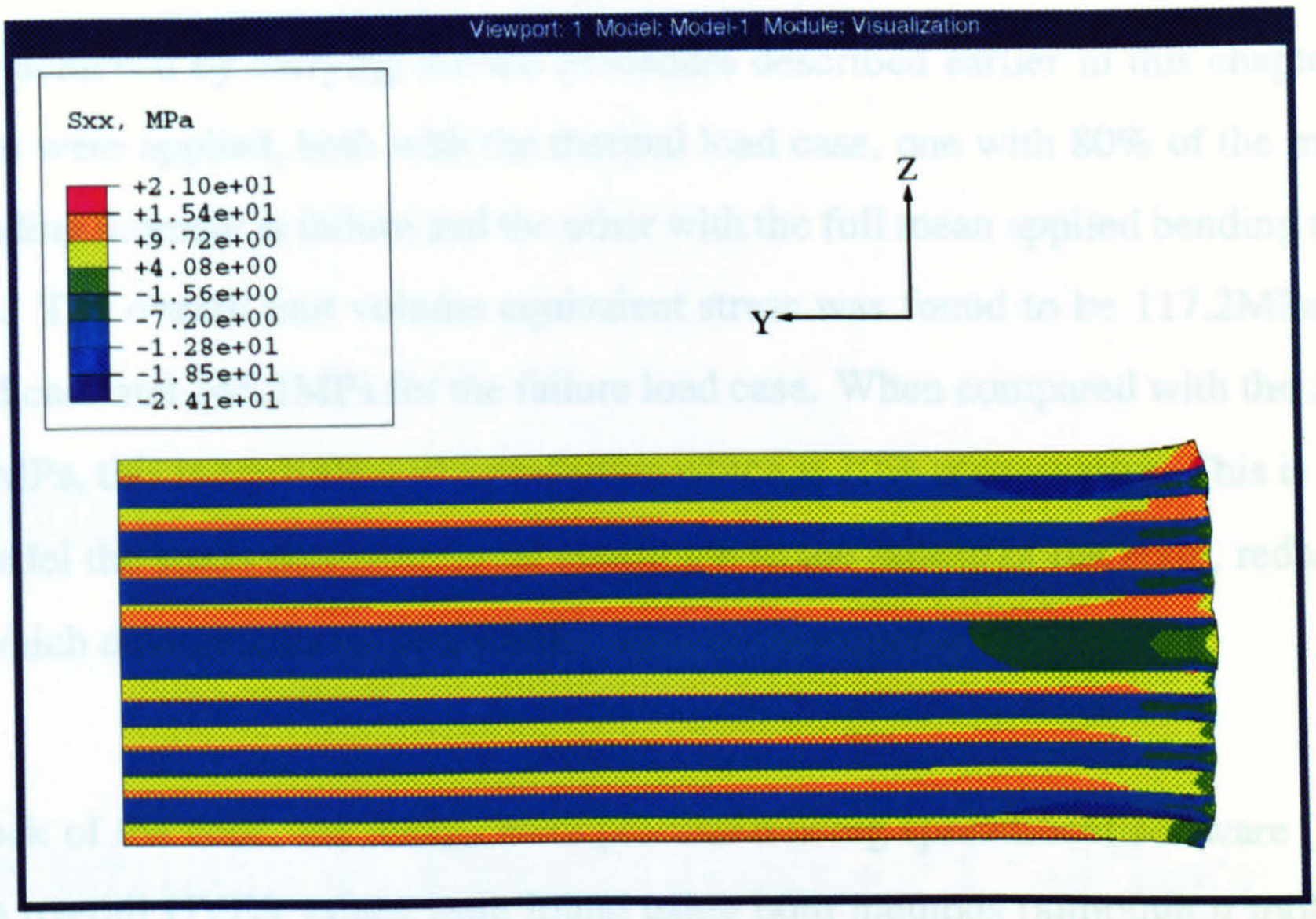

Figure 4.6: Longitudinal In-Plane Thermal Stress in Non-UD HBB Specimen

4.3.3 Delamination Load Correlation

The same strength values as those calculated from the uni-directional HBB analyses were applied to this failure analysis ($m = 18.1$ and $S_0 = 130.5$). The delamination prediction method was designed to take the increased transverse stresses into account when predicting failure. These stresses contribute to the stresses acting in the matrix, and therefore influence the failure of the matrix, affecting the delamination. The failure was still highly dominated by the interlaminar tension, but in this non-UD case, the other stresses contributed more to the failure.

Looking purely at the interlaminar tension, the interlaminar tensile stress is 7% lower at delamination in the non-UD specimens. The non-UD specimens had double the material volume, which would reduce the strength by around 4%. Therefore there is only a 3% reduction in the interlaminar tensile strength from a UD to a non-UD laminate for the HTA/913C material, which is not significant.

The proposed method was applied to a 3-D slice model of the non-UD HBB specimen.

This was achieved by carrying out the procedure described earlier in this chapter. Two load cases were applied, both with the thermal load case, one with 80% of the mean applied bending moment at failure and the other with the full mean applied bending moment at failure. The overall unit volume equivalent stress was found to be 117.2MPa for the 80% load case and 145.1MPa for the failure load case. When compared with the S_0 value of 130.5MPa, this is equivalent to a prediction which is 10% conservative. This is because in the model the stress components all contribute to the failure of the resin, reducing the load at which delamination is predicted.

As a check of the code, the results were processed using spreadsheet software [71], and the same overall UVES values were found using both methods (although it took around one hour compared to fifteen seconds to produce the result.)

The delamination prediction method, and the Fortran codes which calculate the UVES value are complete and have been correlated with the HTA/913C material interlaminar strength. The method will now be used on a number of specimen types to validate the method and to improve the design of some structures. The first of these specimens is the 'T'-Piece and is reported on in the next Chapter.

Chapter 5

Delamination Prediction - 'T'-Piece

5.1 Introduction

In the previous chapters, a method for predicting interlaminar failure using a stress based method was introduced. It was developed to predict inter-fibre failure in uni-directional specimens or regions composed of fibre-reinforced composite material. It was applied to a series of interlaminar tensile strength specimens to correlate it for delamination prediction in structures made from HTA/913C carbon-epoxy composite. It will be applied to a 'T'-piece specimen in this chapter.

One of the critical areas of composite design is the interface between skins and stiffeners and the associated load transfer that occurs in that joint. As the joint is required to transfer load through the thickness of the composite material, the problem of inter-fibre failure (IFF) can be an issue. This can be reduced through careful design of the interface region. The design of these composite joints, also known as 'T'-joints, has been widely investigated in the literature. The work has concentrated on large-scale sandwich structures, which are generally used in marine applications. They usually involve the termination

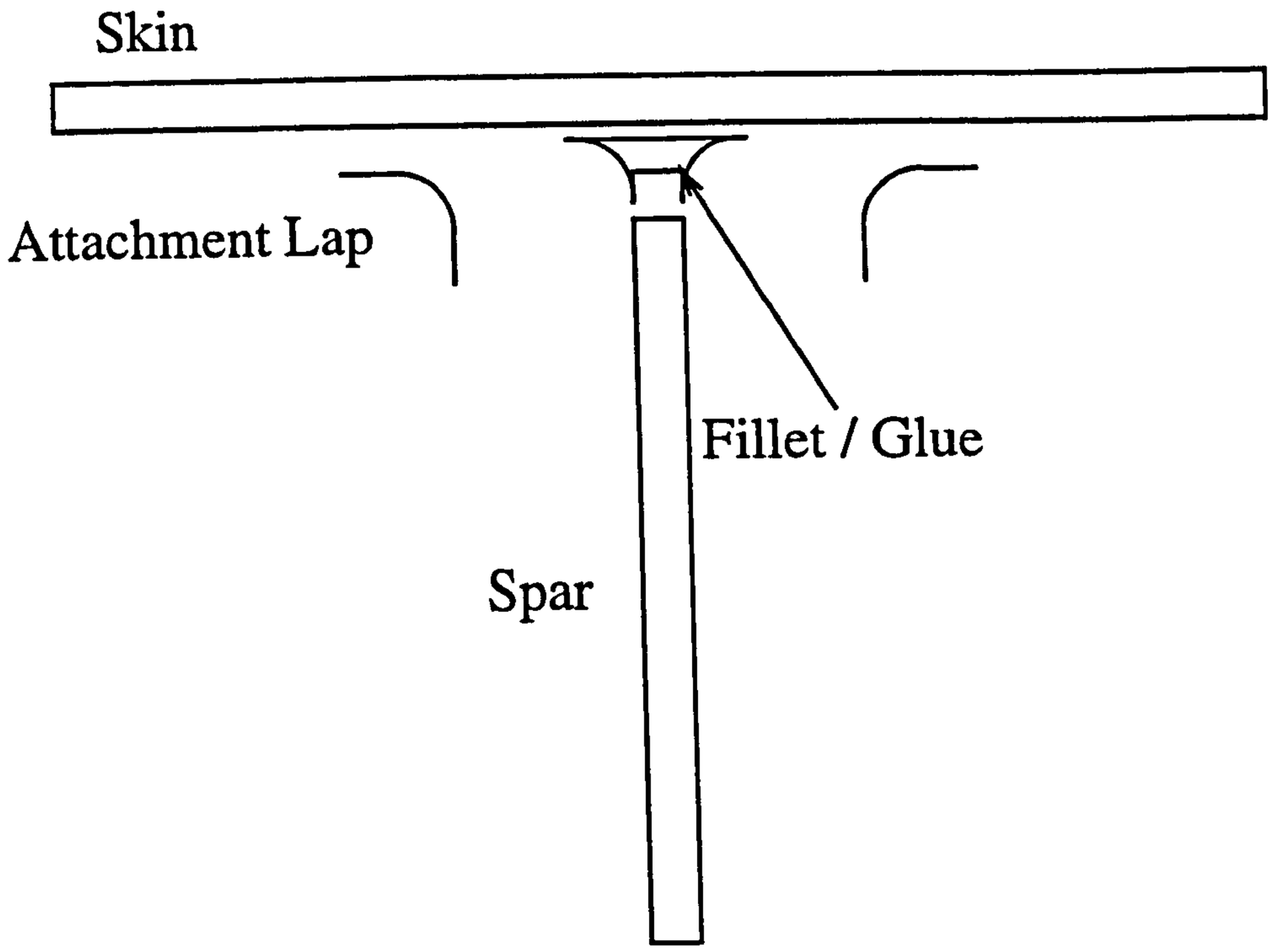

Figure 5.1: Exploded View of Typical Spar-Skin Joint Analysed in the Literature

of the spar prior to contact with the skin, most of the load transfer being controlled by attachment laps and the glue/fillet region between the components. The general layout can be seen in Fig 5.1.

Shenoi and Hawkins [75] investigated how varying the geometry of a bonded 'Tee Connection' affected the stress distributions in the various components. They then attempted to quantify failure using Tsai-Wu [32] but were unsuccessful due to a lack of material data. Rispler et.al [76] analysed 'T-Joints' and predicted the failure using a number of different methods, the 'Interlaminar Peel Index' being more successful than the others.

Cope and Pipes [77] varied the size and shape of a spar-wingskin joint in order to optimise the strength and weight of the design. They found that having a smooth or radius joint transition was stronger than a triangular design due to eliminating the sharp corners at the points of the triangle producing 'Discontinuities in the overlap geometry.' The strength of the joint was also improved by enlarging the radius of the joint. The work carried out indicated that by keeping the transition smooth and maximising the radius, the stress

concentrations were reduced. This sort of approach would be reasonable in areas where weight is not an issue in the design, but in aircraft structures it is critical to minimise the weight of all components. Therefore, the amount of material used in any component would have to be reduced as much as possible and the structure optimised.

In this chapter, the manufacture and testing of two specimen designs, one with a radius of 5mm and the other with a 10mm radius on the controlled curve are presented. A failure prediction is also carried out using the method described in the previous chapters.

5.2 The 'T'-Piece Design

The concept of a 'T-Piece' specimen has been introduced, with a description of one type of design which enables relatively straightforward manufacture for large-scale joints.

The basic design of the 'T'-piece used in this research is shown in Figure 5.2. It was based on a simpler design of the joint shown earlier, and is one such as that which might be used between the web and the flange in an aircraft structure. The design consists of three separately laid up sections, two curved and one straight, and a fill-in region made from 0° tows. The three main sections each had 16 plies with a lay-up of $[90_2/\pm 45]_{2S}$, and were made from HTA/913C carbon fibre pre-preg material. The figure shows the ply 90° directions defined, the 0° is perpendicular to the plane of the section.

As shown later, the strength of the 'T'-piece structure, when tested in the manner shown here, is largely governed by the size of the fill-in region. The size of the fill-in region is governed by the form of the controlled free surface, which is related to the tooling shape. By altering the radius of the curve, the fill-in shape is changed and this can affect how the load is transferred within the structure. Another factor in the design of the fill-in is the material inserted during manufacture. A common approach is to put UD tows of the same material longitudinally along the spar to add longitudinal stiffness.

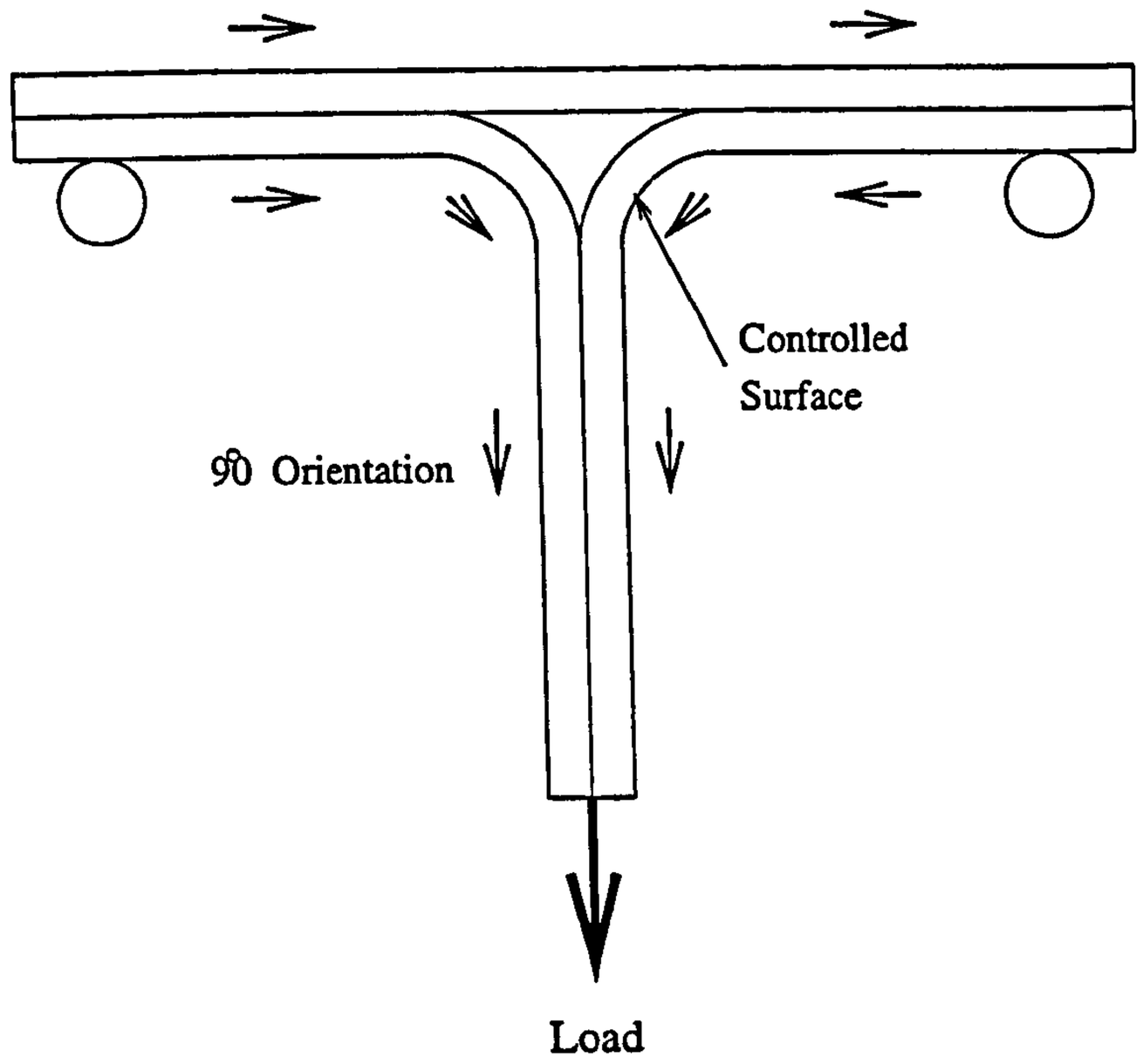

Figure 5.2: 'T'-Piece Specimen Geometry

5.3 Manufacture

Two 'T'-piece specimen types were manufactured as part of this research, one with a 5mm controlled outer radius, and the other with a 10mm controlled radius. These sizes were chosen because of ease of manufacture, and the opportunity for failure correlation with the same failure modes.

The tooling was made from aluminium blocks with machined radii. A schematic of the tooling is shown in Figure 5.3 with the 'T'-piece layed up over two such tools. Each piece of tooling was covered in release film prior to laying up. A beam was made that was long enough to be cut up into several 20mm wide specimens. The $[90_2/\pm 45]_{2S}$ laminates were laid up over the tooling and butted together as shown in Figure 5.3. The fill-in region was packed with UD tows of the same HTA/913C material. In an attempt to avoid underfilling and voidage, 5% more than the calculated volume was put in. A precured top laminate was applied, and film adhesive (AF-163-2K-0.06 lbs/ft^2 from 3M[78]) used to ensure a

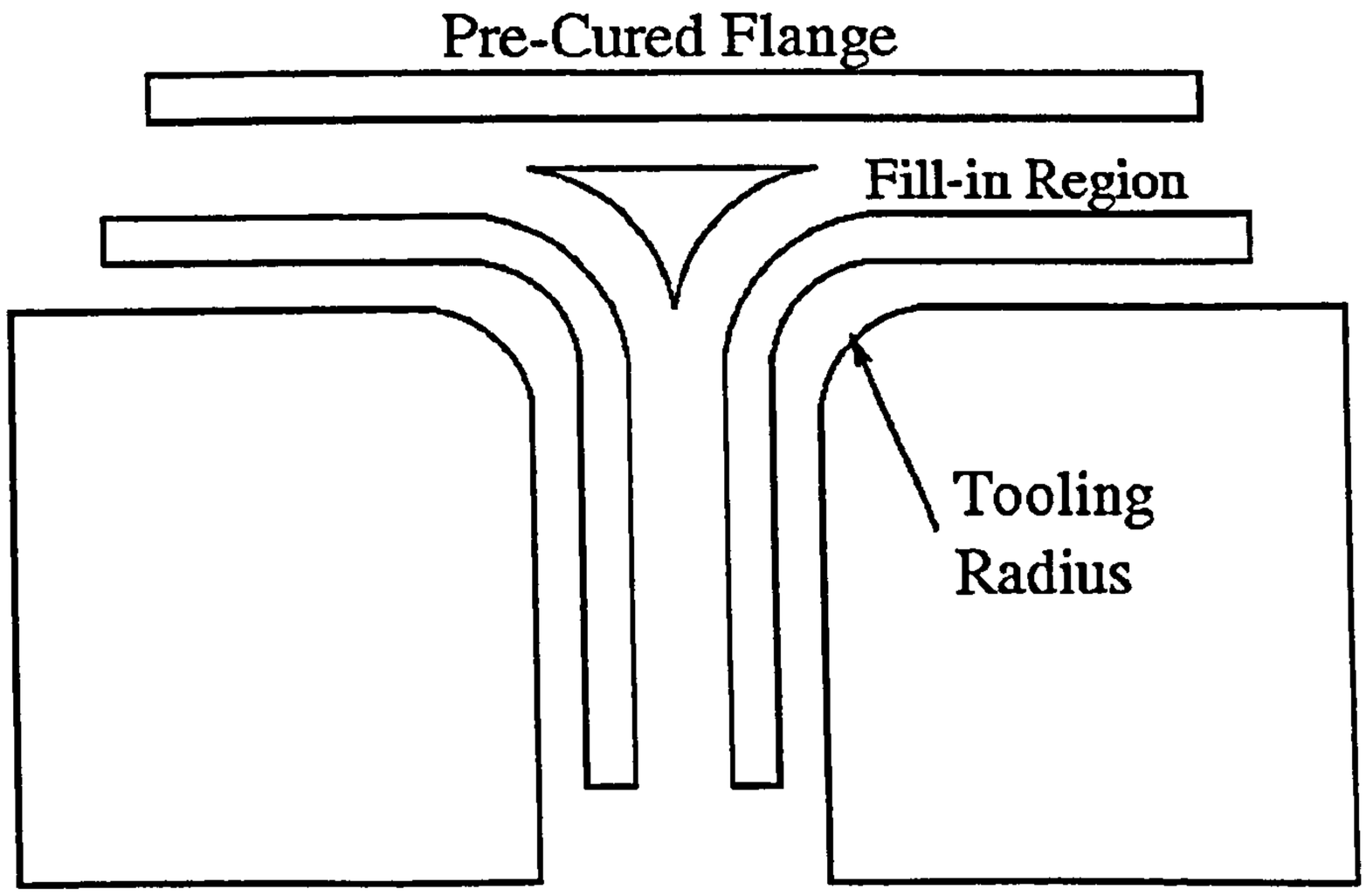

Figure 5.3: Exploded 'T'-Piece Specimen and Tooling

good bond. Specimens were cured according to the supplier's instructions, i.e. 120°C and a pressure of 7bar for 1 hour.

The specimens were cut to size using diamond saw, each specimen having a width of 20mm. The sides were polished prior to testing to reduce the effect of edge problems.

5.4 FE Modelling

The geometry of each model was taken directly from the manufactured specimens. The mean thickness of the arms was 4.7mm for the 32 plies and the film adhesive. This value was consistent across all of the 5mm and 10mm radius specimens, and so was used throughout the modelling process. The ply thickness was calculated to be 0.142mm and was used in the web as well as the flanges. The film adhesive was modelled separately with the same thickness as the other plies.

Material Property	HTA/913C 90°	HTA/913C ±45°	HTA/913C 0°	Film Adhesive
E_X	131.5GPa	17.2GPa	9.2GPa	1.1GPa
E_Y	9.2GPa	9.2GPa	9.2GPa	1.1GPa
E_Z	9.2GPa	17.2GPa	131.5GPa	1.1GPa
ν_{XY}	0.3	0.114	0.45	0.3
ν_{YZ}	0.45	0.061	0.021	0.3
ν_{XZ}	0.3	0.766	0.021	0.3
G_{XY}	4.875GPa	3.9GPa	3.103GPa	0.423GPa
G_{YZ}	3.103GPa	3.9GPa	4.875GPa	0.423GPa
G_{XZ}	4.875GPa	30.77GPa	4.875GPa	0.423GPa

Table 5.1: Orthotropic Material Properties

Two finite element models were initially produced for this research investigating the different geometries. The meshes for each geometry were produced within I-DEAS Master Series [79] and the analyses carried out using ABAQUS/Standard [70]. The models were created in 2-D using 6 and 8-noded elements with quadratic displacement functions in the plane strain domain. Plane strain was used because the fill-in region was composed of 0° material which has a very low Poisson ratio for the cross-width direction. The material properties had to be defined in the local element X-Y plane, therefore the composite ply plane was X-Z within the elements. The properties used for the composite materials are shown in Table 5.1. A 3-D model was also produced later to evaluate the accuracy of modelling these specimens in plane strain. This model is reported on later in the chapter.

As stated previously, data from the supplier, Hexcel Composites [65], gave the tensile modulus in the fibre direction of HTA/913C as 142GPa and the compressive modulus as 121GPa. The averaged value of 131.5GPa was used to calculate the ±45° properties by laminated plate theory. Interlaminar stiffness properties were not available, so transverse isotropy was assumed. The thermal expansion coefficients from the previous Chapter were applied to the model.

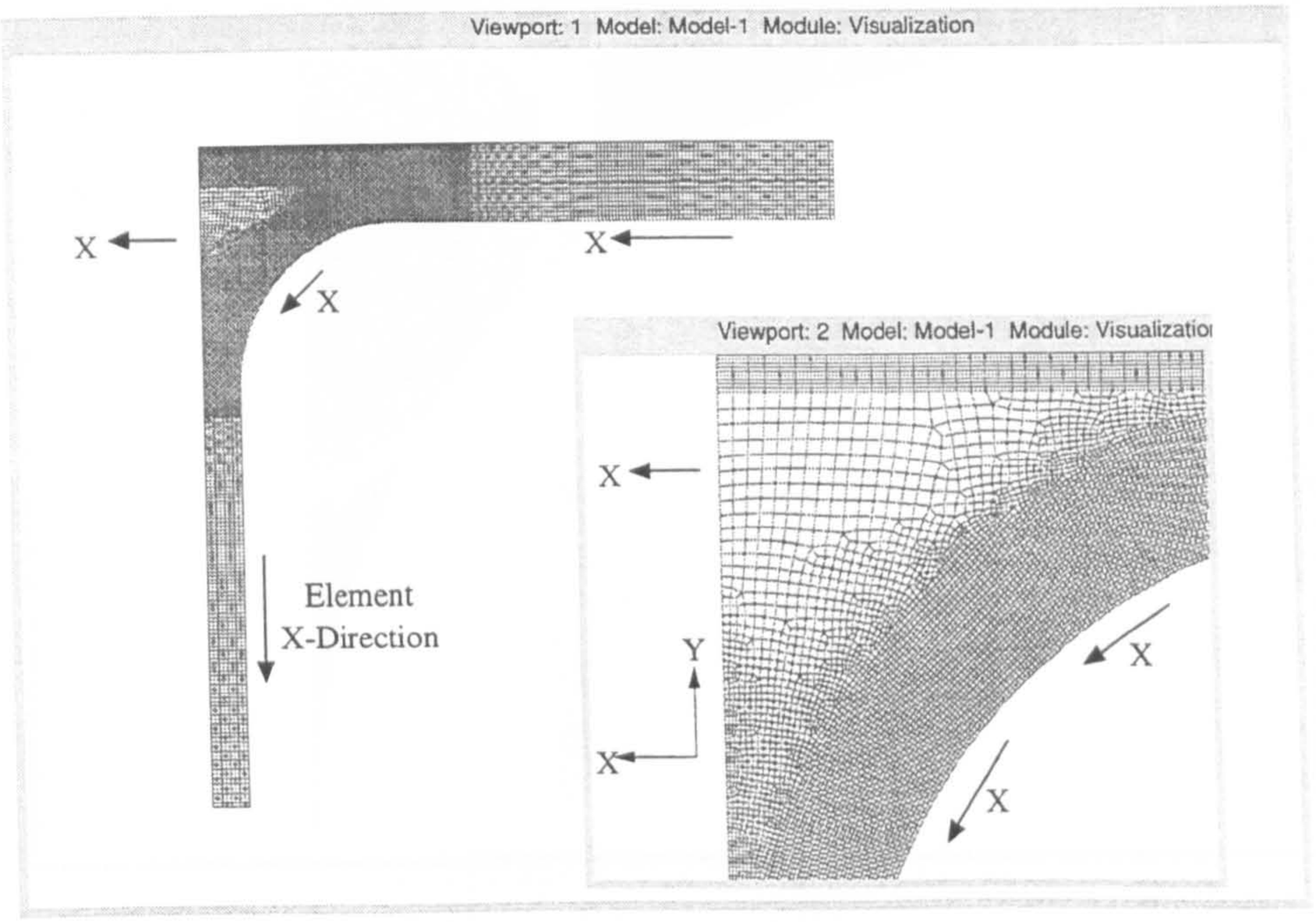

Figure 5.4: Typical 'T'-Piece Model Mesh

The 10mm radius model mesh is shown in Figure 5.4. Only half of the specimen was modelled due to the symmetry of the specimens and the applied load case. The mesh density is high, with 2 elements per ply through the thickness of the curved laminates in the region of the fill-in. The aspect ratio (ratio of element length to width) of the 8-noded elements was not allowed to exceed 1.5. There were 15 000 elements in the 5mm radius model and 16 000 in the 10mm radius model. The local material X-axes are shown as arrows on the diagram.

In the models, the boundary conditions were applied to simulate symmetry at the left-hand edge and provide support vertically under the flanges at 40mm from the centre-line. The mechanical load (equivalent to 100N/mm width) was applied at the bottom of the web as shown in Figure 5.2. The temperature of all the nodes in the model was reduced from the cure temperature of 120 to 20°C as part of the loading step. The models in this research had linear elastic material properties and linear geometric response.

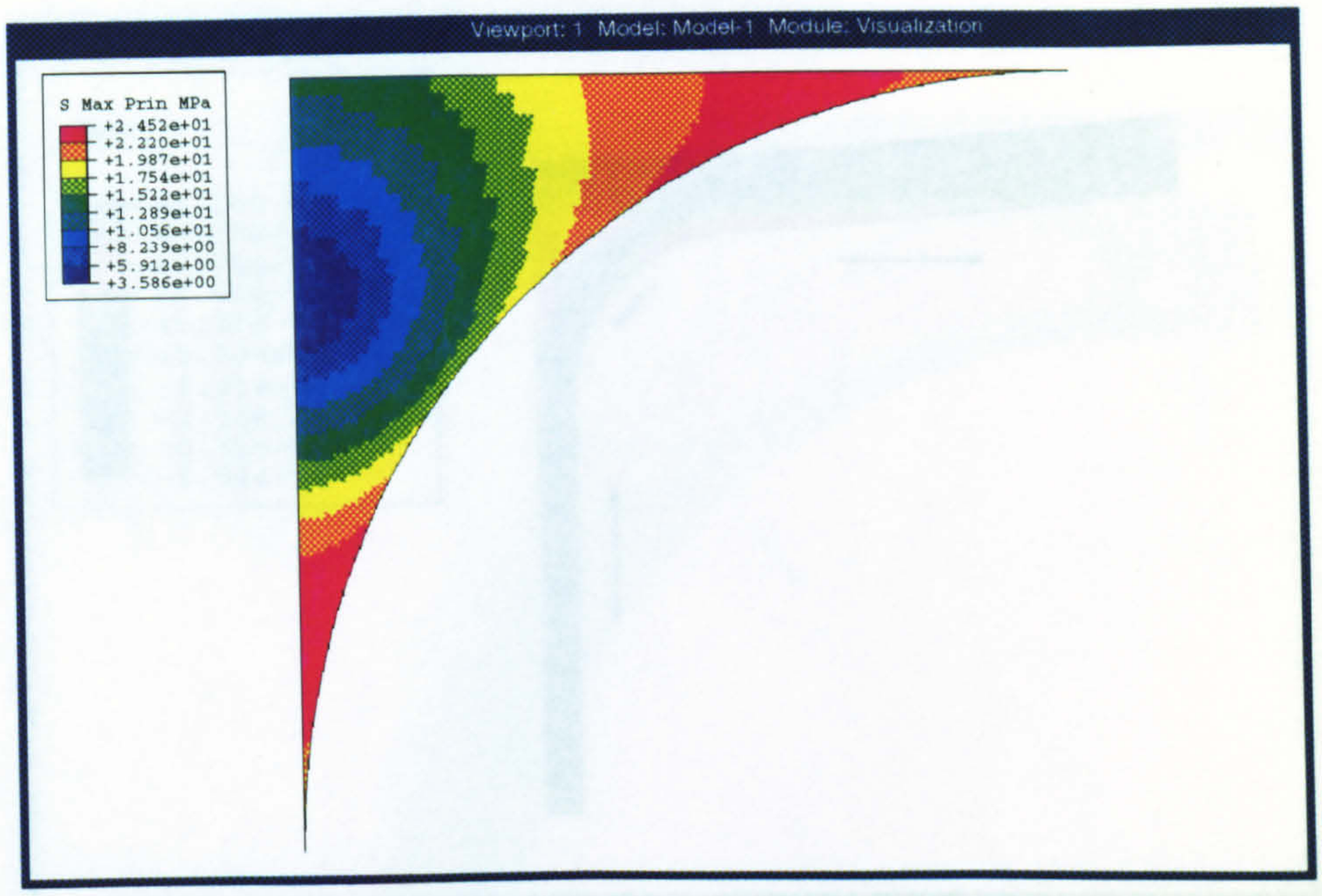

Figure 5.5: Thermal Residual Stress in Fill-in Region

5.4.1 Results

The first results shown (Fig.5.5) are those of just the thermal residual stresses in the fill-in region of the 10mm radius specimens. The maximum principal stresses in the plane of the section are shown as they are the effective inter-fibre tensile stresses acting. This shows the significance of the thermal residual stresses in the matrix due to curing which are often ignored in failure analysis of composite material structures. The stress 'radiates' from a minimum at the centre to peak in the extremities of the fill-in, at a magnitude of 25MPa in tension. This is as a result of the constraint of the laminates surrounding the fill-in. These laminates do not contract significantly in the plane of the section due to the low expansion coefficient of the fibres. These stresses are very important in achieving an accurate failure prediction for these specimens.

The local X-direction strain results plotted on a deformed mesh (Figure 5.6) for the applied load case of 100N/mm width combined with thermal residual stresses show that the peak is in the fill-in region. This is caused by tensile load from the stiff flanges being carried across the relatively flexible fill-in material. Along the flange, the strain peaks at

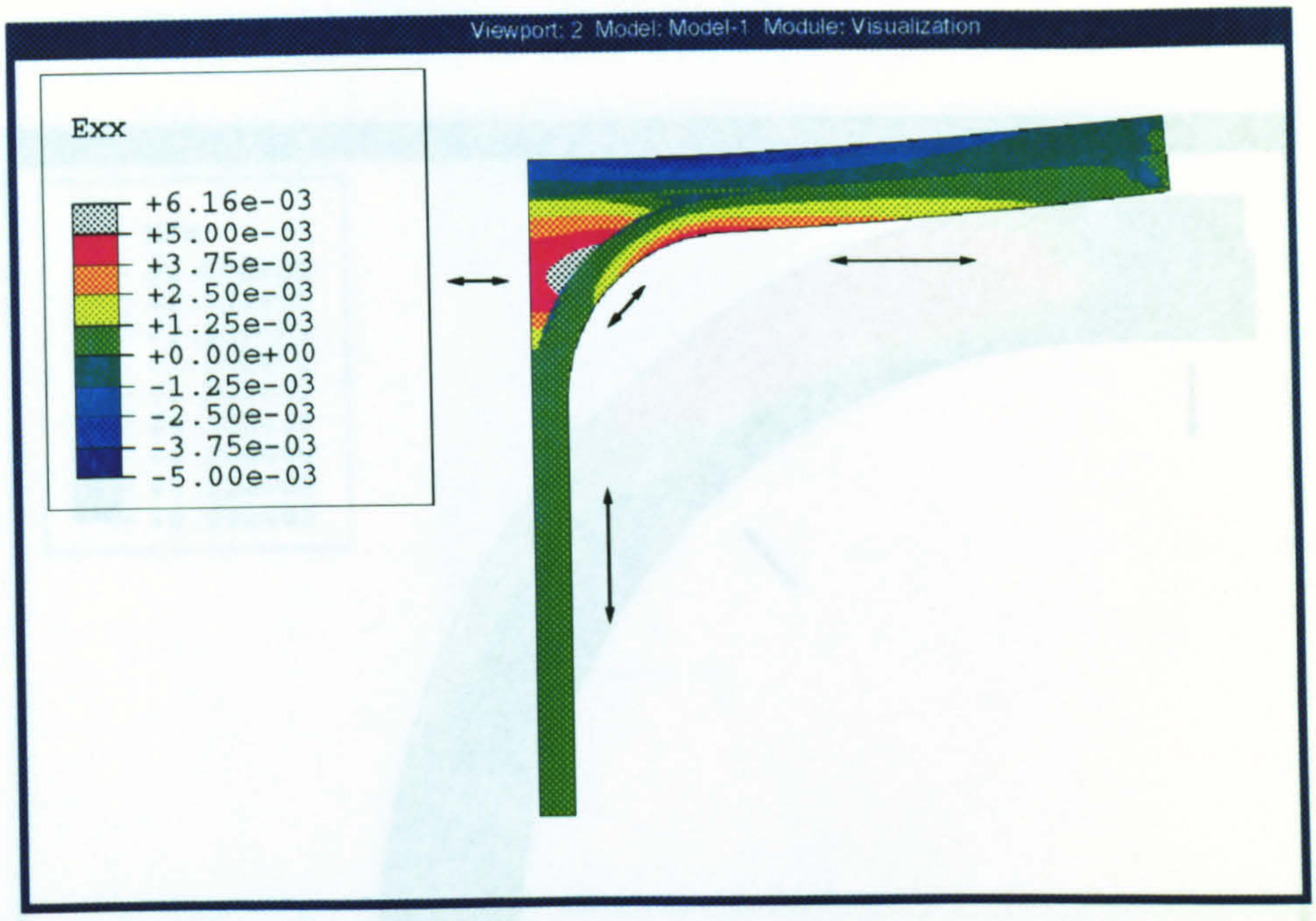

Figure 5.6: Longitudinal In-Plane Strain at 100N/mm Load

the top and bottom of the arm are due to bending. The peaks are at the start of the curve because the structure's bending stiffness increases to the centre from that location and despite the increase in bending moment, cannot bend as much.

Moving on to concentrate on the curved laminate, the interlaminar stresses show an interesting distribution. The interlaminar tension due to bending around the curve is shown in Figure 5.7. The peak in the top half of the curve is caused by the bending moments carried by the laminate at that point. It reduces rapidly from there towards the web because the amount of bending reduces. The magnitudes are fairly low at this load case, and are much less than those in the fill-in region as shown later. There is a small peak on the left edge of the curve lower down which is related to the tension in the fill-in. The stress on the free surface is close to zero, so the mesh is refined enough.

The interlaminar shear stresses in the curve are shown in Figure 5.8. The main stress peak is in the centre of the curve, and causes the dissipation of the bending stresses shown earlier in the laminate. It is not enough, on its own, to cause delamination of the laminate, although it could act with the interlaminar tensile stress shown previously.

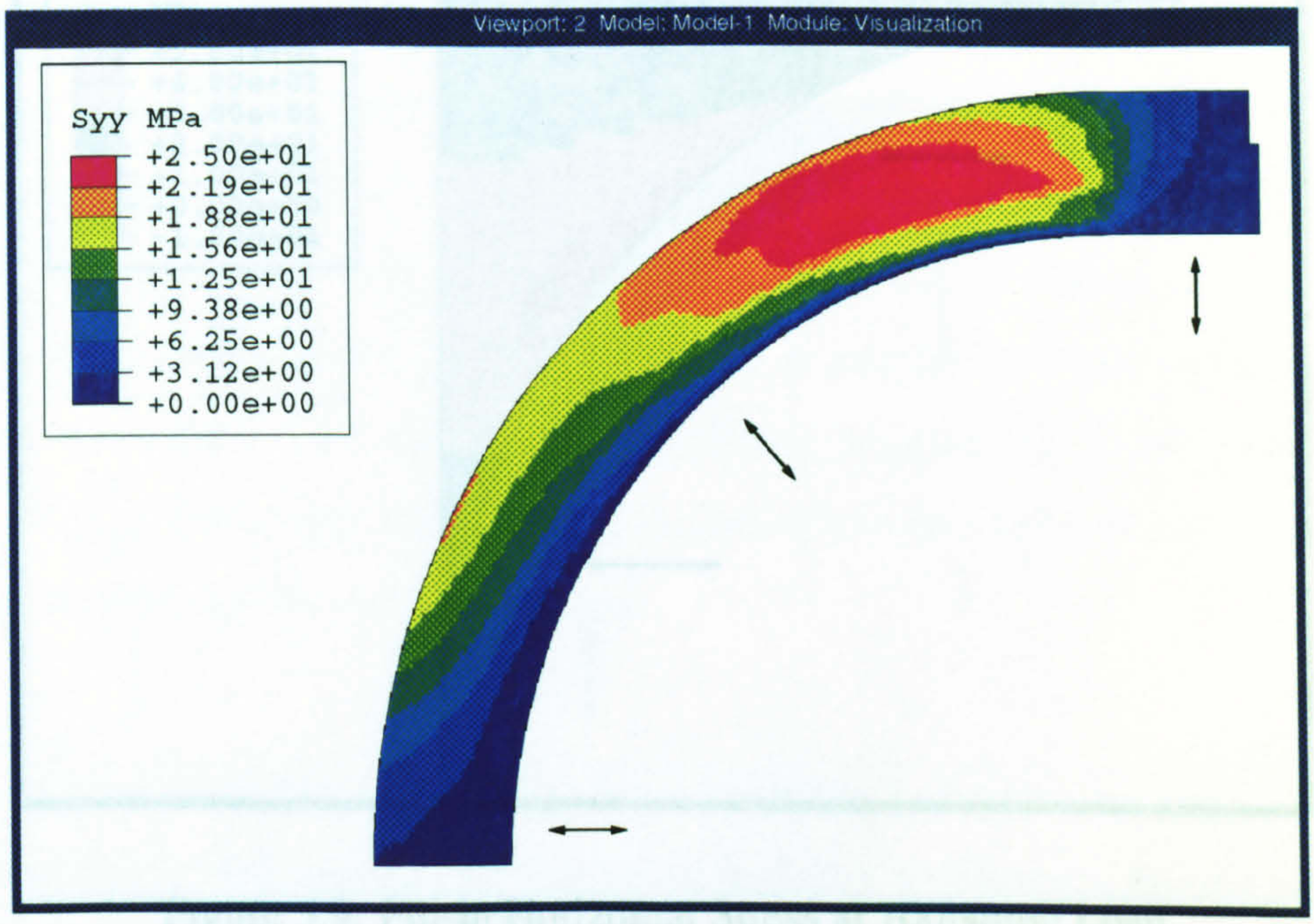

Figure 5.7: 'T'-Piece Curve Interlaminar Tensile Stress at 100N/mm Load

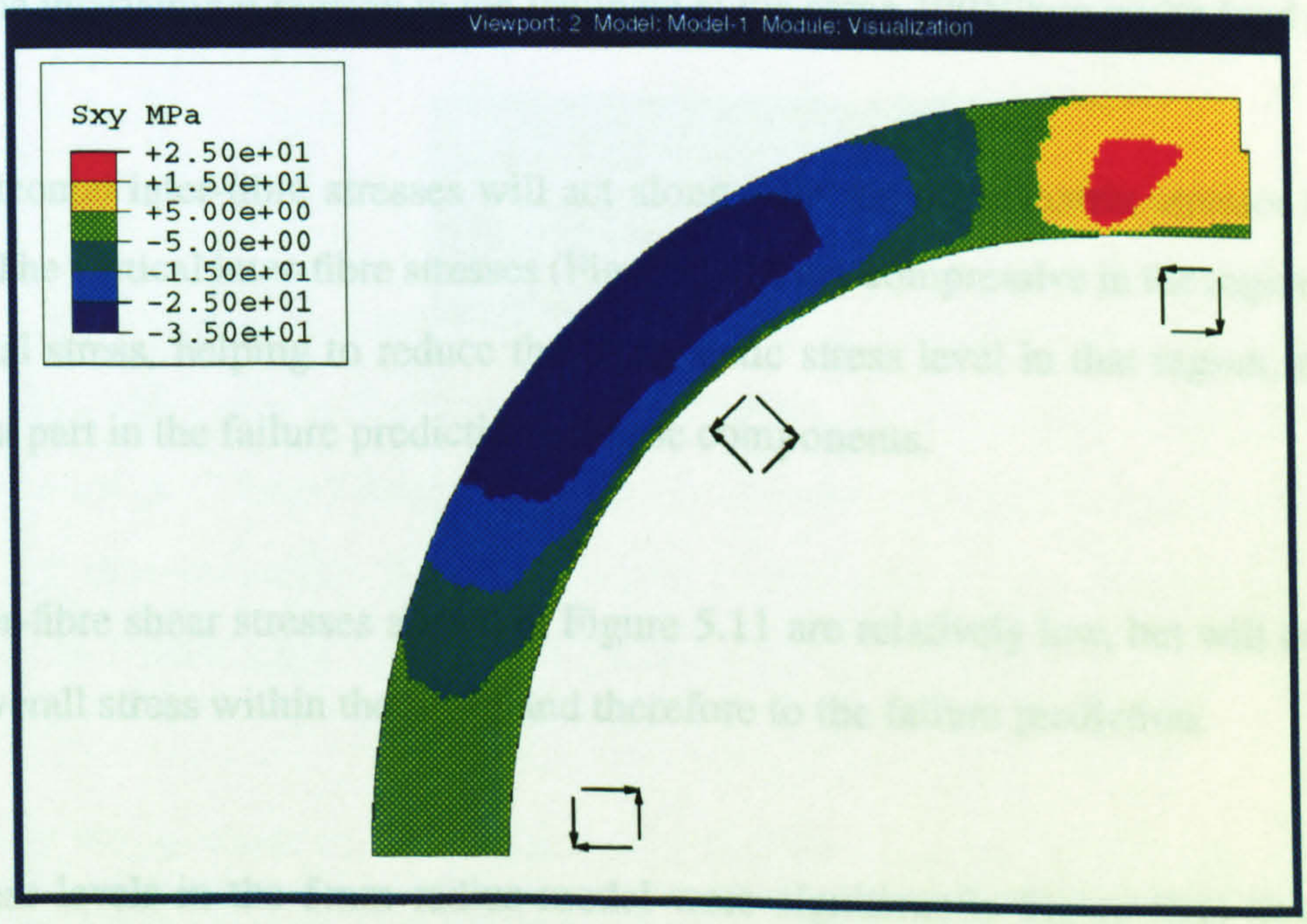

Figure 5.8: 'T'-Piece Curve Interlaminar Shear Stress at 100N/mm Load

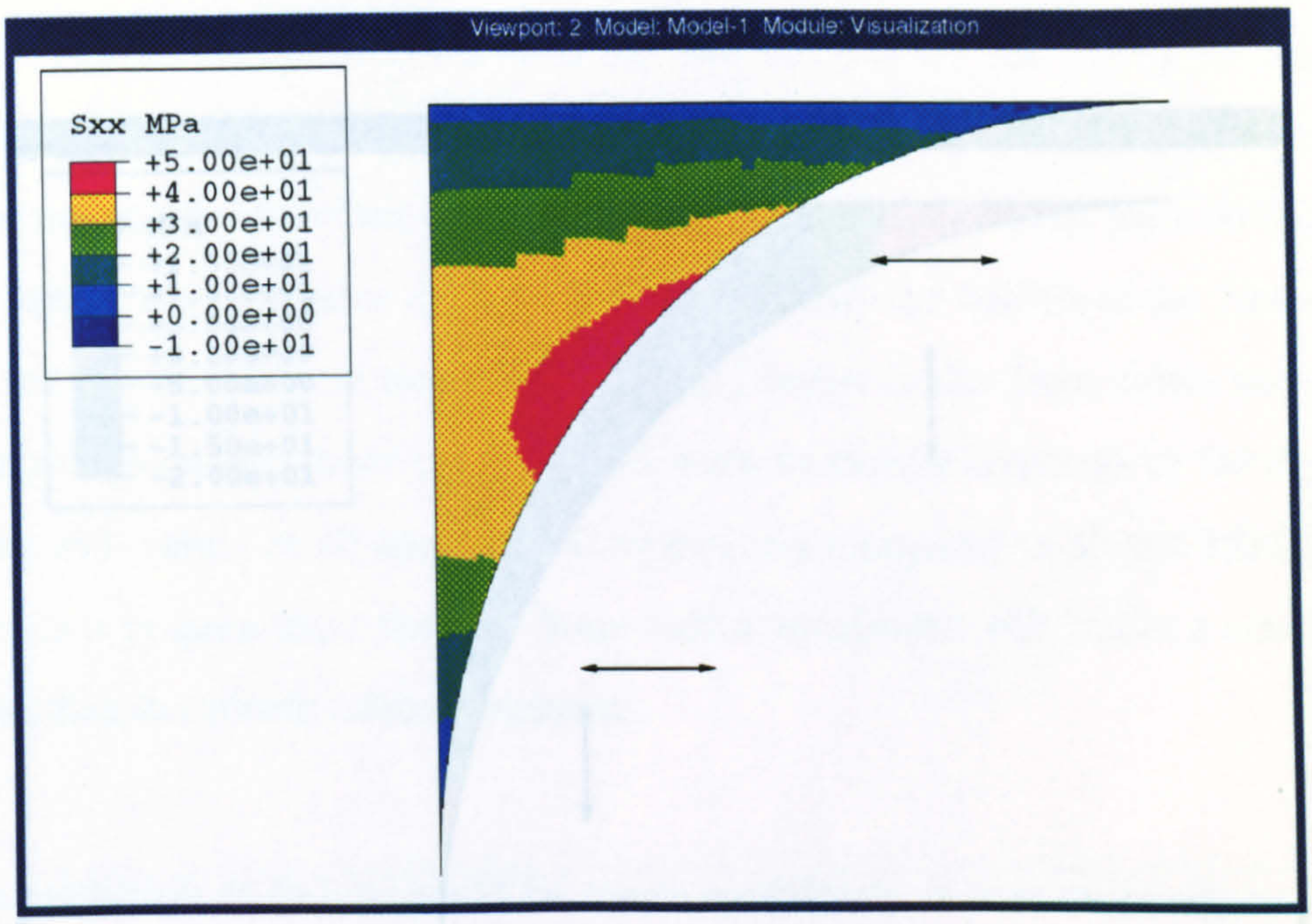

Figure 5.9: Fill-in Horizontal Stress at 100N/mm Load

The horizontal inter-fibre stress levels in the uni-directional fill-in region are much higher than those in the laminate, as shown in Figure 5.9. The peak is on the interface between the fill-in and the curved laminate. The magnitude of the stress (46MPa) is almost twice that of the interlaminar tension in the laminate at the same 100N/mm width load case.

The horizontal inter-fibre stresses will act along with the other matrix stresses to cause failure. The vertical inter-fibre stresses (Figure 5.10) are compressive in the region of high horizontal stress, helping to reduce the hydrostatic stress level in that region, therefore playing a part in the failure prediction of these components.

The inter-fibre shear stresses shown in Figure 5.11 are relatively low, but will contribute to the overall stress within the fill-in and therefore to the failure prediction.

The stress levels in the 5mm radius model were significantly higher than those in the 10mm radius model for the same 100N/mm width load case. This is because the tighter radius of the curved laminates causes larger stress concentrations around the fill-in region. The results are not shown because they have very similar distributions to the 10mm model.

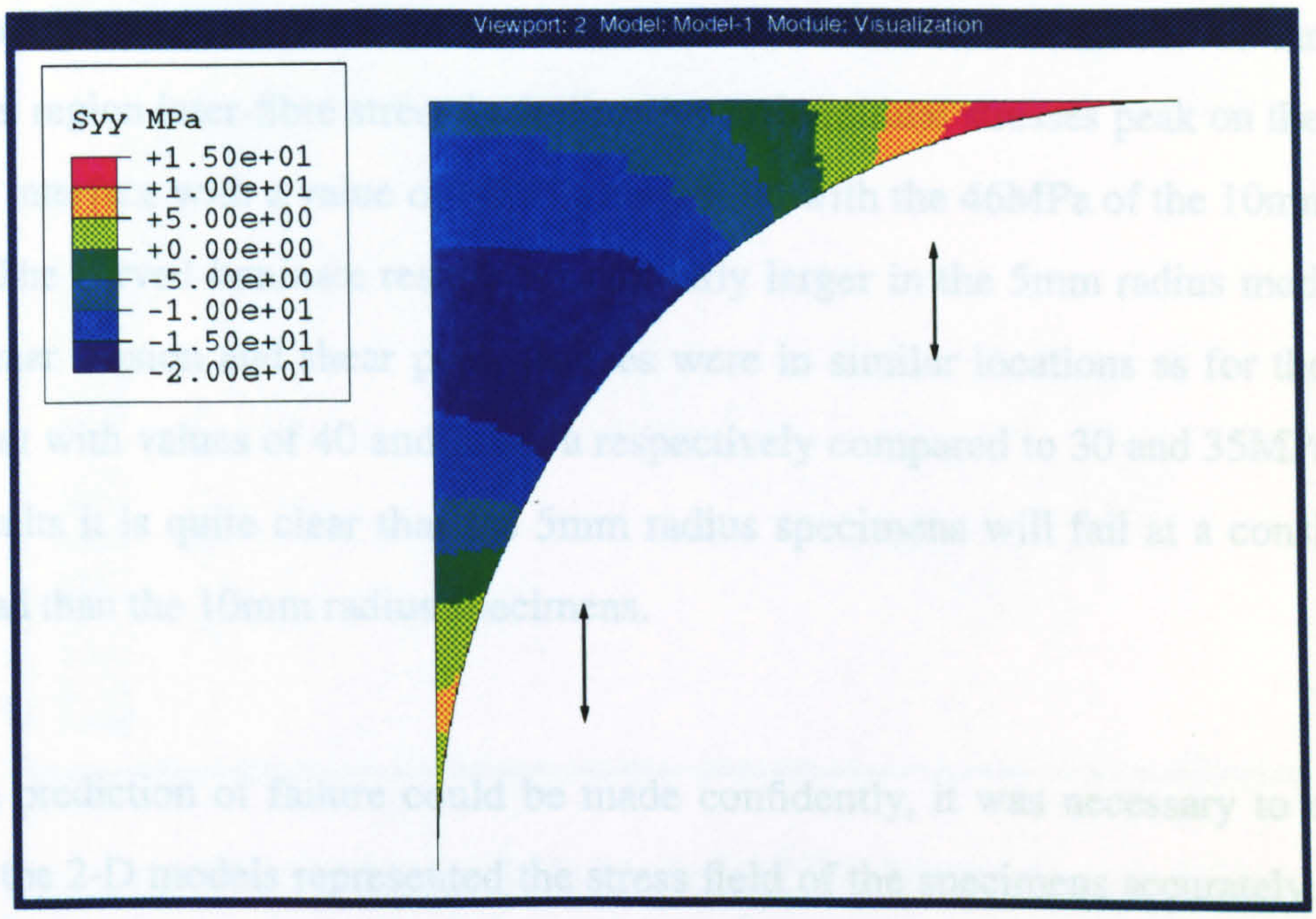

Figure 5.10: Fill-in Vertical Stress at 100N/mm Load

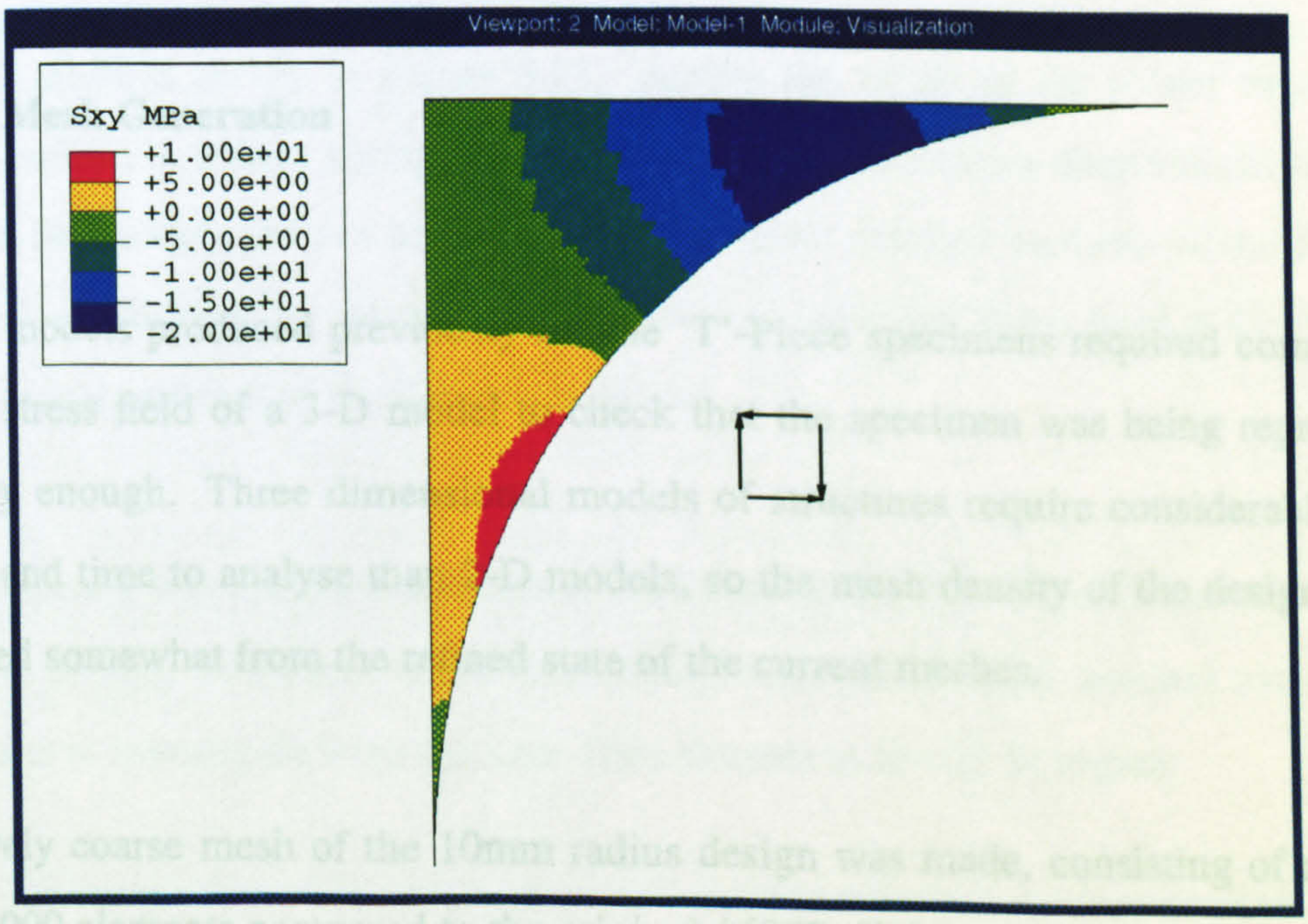

Figure 5.11: Fill-in Shear Stress at 100N/mm Load

The key values for comparison between the two designs are the inter-fibre stresses in the fill-in region and the interlaminar shear and tensile stresses in the curved laminates. The fill-in region inter-fibre stress including thermal residual stresses peak on the curved laminate interface with a value of 68MPa compared with the 46MPa of the 10mm radius design. The curved laminate results are similarly larger in the 5mm radius model. The interlaminar tension and shear peak stresses were in similar locations as for the 10mm model, but with values of 40 and 50MPa respectively compared to 30 and 35MPa. From these results it is quite clear that the 5mm radius specimens will fail at a considerably lower load than the 10mm radius specimens.

Before a prediction of failure could be made confidently, it was necessary to establish whether the 2-D models represented the stress field of the specimens accurately enough. In order to check this, a 3-D model of the 10mm radius design was made.

5.4.2 3-D Model

5.4.2.1 Mesh Generation

The 2-D models produced previously for the 'T'-Piece specimens required comparison with the stress field of a 3-D model to check that the specimen was being represented accurately enough. Three dimensional models of structures require considerably more memory and time to analyse than 2-D models, so the mesh density of the design had to be reduced somewhat from the refined state of the current meshes.

A relatively coarse mesh of the 10mm radius design was made, consisting of approximately 1000 elements compared to the original 16000. This was achieved by using only 1 element through-thickness for every 2 plies in the laminates. The mesh is shown in Figure 5.12. This mesh, when analysed, produced overall UVES results within 2% of the refined mesh model, and could therefore be considered as being refined enough to repre-

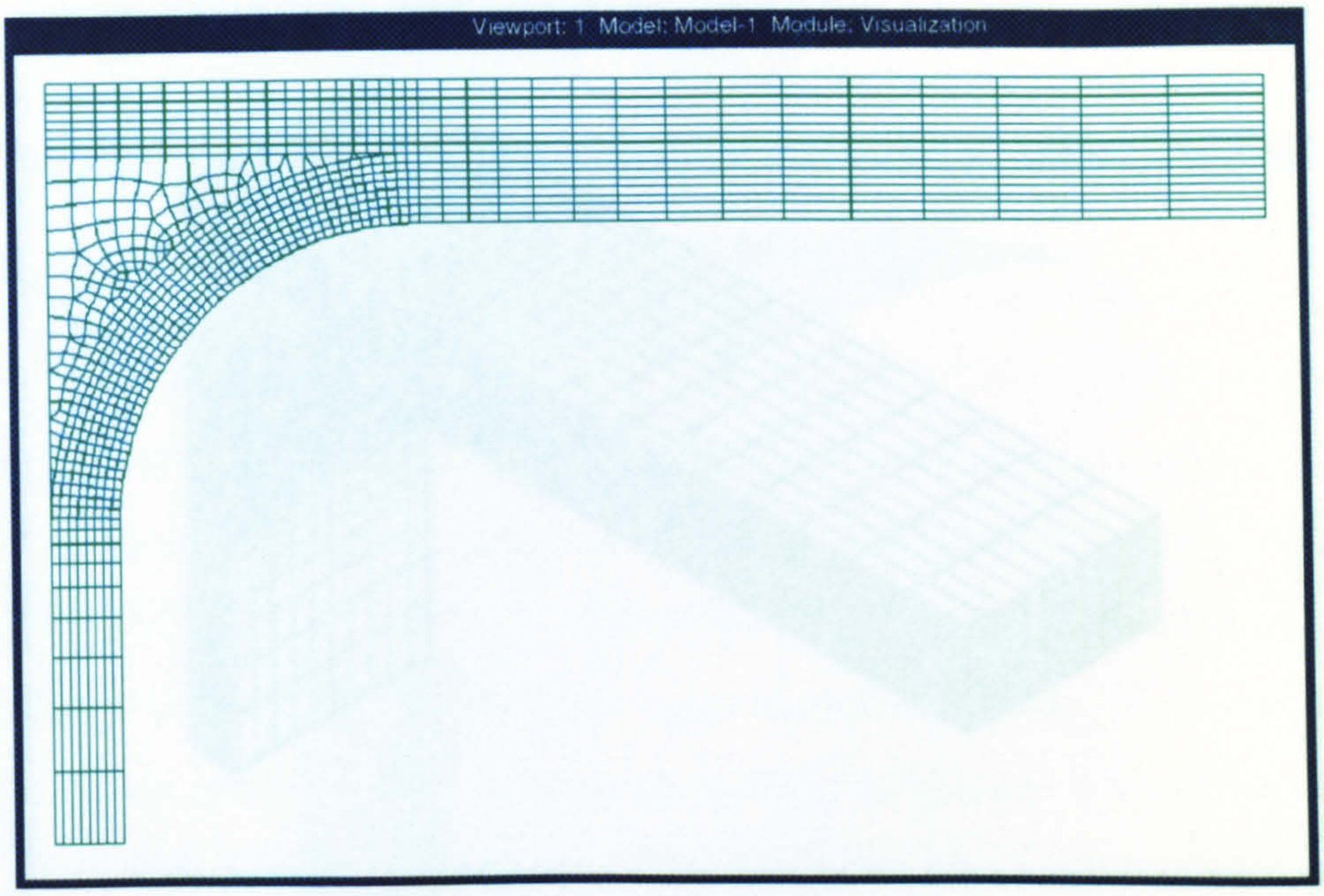

Figure 5.12: Optimised 2-D Mesh

sent the 2-D stress-field. This mesh was then extruded to half the width of the specimens (10mm), producing a quarter model. This model would require boundary conditions on the symmetry faces to simulate the presence of the rest of the specimen.

The 3-D mesh is shown in Figure 5.13. Across the width of the model there are 10 elements which is refined enough to identify any significant stress distributions across the width of the model, but not refined enough to allow detailed analysis of the free edge stresses. It is adequate for this model as it shows an increased stress level at the free edge, but this is insignificant in the failure prediction.

The 3-D model was analysed at the same load case as the 2-D model of the 10mm radius specimen design, 100N/mm width mechanical load with thermal residual stresses. The key results to investigate were the inter-fibre stresses in the fill-in region.

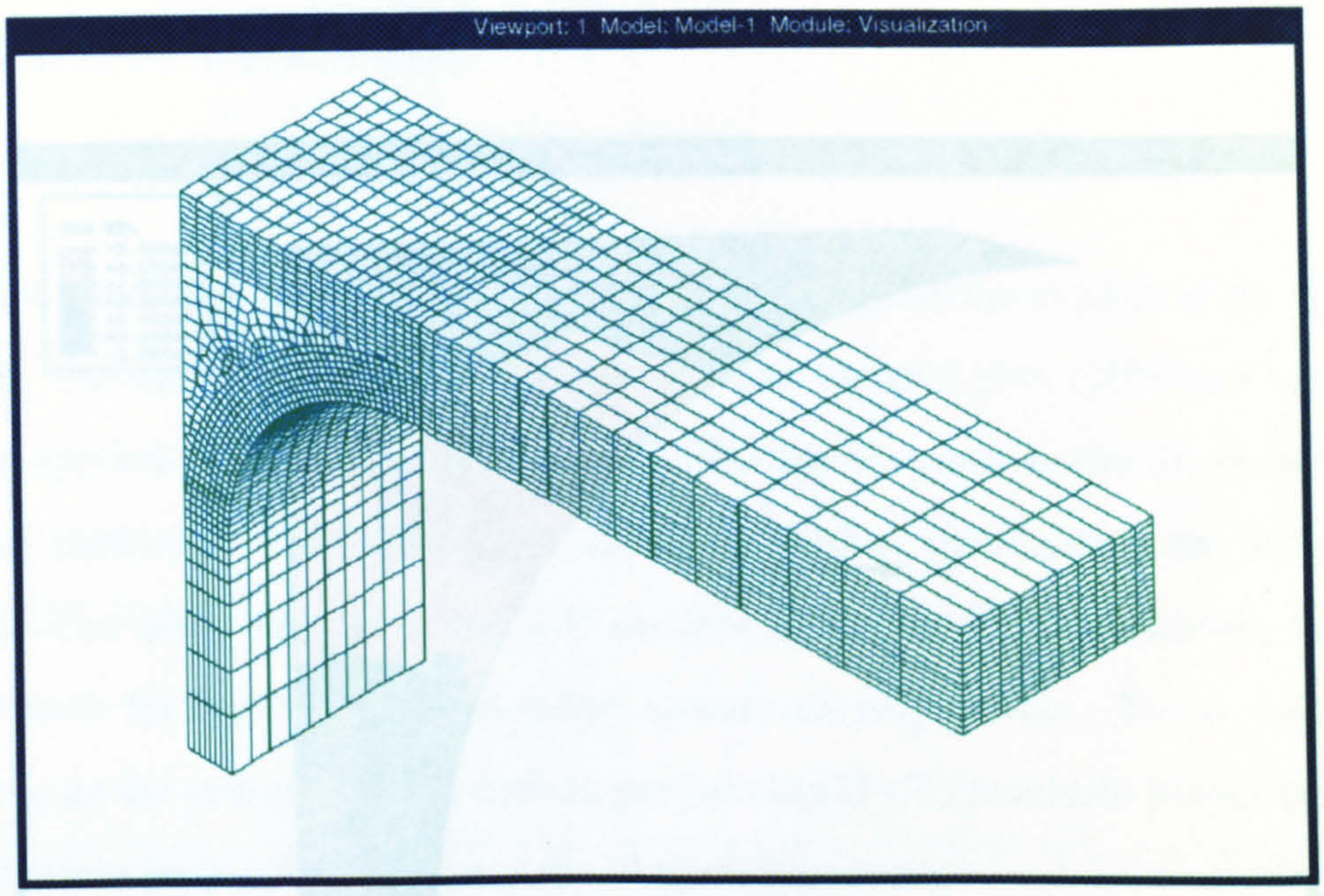

Figure 5.13: 3-D 'T'-Piece Model Mesh

5.4.2.2 3-D Results

The 3-D model was produced to evaluate the accuracy of a 2-D model to the behaviour of the specimens. The stress results in the fill-in region were found to be the most critical for failure, so these were investigated in the 3-D model.

At the applied load case of 100N/mm width with thermal residual stresses, the stress component with the largest magnitude was the horizontal stress in the 2-D plane strain model which peaked at 46MPa on the laminate/fill-in boundary. The 3-D model produced similar stresses as can be seen in Fig.5.14. The stresses in the middle of the model (left hand side of the image) peak at 44MPa on the laminate interface, 4% down on the 2-D plane strain model.

At the free edge (Fig.5.15), the stress levels increase slightly to peak at 48MPa on the laminate interface. From this information it should be reasonable to assume that the stress distribution across the width of the specimens has little effect on the failure prediction. This is expanded upon in the next section.

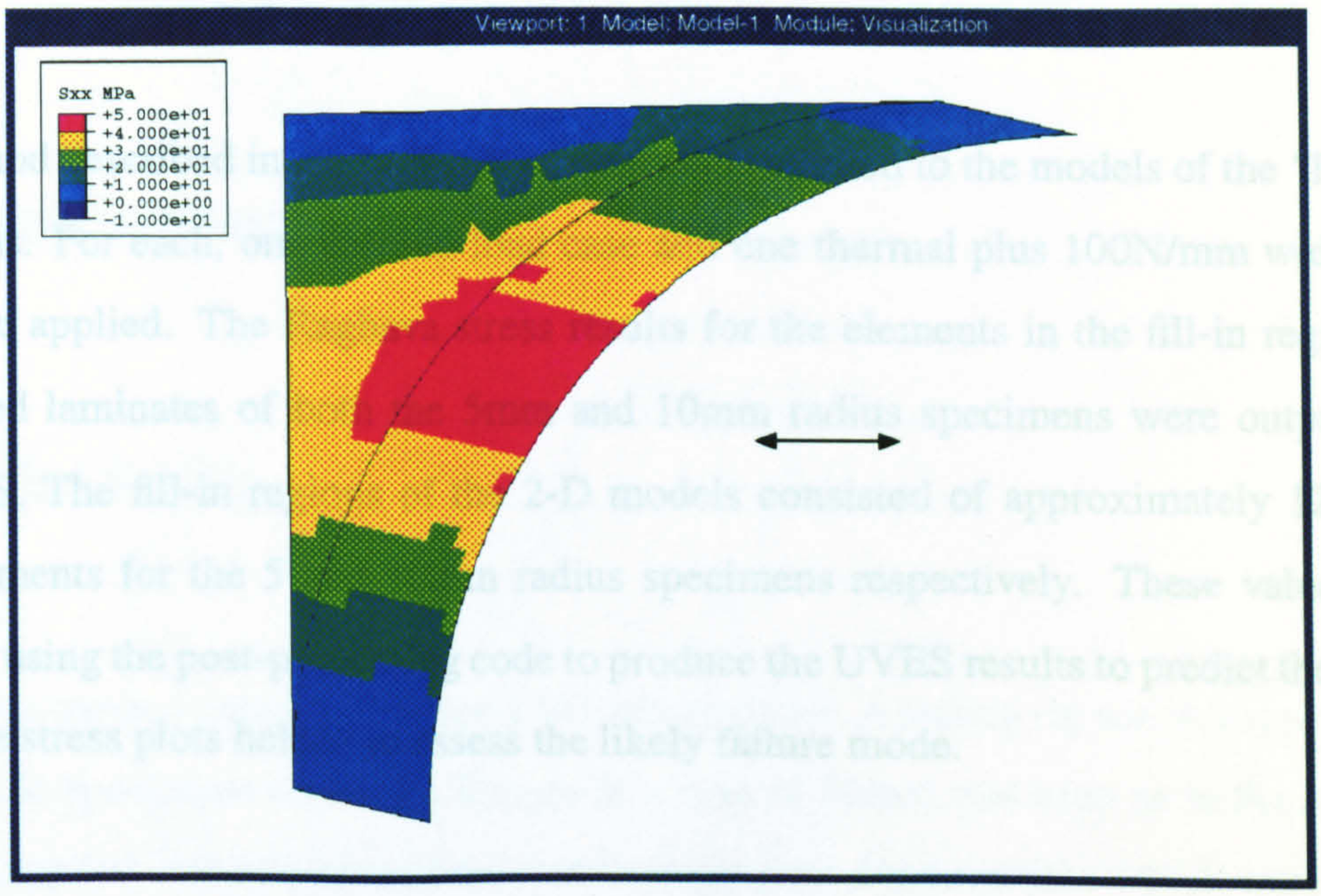

Figure 5.14: 3-D 'T'-Piece Fill-in Region Horizontal Inter-Fibre Stress in Centre

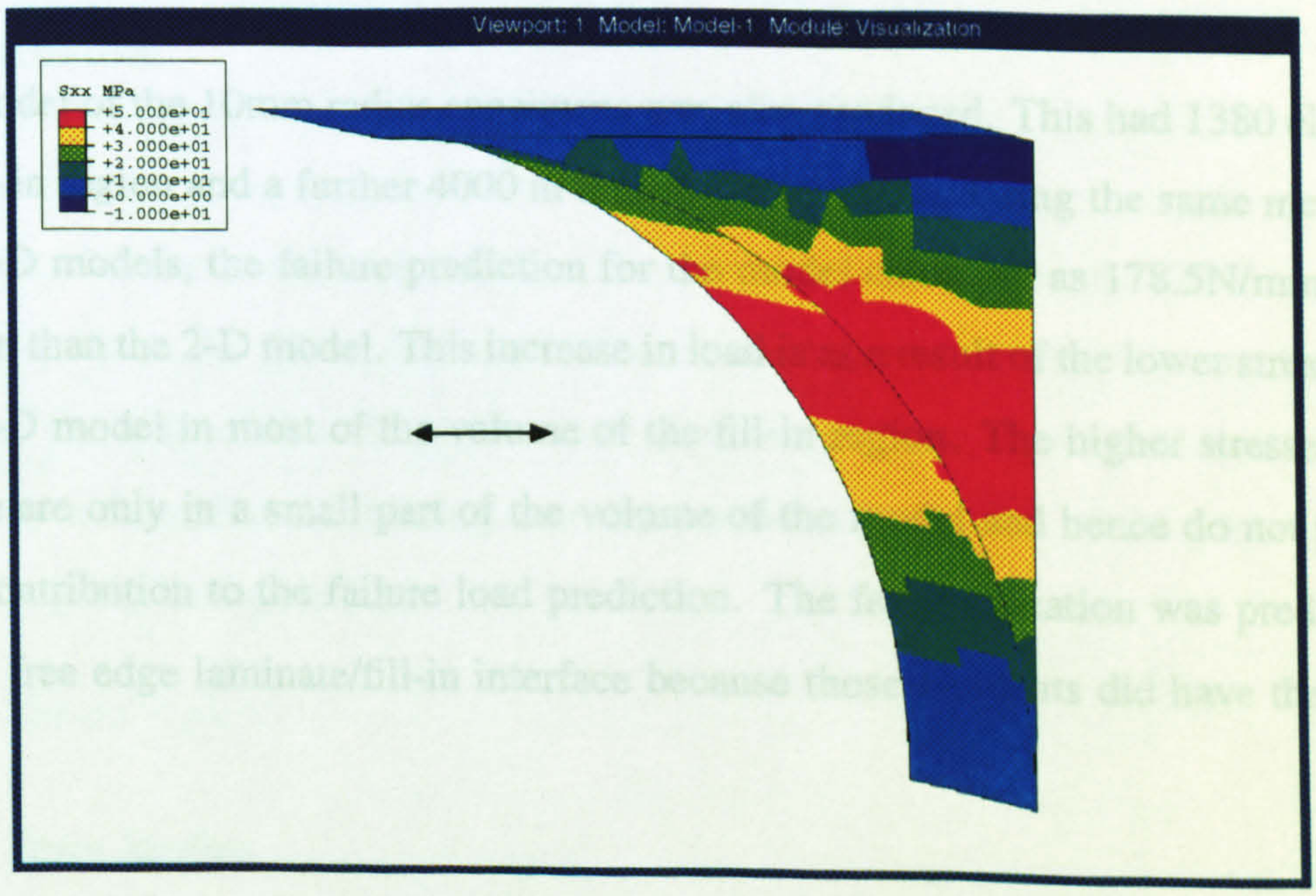

Figure 5.15: 3-D 'T'-Piece Fill-in Region Horizontal Stress at Free Edge

5.5 Failure Prediction

The method described in the previous chapters was applied to the models of the 'T'-piece specimens. For each, one thermal load case and one thermal plus 100N/mm width load case were applied. The Raghava stress results for the elements in the fill-in region and the curved laminates of both the 5mm and 10mm radius specimens were output from ABAQUS. The fill-in regions of the 2-D models consisted of approximately 1200 and 1900 elements for the 5 and 10mm radius specimens respectively. These values were analysed using the post-processing code to produce the UVES results to predict the failure load. The stress plots helped to assess the likely failure mode.

The 5mm model produced a failure load prediction of 101.5N/mm width. The 10mm prediction was 167.0N/mm width. In both cases, the failures were predicted to occur in the fill-in region. The elements shown as having the highest failure index were on the interface between the fill-in and the curved laminate, indicating that this was the most likely failure location.

A 3-D model of the 10mm radius specimens was also produced. This had 1380 elements in the fill-in region and a further 4000 in the curved laminate. Using the same method as for the 2-D models, the failure prediction for the model came out as 178.5N/mm width, 7% higher than the 2-D model. This increase in load is as a result of the lower stress levels for the 3-D model in most of the volume of the fill-in region. The higher stresses at the free edge are only in a small part of the volume of the model and hence do not provide a large contribution to the failure load prediction. The failure location was predicted to be at the free edge laminate/fill-in interface because those elements did have the higher stresses.

As the difference between 2-D and 3-D was relatively small, it was concluded that the 2-D predictions should be reasonable for both the 10 and 5mm radius specimens. It should be noted that the processing time required to produce this result was approximately 6 hours

compared with less than 15 minutes for the 2-D models.

5.6 Testing and Results

5.6.1 Test Set-Up

Testing was carried out on an Instron 1341 test machine. A testing rig which supported the 20mm wide specimens under the flanges at a span of 80mm was used as in Fig.5.2. The load was applied at the bottom of the web through glass fibre end tabs which were used to limit damage to the laminate from the grips. The tests were carried out using displacement control at a rate of 1mm/min. Failure was considered to have occurred when there was a distinct drop in the load-displacement curve.

5.6.2 Results

In all cases, failure occurred suddenly. Most failures occurred in the fill-in region as a vertical crack in the fill-in region which continued down between the two laminates making up the web of the 'T'-piece. One of each specimen type failed in the curved laminate by a delamination running round one side. A schematic of the general failure locations is given in Figure 5.16.

5.6.2.1 5mm Radius

The test results are summarised in Table 5.2. The failure location was measured from the symmetry line in millimetres, so a value of 0 indicates a failure directly through the centre

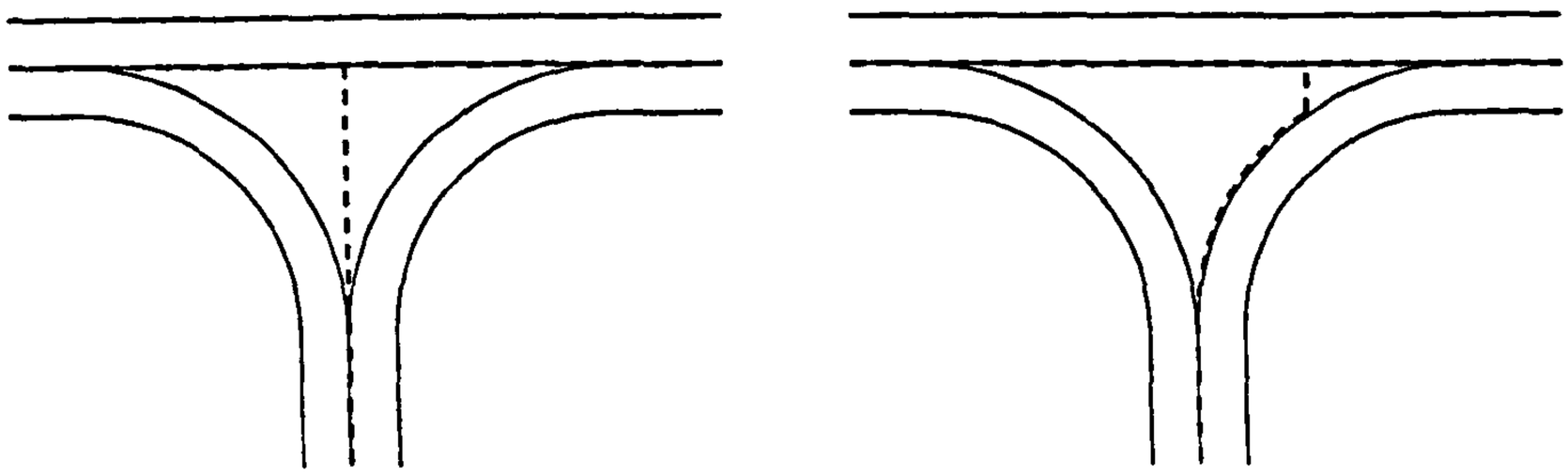

Figure 5.16: Failure Modes of the 'T'-Piece Specimens

of the specimen. If the specimen failed in the curved laminate, then it is indicated as such. Two specimens had a clearly visible void (approximately 0.5mm in diameter) in the fill-in region, which reduced the failure load in these specimens significantly. The results from these specimens were not used in calculating the mean failure load of the specimens as they were not consistent. These specimens should serve as a warning that voidage can occur even in carefully manufactured composite structures, significantly reducing the inter-fibre strength of the material.

The mean load at failure, excluding the specimens with visible voids, was calculated to be 112.6N/mm width, with a coefficient of variation of 5.4%.

5.6.2.2 10mm Radius

The test results for the 10mm radius specimens are shown in Table 5.3. All failures occurred suddenly, the failure location again given as a distance from the symmetry-line running through the centre of the fill-in region. As with the 5mm radius specimens, one

Test no.	Load/Unit Width @ Failure N/mm	Failure Location mm
1	112.2	Curved Laminate
2	119.3	3
3	113.6	0
4	112.7	1.5
5	47.2	Void
6	110.4	3
7	62.8	Void
8	101.6	0
Mean	112.6 c.v.5.4%	Excl. Voids

Table 5.2: 5mm Radius 'T'-Piece Specimen Test Results

10mm radius specimen failed by delamination in the laminate.

The mean failure load per unit width was calculated to be 193.1N/mm with a coefficient of variation of 5.3%.

5.6.3 Discussion

5.6.3.1 Failure Locations

The load at failure, and the location of the crack within the fill-in region followed a pattern. The specimens with higher failure loads tended to fail away from the stress peaks (within 1mm of the centre in the 5mm specimens and within 2mm for the 10mm radius specimens), or in the laminate. This is seen more clearly in the 10mm radius results than those for the 5mm radius specimens. From this it can be reasoned that the failure location was not totally stress dependent, and that the failure was governed by defects in accordance with the volume effect theory. This helps support the use of the volume effect

Test no.	Load/Unit Width @ Failure N/mm	Failure Location mm
1	193.8	6
2	186.2	3
3	181.1	3
4	204.3	8
5	202.4	Laminate
6	190.6	6
Mean	193.1 c.v. 5.3%	

Table 5.3: 10mm Radius 'T'-Piece Specimen Test Results

theory within the delamination prediction method.

5.6.3.2 Comparison with Prediction

Overall, the failure load predictions and the mean failure load found in testing compare well. The 2-D models therefore appear to be accurate enough to represent the specimen stress fields. The 5mm specimens were predicted to fail at 101.5N/mm, whereas the mean test result was 112.6N/mm width, 10% conservative. The 10mm specimen prediction was calculated to be 167N/mm width and the test result was 193.1N/mm, 13% conservative. The 3-D failure prediction was 178.5N/mm which is only 8% conservative, a useful improvement over the 2-D model.

5.7 Conclusions

Most of the specimens failed in the fill-in region due to high stresses acting between the fibres, causing delamination. The finite element analyses predicted failure in the fill-in region, comparing well with experiment. The mean failure loads also compared well with

the failure predictions which were all within 13% and conservative. The defect controlled nature of the failure in the fill-in was also made apparent, supporting the applied volume effect theory. The 3-D prediction of the 10mm radius specimens was the most accurate, but at a cost in terms of processing and modelling time.

Two of the specimens did not fail in the fill-in region, but suffered delamination in the curved laminate. The method coped with this problem without any concerns as the curved region results did contribute to the overall failure prediction. The next chapter reports the method being applied to a more complex specimen type, a composite edge closure of a sandwich panel.

Chapter 6

Failure Prediction of the 90° Sandwich Panel

6.1 Introduction

In the previous chapter, the stress based delamination prediction method was applied to a specimen which failed in a block of unidirectional material. It will now be applied to a sandwich panel edge element which features curvature, angled plies and resin pockets.

Sandwich panels manufactured using composite materials have been used widely as weight-saving structures for many years. Some of the uses are for lightweight body shells such as Formula 1 Racing car monocoque chassis, floor panels in aircraft and in other applications which require high flexural rigidity with low weight.

There is a large amount of published material on the design of sandwich panels, such as Allen [80] and Teti [81]. Early research on sandwich panel constructions has concentrated on the behaviour of the core material and top and bottom surface skins. Honeycomb cores

have been studied regarding the buckling or crushing failure when subjected to impact loading e.g. Kim&Jun[82]. The buckling of the skins has been studied to a large extent [80], and the effects of delaminations [83] and debonds from the core [84] on buckling have also been worked on. The effect that the edge closure element (sometimes referred to as the diaphragm) has on stress concentrations and failure due to peeling has been studied [85], but little work has been seen investigating the detailed design of the edge closure element.

A design drawing of a carbon composite/aluminium honeycomb floor panel from the EH101 helicopter was supplied by GKN/Westland Helicopters Limited (GWHL). The basic geometry consisted of two 'Z'-sections (two horizontal flanges with a vertical web forming a 'Z'-shape) and aluminium honeycomb separating the skins which were 38mm apart. It was important for the specimens to fail by delamination in a composite component whilst using a realistic design geometry.

The local geometry of a composite structure can vary significantly due to manufacturing variation. A ply drop can have a tolerance of 1 to 2mm on the location of the ply termination [33], which can lead to asymmetric ply drops and ply thickness variation. Variations such as these also result in changes in taper angle and therefore the stress state. This in turn can lead to a change in the location of failure, which makes the use of nominal geometries questionable in detailed analysis, although, it is reasonable if the geometry has come about from detailed investigation of the manufacturing processes involved. It should be noted that this variation cannot be eliminated, even with careful and proper handling of the material.

In this chapter, the effect of local minor geometric changes on the stress levels, and hence the delamination prediction are shown. The stress based prediction method was used to predict the delamination of the specimens.

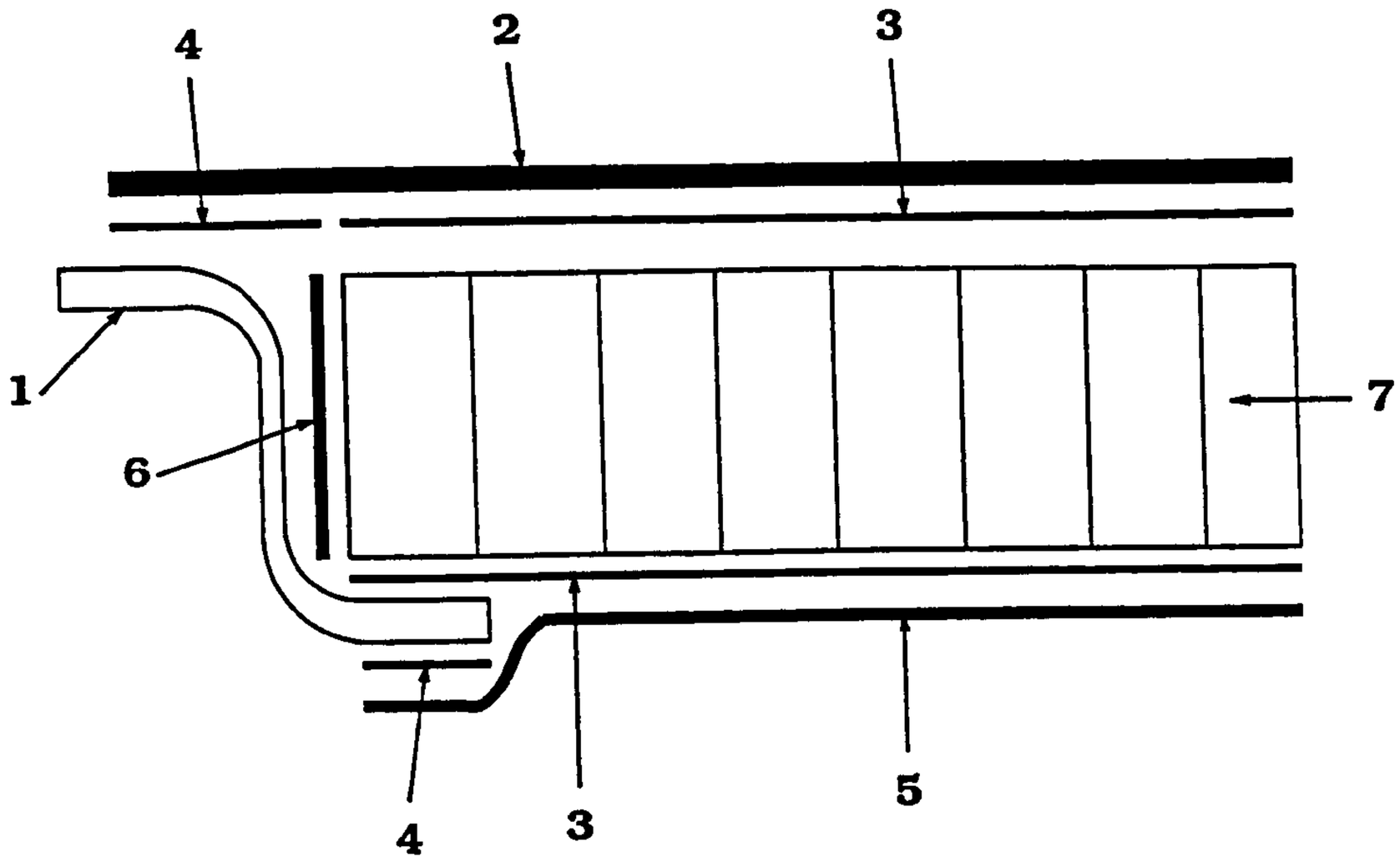

1. Pre-Cured Edge Closure
2. Pre-Cured Top Skin [0/90/0/90/0]
3. Film Adhesive AF-163-2U-03
4. Film Adhesive AF-163-2K-06
5. Bottom Skin [0/90/0]
6. Foaming Adhesive AF-3024-50
7. Core - Aeroweb 6.9-3/16-25

Figure 6.1: Basic Sandwich Panel Construction

6.2 Specimen Design

The sandwich panel design supplied by GWHL (constructed with carbon/PEEK skins) was altered to produce a specimen of a convenient size for manufacture. The specimens were manufactured in panels which were large enough to be cut into 5 specimens.

The basic construction and dimensions of the 90° sandwich panel design is shown in Figure 6.1. The 'Z'-section consisted of 2 surface 0° plies and 4 pairs of ±45° plies interspersed with 5 pairs of 90° plies which are only present in the flanges of the 'Z'. The thicker, compression loaded upper skin was made with a [0/90/0/90/0] lay-up, whilst the lower tension skin had a [0/90/0] lay-up.

The critical area of the sandwich panel design in this work was the 'Z'-section, and more specifically the upper curved region. The overall dimensions of the panel are shown in

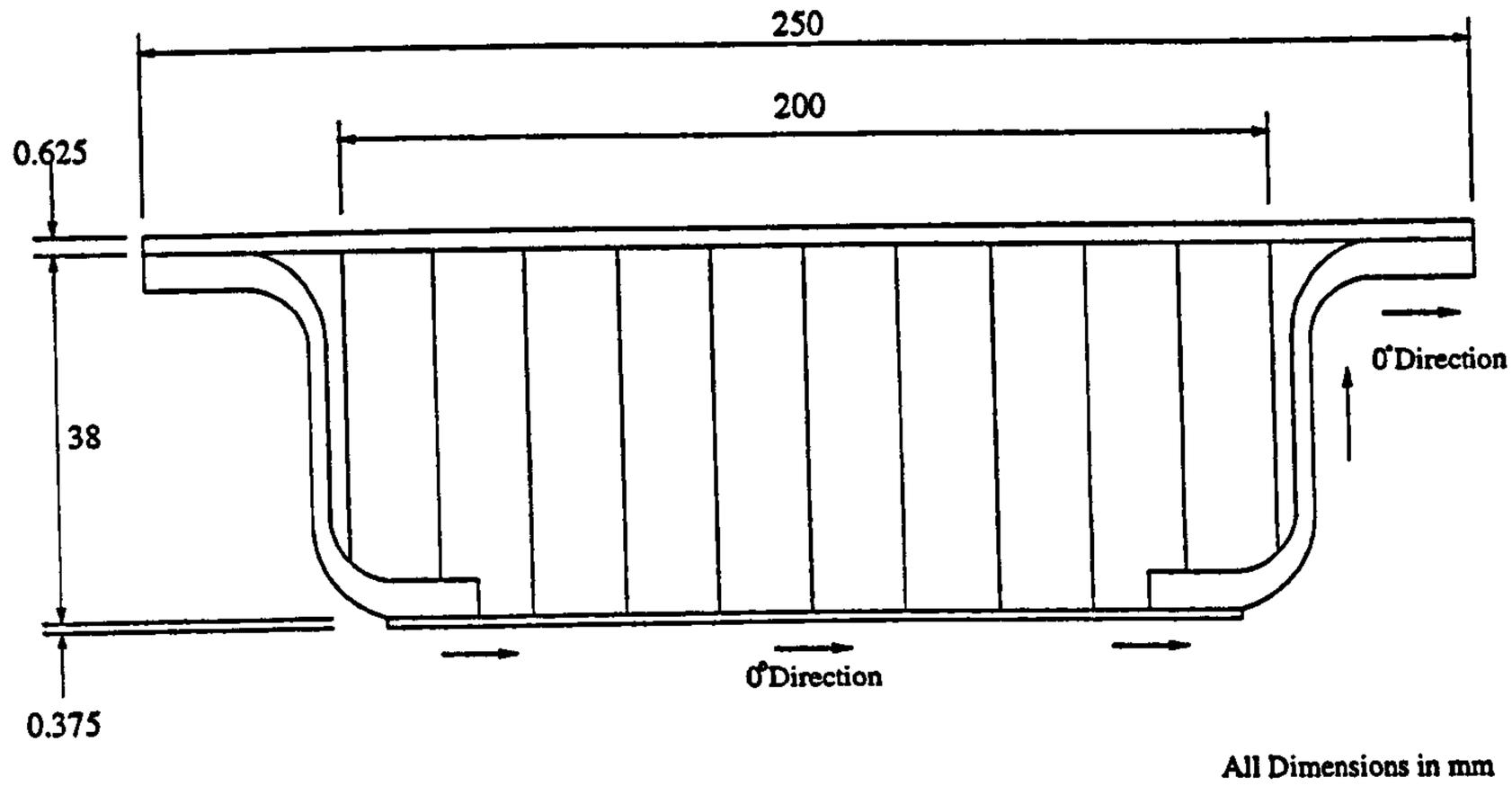

Figure 6.2: 90° Sandwich Panel Geometry

Figure 6.2.

6.3 Manufacture

As for the humpback bridge and 'T'-piece specimens, the composite material used was HTA/913C. The lay-ups for the sandwich panel skins were [0/90/0/90/0] for the top skin and [0/90/0] for the bottom skin. The edge closure lay-up was [0/90_2/ ± 45/90_2/ ± 45/90_2/ ± 45/90_2/0] and is shown schematically in Figure 6.3, with the 90° ply drops. The core material was aluminium honeycomb, designation Aeroweb 6.9-3/16-25(5052)T from Hexcel [65]. The honeycomb to composite skin bonding was carried out using an unsupported film adhesive, AF-163-2U-0.03. A supported film adhesive, AF-163-2K-0.06, was used to bond the skins and edge closures.

The edge closure was manufactured first in a section approximately 450mm long. The tooling used to control one surface of the edge closure is shown in Figure 6.4. It had a 1° slope to compensate for the 'spring forward' effect due to differential thermal contraction of the material during cooling from cure. The tooling was only used in the precure stage of the manufacturing process. The edge closure was then cut in half, and both halves were

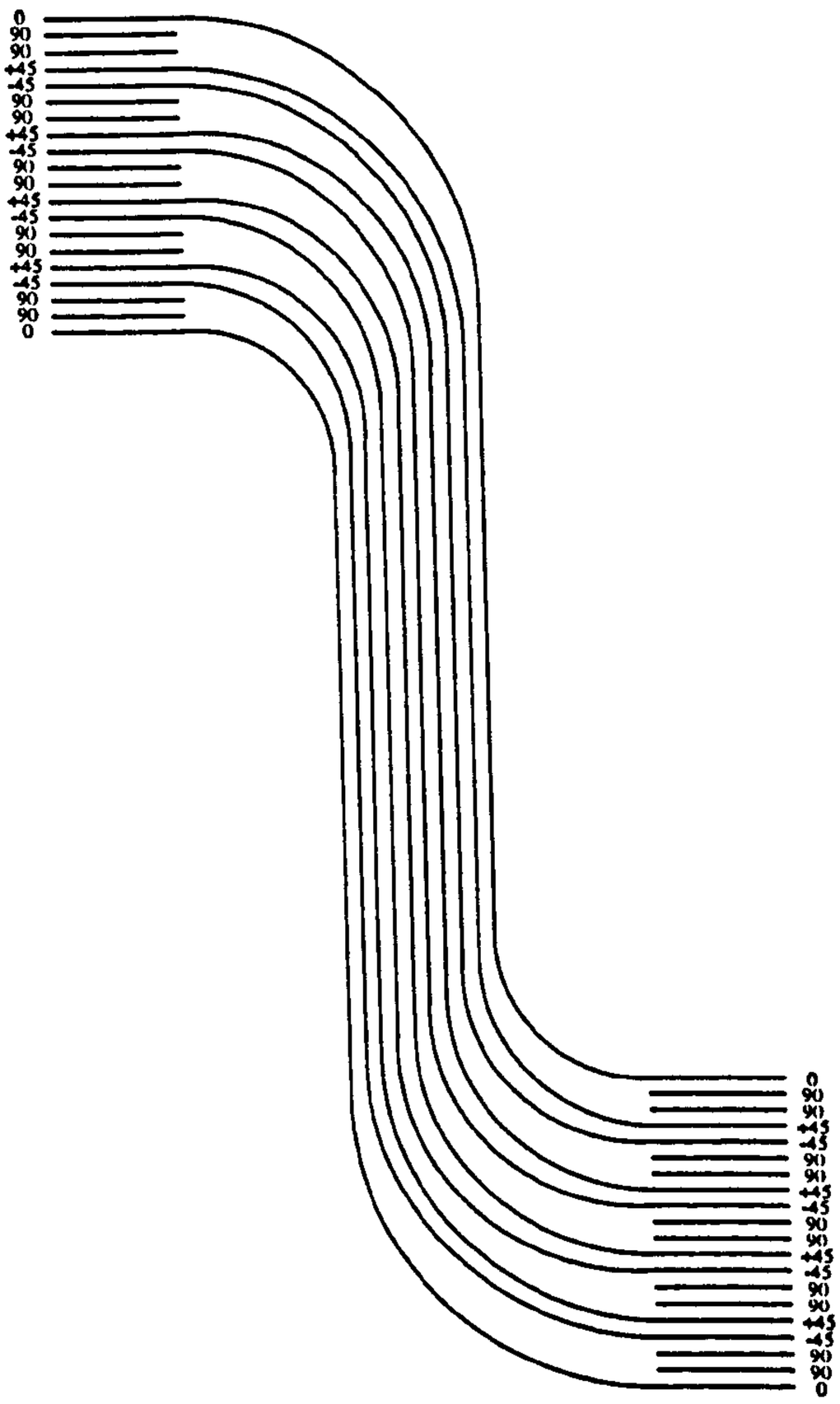

Figure 6.3: Schematic Representation of Sandwich Panel Edge Closure Lay-Up

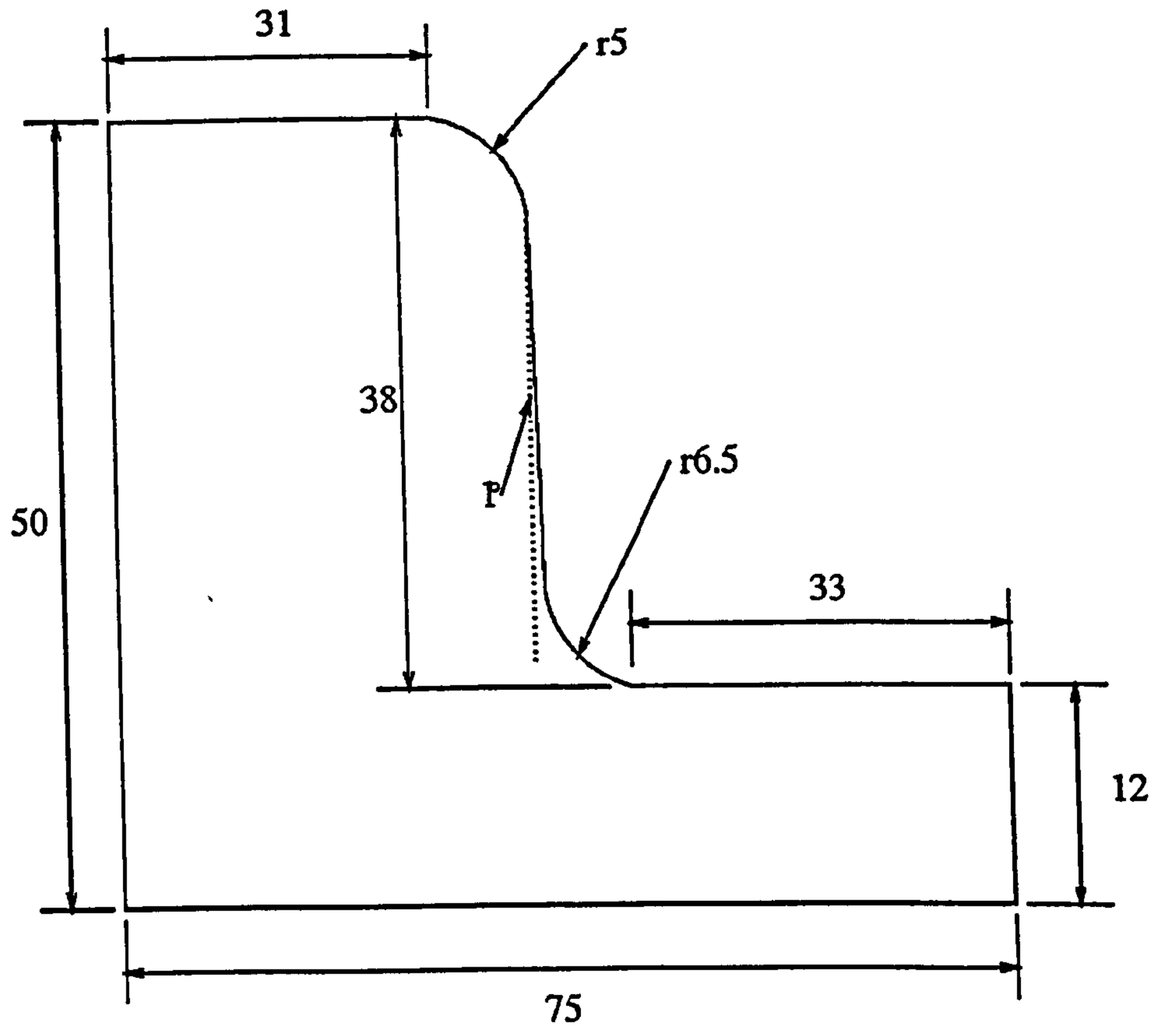

Figure 6.4: Tooling for 90° Sandwich Panel Edge Closure

used to make a panel of 220mm width, enough for 5 specimens.

Foaming adhesive was used between the edge closure and the edge of the honeycomb, designation AF-3024-50 from 3M [78]. During the cure process, the adhesive expands and fills up any available space, contacting all free surfaces. The foam provided load transfer between the core and the edge closure, improving the stiffness of the structure significantly.

Prior to assembly, all precured surfaces which required bonding were degreased with acetone, grit blasted for a good adhesive surface and then degreased again. The honeycomb was degreased with 1,1,1 trichloroethane and dried.

The top skin was precured to eliminate wrinkling during cure. All of the components

were assembled for the final assembly cure which was carried out at 2.5bar. This is less than the specified 7bar for the material, and was done to avoid core crushing. All of the composite components apart from the bottom skin were cured at the full 7bar pressure, so there should be no issues regarding interlaminar strength.

6.4 Finite Element Analysis

The assumed and measured geometries of the sandwich panel were analysed as 2-dimensional plane strain finite element models. The two models were based on the same specimen, yet produced different stress distributions around the failure region. The reasons for this are explained and the importance of modelling geometry accurately for failure prediction is emphasised. Both geometries in the study were modelled using the geometry creation and meshing functions of I-DEAS [79]. The analysis and graphical post-processing of the results were carried out using ABAQUS [70].

6.4.1 Material Properties

The composite material properties which were used are the same as those used previously, and are shown in Table 6.1. The plies lie in the X-Z plane and the interlaminar direction is in the Y direction of the 2-D elements. The out-of-plane properties were found by assuming transverse isotropy. The properties for the $\pm 45^{o}$ plies were calculated using laminated plate theory and averaged. The aluminium honeycomb material properties were taken from data sheets supplied by Hexcel [65] and are in Table 6.1. The film and foaming adhesive properties were taken from data sheets supplied by 3M [78] and are shown in Table 6.2. It should be noted that the user defined material code routine only required the basic UD ply properties and the ply angle. This was only applied in the region of failure, however, so the other ply angle properties were required to complete the model.

Material Property	HTA/913C 0°	HTA/913C ±45°	HTA/913C 90°	Honeycomb
E_{XX}	131.5GPa	17.2GPa	9.2GPa	0.01GPa
E_{YY}	9.2GPa	9.2GPa	9.2GPa	2.7GPa
E_{ZZ}	9.2GPa	17.2GPa	131.5GPa	0.01GPa
ν_{XY}	0.3	0.114	0.45	0.01
ν_{YZ}	0.45	0.061	0.021	0.01
ν_{XZ}	0.3	0.766	0.021	0.4
G_{XY}	4.875GPa	3.9GPa	3.103GPa	0.37GPa
G_{YZ}	3.103GPa	3.9GPa	4.875GPa	0.58GPa
G_{XZ}	4.875GPa	30.77GPa	4.875GPa	0.01GPa

Table 6.1: Orthotropic Material Properties

Material Property	913C Matrix	Film Adhesive	Foaming Adhesive
Young's Modulus	3.39GPa	1.1GPa	0.4GPa
Poisson Ratio	0.4	0.4	0.1
Shear Modulus	1.21GPa	0.393GPa	0.182GPa

Table 6.2: Isotropic Material Properties

6.4.2 Meshing

The design of the sandwich panel specimen required finite element analysis to be carried out to assess the failure mode and to indicate any likely problems. The mesh had to be created without any knowledge of the final geometry of the specimen, especially in the region of ply drops. The model which was produced was quite reasonable in terms of predicting the failure location and load, but when the geometries of the specimen and the model were compared, it was clear they were quite different. This led to some research into local geometry effects, and the measured geometry mesh for this specimen was produced.

In both cases the mesh generation guidelines stated in Chapter 3 were adhered to. Each load bearing ply had at least 1 element through the thickness. The aspect (side length) ratios of the elements were kept below 2 where it was possible to do so. This was not feasible near the tips of the resin pockets where triangular elements had to be used.

The following assumptions were made for the analyses:-

- All applied mechanical load cases were 3-point bending acting over the same span, so only approximately 40mm of the specimen was modelled in the spanwise direction. This reduced the number of elements required in the model without affecting the load distribution around the critical failure region.
- The distance of the support roller from the curve was the same in each model.
- The same material properties were used in each case (Tables 6.1&6.2).
- All analyses were linear with 6 and 8 noded parabolic elements in a plane strain domain.

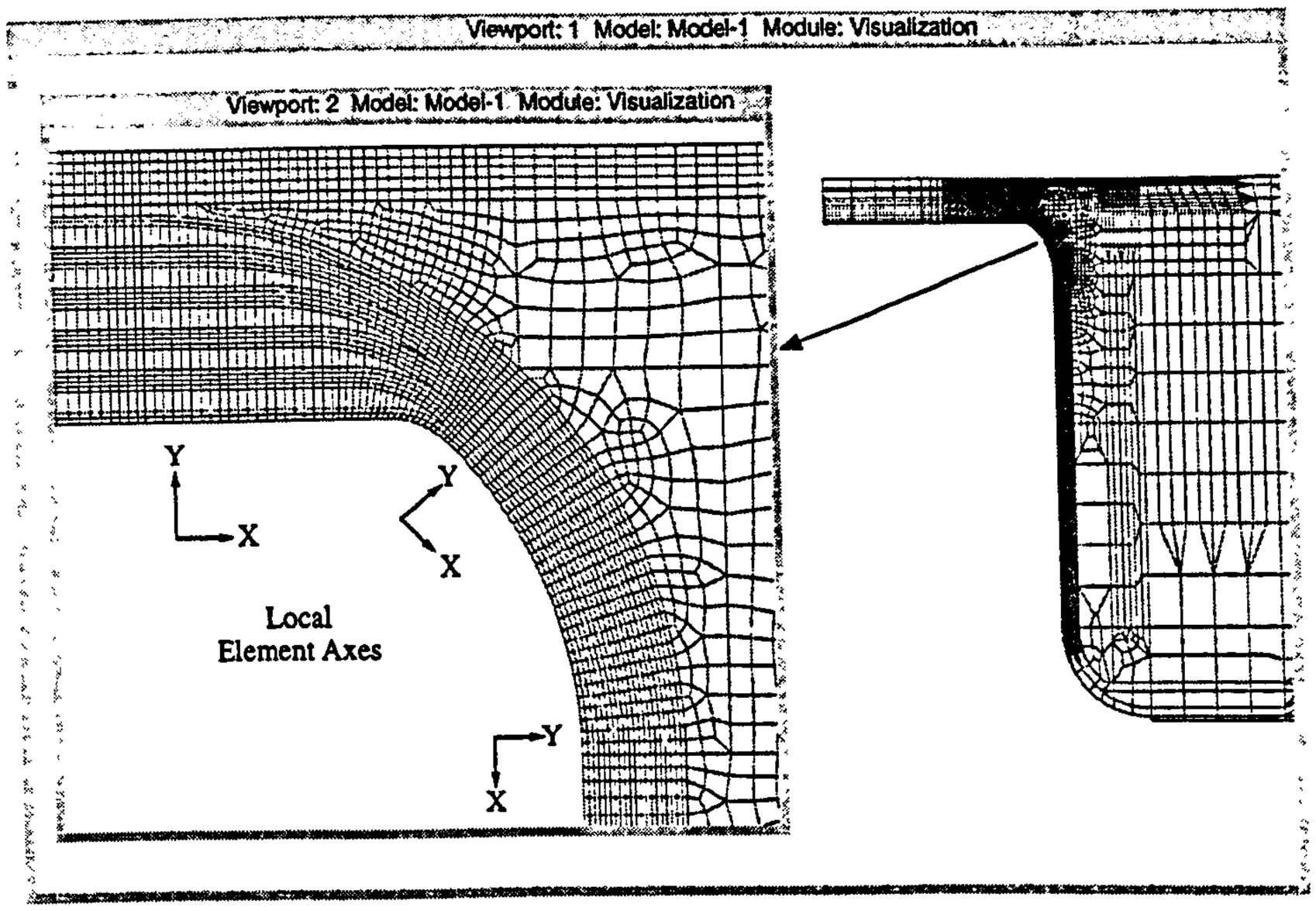

Figure 6.5: Assumed Geometry Mesh of Sandwich Panel

6.4.2.1 Assumed Geometry Mesh

The FE model was constructed using a largely assumed geometry, with most of the dimensions taken as the nominal, but some taken from the specimens. The ply thickness was assumed to be 0.125mm throughout the specimen. The radius of the top ply was taken to be 6.5mm, that of the tooling. The radius of the lowest ply was taken from the geometry and was found to be 1mm. The radius of each ply pair within the laminate was linearly interpolated between these two values. Each ply was assumed to remain straight until close to the curved part of the 'Z'-section, where the curvature was applied using a fillet radius. The 90° plies were all assumed to drop at approximately the same point along the model, 6mm from the loading point. At this location, the material properties are changed from those of 90° plies to that of pure 913 resin. The mesh is shown in Figure 6.5. Only 20mm of the honeycomb was modelled at which point all nodes were fully restrained. This was found to produce the same load path as an entire model of the specimen, and used less elements. The load was applied at a point 7mm from the start of the tight curve on the lower ply.

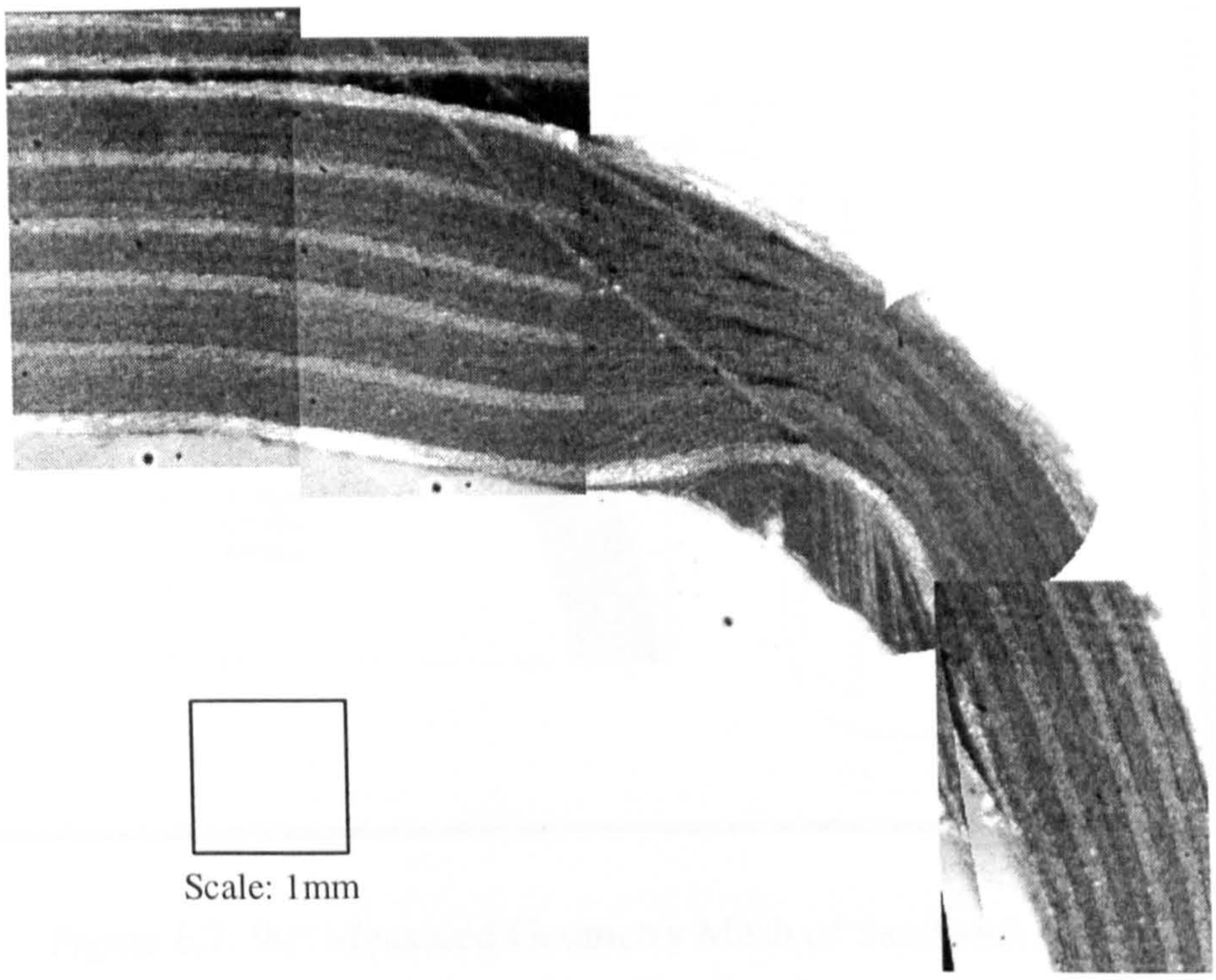

Figure 6.6: 90^o Sandwich Panel Specimen Geometry

6.4.2.2 Actual Geometry Mesh

The actual manufactured geometry of the specimens is shown in Figure 6.6. The 90^o curve of the upper edge closure was found to be critical and was modelled accurately. This was done to establish the importance of the local geometry on both the predicted failure load and the location. The model geometry was taken from this photograph of a specimen cross-section.

In testing, the load was applied at a point 7mm from the thinnest point of the specimens. For consistency, the load was applied at a node 7mm from the thinnest point of the model. Only 40mm of the specimen was modelled to reduce the number of elements used in the analysis. The cross-width restraining nature of the 90^o plies in the edge closure meant that plane strain was a reasonable assumption to make.

Figure 6.7 shows the mesh which resulted from the detailed modelling process. The

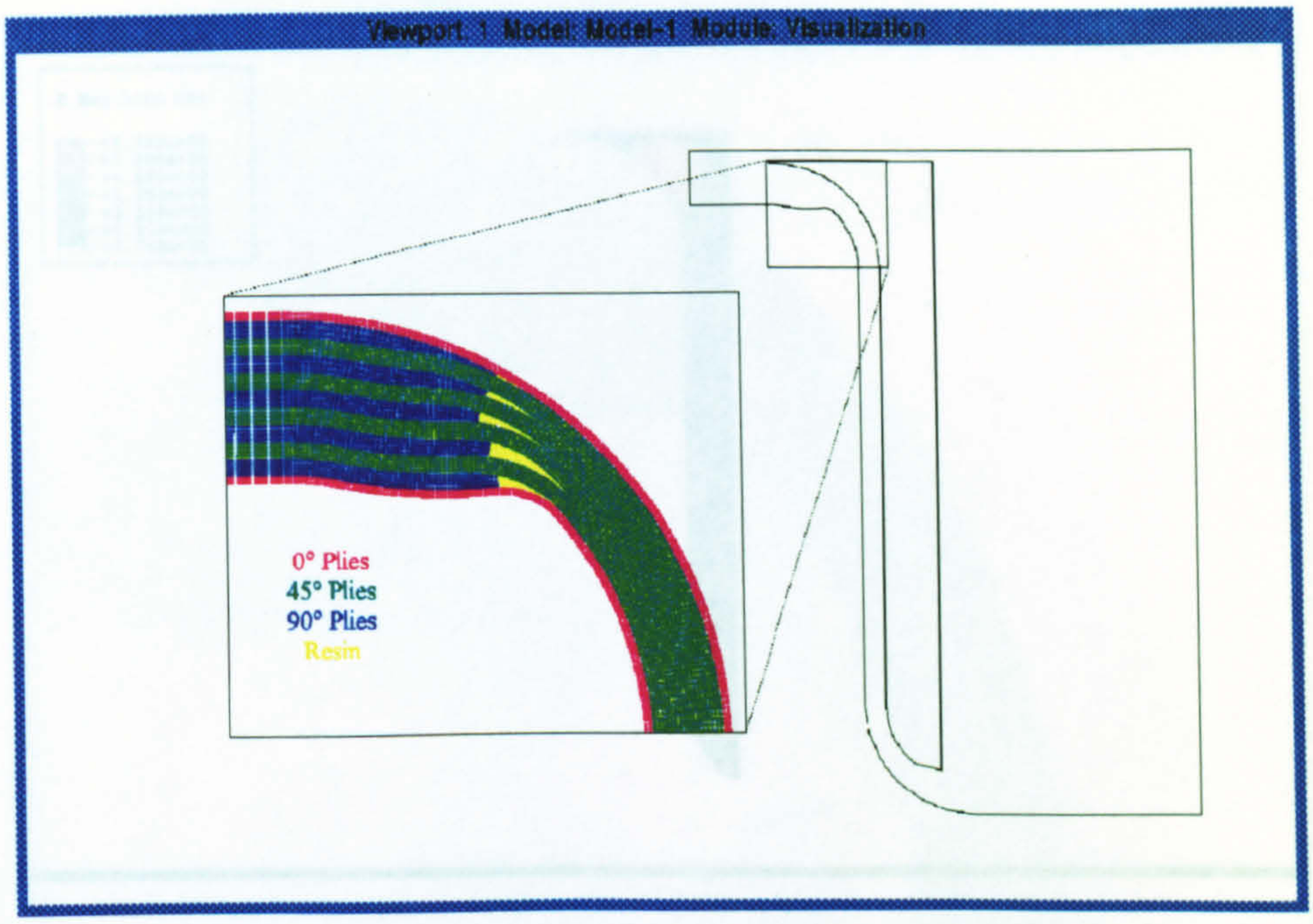

Figure 6.7: 90° Measured Geometry Mesh of Sandwich Panel

intention was to produce an FE mesh which modelled all the features of the specimen geometry accurately. This was achieved by scaling the dimensions of the image to that measured on the specimens. The geometry is complex, but was quite feasible to reproduce with the geometry creation tools within I-DEAS. The different material properties used in the model are shown by the colour of the element, the key is included in the Figure. The complete model mesh is shown, with only 20mm of the sandwich section simulated. This model is long enough, however, to produce the same load transfer in the failure region as a half model of the specimen.

6.4.3 Analysis Results

The objective was to investigate the effect of local geometry on the stress due to loading, so thermal stresses were not included at this stage. The applied load for both models was 50N/mm width, and was applied at a node 7mm from the thinnest point in both cases, so the same shear load and bending moments should be present in the critical region in the models.

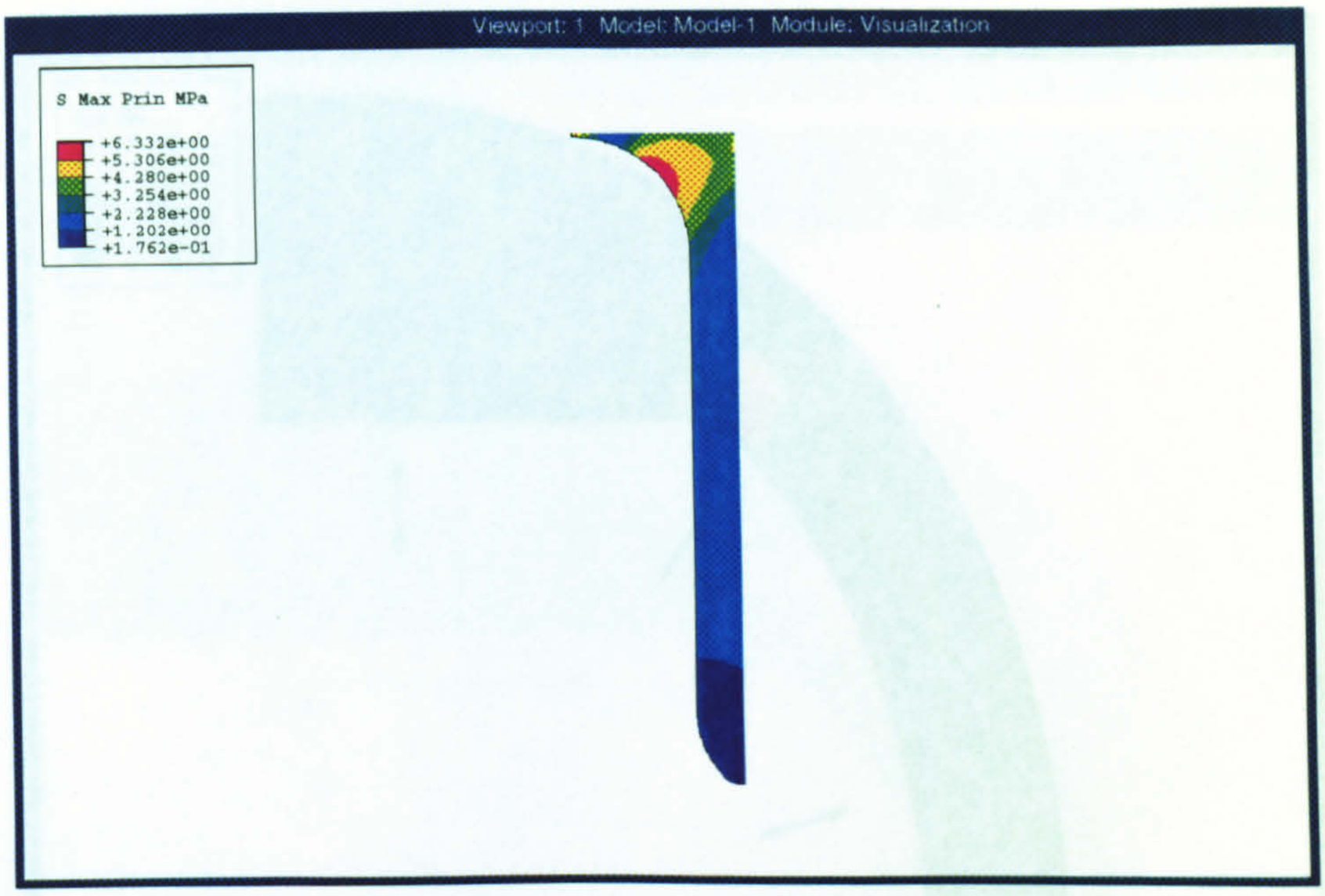

Figure 6.8: Maximum Principal Stress in Foaming Adhesive at 50N/mm

6.4.3.1 Assumed Geometry

The critical areas in terms of failure were found to be the upper curve of the 'Z'-section and the foaming adhesive. The tensile strength of the foam was quoted at 939psi when bonded to honeycomb material, which is approximately 6.5MPa. The maximum principal stress levels in the foam at 50N/mm are shown in Figure 6.8. They show the peak tensile stress acting at each point and indicate failure at this load case by using a simple failure criterion such as maximum stress.

The interlaminar stress levels (Figure 6.9) in the curve at this point are much lower than those which should cause failure (the order of 100MPa). The other stress components are also low, so the foam is likely to fail before delamination of the composite can occur. Therefore the foam was removed for the rest of the analysis and delamination failure predictions in both specimens. It is reported later that the specimens did fail in the foaming adhesive prior to delamination, confirming this assumption, changing the load path in the structure significantly.

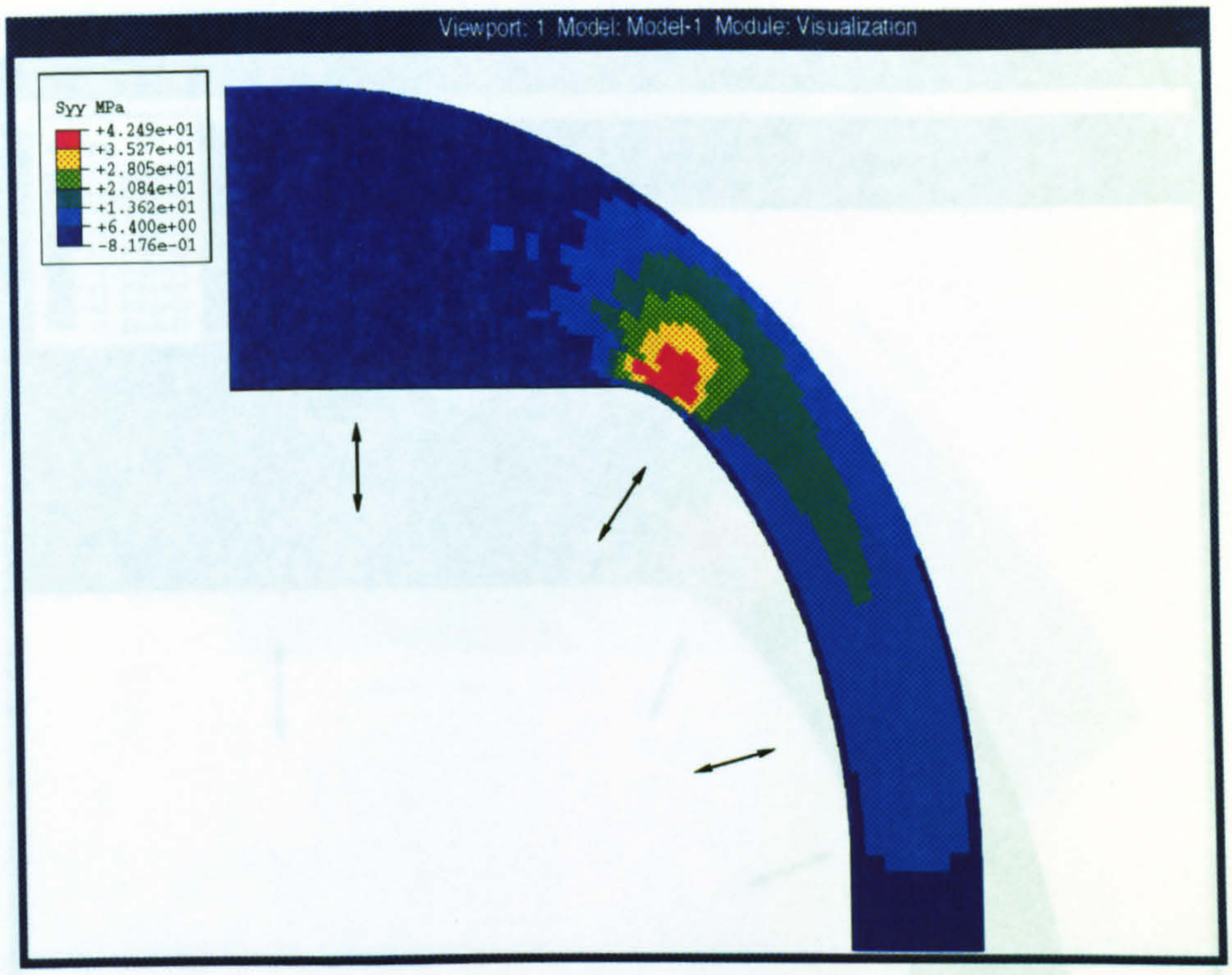

Figure 6.9: Interlaminar Tensile Stress in Curve at 50N/mm with Foaming Adhesive

With the foaming adhesive removed, the stress levels in the critical curved region increased by around 50% (Figure 6.10). This is a clear indication of the effectiveness of the foaming adhesive at supporting the edge closure and increasing the overall performance of the sandwich panel. The peak stress is within the first resin pocket and is caused by the bending of the curved region. The tight radius of the surface ply is responsible for the large magnitude of these stresses.

The interlaminar shear stress levels in the curve at this point are shown in Figure 6.11. The peak stresses are in and between the second and third resin pockets and are central within the laminate. The stresses will combine to cause failure in this model, so an interactive method, such as that proposed, would be required to predict failure.

The interlaminar tensile and shear stresses in the curved laminate are caused by bending. This is shown in a plot of the longitudinal in-plane strains in the region (Figure 6.12). The peak of the bending is slightly away from the region of ply drops and tight curvature. The magnitudes of these strains do not cause concern regarding in-plane failure of the plies as

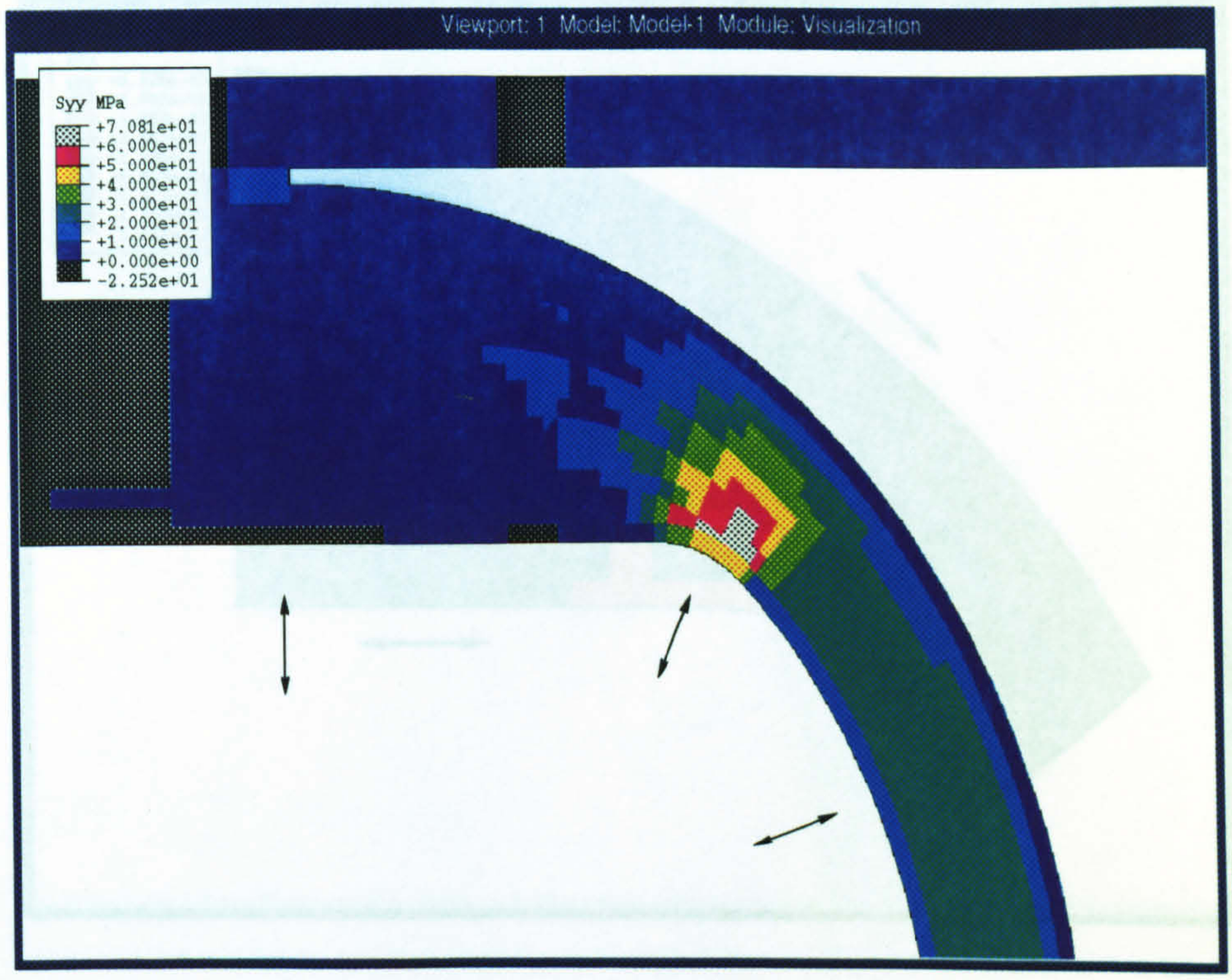

Figure 6.10: Interlaminar Tensile Stress at 50N/mm without Foaming Adhesive

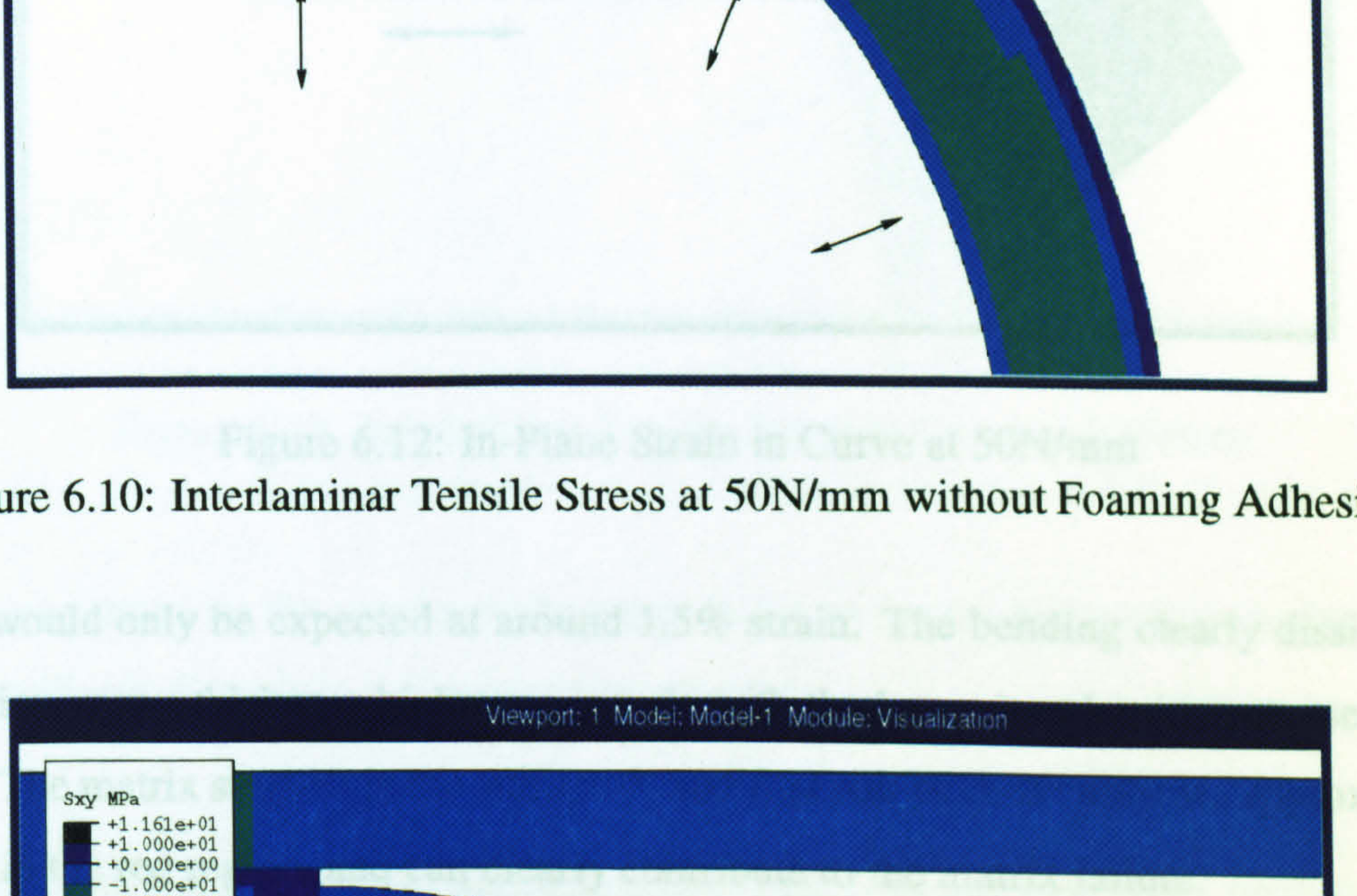

Figure 6.11: Interlaminar Shear Stress in Curve at 50N/mm

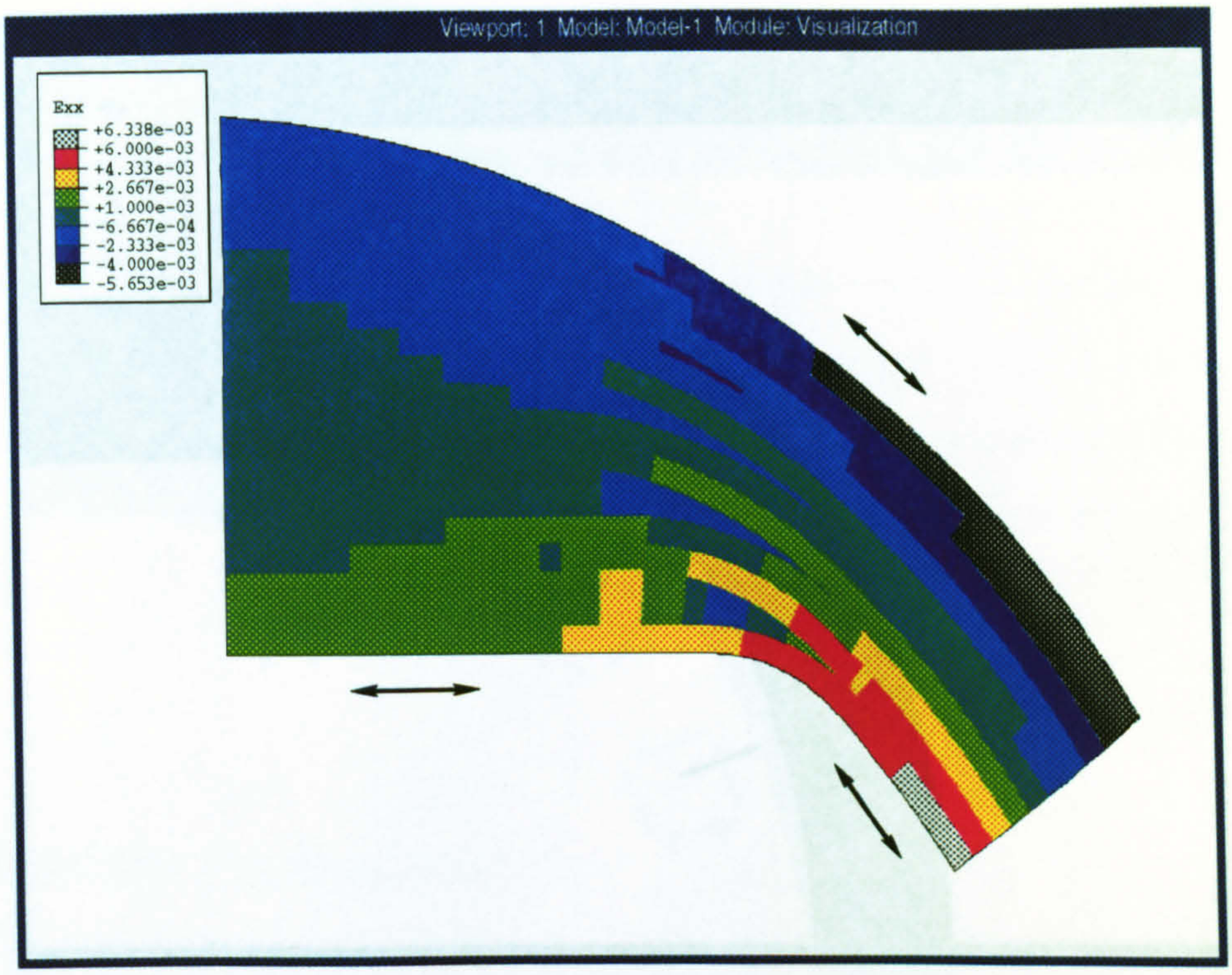

Figure 6.12: In-Plane Strain in Curve at 50N/mm

failure would only be expected at around 1.5% strain. The bending clearly dissipates as the section grows thicker, which corresponds with the lower interlaminar stresses in this region. The matrix stresses in the surface 0^o and first pair of $\pm 45^o$ plies are approximately 20MPa in the red region, and can clearly contribute to the matrix failure.

6.4.3.2 Measured Geometry

At the same applied load of 50N/mm and with no thermal residual stress, the stress levels in the curved region are the only critical ones, and are shown here for comparison. Firstly, the interlaminar tensile stress in the accurate model is shown in Figure 6.13. The stresses are plotted using the same contours and range, making any differences easier to spot and interpret. When the accurate model is compared to Figure 6.10, there is a fairly similar pattern, with the highest stresses being around the centre of the curve and the ply drops. The two models show only a 4% difference in the stress-levels, the accurate model having a stress peak of 74MPa, compared with 71MPa. The stresses should be more accurate to

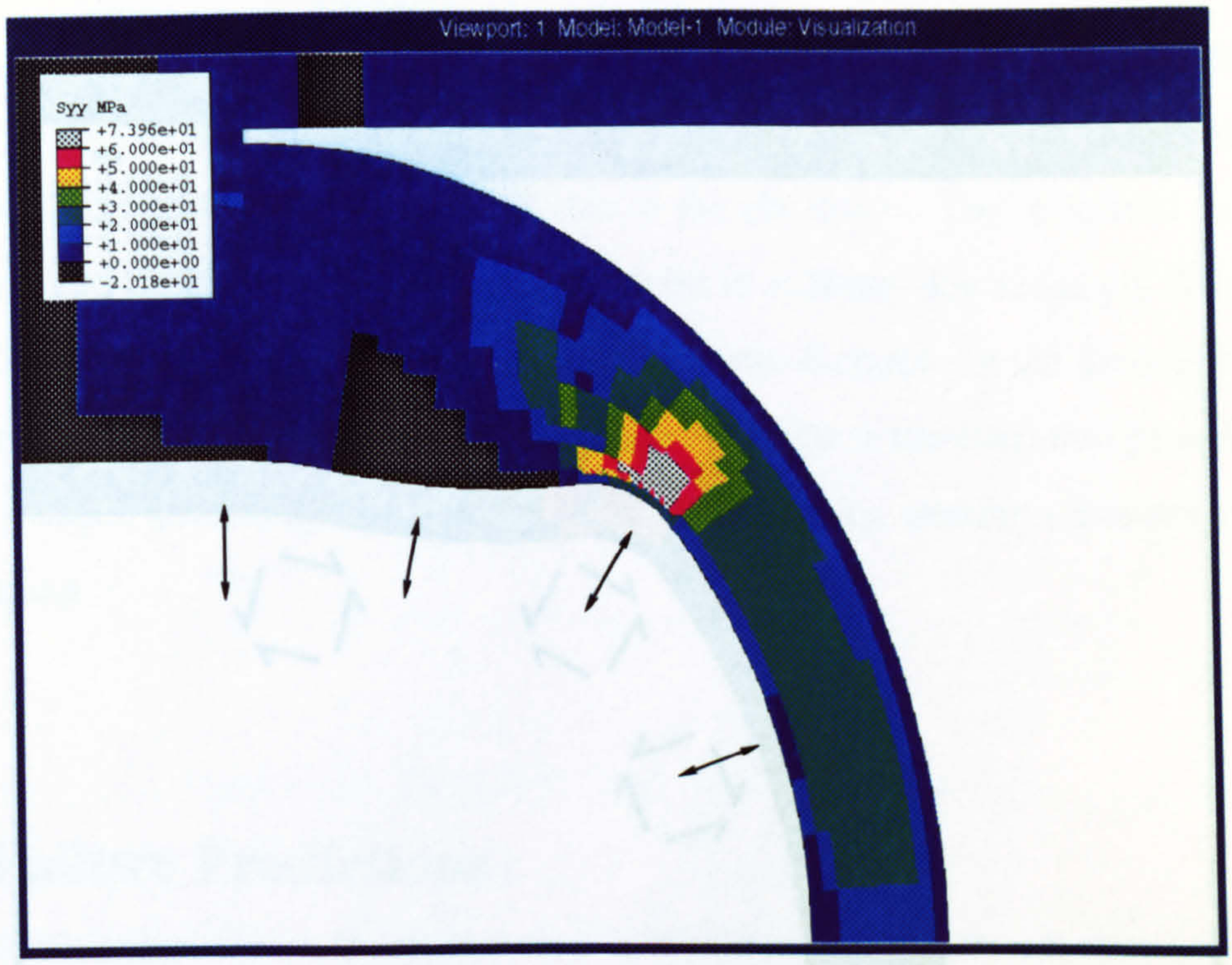

Figure 6.13: Interlaminar Tensile Stress in Curve at 50N/mm

those experienced by the specimens because of the geometry being accurate, but there is not a significant difference between the two models.

The interlaminar shear stresses are shown in Figure 6.14 and also show similar patterns to those seen in the assumed geometry model (Figure 6.11.) The highest stresses in both cases are around the ply drops and curve, both of them introducing stress concentrations for the applied shear loading at the support node. The stress peak (-62MPa c.f. -51MPa) is 22% higher than the assumed geometry, significantly affecting any strength predictions.

The longitudinal in-plane strains for the accurate geometry are shown in Figure 6.15. The magnitude of the strains in the region is only around 4% different to the assumed model geometry, which compares well with the interlaminar tensile stress level increase. The higher interlaminar shear stress, however, can only be explained by the difference in geometry. The location of the peak strains in the measured model is closer to the to the ply drop region, and so they dissipate in a shorter distance. As the shear stresses are higher, the bending develops over a shorter distance.

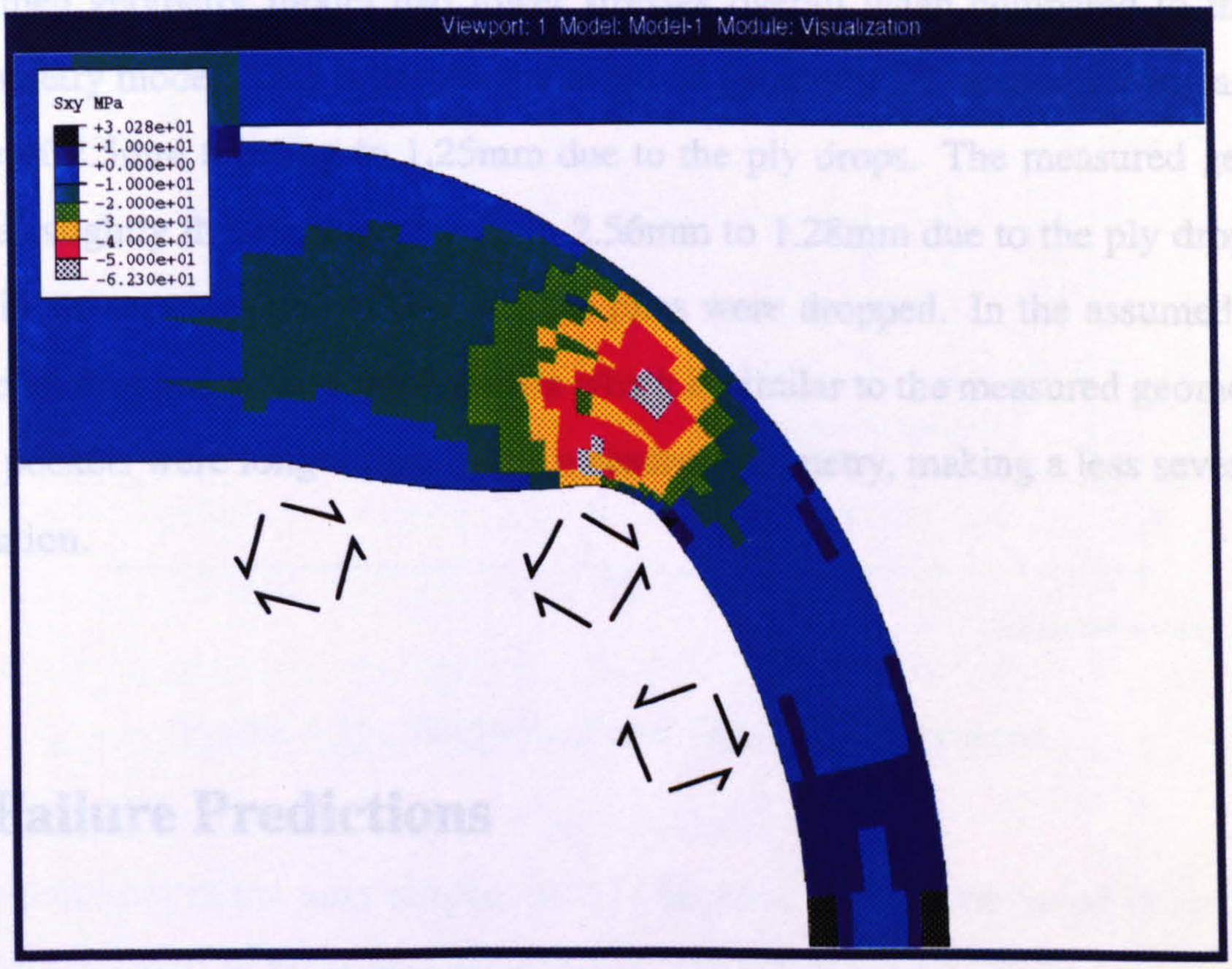

Figure 6.14: Interlaminar Shear Stress in Curve at 50N/mm

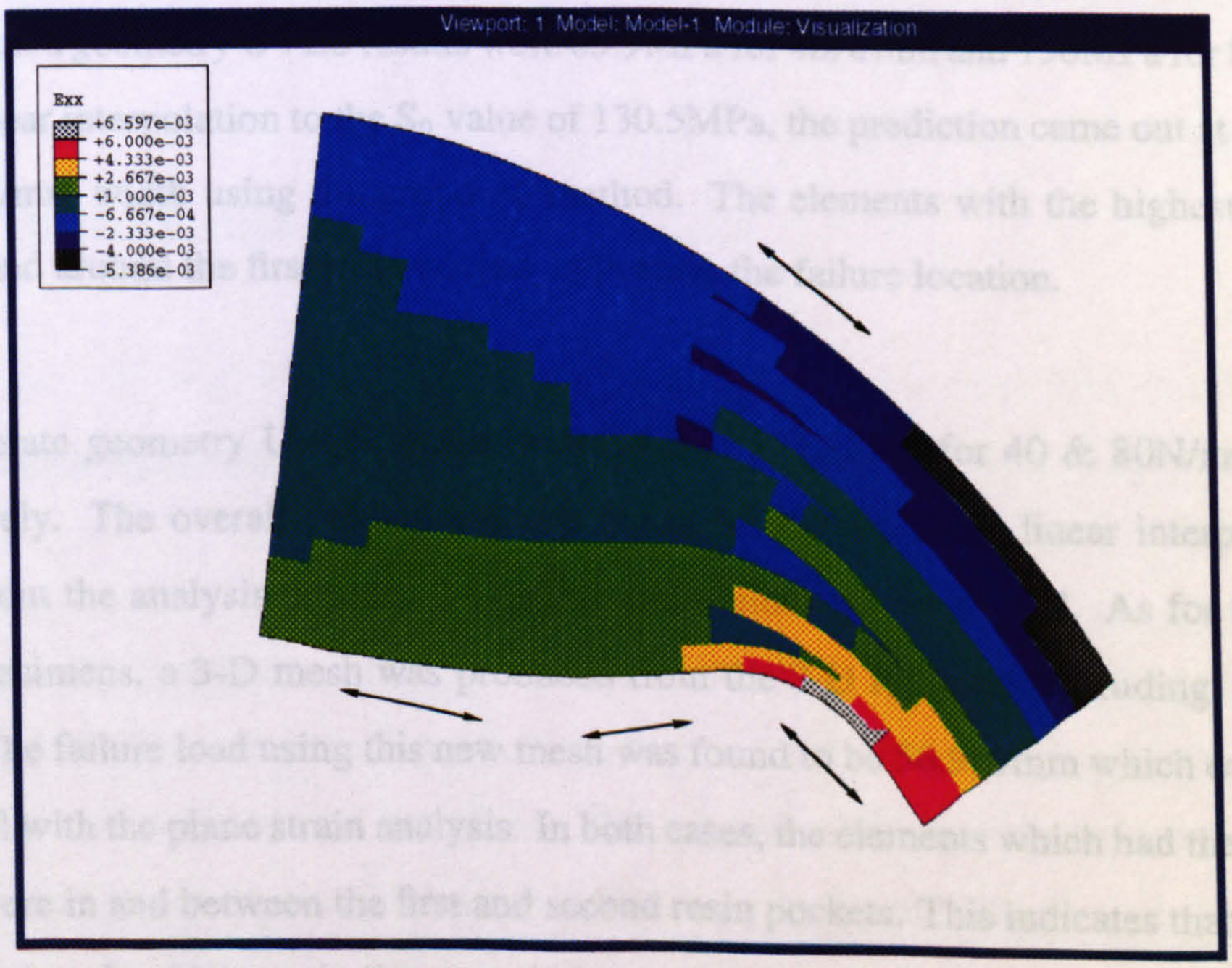

Figure 6.15: In-Plane Strain in Curve at 50N/mm

The assumed geometry model had lower stresses overall when compared to the measured geometry model. This is despite the assumed geometry 'Z'-section having an initial thickness of 2.5mm tapering to 1.25mm due to the ply drops. The measured geometry model was slightly thicker, tapering from 2.56mm to 1.28mm due to the ply drops. The increase in stresses was due to the way the plies were dropped. In the assumed model, they were all dropped at the same location which is similar to the measured geometry, but the resin pockets were longer than in the measured geometry, making a less severe stress concentration.

6.5 Failure Predictions

Both models were re-analysed with the thermal residual stresses included and with load cases of 40 and 80N/mm width applied.

The assumed geometry UVES results were 85.9MPa for 40N/mm and 156MPa for 80N/mm. Using linear interpolation to the S_0 value of 130.5MPa, the prediction came out at a value of 64.8N/mm width using the proposed method. The elements with the highest values were in and around the first resin pocket, indicating the failure location.

The accurate geometry UVES results were 94.2 & 171.1MPa for 40 & 80N/mm load, respectively. The overall prediction came out at 58.9N/mm using linear interpolation. Throughout the analysis process, 2-D plane strain elements were used. As for the 'T'-Piece specimens, a 3-D mesh was produced from the 2-D mesh by 'extruding' the elements. The failure load using this new mesh was found to be 56.9N/mm which compares very well with the plane strain analysis. In both cases, the elements which had the highest values were in and between the first and second resin pockets. This indicates that the first delamination should occur in that area during testing.

From these results, it was decided to analyse the failures of the two 90° models and also

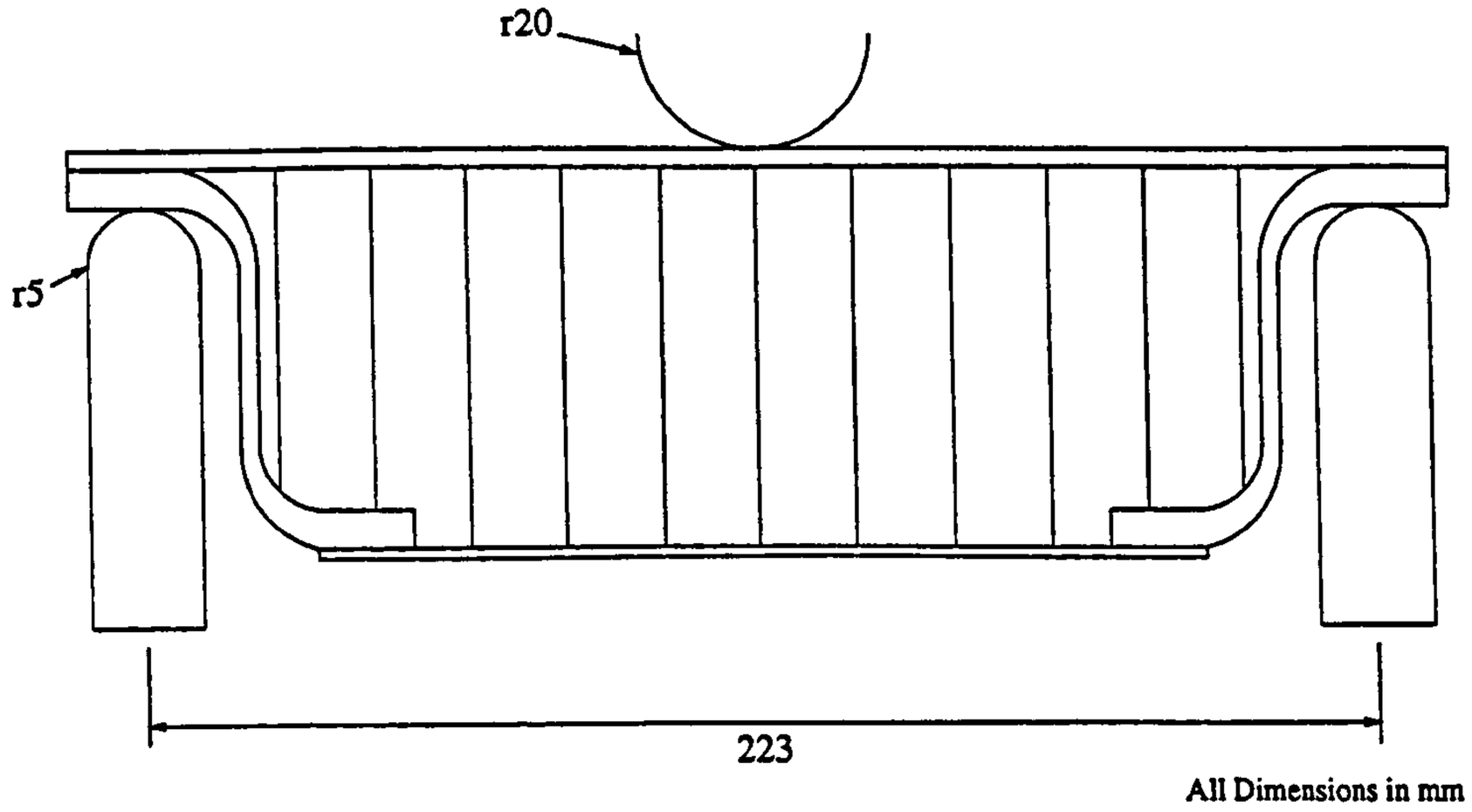

Figure 6.16: Sandwich Panel Test Rig Dimensions

the 30° specimens in the next chapter in 2-D because of the time saved in creating the models and analysis without loss in accuracy. The 3-D model of the accurate geometry required approximately 3 hours to be analysed, whereas the 2-D mesh took only 4 minutes. The overall failure predictions of the 2-D and 3-D models were very similar, therefore only 2-D models were used to predict failure in all cases.

6.6 Testing and Results

6.6.1 Test Method

The 40mm wide specimens were tested in 3-point bending. The layout of the rig is shown in Figure 6.16. Tests were performed on an Instron 1341 test machine operating in displacement control at a rate of 1mm/min. The support rollers were located at a distance of 7mm from the thin part of the curved section at each end. The overall span of the specimens on the rollers was 223mm.

6.6.2 Test Results

During the tests the applied load, the cross-head displacement and the time were recorded. The load-displacement behaviour for the first test is shown in Figure 6.17. The specimen exhibited a linear increase in load with displacement until the foaming adhesive failed, indicated by point 1 on the graph, which caused a drop in load and a loss of stiffness as shown by the reduction in slope. The initial non-linearity was due to the specimen bedding in and some core crushing under the roller. This did not affect the load path around the edge closure and was ignored. The foam failure only occurred at one end, that end losing stiffness and integrity. From that point, each delamination occurred at that end because the composite was under much higher stresses.

In the analysis this failure was modelled prior to the delamination prediction being carried out, the predicted failure load is therefore not affected. With only one end of the specimen failed, the use of symmetry in the model could be called into question. It should be noted that the 3-point bend load case is statically determinate, with the two supports taking an equal share of the load applied at the centre, regardless of the stiffness of the edge closure. Therefore the model is still valid as the force acting on the specimens is the same at each end.

The second load drop (point 2) was due to a delamination in the curve at the end of foam failure. This occurred in the second resin pocket in all specimens and at initiation extended approximately 4mm. With further loading the delamination propagated, and other delaminations occurred (e.g. point 3) around it as shown by the peaks on the curve. The stiffness of the specimen reduced with each new delamination and crack propagation. The failure locations corresponding to points 1-3 on Figure 6.17 are shown in Figure 6.18.

All test results for foaming adhesive failure and first delamination are shown in Table 6.3. The fourth specimen failed simultaneously in the foaming adhesive and the composite, so the failure load is not available for the composite. The mean failure load of the composite

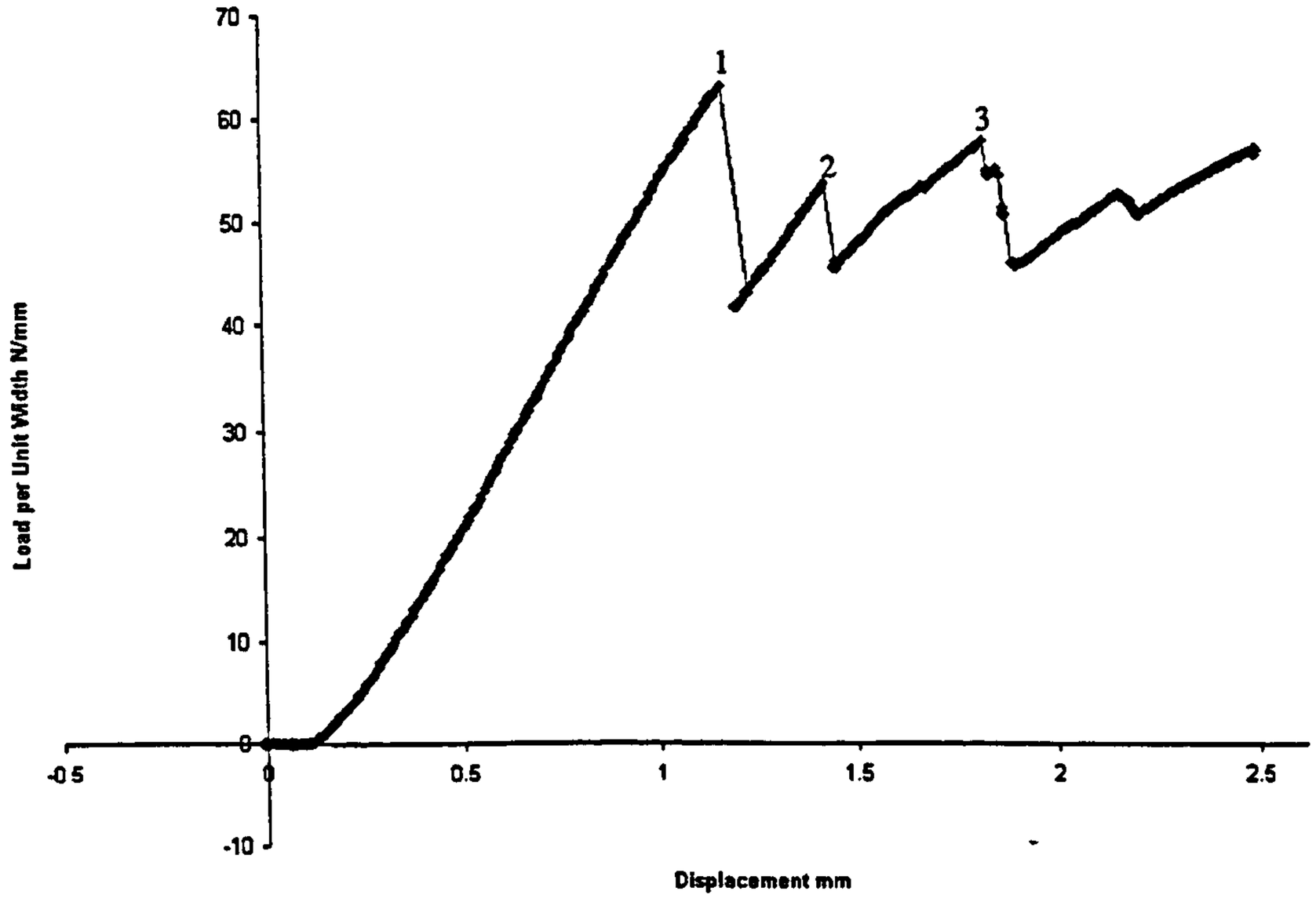

Figure 6.17: Load Displacement for Typical Sandwich Panel

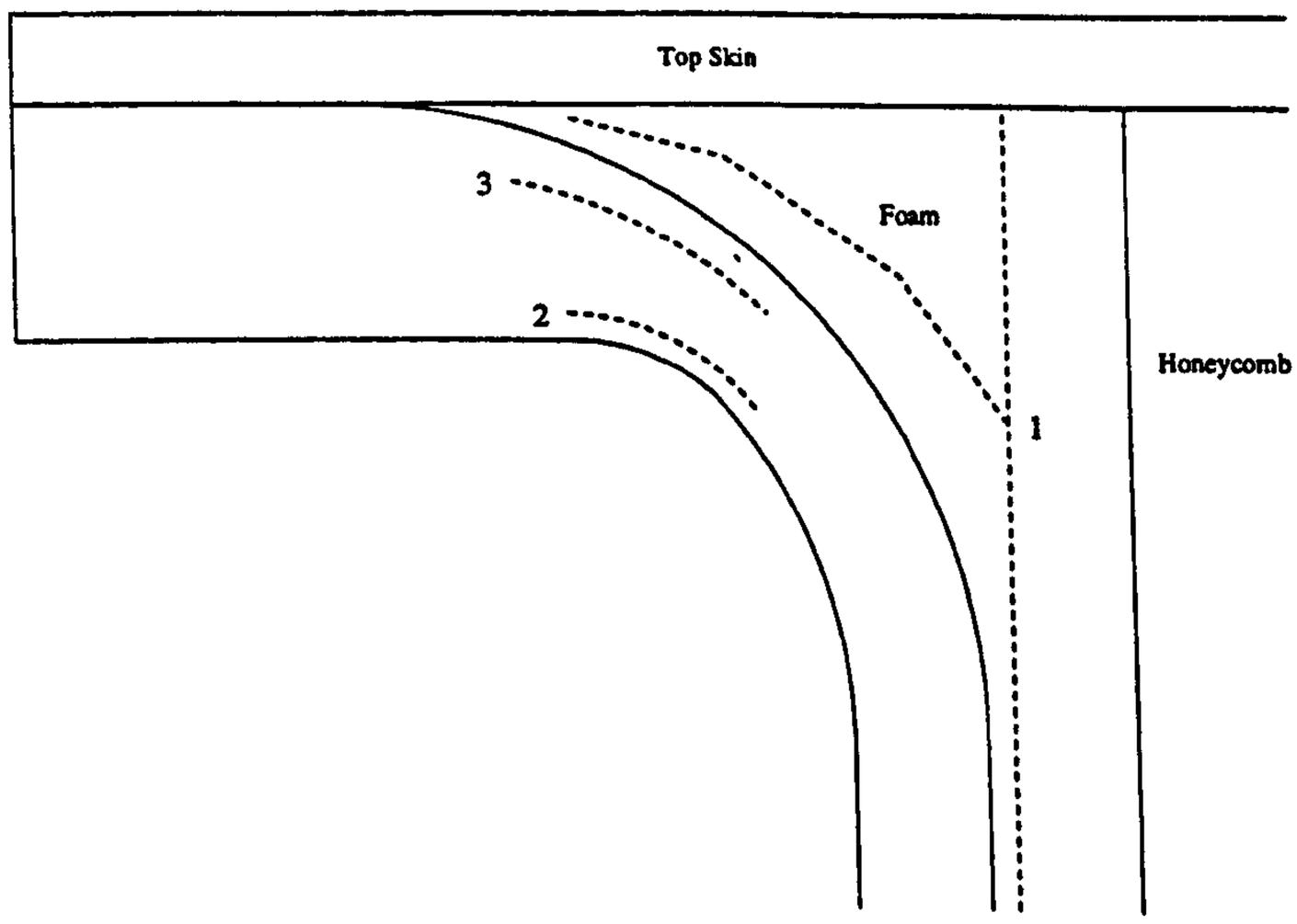

Figure 6.18: Failure Locations in Sandwich Panel

Test	Foaming Adhesive Failure (N/mm)	Delamination Failure (N/mm)
1	61.6	51.4
2	63.3	53.6
3	63.2	69.9
4	67.8	—

Table 6.3: 90° Sandwich Panel Test Results

material came to be 58.3N/mm with a c.v. of 17.3%. This is quite a large degree of scatter, and it is clear that more test results would have been useful in establishing the mean strength.

6.7 Conclusions

In testing, the specimens failed in the foaming adhesive before delamination occurred, changing the load distribution in the structure. This could be accounted for in the delamination predictions fairly easily. It was achieved by removing the elements representing foaming adhesive, which was reasonable because the failure was tensile with no contact between the sections and hence no load transfer across the crack.

Two models of the specimens were produced, one using assumed geometry, and the other using geometry measured from the specimens. The failure prediction using the assumed geometry was quite reasonable. The predicted load was only 12% unconservative and the location was only one resin pocket out. The measured geometry model was significantly better in the failure prediction, however. The delamination load was 1% unconservative and the predicted delamination location was within the correct resin pocket.

The method has been shown to be good at predicting the delamination of the curve in the edge closure. It gave a good comparison in terms the load, and also in terms of the failure

location. The accuracy of the model to the specimens being analysed has been shown to have a significant effect on the accuracy of the method.

As part of the research of the sandwich panel, a parametric study was carried out. The investigation concentrated on the thickness and angle of the edge closure on the overall strength of the panel. The conclusions drawn showed that the strength and stiffness of the structure could be improved by reducing the angle of the edge closure to 30°. This specimen design is reported in the next chapter.

Chapter 7

Delamination Prediction - 30^o Sandwich Panels

7.1 Introduction

In the previous chapter, a sandwich panel specimen was developed which delaminated in the composite edge closure. The delamination prediction method was shown to be accurate despite the presence of ply drops, resin pockets and different ply angles in the local, curving geometry. A study of the effect of angle on the strength of the edge closure was carried out which established that the interlaminar stresses reduced considerably with the angle of the edge closure. An angle of 30° was chosen as it was the shallowest angle which would allow the full 38mm honeycomb depth with the same specimen length, and would minimise the stresses in the edge closure the most.

Specimens were made with 30° edge closures using the assembly techniques of precuring and cocuring. Two specimens types were manufactured because of a desire to investigate how using a lower cost manufacturing method (co-curing is a one shot process which does

not require tooling for the edge closure) would affect the overall strength of the design. The two specimen types had different local geometries in the delamination region due to the differences in manufacture, which required the tailored modelling technique which was used on the 90° sandwich panel specimen. The analysis and failure prediction of each specimen type are presented within this chapter.

7.2 Specimen Design

The sandwich panel geometry from the previous chapter had been shown to be stronger and stiffer with an edge closure at 30°. This was due to the way in which the edge closure carried the load and how it was supported. In the 90° specimens, the curved part of the edge closure was not supported after the foaming adhesive had failed, and mainly carried the load as a shear force which acted through the thickness of the composite material. This gave rise to high interlaminar shear stresses, leading to a high degree of bending which produced interlaminar tensile stresses. In the 30° specimens, the edge closure was supported by the honeycomb, and could carry the force as a direct tension acting along the edge closure. This reduced the interlaminar shear stress levels, therefore the amount of bending was less and the interlaminar tensile stresses were lower.

This new edge closure design was manufactured in two ways, leading to two separate specimen types which were designated as precured and cocured. The overall specimen geometry was the same for each and is shown in Figure 7.1.

The edge closures of the precured specimens were cured at a pressure of 7bar over tooling which controlled the radius of the curve. The cocured edge closure was cured at the lower pressure of 2.5bar directly over the honeycomb which did not control the curve radius. This led to different local geometries in the region of the dropped plies which are described in the next section.

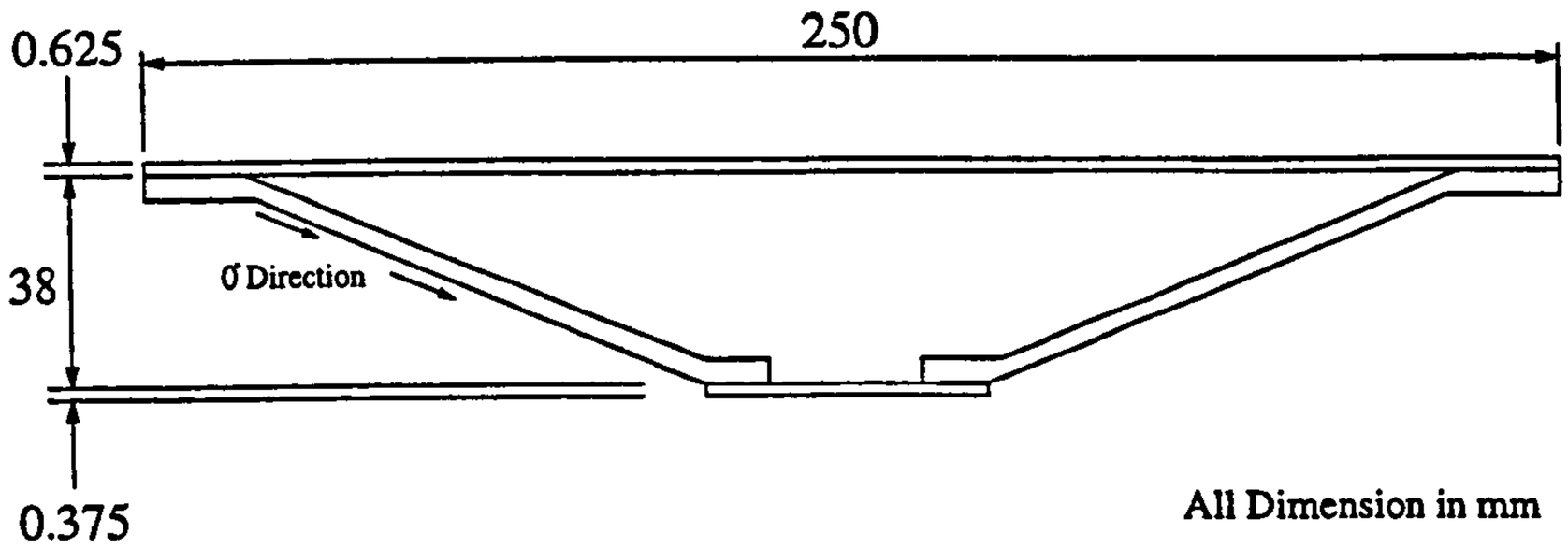

Figure 7.1: 30° Sandwich Panel Geometry

7.3 Manufacture

The composite material used for both specimens was HTA/913C from Hexcel Composites [65]. The lay-ups of each part of the specimens were the same as for the 90° specimens. The top skin lay up was [0/90/0/90/0] and the bottom skin was [0/90/0]. The lay up of the edge closures was $[0/90_2/\pm 45/90_2/\pm 45/90_2/\pm 45/90_2/\pm 45/90_2/0]$ as for the 90° specimens in the previous chapter. The core material was aluminium honeycomb, designation Aeroweb 6.9-3/16-25(5052)T from Hexcel. The honeycomb to composite bonding was performed with unsupported film adhesive AF-163-2U-0.03. The skin to edge closure bonding was done with film adhesive AF-163-2K-0.06. Four specimens using each manufacturing method were made in large panels, which were cut to 40mm width using a diamond saw for static testing.

In both cases, the top skin was precured to eliminate wrinkling during cure as it was vital that it was flat to maximise the strength of the skin in compression. If the skin was not flat, then the edge closure would take more of the load and fail much earlier than expected. The final assembly cure was carried out at 2.5bar as with the 90° specimens, ensuring that the honeycomb core was not crushed.

Prior to assembly, all surfaces that were precured and required bonding were degreased with acetone, grit blasted for a good adhesive surface, then degreased again. The aluminium honeycomb was degreased with 1,1,1 trichloroethane and dried.

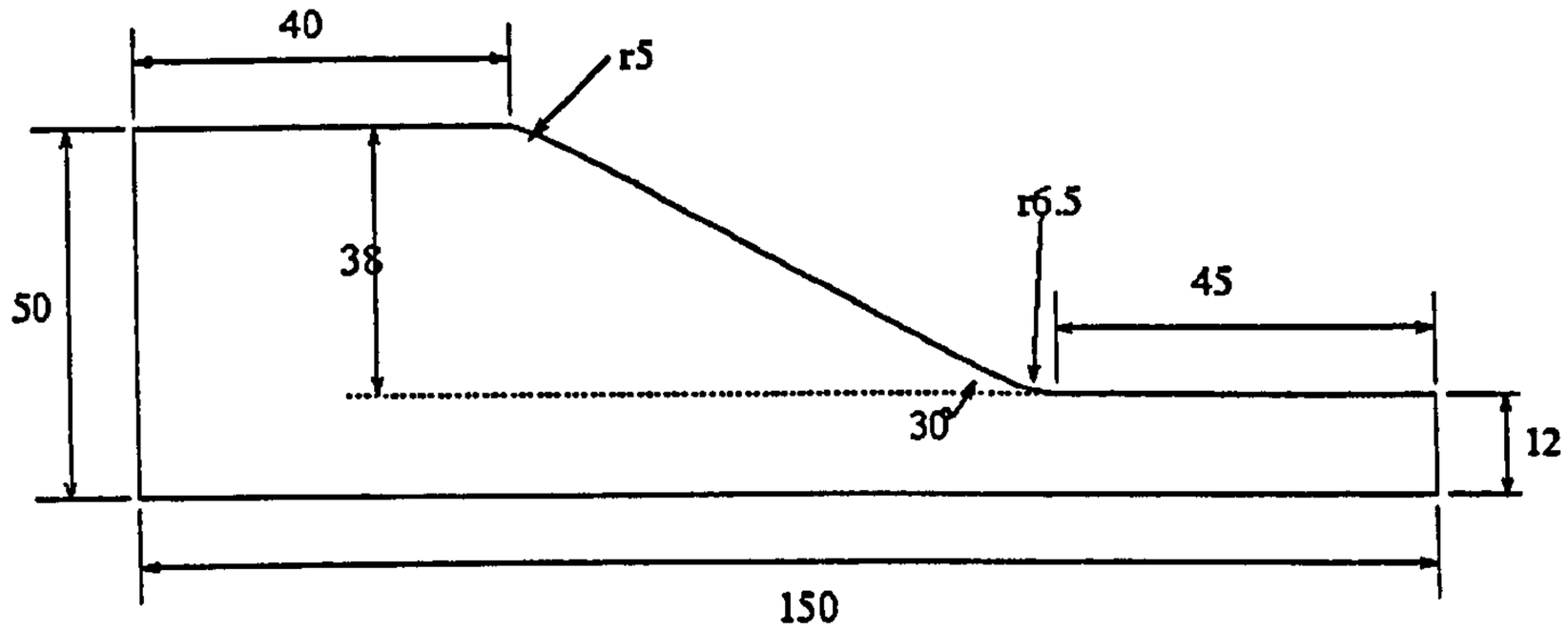

Figure 7.2: 30° Precured Sandwich Panel Tooling Geometry

7.3.1 30° With Precured Edge Closure

A diagram of the tooling used for the lay-up and cure of the edge closure for these specimens is shown in Figure 7.2. Bonding between the edge closure and honeycomb was done using an unsupported film adhesive. The honeycomb was machined to 30° using a bandsaw with a fine 24tpi blade. A panel approximately 200mm wide was made, enough for 4 specimens.

7.3.2 30° With Cocured Edge Closure

No tooling was used to form the edge closures which were laid up directly over the machined honeycomb with the bottom skin. Curing was done at a lower cure pressure, 2.5 bar, that of the assembly cure for the other specimens. This reduced pressure cure of the edge closure gave rise to some voidage in the curve which will be reported on later. Four specimens were made in a panel 200mm wide.

7.4 Modelling

In both cases, the model geometries were taken from photographs of the specimen cross-sections in the curved portion of the edge closure and where the plies were dropped. This was done to produce accurate stresses in the failure region. The load was applied at a node 7mm from the thinnest point of every specimen, as for the 90° specimens in the previous Chapter. Only 40mm of the honeycomb was modelled at which point all nodes were fully restrained. This was found to produce the same load path as an entire model but with less elements. The 90° plies in the edge closure meant that plane strain behaviour was a reasonable assumption, as with the 90° model. The same material properties as those for the 90° specimens were used, and are shown in Tables 6.1&6.2.

7.4.1 30° With Precured Edge Closure

7.4.1.1 Failure Region Geometry

Figure 7.3 shows an image of the critical region in the edge closure of the precured 30° sandwich panels. It was obtained by taking a section through an already tested specimen which was polished and then photographed. The 5 ply top skin is curved, caused by the potting process crushing the honeycomb. This did not affect the geometry of the edge closure significantly. The individual plies in the edge closure can be seen, the different brightness of each ply angle caused by the amount of reflected light. Pure resin absorbs the most light, whereas the carbon fibres tend to reflect most when parallel to the section. The resin pockets at the end of the dropped plies are evenly sized and located in similar locations longitudinally in the section. It should be noted that this was as a result of careful manufacture and would not always be possible in large scale manufacture where variation is a continual problem, as discussed later.

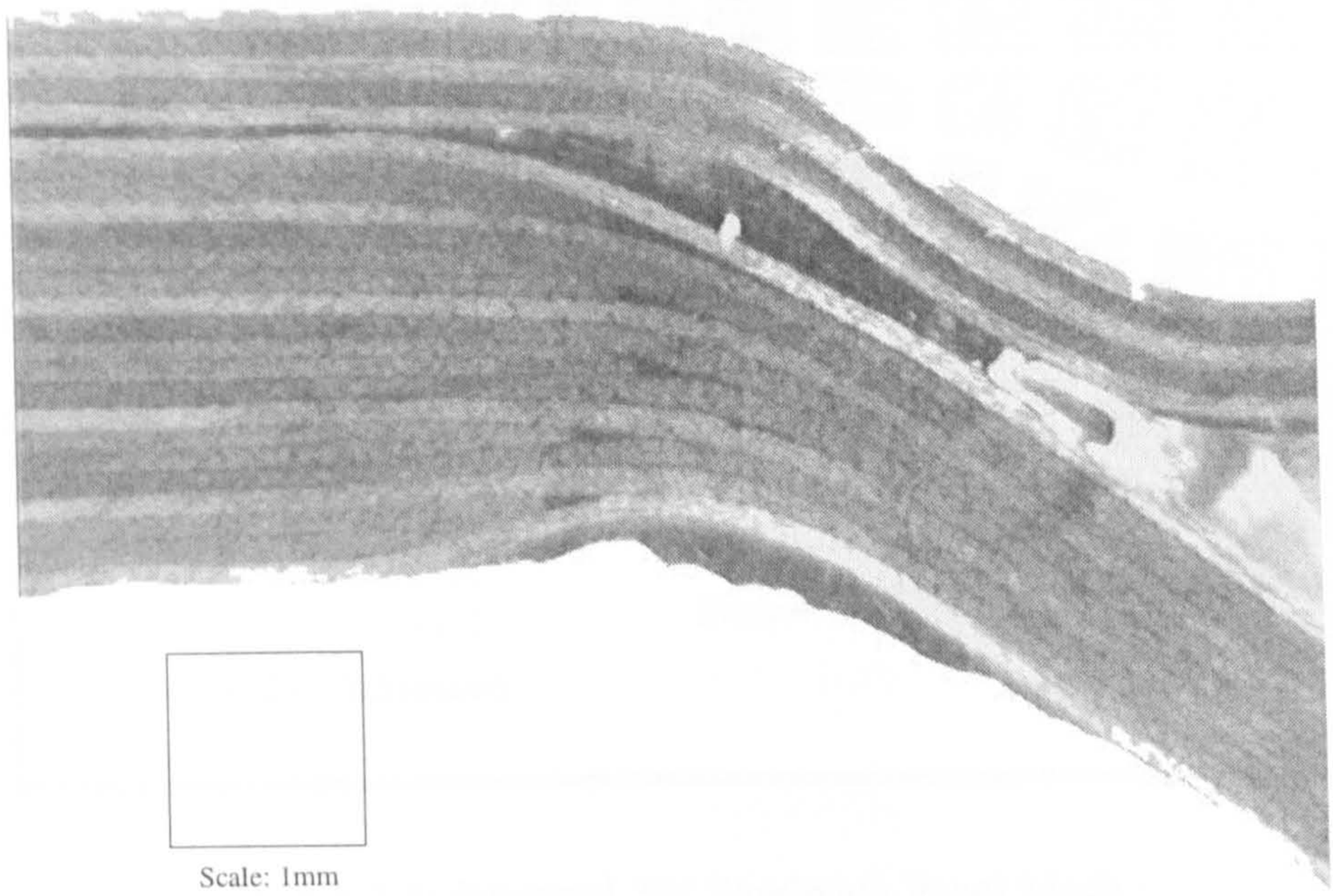

Figure 7.3: Precured 30^o Sandwich Panel Geometry

The geometry which has resulted for this edge closure was difficult to model accurately. The simultaneous curvature of all the plies and tapering of the dropped 90^o plies made the use of a pre-processor vital to achieve a good mesh in a reasonable time. The 'Master Modeller' and 'Meshing' Tasks of I-DEAS Master Series Versions 5&6 were put to good use here.

7.4.1.2 Mesh Geometry

Figure 7.4 shows the mesh of the critical region of the precured 30^o sandwich panel. The elements are shown reduced in size and coloured according to the applied material properties. The element shapes were kept within general guidelines for shape and aspect ratio which were detailed in Chapter 3.

It can be seen that the overall geometry of the mesh is very similar to the geometry of the

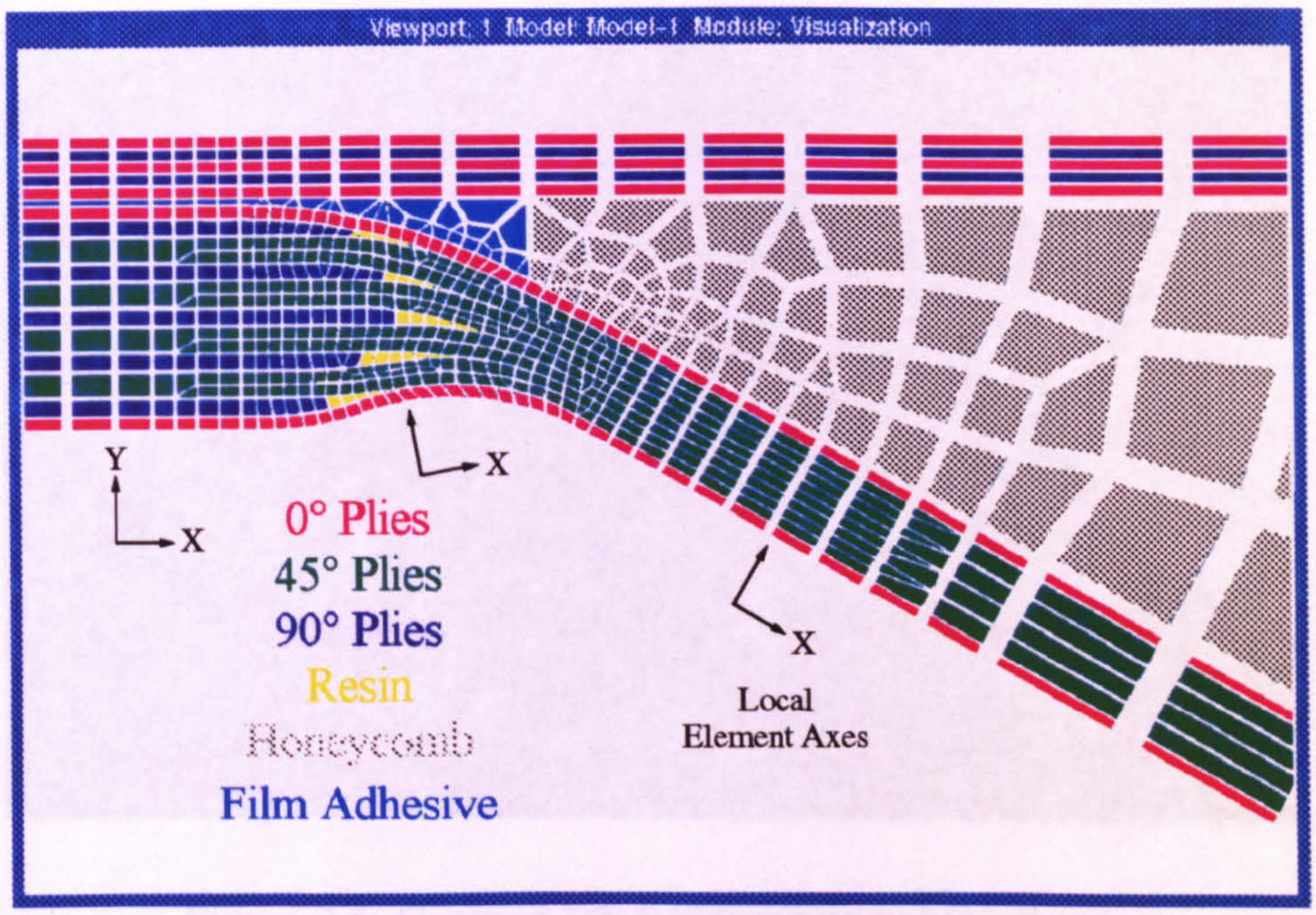

Figure 7.4: Precured 30^o Sandwich Panel Mesh

specimens. This was achieved by measuring the dimensions of a specimen to provide a scale for the photograph. The location of any point within the dimensioned image could be found and placed accurately in the model.

7.4.2 30^o With Cocured Edge Closure

7.4.2.1 Failure Region Geometry

The geometry of the specimens did not vary significantly, Figure 7.5 shows a typical specimen. The critical area, once again, is the thicker, tapering and curving, laminate. As with the precured specimens, the top skin was affected by the potting process and has curved, when it was initially straight. The curved laminate was not affected significantly by this, and the location of the ply drops and general shape were taken as shown.

The picture shows a significantly different geometry to the precured specimens. The

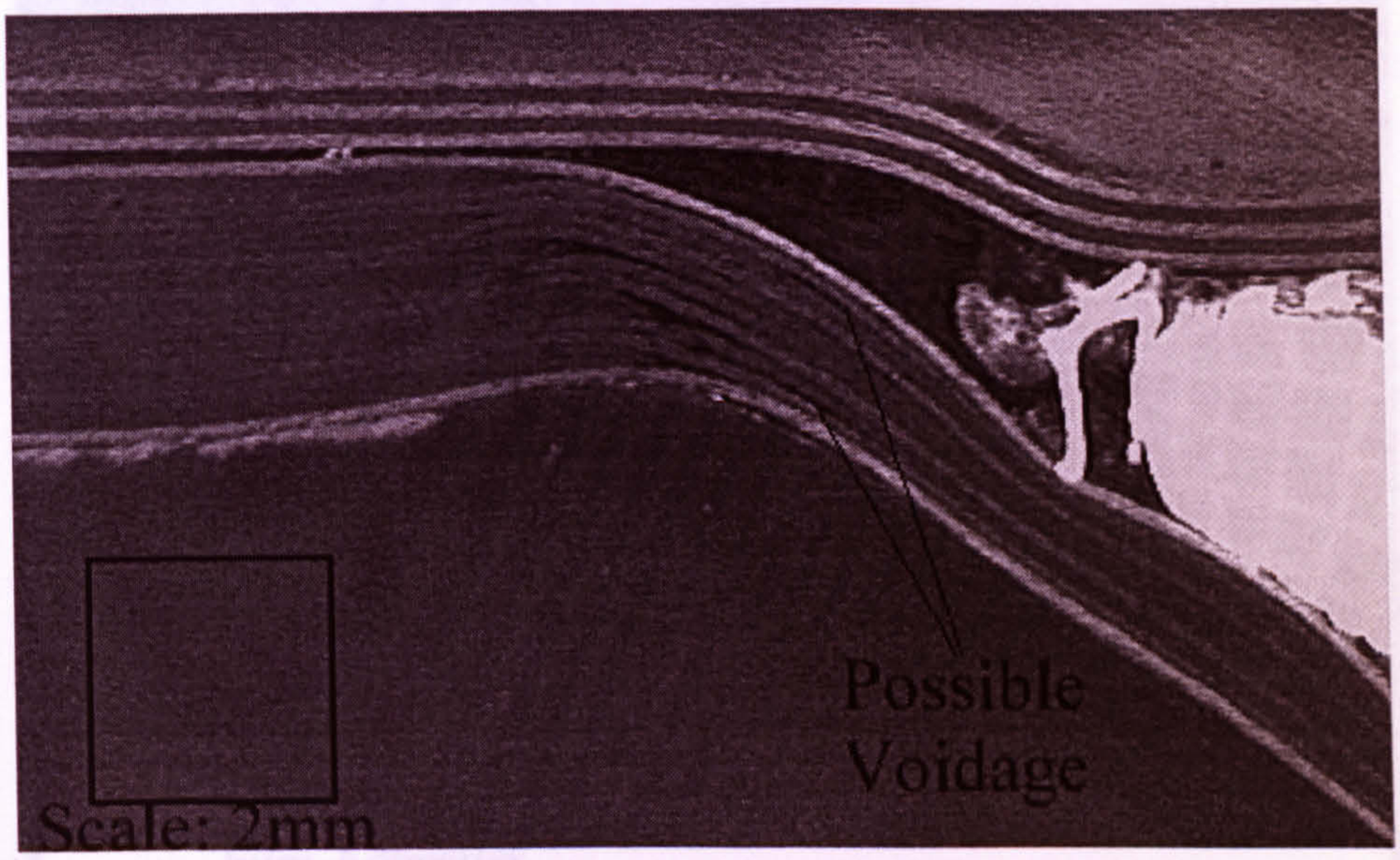

Figure 7.5: Cocured 30^o Sandwich Panel Geometry

region is not so uniform and ordered, despite the care taken during manufacture. There are two large resin pockets towards the bottom surface of the curve, and two small ones higher up. A number of the plies above the middle of the laminate show a reverse curvature. There are even voids apparent in the section, between plies 2 and 3 and plies 8 and 9 At the start of the straight section. It is possible that these could affect the strength of the material in this area. An important factor in the geometry is that the start of the straight portion of the 'Z' was actually at 35^o for approximately 4mm before continuing at 30^o. This increased the stress levels in the specimens significantly as the stress concentration was more severe.

7.4.2.2 Mesh Geometry

Figure 7.6 shows the mesh used in the analysis of the cocured specimens. The local geometry of the ply drop region matches the specimens closely. In the curing of these specimens, the thin portion of the edge closure was not initially at 30^o. Before the closure reached the honeycomb and was well supported, the closure had an angle of 35^o. The transition from 35 to 30^o occurs at the edge of the first honeycomb cell that the edge closure runs over. This had to be included in the modelling as it would affect the stress

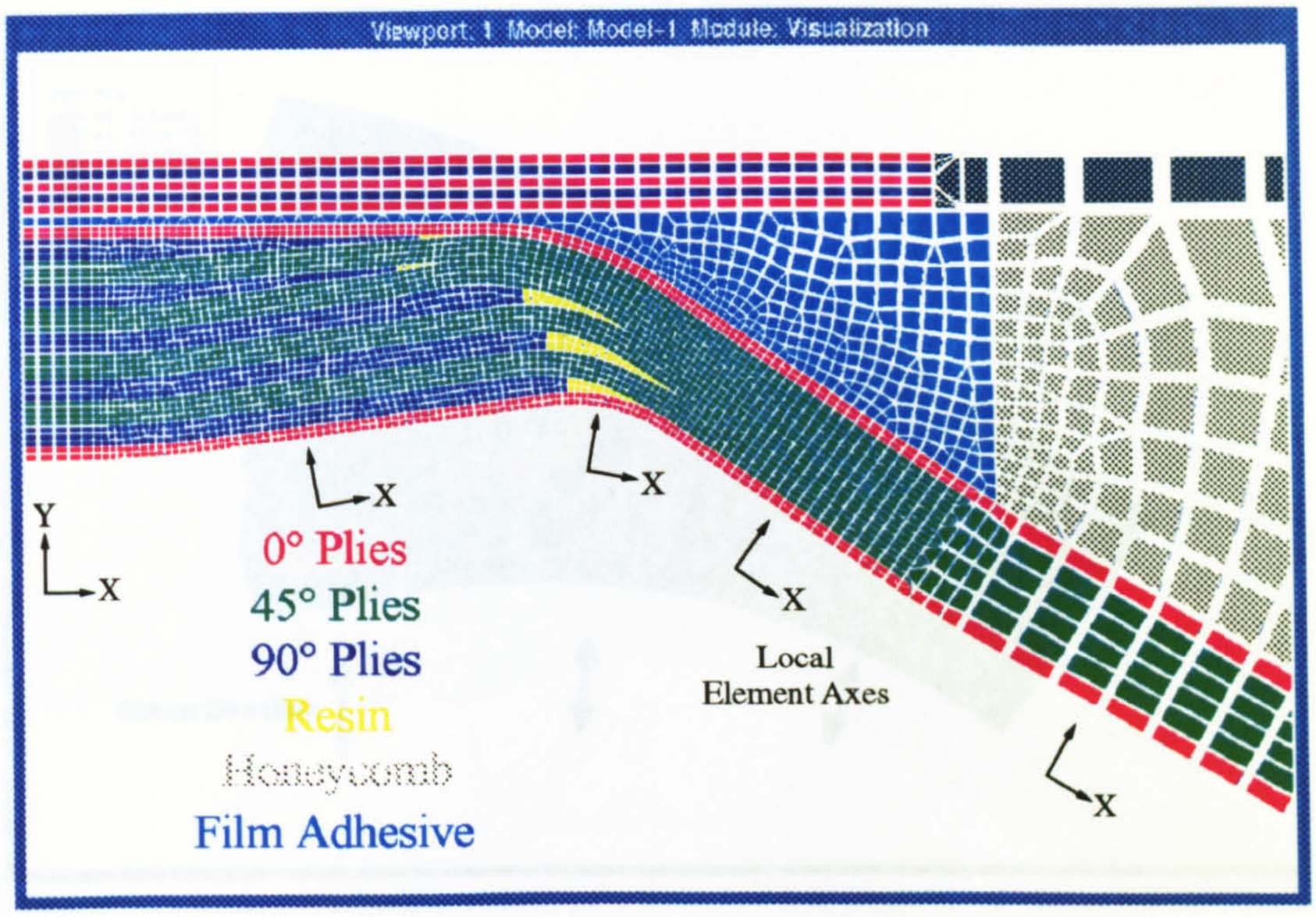

Figure 7.6: Mesh of Cocured 30^o Model

levels seen in the failure region.

7.5 Failure Predictions

7.5.1 30^o With Pre-Cured Edge Closure

The precured edge closure specimen model was analysed with two separate load steps, both including thermal residual stresses. The first case was equivalent to 100N/mm width in the specimens and the second was with a load equivalent to 200N/mm. As explained previously, the user defined material code was applied to the elements in the region of highest interlaminar stresses, the curved part of the edge closure. The different material properties were applied according to the mesh shown in Figure 7.4. The interlaminar direction is defined as that perpendicular to the ply direction in the plane of the 2-D cross-section model.

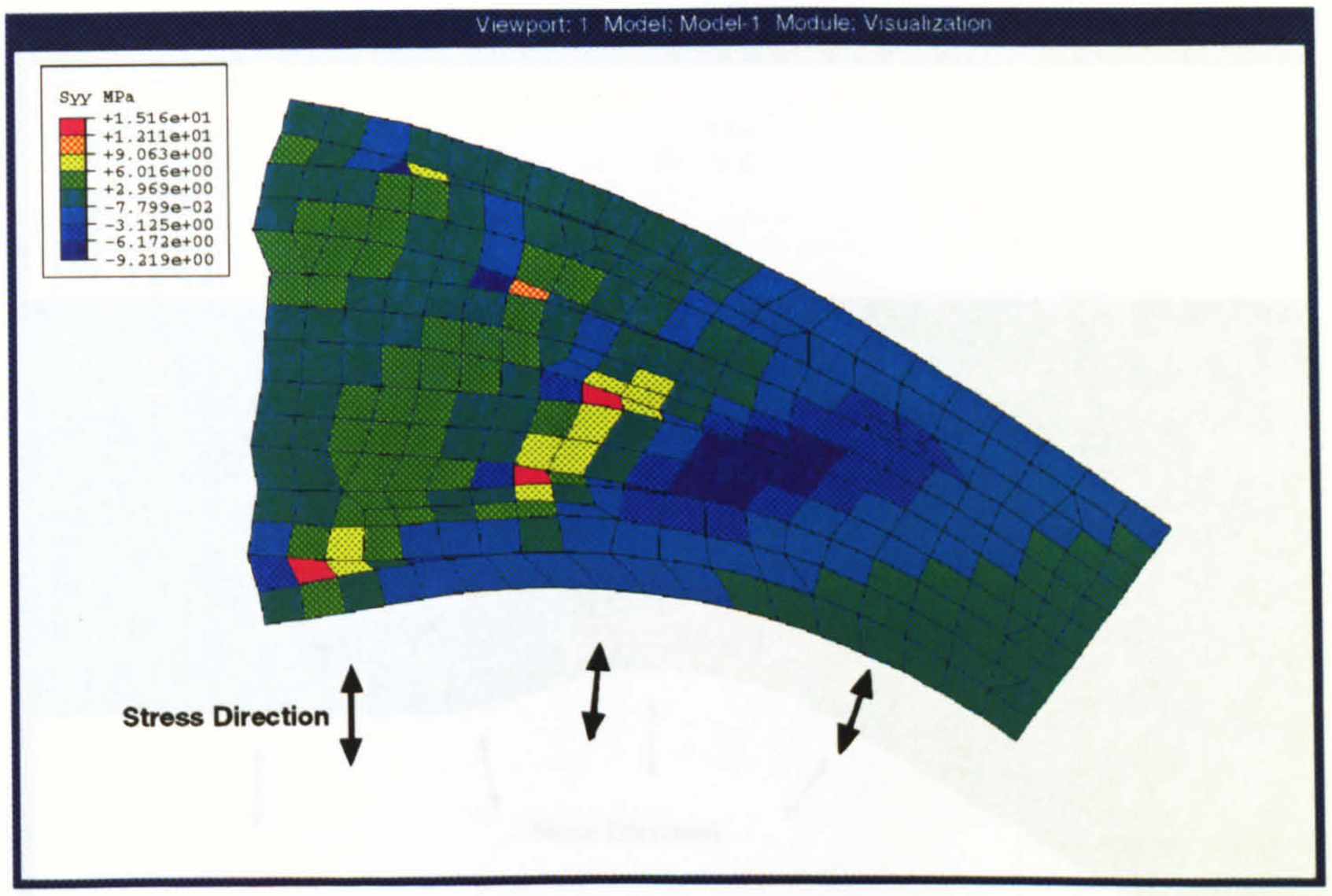

Figure 7.7: Interlaminar Tensile Residual Stress in Precured 30^o Model

The tensile interlaminar thermal residual stresses are shown in Figure 7.7. The peak tensile stresses are seen in the first elements in the resin pockets at the end of the terminated plies. This is caused by the relatively large expansion coefficient of the matrix compared to the 90^o material. The large area of compressive stress in the middle of the region are as a result of the curvature.

Stress plots in the edge closure are shown for the 200N/mm load case with thermal residual stresses. The failure prediction method uses averaged element values at the centroid, so these are shown for the critical components. The interlaminar tensile stress peak is located in the second ply at the thinnest end of the tapered and curving section as shown in Figure 7.8. The peak value at this load is 84MPa, not enough to cause failure without contribution from other stress components. The region of compressive stress on the left is caused by longitudinal tension in the outer 0^o ply straightening it, and pulling it inwards.

The interlaminar shear stress for this load case is shown in Figure 7.9. The peak stresses occur in and around the first pair of 45^o plies. The positive peak of 82MPa is at the right-hand end of the high interlaminar tension, so the action of combined stresses in the matrix could lead to failure here. The negative stress peak of -105MPa is in a region

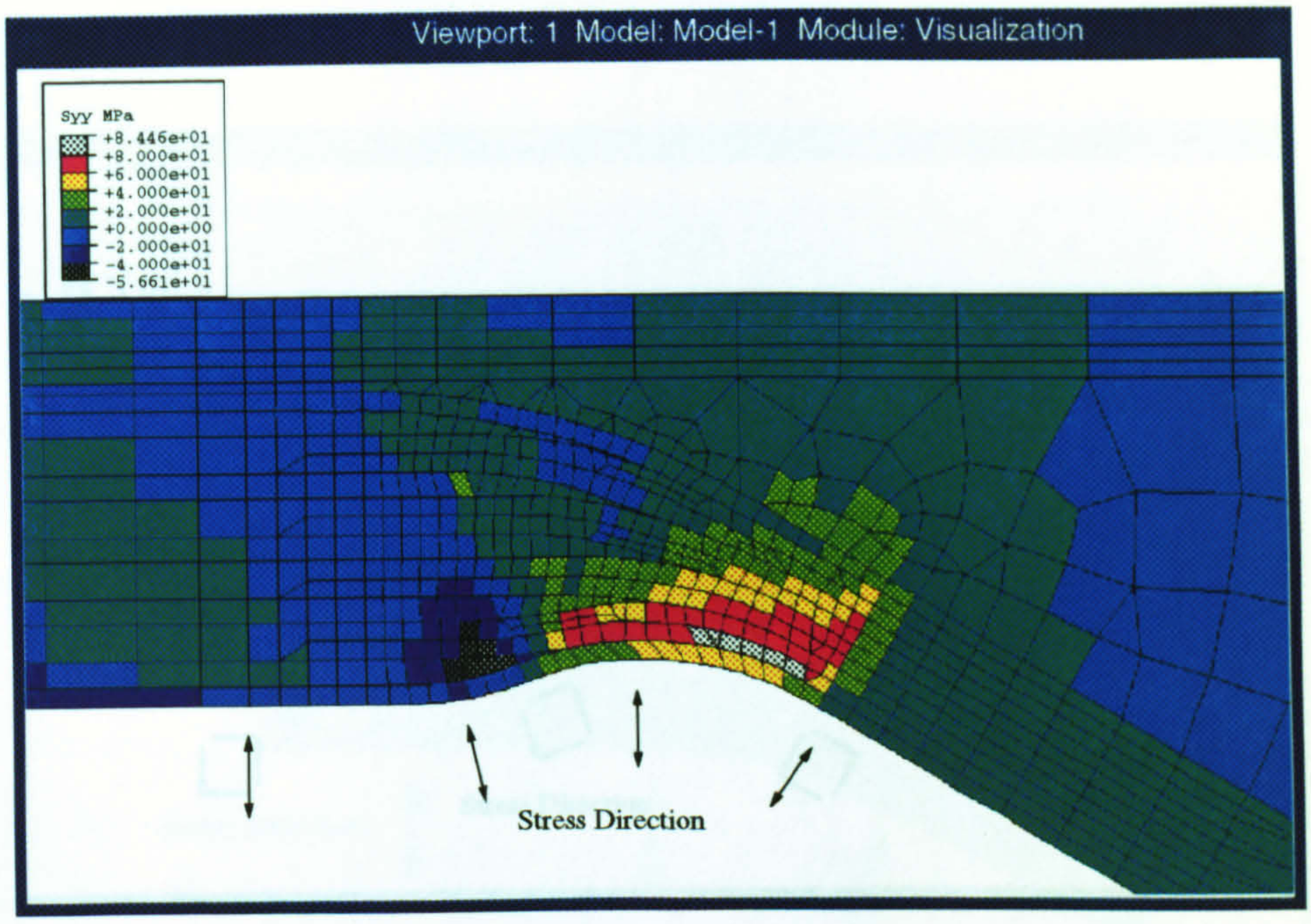

Figure 7.8: Interlaminar Tensile Stress in Precured 30° Model at 200N/mm

of moderately high interlaminar tensile stress, and is of a higher magnitude, so failure is more likely to occur here. Failure in either of these locations is going to be due to a combination of tension and shear.

The delamination prediction was based on the modelled geometry. At 100N/mm, the UVES was 70.9MPa, and at 200N/mm, the UVES was 134.0MPa. By linear interpolation, the failure load was predicted to be 194.4N/mm width. The failure location was predicted by looking at individual element results after the volume effect had been taken into account. The highest UVES results were in the 2nd resin pocket and the first 45deg ply pair by that pocket. From these results, the specimens are likely to fail in and around the second resin pocket, and at a mean load of around 194N/mm.

7.5.2 30° With Cocured Edge Closure

The stress plots in the expected failure region for the cocured elements are simpler and cleaner than the precured model. This is because the overall geometry is simpler than the

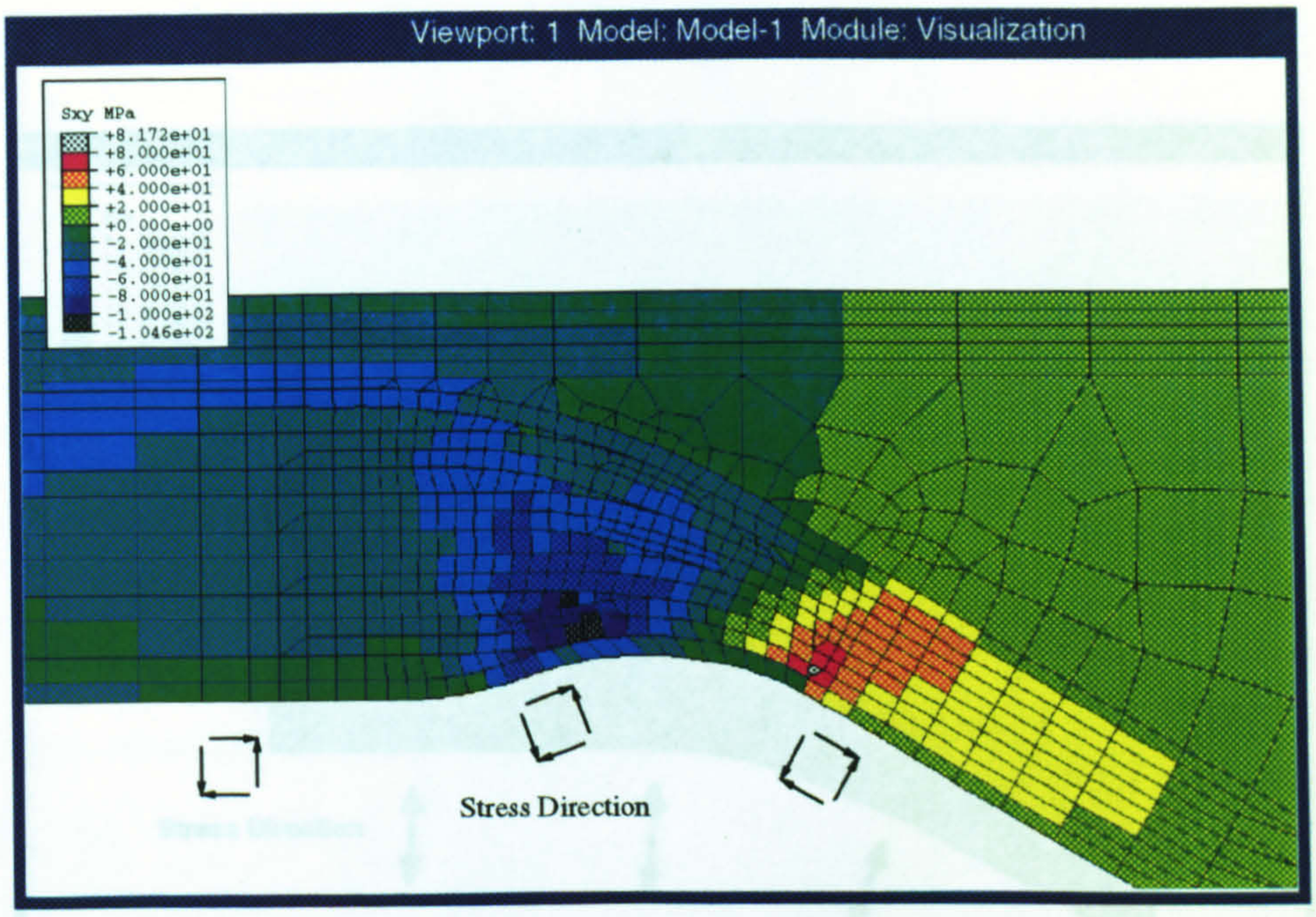

Figure 7.9: Interlaminar Shear Stress in Precured 30° Model at 200N/mm

precured with only one region where the plies have significant curvature.

The tensile interlaminar thermal residual stresses are shown in Figure 7.10. The area behaves similarly to the precured model because the general shapes of the two are comparable. As with the precured model, the highest tensile stresses are in the first elements of the resin pockets.

The interlaminar tensile stresses at the applied load of 200N/mm with the thermal residual stresses included are shown in Figure 7.11. The tensile stress peak is in and around the first pair of ±45° plies from the surface. The highly stressed area is in a different location to that seen in the precured specimens. The magnitude of the stresses is around 20% higher than before, the very highest stress being in the first resin pocket. This will not necessarily dominate the failure because it is only a small stressed volume compared to the rest of the high stress area.

The interlaminar shear stress at this load case is shown in Figure 7.12. The negative stress peak is located around the first resin pocket, like the tensile stresses. This gives a clear

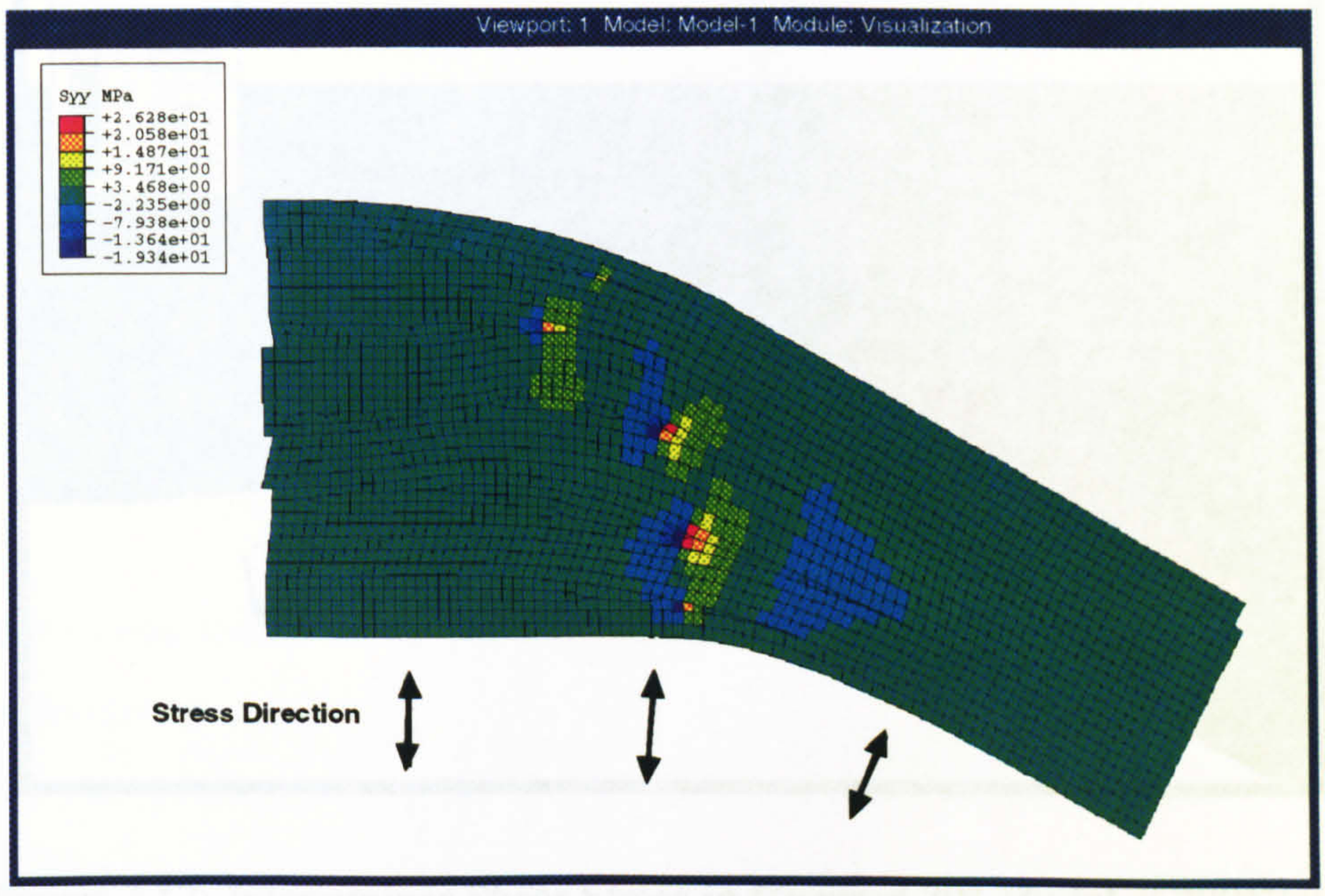

Figure 7.10: Interlaminar Tensile Residual Stress in Cocured 30^o Model

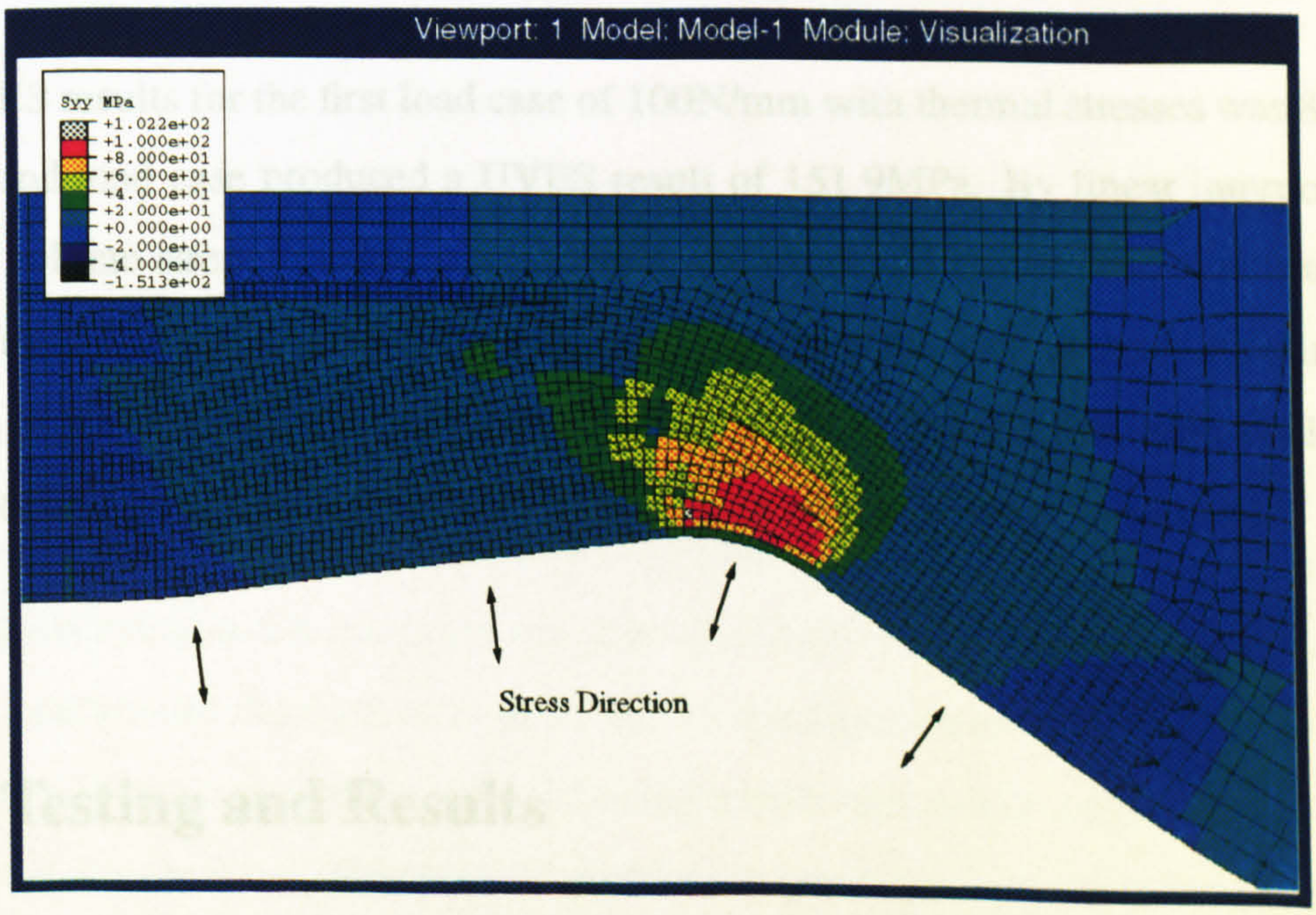

Figure 7.11: Interlaminar Tensile Stress in Cocured 30^o Model at 200N/mm

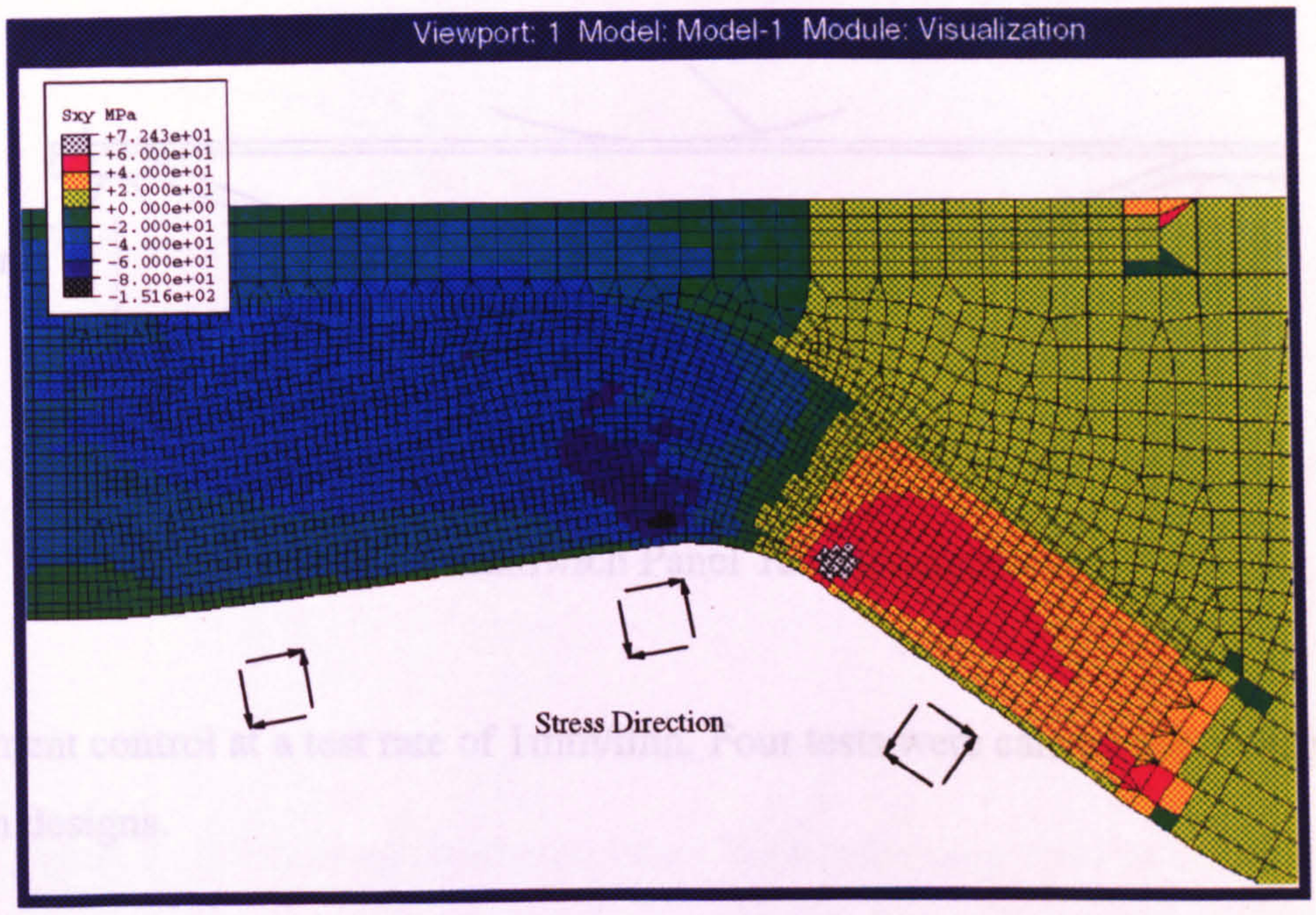

Figure 7.12: Interlaminar Shear Stress in Cocured 30° Model at 200N/mm

indication that the failure is likely be in this region. The positive stress peak is also within the significant interlaminar tensile stresses, but is of a lower magnitude, so is unlikely to be the first failure location.

The UVES results for the first load case of 100N/mm with thermal stresses was 81.6MPa. The second load case produced a UVES result of 151.9MPa. By linear interpolation to the unit volume strength value of 130.5MPa, the predicted failure load was found to be 169.6N/mm. The elements with the highest stress resultant were in the first resin pocket, and just at the interface of the 0° and 45° plies at the tip of the first resin pocket. This implies that failure should be around the first resin pocket in these specimens.

7.6 Testing and Results

The 40mm wide specimens were subjected to 3-point bend testing as shown schematically in Figure 7.13. Tests were performed on the Instron 1341 test machine operating in

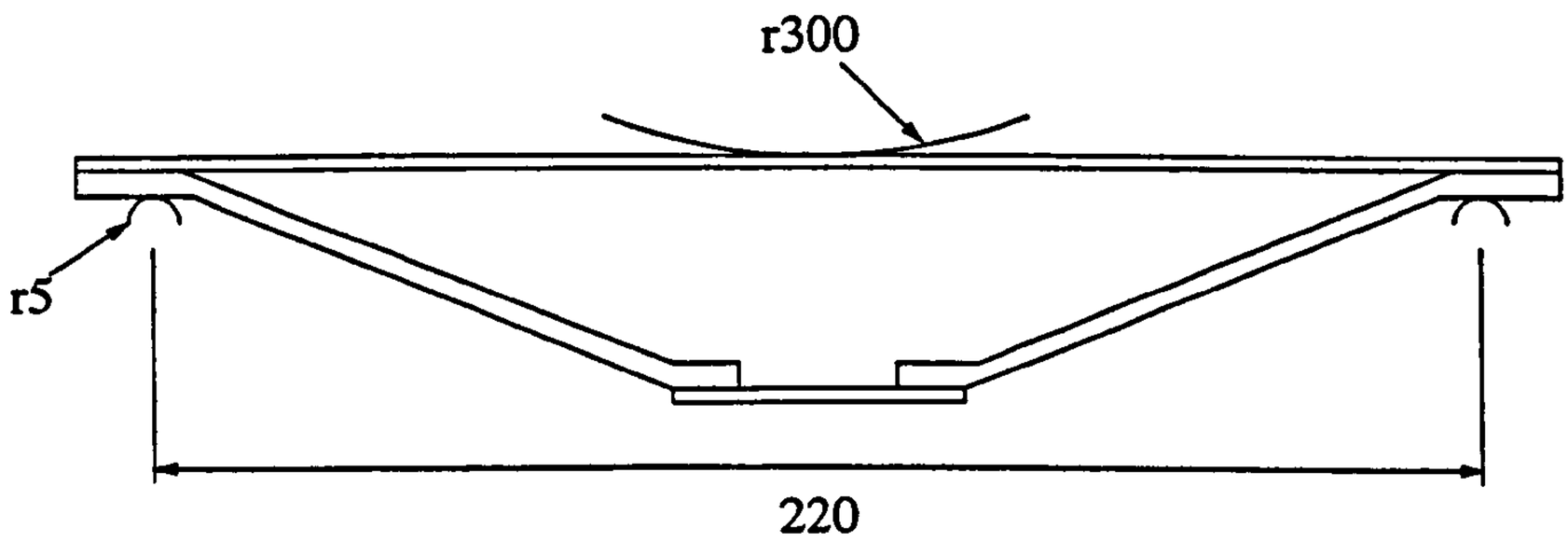

Figure 7.13: Sandwich Panel Test Arrangement

displacement control at a test rate of 1mm/min. Four tests were carried out on each of the specimen designs.

It was anticipated that core crushing under the loading roller could be a problem because the 90° specimens suffered some crushing under the roller at much lower loads than those which were expected for the 30° specimens. A large, 300mm radius nose was used to limit this problem, the larger radius of the tooling spreading the load over a wider area, reducing the compressive stresses in the honeycomb. The stress levels in the edge closure were not affected by this change as they are dominated by the location of the support rollers near the failure region.

7.6.1 Precured Edge Closure

Although the specimens were made carefully, there was clear evidence that the edge closures and honeycomb did not bond together correctly. There was an area of unbonded interface near one of the tapered ends of all the specimens (see Fig 7.14). This was approximately 14mm long when measured using a ruler just before delamination, and was investigated after testing. This kind of problem is inevitable if there is any dimensional mis-match between the honeycomb and a precured edge closure.

When the specimens were tested, it was clear that the debonded honeycomb region was

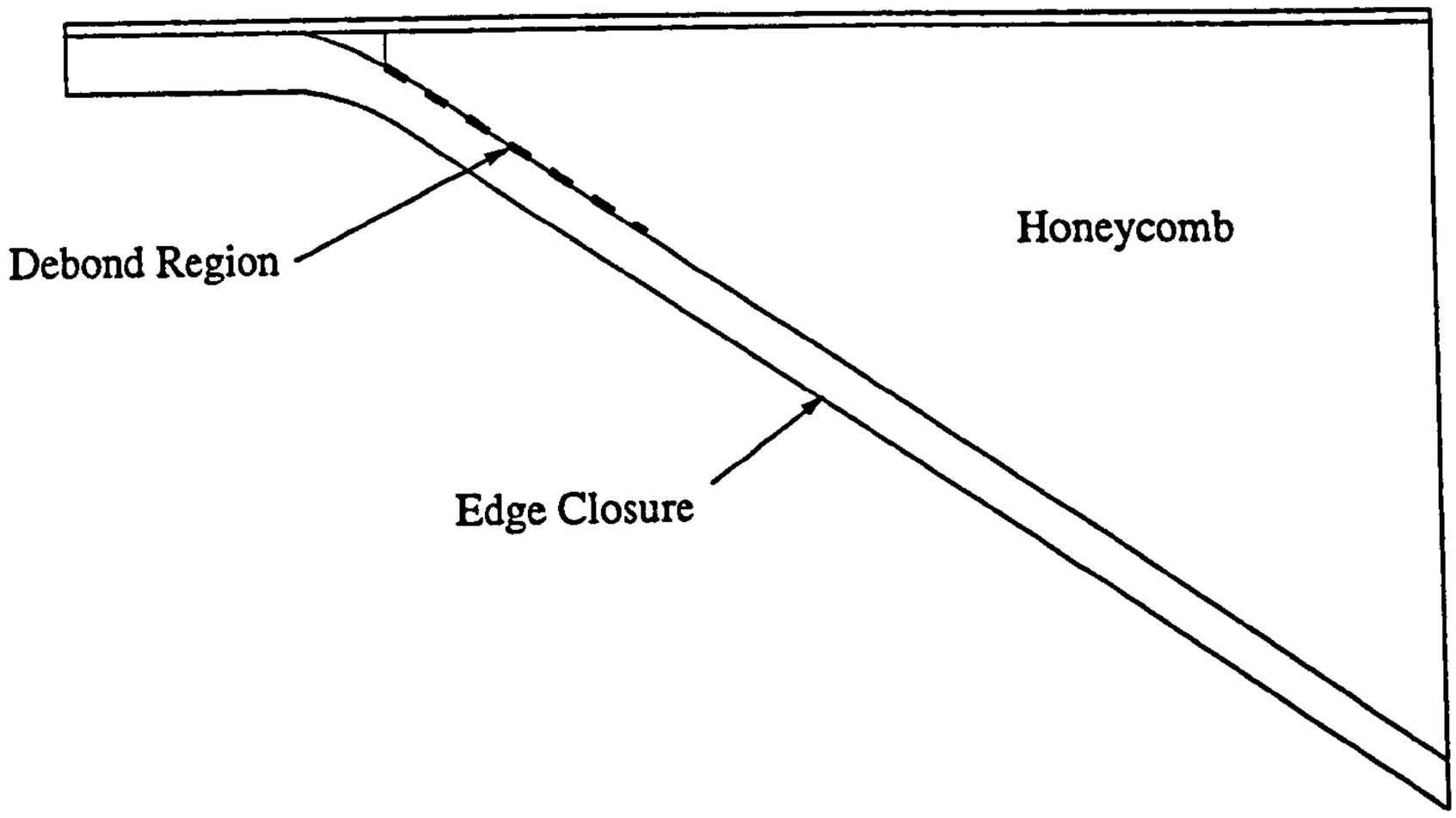

Figure 7.14: Precured Sandwich Panel Visible Debond Prior to Testing

Test no.	Mean Width mm	Failure Load N	Failure Load per Unit Width N/mm
1	39.92	6280	157.3
2	39.89	6726	168.6
3	40.01	6006	150.1
4	39.94	6158	154.2
		Mean	157.6 c.v. 5.04%

Table 7.1: Precured Sandwich Panel Test Results

not providing the support intended by the design. The debond was observed in all four tests, the length did not appear to grow during the loading procedure until delamination occurred in the edge closure. It should be mentioned that the end with the debond failed each time, and that end had a larger upward displacement than the other, and would have endured higher stress levels. The load-displacement plot from test number 3 is shown in Figure 7.15. The peak in the middle of the loading curve was caused by honeycomb crushing under the roller which stopped after around 1mm of crosshead displacement, allowing the load to be applied up to delamination. The slope of the curve after the peak is lower than before, implying that the stiffness of the structure reduced in the period of honeycomb crushing. It is possible that the honeycomb debond length could have increased during this period, although it was not observed at the time. The delamination loads measured in testing are shown in Table 7.1.

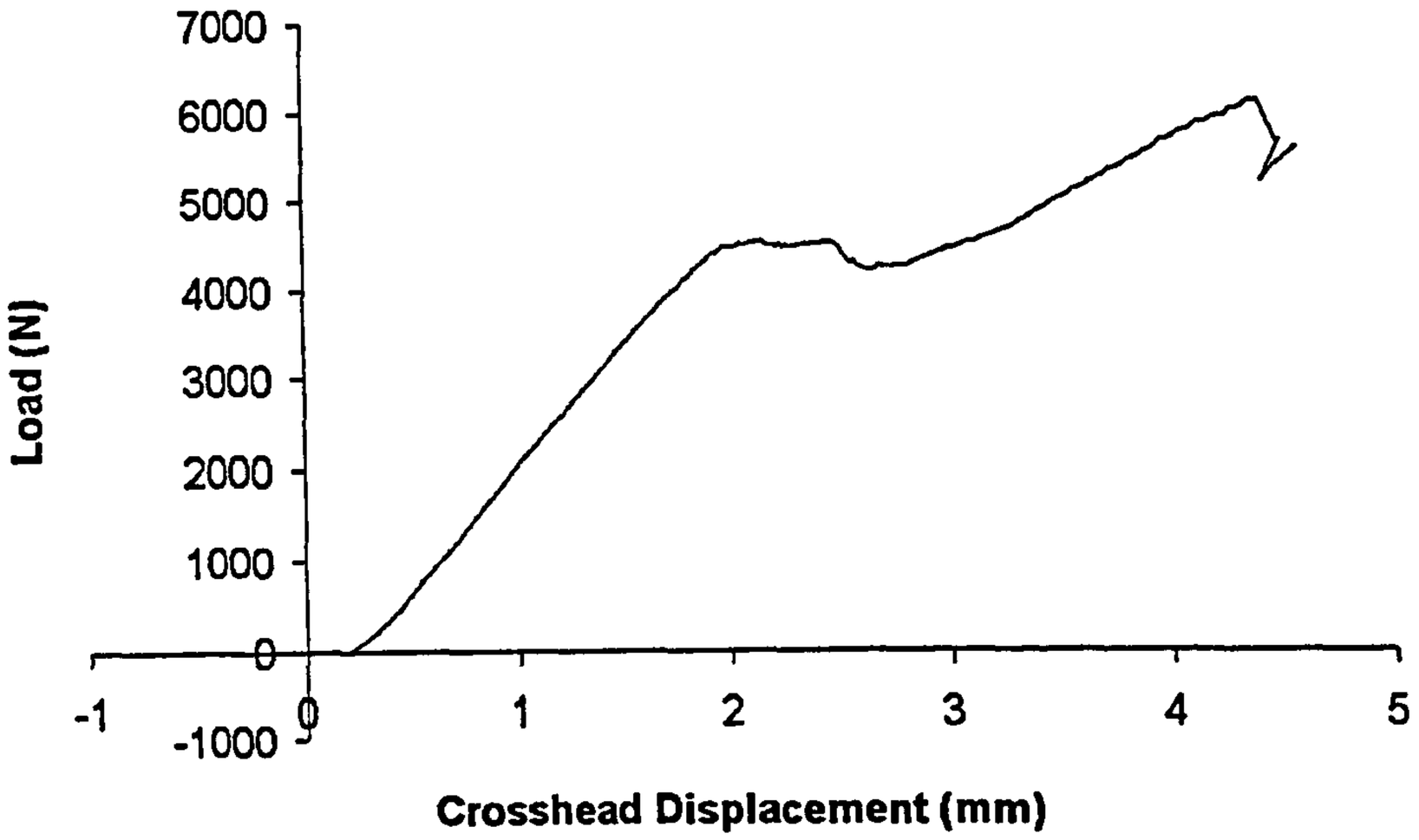

Figure 7.15: Precured Sandwich Panel Load-Displacement Plot

The mean test result was 157.6N/mm with a c.v. of 5.04%. All the specimens failed suddenly in and around the second resin pocket.

7.6.2 Cocured Edge Closure

In all cases, delamination occurred suddenly in the CFRP edge closure at the top corner. A typical load-displacement plot is shown in Figure 7.16. The curve is reasonably straight apart from a kink in the middle caused by core crushing, and shows the sudden delamination failure. All of the failure loads for the specimens are shown in Table 7.2. The first three specimens had very similar failure loads, but the final one failed at a comparatively low load. It is believed that this is due to a relatively large defect in the specimen. It was noted earlier that these specimens showed evidence of voidage in the failure region. This would affect the strength of the material significantly in interlaminar shear [29] and tension [86].

The mean failure load from all tests was 146.5N/mm with a c.v. of 14.4%. All specimens failed in and around the first and second resin pockets by delamination.

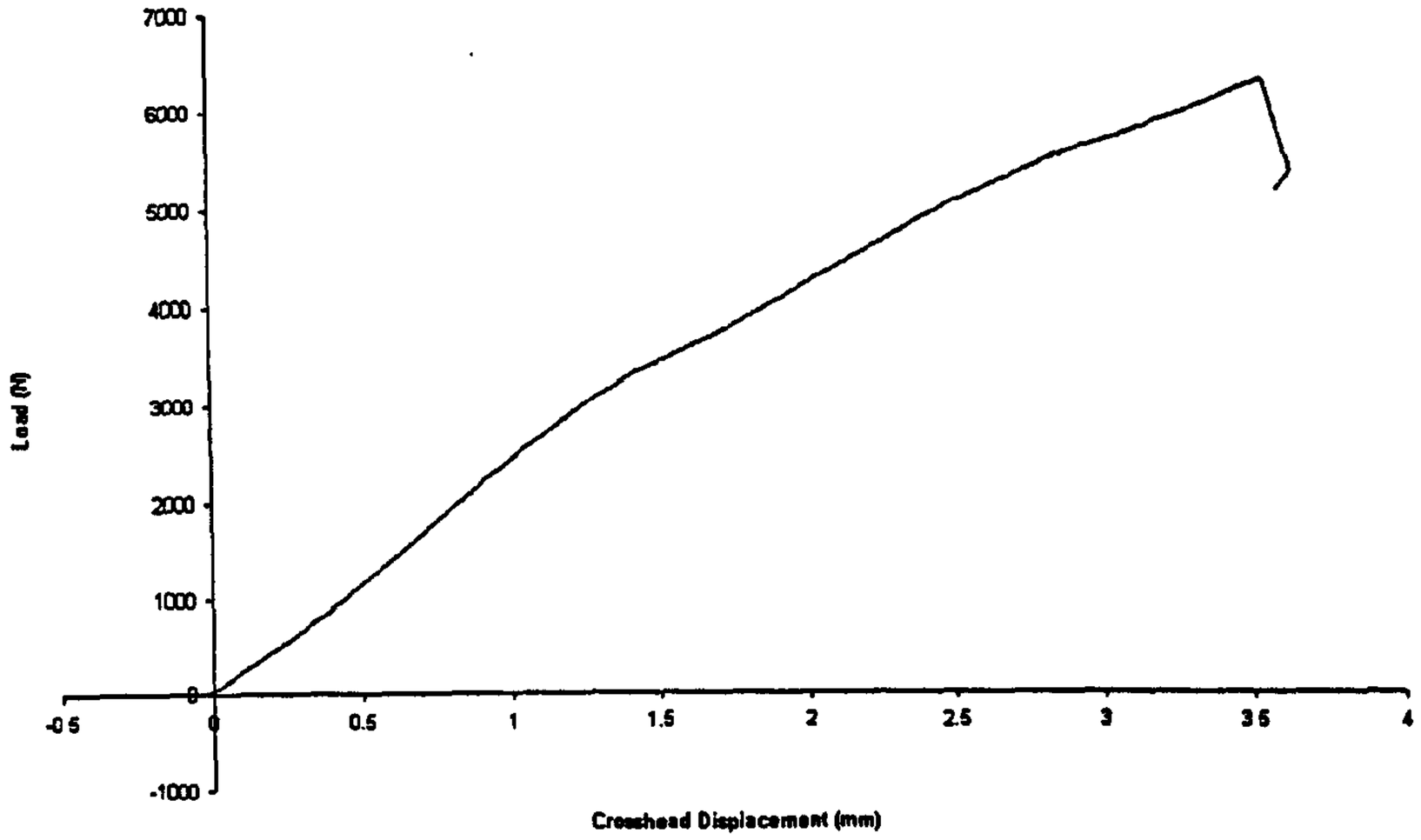

Figure 7.16: Cocured Sandwich Panel Load-Displacement Plot

Test no.	Mean Width mm	Failure Load N	Failure Load per Unit Width N/mm
1	40.04	6293	157.1
2	39.98	6195	155.0
3	40.03	6366	159.0
4	40.06	4608	115.0
		Mean	146.5 c.v. 14.4%

Table 7.2: Cocured Sandwich Panel Test Results

7.7 Correlation of Prediction and Test

The accuracy of the failure predictions for these two specimens was reasonable. The failure locations were predicted accurately in both the precured and cocured specimens. The precured specimen prediction was 23% unconservative and the cocured specimen was 16% unconservative. The reasons for these unconservative predictions are discussed in the following sections.

7.7.1 30° With Precured Edge Closure

As mentioned earlier, the precured specimens showed evidence of debonded honeycomb core prior to delamination, and as before with the 90° sandwich panels and the foaming adhesive failure, this effect was now modelled.

The failed specimens were examined in the region of failure, an image of the debonded region, now dissected, is shown in Figure 7.17. The three composite laminate parts seen in the picture are from the edge closure. The left-hand one was bonded to the top skin of the sandwich panel, and includes start of the curved region. The right edge of this slice is the start point of where the honeycomb was initially modelled, providing support. The next section shows some bonding of the honeycomb, and the third piece shows that a good bond had been formed during manufacture. It can be seen that the first 6mm of the 'contact area' was not bonded at all, the next 8mm were partially bonded, and after that the core was well bonded to the edge closure prior to testing.

It was clear that the first 6mm of the 'contact area' would not have provided any support at all to the edge closure, so modelling that as debonded would be accurate to the specimens under test. The next 8mm being partially bonded would have provided some support, but in testing, there was evidence of a clear debonded region approximately 14mm long. This suggests that the partially debonded region suffered failure of the honeycomb to edge

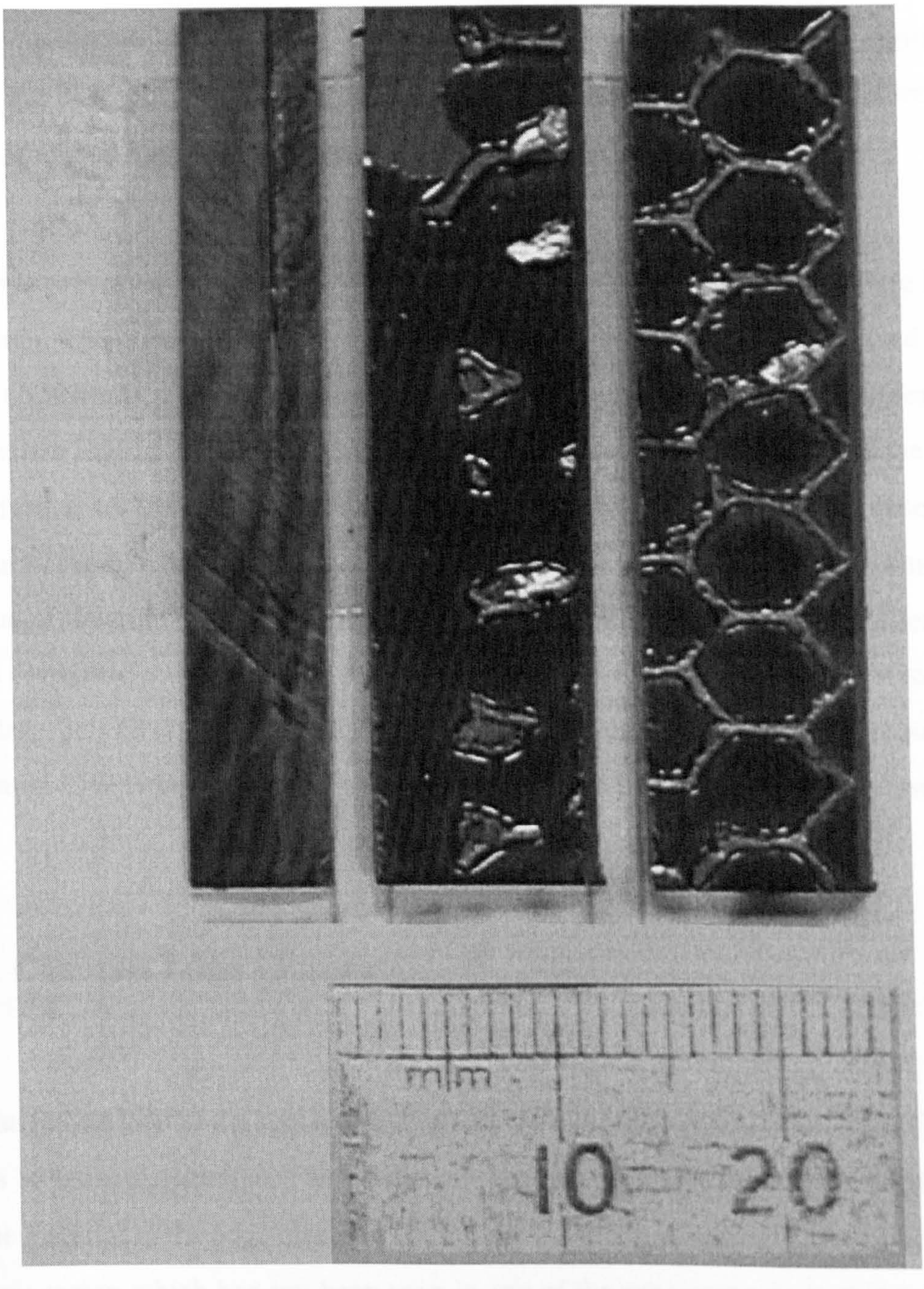

Figure 7.17: Debonded Region of Precured Sandwich Panel

closure bond prior to delamination in the tests. Modelling this region as a completely debonded area was also felt to be a reasonable approach to take. The next 6mm of bonded honeycomb were also checked in the model to investigate the effect of the lengthening debond, and how it would have affected the strength of the specimens if it had debonded before delamination had occurred. The process of growing the debonded region was achieved quite simply by removing elements from the honeycomb core in the model to produce debonded honeycomb lengths of 6, 14 and 20mm.

As reported previously, the completely intact model produced a predicted failure load at 194.4N/mm. The cleanly debonded region, when removed, reduced the predicted failure load to 166.7N/mm, a 14% reduction. The partially debonded area, when also removed, led to a failure load of 145.6N/mm, and extending the debond to 20mm reduced the failure slightly further to 138.8N/mm. It is most likely that the 14mm debond represents the behaviour of the specimens under test most closely, as the visible debond was 14mm. The prediction of delamination using this dimension observed in testing is 8% conservative. This is a correlated result based on observations which were not expected prior to testing taking place. It is clear from the failure prediction, however, that the specimens could have been around 25% stronger had the honeycomb been well bonded to the edge closure.

7.7.2 Cocured Edge Closure

The mean failure load of the specimens was 146.5N/mm and the prediction was 169.6N/mm, which is 16% unconservative. This discrepancy can be explained by considering the quality of the material in the edge closure. The cocured specimens had evidence of voidage in the failure region which had not been seen in any of the specimens up to this point. The presence of voidage is supported by the one low result of 115N/mm width. The failure prediction method being used is reliant upon accurate material strength data from scaled interlaminar tensile test specimens. It is reasonable to assume that the method will be accurate in specimens with well made, consolidated lay-ups and is likely to be less accurate in specimens that are not as well consolidated and have voidage. In order for the predic-

tions to be accurate in these cases, it is necessary for the interlaminar test specimens to be made with voidage at a similar level as that seen.

7.8 Conclusions

Two methods of manufacture were used to make sandwich panels with 30° edge closures. One group of specimens was created using a precured edge closure, and the other group with cocured edge closures. They had significantly different geometries which were accurately modelled. The precured specimen geometry had less severe stress concentrations and up to 20% lower stresses, despite being based on the same lay-up and nominal geometry.

The delamination prediction method was shown to be accurate in the precured specimens after accounting for the honeycomb debonding from the edge closure reducing the structural integrity. The failure prediction was 8% conservative and within the correct resin pocket.

The prediction of the failure in the cocured specimens was reasonable at 16% unconservative. The method relies heavily on accurate material data from strength tests. In the case of the HTA/913C material used within this research, the data came from well-consolidated specimens. The cocured specimens displayed evidence of voidage in the region of failure, and so the strength of the material must be questioned. There was one low result from the tests and if this was removed, the failure prediction was only 8% unconservative.

An important point to come out of this work was in relation to manufactured geometry of composite components. The variation that can occur from build to build is significant and something that a designer should be aware of. It would be prudent for a large number of components to be made and analysed to see whether there are variations. Any variations from build to build could make a critical difference in the failure load of each component.

From this it would be possible to establish a worst case scenario for each feature and this is what should be used for the analysis geometry. An alternative approach would be to use finite element analysis along with this method to set an acceptable range of geometries for manufacture.

Chapter 8

Delamination Prediction - Tapered I-Beam

8.1 Introduction

The delamination prediction method has been applied to a number of different geometries which could be approximated as 2-dimensional. To be effective, the delamination prediction method should also be accurate in 3-dimensional geometry with 3-dimensional stress fields. This chapter reports on the design, analysis and test of such a specimen, the tapered I-beam.

Load bearing structures in aircraft are commonly curved and can be required to carry large bending moments. The most efficient way of carrying a bending moment is to use an I-shaped section as it maximises the second moment of area whilst minimising the structural mass. When a straight I-beam is made from a laminated composite material, there are regions of tight curvature around the web-flange interface which introduce interlaminar stress concentrations that would not be of concern in a metal I-beam. If the composite

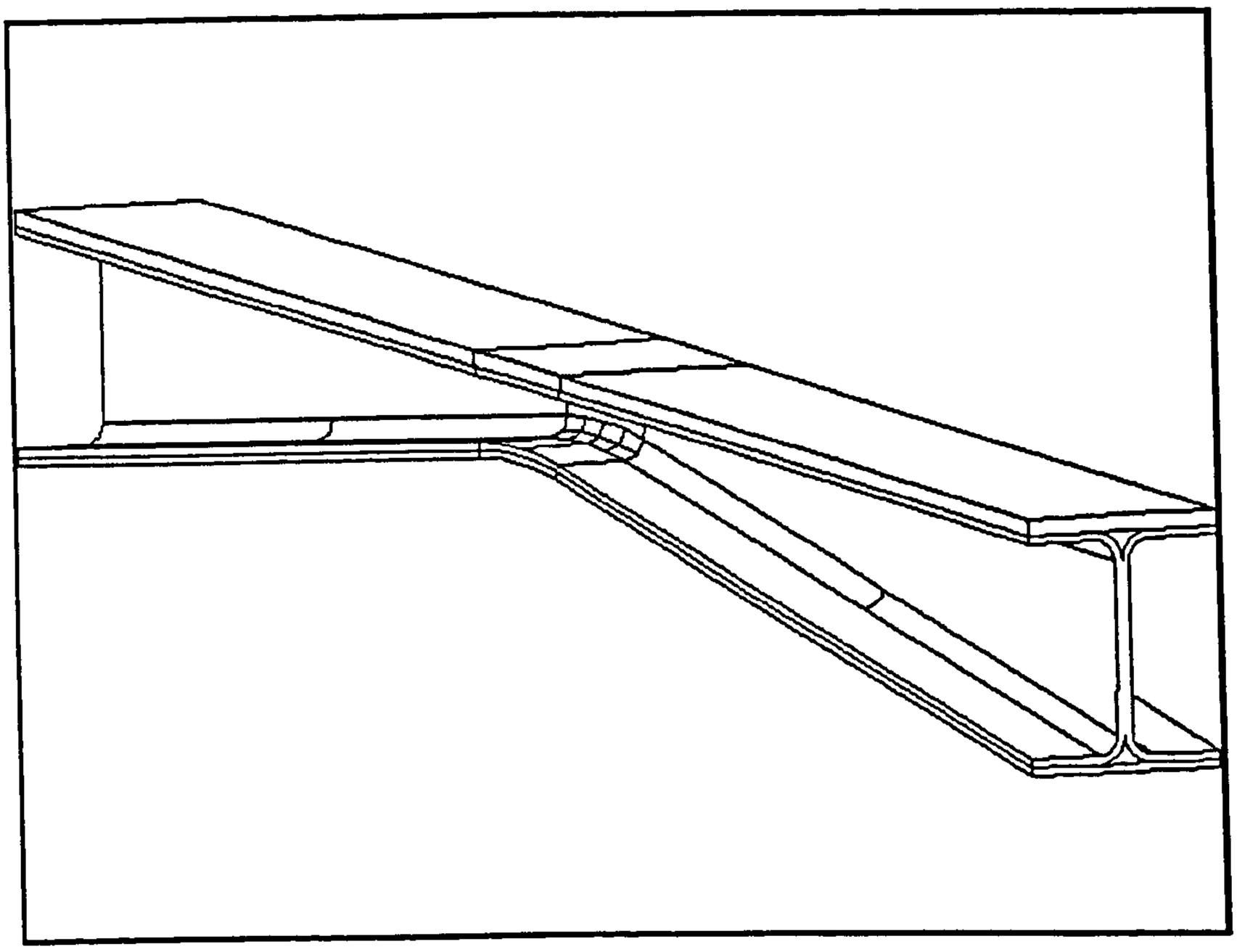

Figure 8.1: Schematic of the Tapered I-Beam Design

I-beam is curved, then the laminates will be doubly-curved which would lead to a 3-dimensional stress field.

Initial attempts to manufacture a continuously curved I-beam highlighted problems in maintaining accurate fibre alignment. A tapered I-beam was therefore designed with a curved flange to web connection only in the centre of the beam, as shown in Figure 8.1. It was designed to ensure that delamination was the first failure and it would occur in the doubly-curved laminate region in the centre of the specimen.

8.2 Specimen Design

Each component comprised of two 'C'-shaped sections joined back-to-back, with two triangular fillets and two flange caps. The arrangement of all the separate components in the final specimens can be seen in Figure 8.2.

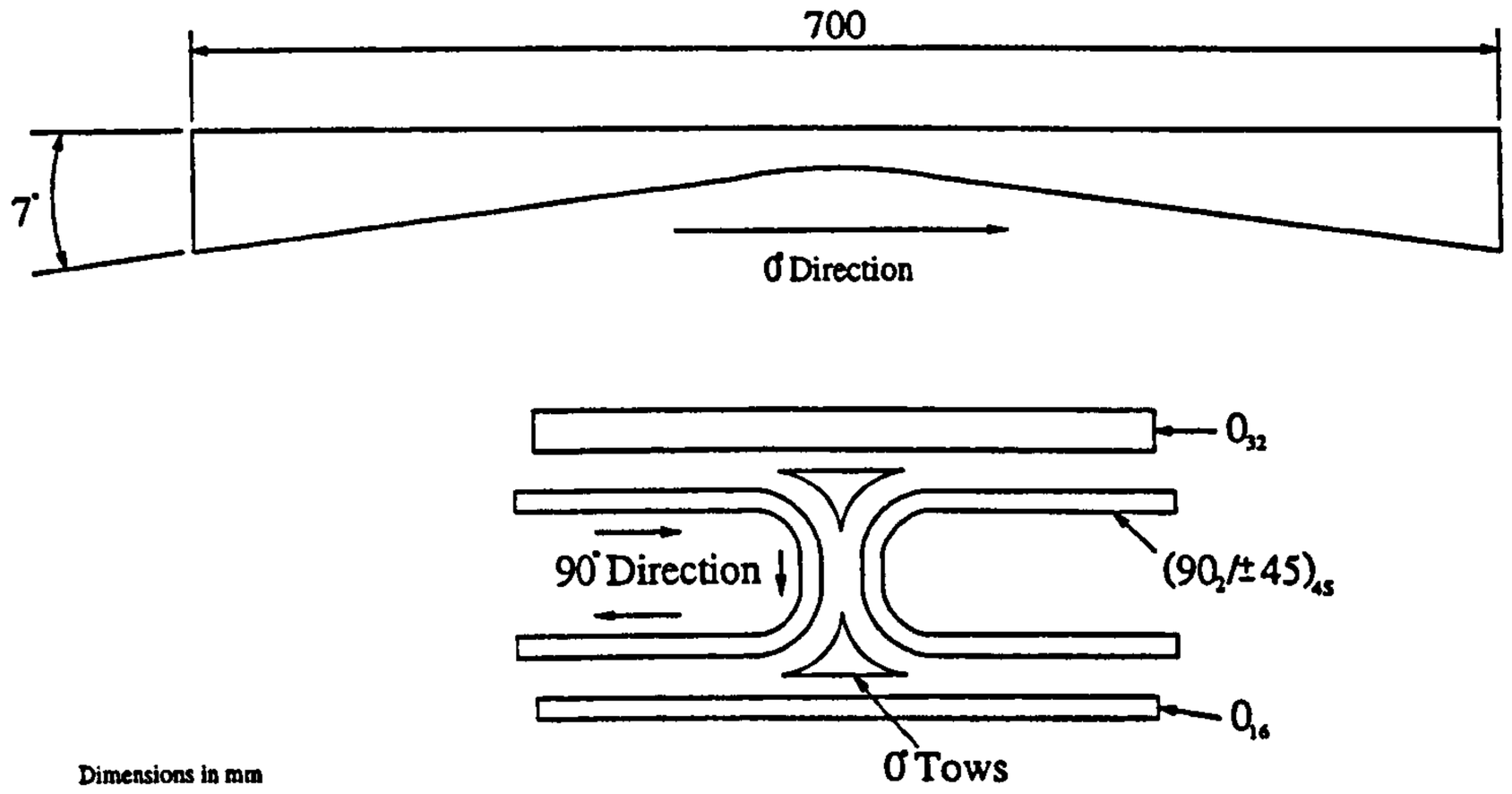

Figure 8.2: Tapered I-Beam Assembly

The flange caps were precured to prevent wrinkling during cure and joined on to the 'C'-sections using film adhesive. The flange caps were designed with different thickness top and bottom. The top flange was under compression when the beam was loaded, and buckling of the top flanges had to be eliminated. The lower flange was thinner because it would require less load for delamination to occur.

8.3 Manufacture

The manufacturing process used on these components was basically an extension of that used on the 'T'-piece specimens. A diagram of the tooling used for the manufacture of the 'C'-sections is shown in Figure 8.3.

Two pieces of this tooling were made, as each 'C'-section would require support during the assembly cure cycle. The tooling was also used for the first part of the manufacturing process, the laying up of the curved bottom flange cap.

This consisted of 16x0° plies running along the length of the beam and was layed up on the 'C'-section tooling to introduce the necessary curvature. This cap was precured along

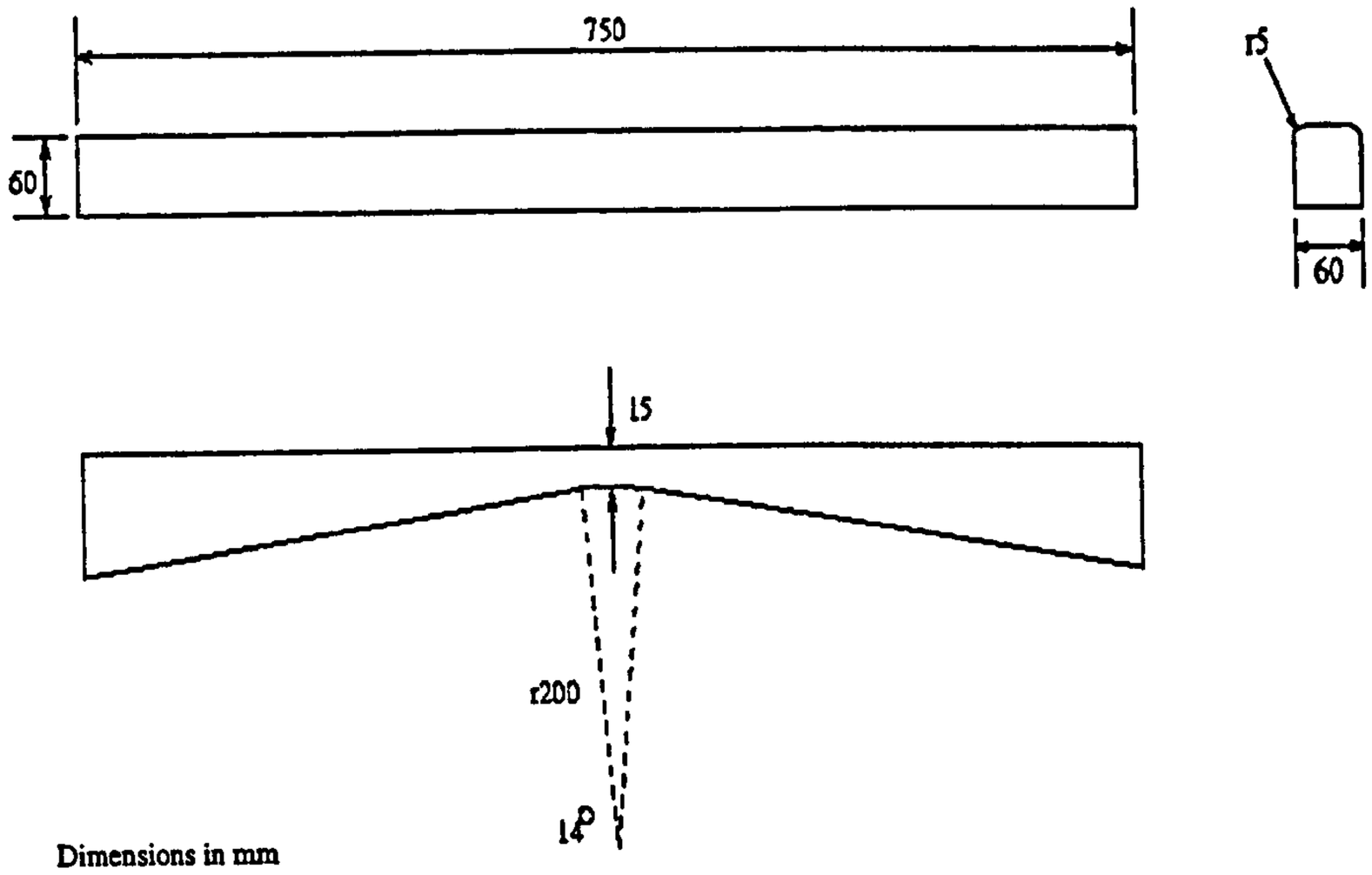

Figure 8.3: Tapered I-Beam Tooling

with the flat 32-ply top flange cap to eliminate the wrinkling of these components. Once cured, the tooling could then be used for laying up the 'C'-sections. Each 'C'-section had a lay up of $[(90_2,\pm 45)_2]_S$. The orientation angles are shown in Figure 8.2.

The laying up process was complicated, even with such a small region of double curvature. The 90° plies had to be split parallel to the fibres to stop the laminate wrinkling in the web of the doubly curved region (see Figure 8.4). These cuts were staggered through the region so that any one part was not significantly thinner than any other. Vacuum consolidation was applied after every ply to ensure good consolidation and shape conformity.

The final assembly phase consisted of bringing the two 'C'-sections back to back, incorporating the 0° triangular fillets and adding the precured flange caps over film adhesive. The precured caps were degreased with acetone, grit blasted and degreased again on the bonded surface to ensure a good bond to the 'C'-sections. The beams were cured at 7bar and 120°C according to manufacturer's instructions.

The first beam made suffered a slippage of the tooling, which rotated about the longitu-

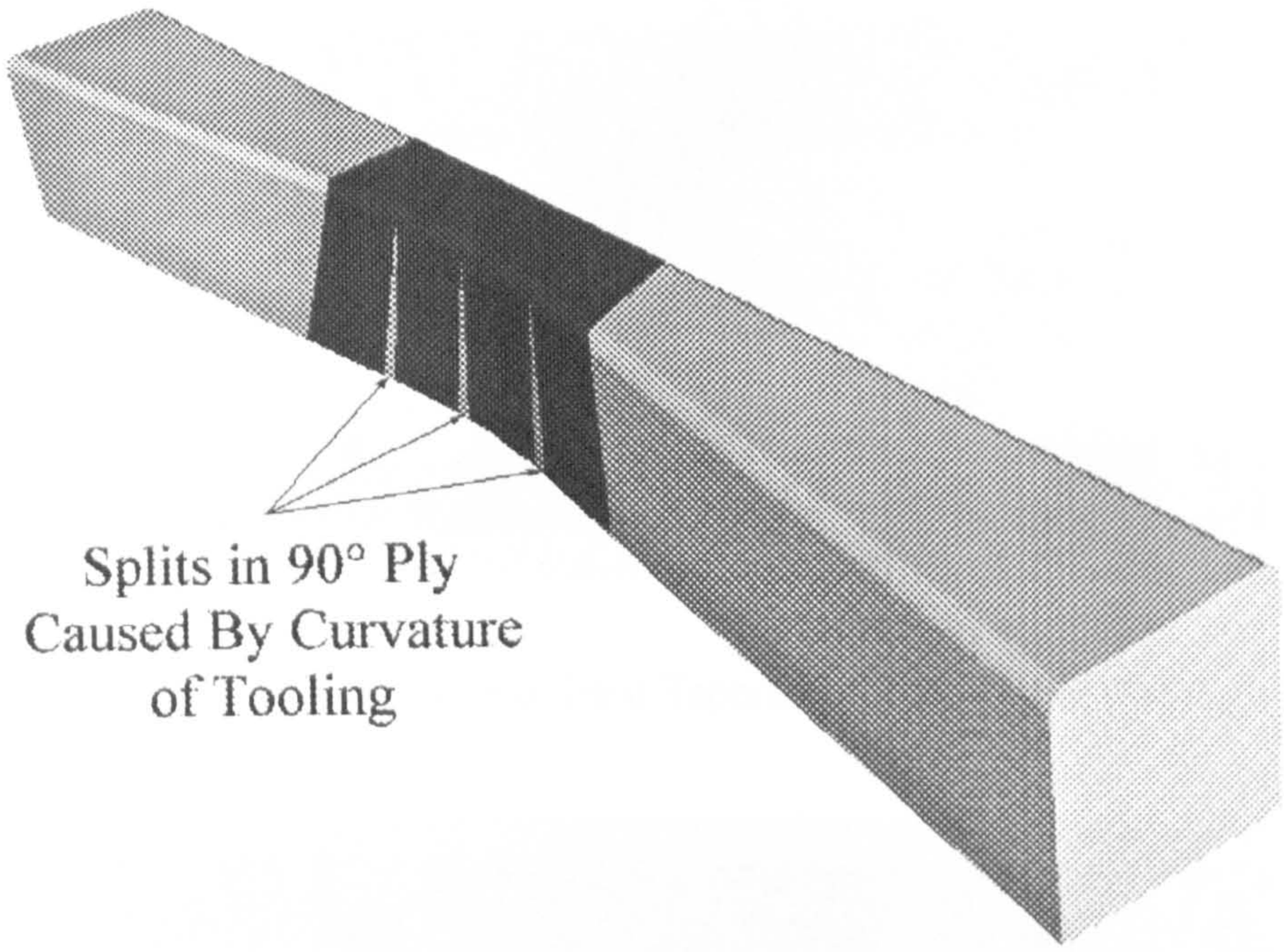

Figure 8.4: Sketch of Ply Splitting in Region of Double Curvature

dinal axes during the cure process. This was caused by the high applied pressure during cure. The top flanges were worst affected by this, each being approximately 2^o out of alignment from the horizontal, which can be seen in a photograph of the cross-section (Figure 8.5). This led to the web and flanges being tapered along the length of the beam. How this affected the strength of the beam is discussed later.

There is a small amount of tapering in the web, but this was not believed to be the most significant factor in the failure behaviour. The critical regions are the lower curved laminates which are not circular arcs like the upper ones. The lower (curved) flange is cracked in this picture as it was taken after testing, but it was found that the lower flanges are thicker at the tips than near the web. This was caused by the rotation of the tooling. The thickness of the lower flange varied from 5mm at the root to 5.6mm at the tip. This is around 25% thicker than the lower flanges for the second beam, and around 1mm thicker than the expected nominal thickness. Most of this discrepancy appears to have been as a result of the lower C-section flanges being thicker than the upper ones (see Figure 8.5), and could have been caused by a loss in consolidation pressure.

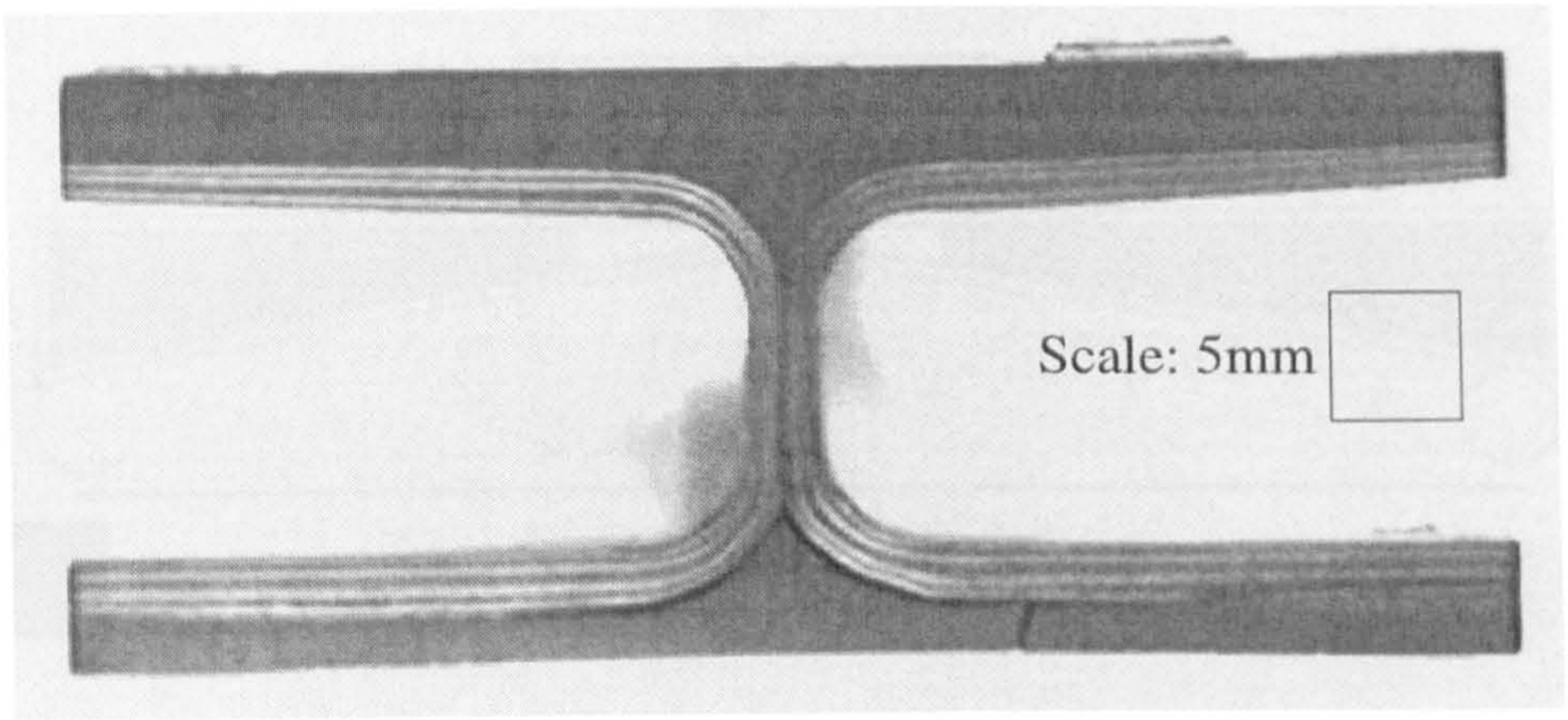

Figure 8.5: Section Through First Tapered I-Beam (After Testing)

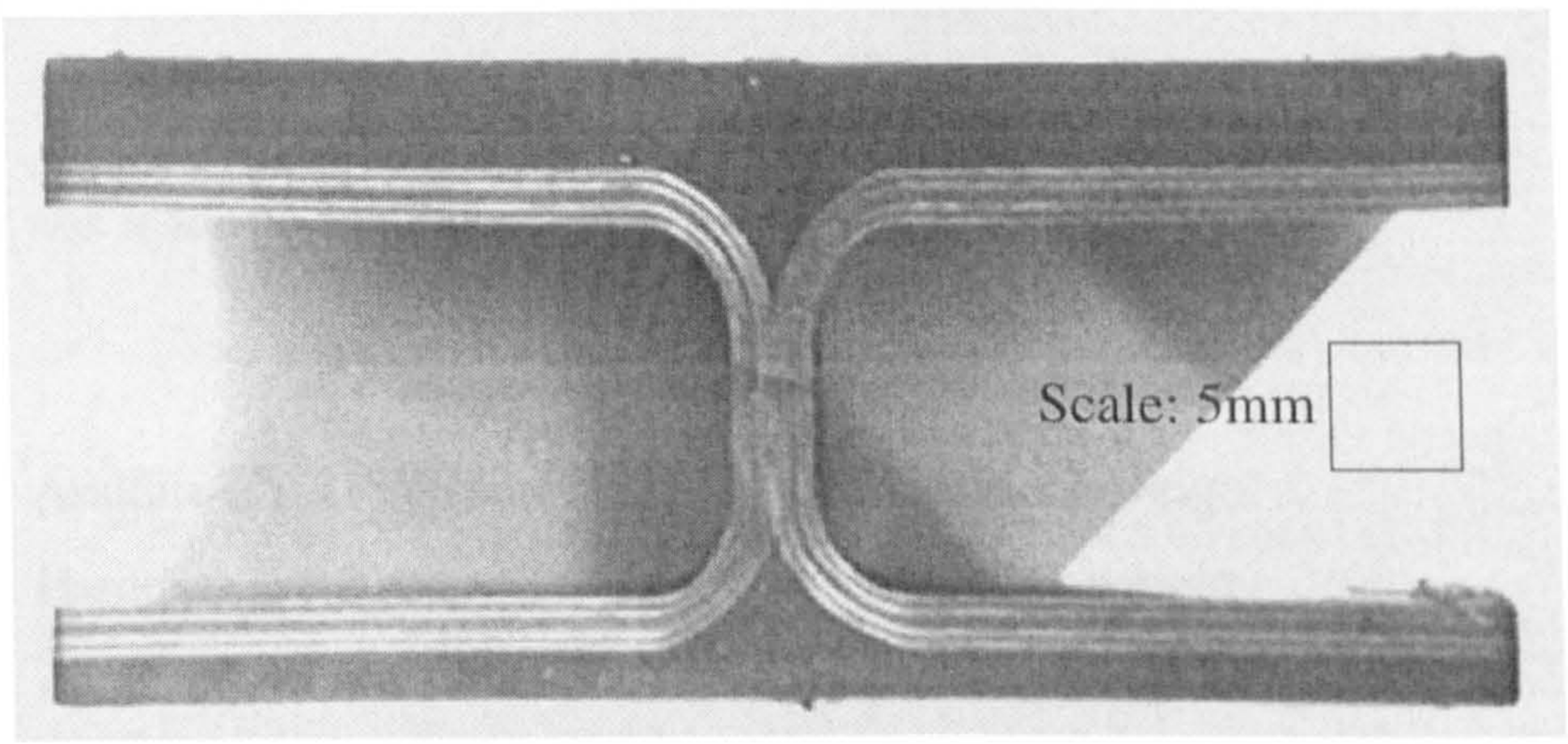

Figure 8.6: Section Through Second Tapered I-Beam

The second beam used modified tooling, with steel pins between the tooling stopping any rotation occurring. Figure 8.6 shows that the lower flanges had consistent thickness, and were only 4.3mm thick, much closer to the nominal expected for the 32 plies and film adhesive after curing. The difference in the lower flange thickness has led to a need for two separate models which are reported on later.

The specimens were designed for testing on a 4-point bend test rig (Figure 8.7). Initial analysis of the tapered I-beam design showed that there would be a risk of the web failing at a similar load level to the expected delamination load. In order to eliminate this possibility, the webs had to be filled in between the loading rollers as shown. After curing was complete, the beams were trimmed to the nominal 80mm flange width using a diamond

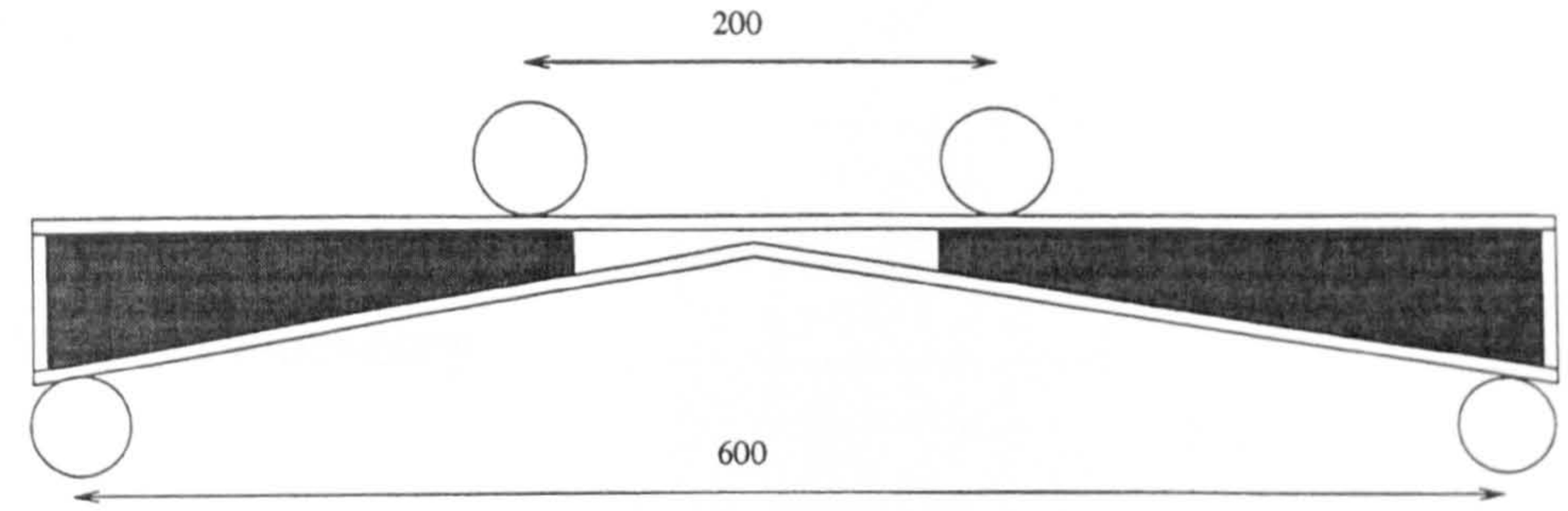

Figure 8.7: Tapered I-Beam Test Arrangement

saw and the webs filled.

The filler was made up using the following ingredients:

Araldite CY 219(Resin)	100 parts by weight
Hardener HY 219	50 parts by weight
Accelerator DY 219	2 parts by weight
Aluminium Powder(Filler)	150 parts by weight

It was applied to the beam after the surfaces were grit blasted to ensure good adhesion and therefore load transfer between beam and filler. Finite element analysis of the specimens showed that the filler had no influence on the load path in the central section of the beam, and would have no effect on the failure of the specimens.

8.4 Analysis

8.4.1 Model Geometry

The finite element analysis of these specimens was carried out as before, the geometry and mesh was formed using I-DEAS and the analysis carried out using ABAQUS. The specimen geometries were taken from the cross-section pictures produced after testing, so the detailed failure predictions took place after testing. The preliminary design work was carried out prior to the testing with nominal geometries to make delamination failure of the beam most likely.

The geometry was measured from the specimen pictures using scaling factors derived from specimen measurements. The lower flange to web connection is curved, but it was not at the expected 5mm radius. It is slightly flattened, with it being wider and shorter, approximately elliptical. This was not easily modelled in full 3-D, and was left as a 5mm radius. This would have an effect on the stress levels in the model, the actual geometry would have had approximately 10% higher stresses in the curved web-flange region. This was established as part of a design study on the 'T'-piece specimens investigating the shape of the fillet[5]. The I-beam specimens are comparable to the 'T'-piece in terms of loading and shape and therefore behave similarly allowing such comparisons to be made.

The modelled geometry was simplified for both specimens, with a lower flange thickness increase the only change between the two. The geometry and dimensions used for both specimens are shown in Figure 8.8.

The mesh used in the model for beam 1 is shown in Figure 8.9. The beams were modelled as quarter sections due to the symmetry of the specimens and the load case. The left hand end of the model as shown is the deeper end, and the right hand end represents the middle of the beam. The centres of the beams were curved, which was reproduced in

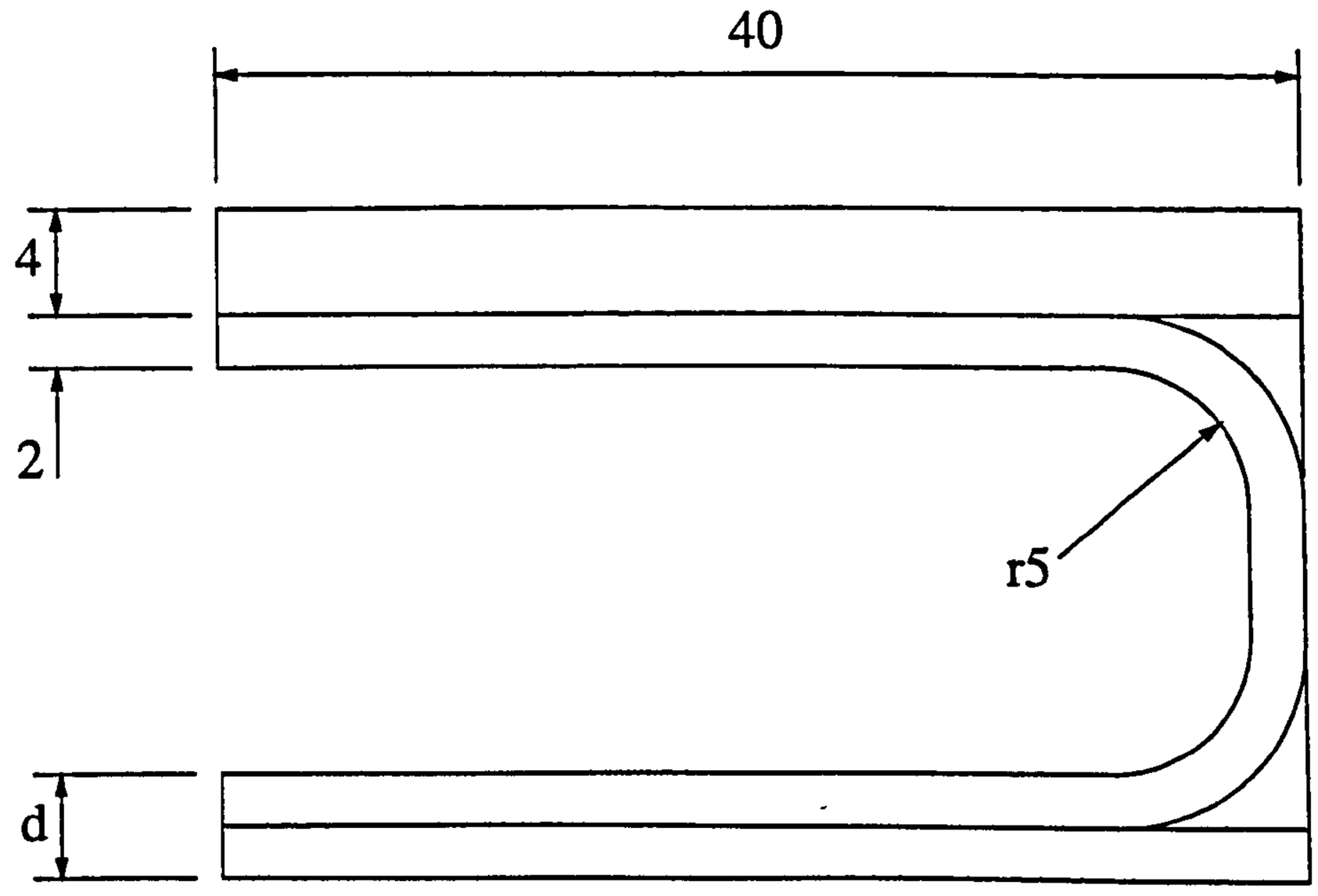

Figure 8.8: Tapered I-Beam Model Geometry

the modelling, and the mesh more refined along the length in this region because of this and the need for good stress results in the location of expected failure. The elements at the thick end of the beam are extremely elongated, but would not affect the load transfer carried to the central portion. The filler was not modelled as it would increase the number of elements and did not affect the stresses in the delamination region.

The material orientation in all elements was such that the X-direction was longitudinally along the beam in the plane of the plies. The Y-direction was defined as the transverse in-plane direction and the arrows on Figure 8.10 show the direction 'flowing' around the section taken from the centre of the model.

The through thickness, Z-direction, was defined as being orthogonal to the in-plane directions in a right-handed co-ordinate system. In the C-section laminates, each element through-thickness represented 2 plies of the same orientation, i.e. 2x90° plies, or a ±45° ply pair with merged properties. The film adhesive was not modelled, only the composite

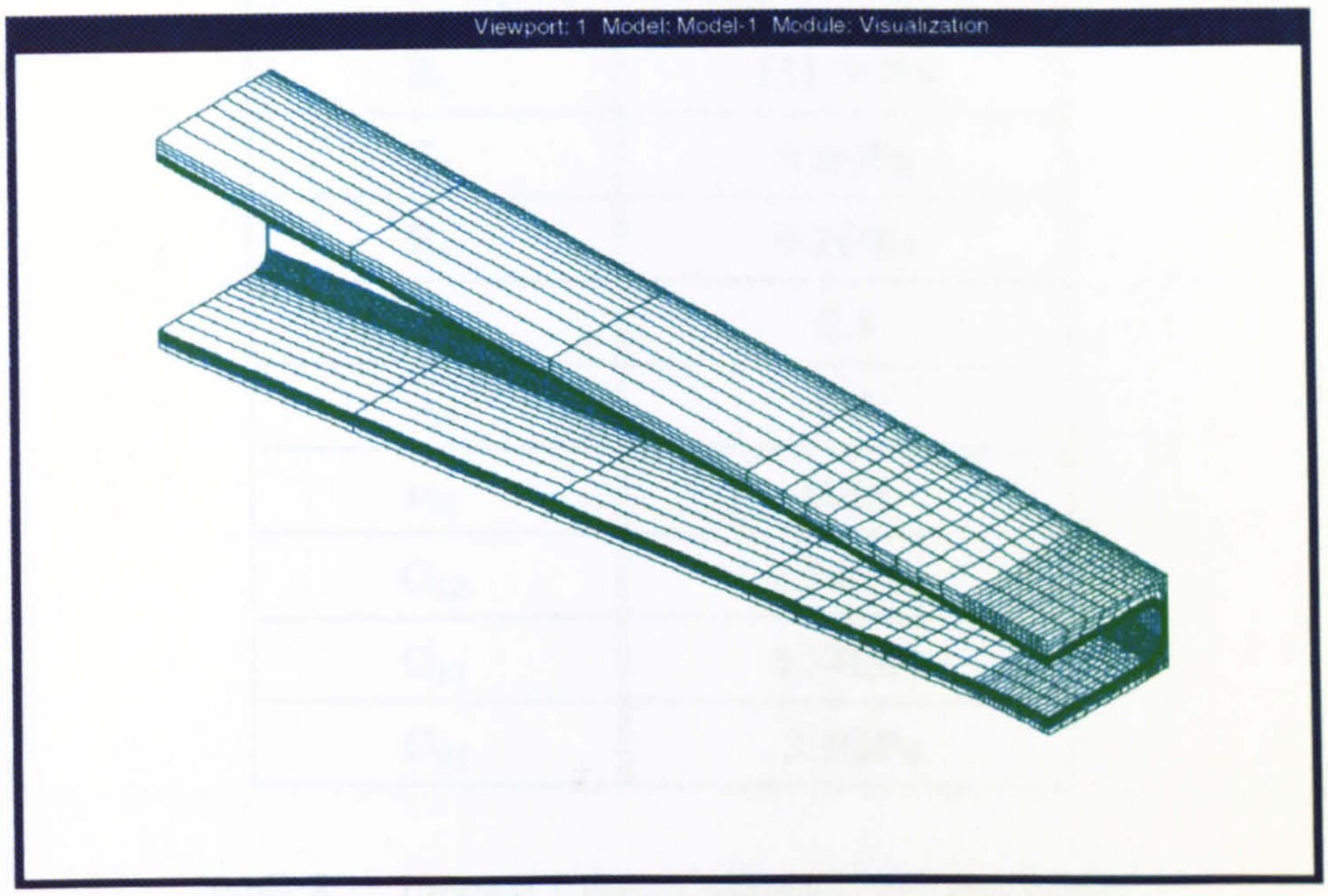

Figure 8.9: Tapered I-Beam Model Mesh

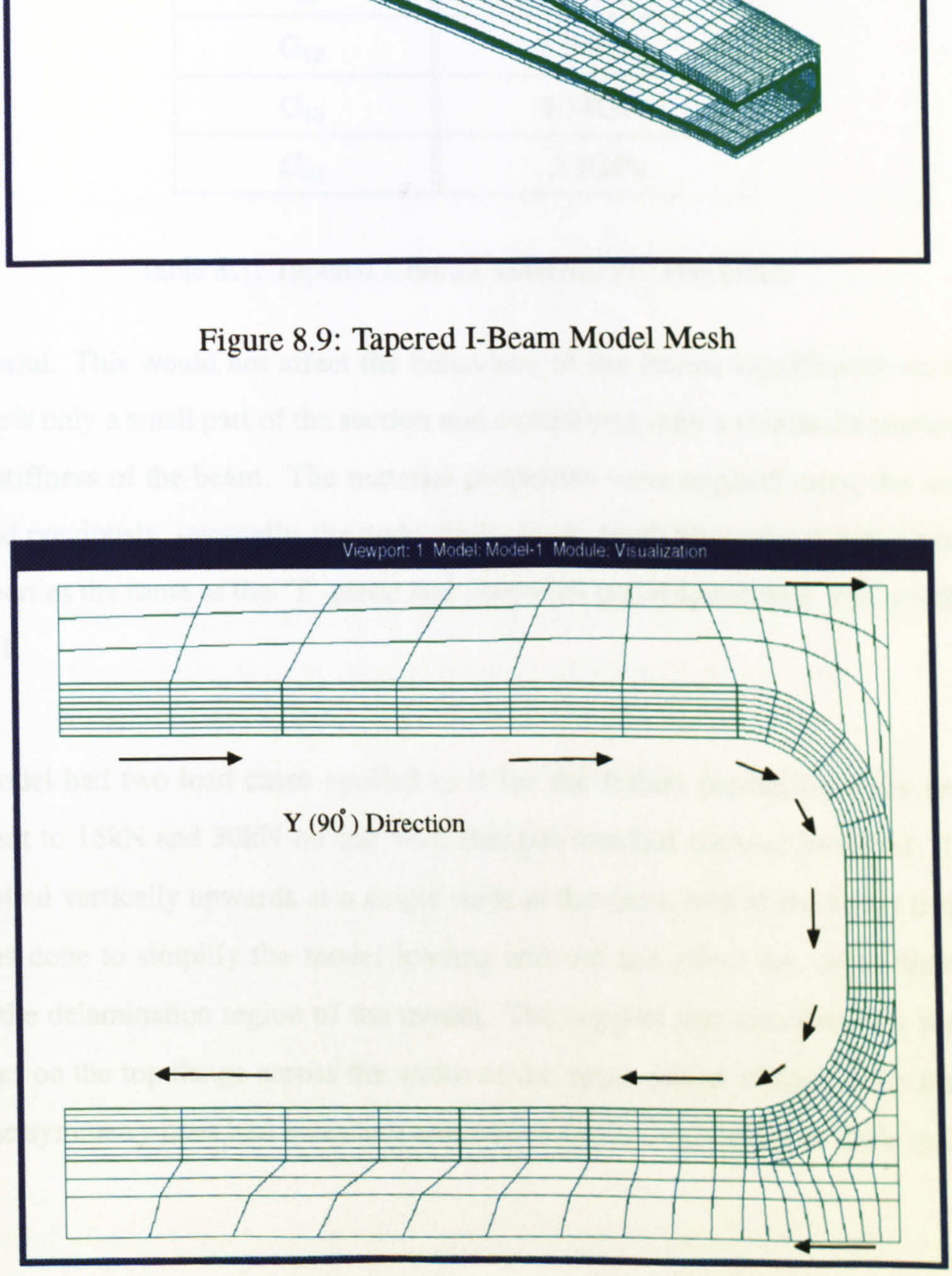

Figure 8.10: Tapered I-Beam Model Mesh at Centre for Beam 1

Material Property	HTA/913C Ply Value
E_1	131.5GPa
E_2	9.2GPa
E_3	9.2GPa
ν_{12}	0.3
ν_{13}	0.3
ν_{23}	0.45
G_{12}	4.34GPa
G_{13}	4.34GPa
G_{23}	3.1GPa

Table 8.1: Tapered I-Beam Material Ply Properties

ply material. This would not affect the behaviour of the beams significantly as the film adhesive is only a small part of the section and contributes only a miniscule portion of the overall stiffness of the beam. The material properties were applied using the user code described previously. Internally, the code works in the local fibre orientation system with ply properties the same as the 'T'-piece and sandwich panel specimens, and are shown in Table 8.1.

Each model had two load cases applied to it for the failure prediction to be produced, equivalent to 15kN and 30kN on test with thermal residual stresses included. The load was applied vertically upwards at a single node at the thick end of the beam in the web. This was done to simplify the model loading and did not affect the stress distributions around the delamination region of the model. The support was simulated by restraining the nodes on the top flange across the width of the specimen at 100mm from the centre-line. The symmetry lines had boundary conditions applied according to their orientation.

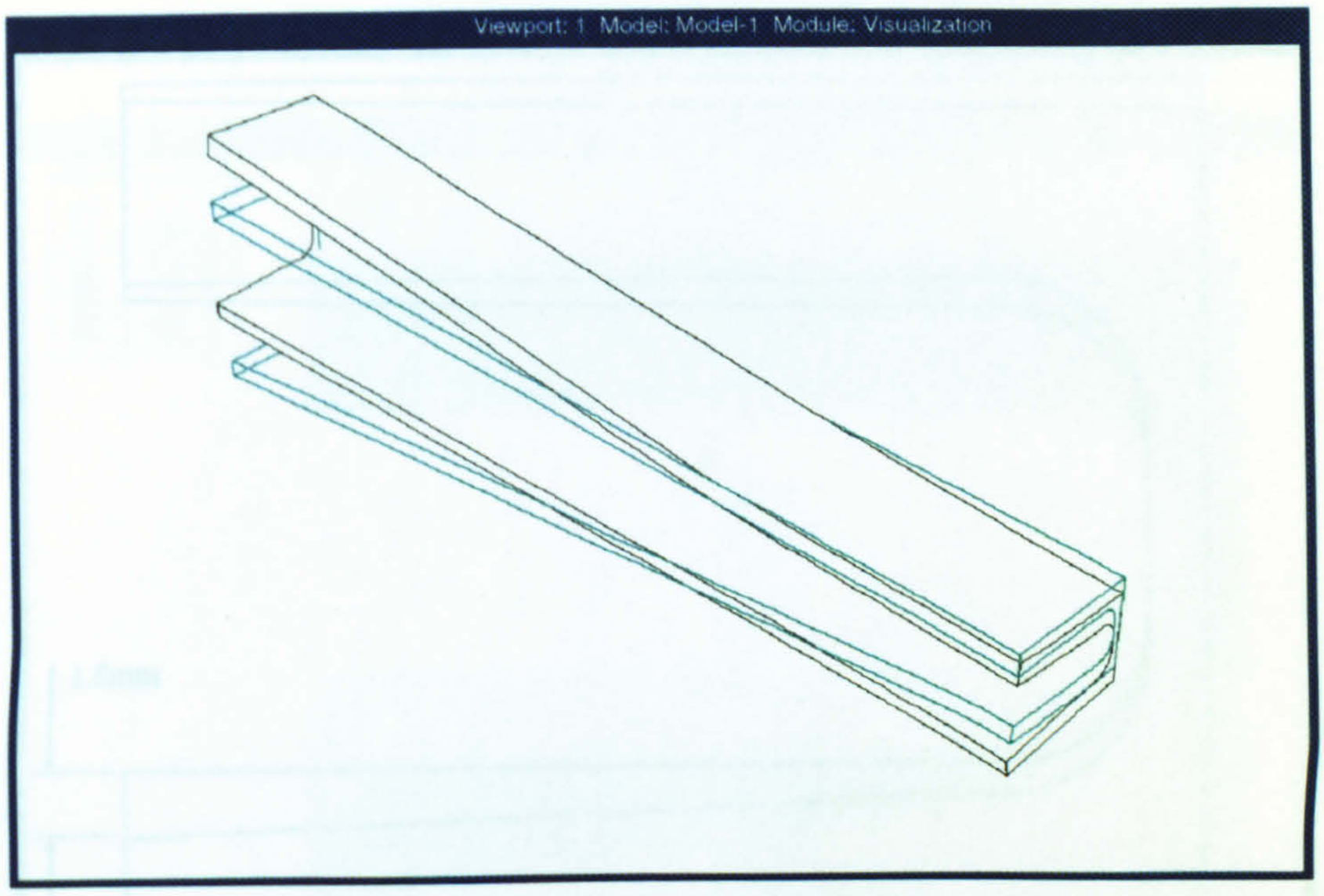

Figure 8.11: Tapered I-Beam Model 1 Exaggerated Displacement

8.4.2 Results

The exaggerated deformed outline of the first beam model at a load of 15kN is shown in Figure 8.11. The bending caused by the upward force at the left hand end being counteracted by the vertically restrained nodes at the inner roller is clearly visible. The scaling factor on the displacement values was 5.

The critical cause of the interlaminar stresses which could trigger delamination in testing is the opening out of the lower flange. This can be seen more clearly in Figure 8.12. This shows a view of the centre slice of the model with an unexaggerated deformation at the applied load of 15kN. This opening out of the flange was observed in testing by hanging a scale at the centre section. The displacements were similar to those seen in the model.

The tapered shape of the beam curvature of the lower flange are the causes of the flange 'opening.' Wherever a curved section is under tension, there is a resultant force acting towards the centre of curvature. In this case, the curved lower flange of the tapered beam had a resultant force acting downwards across the entire flange. This distributed force

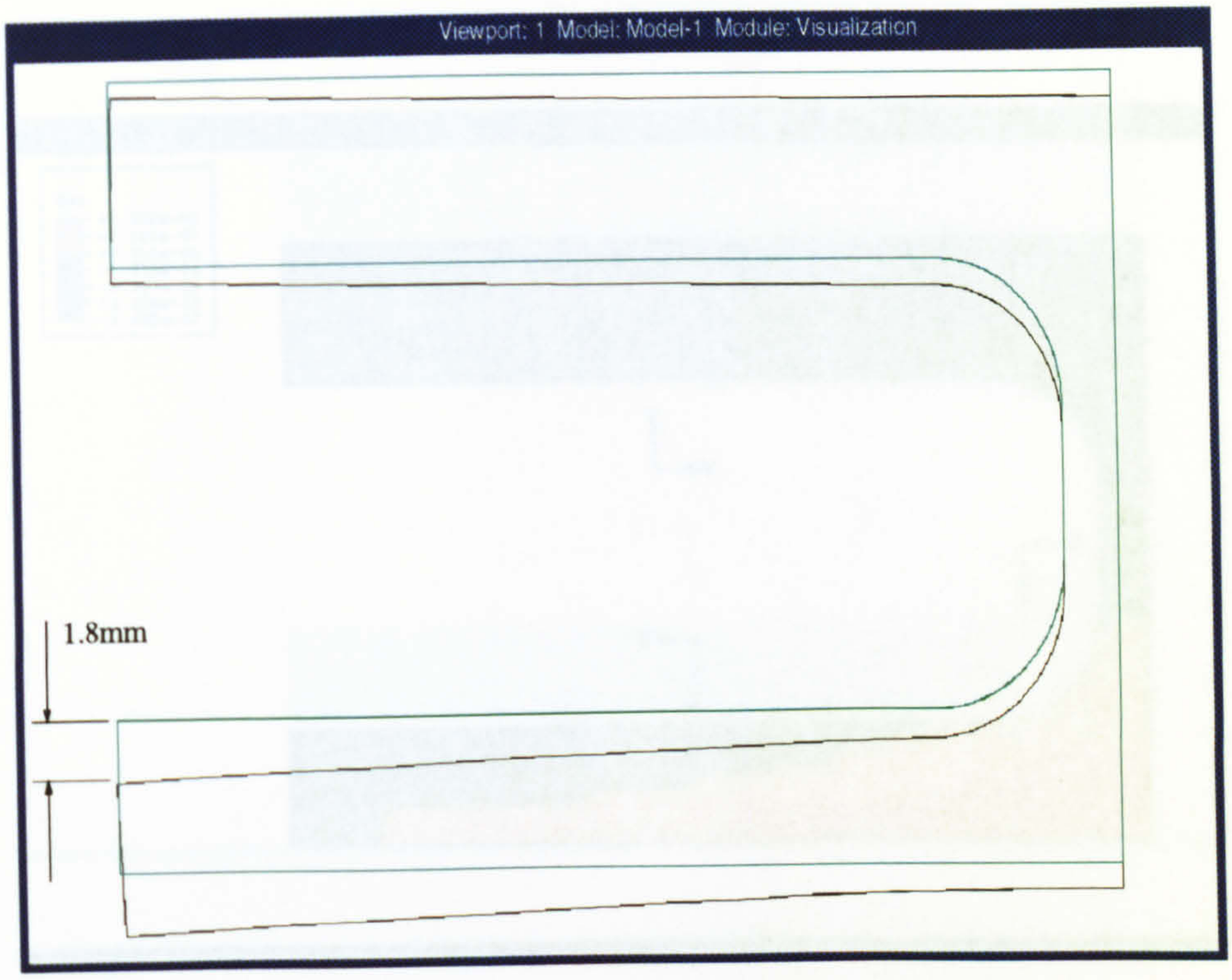

Figure 8.12: Tapered I-Beam Model 1 Displacement at Centre

produced a bending moment, and at the root of the flange, the double curvature of the laminate starts. So, what we have is a moment applied to a tightly curved laminate, and hence interlaminar stresses result as seen later.

The longitudinal strains in the centre of the beam are shown in Figure 8.13. The web shows a stress distribution indicative of bending, with the top being under compression, and the bottom being in tension. The distribution of the bending strains in the web are linear.

There is significant variation to this distribution along the lower flange. The strains reduce moving outwards, eventually turning compressive at the tip. This variation is produced as a result of the bending of the lower flange. The lower flange is curved and the opening displacement is effectively radial. As the radial displacement increases, the tangential (longitudinal) direction of the flange has to reduce in length. This reduction in length is the reason for the strains turning compressive.

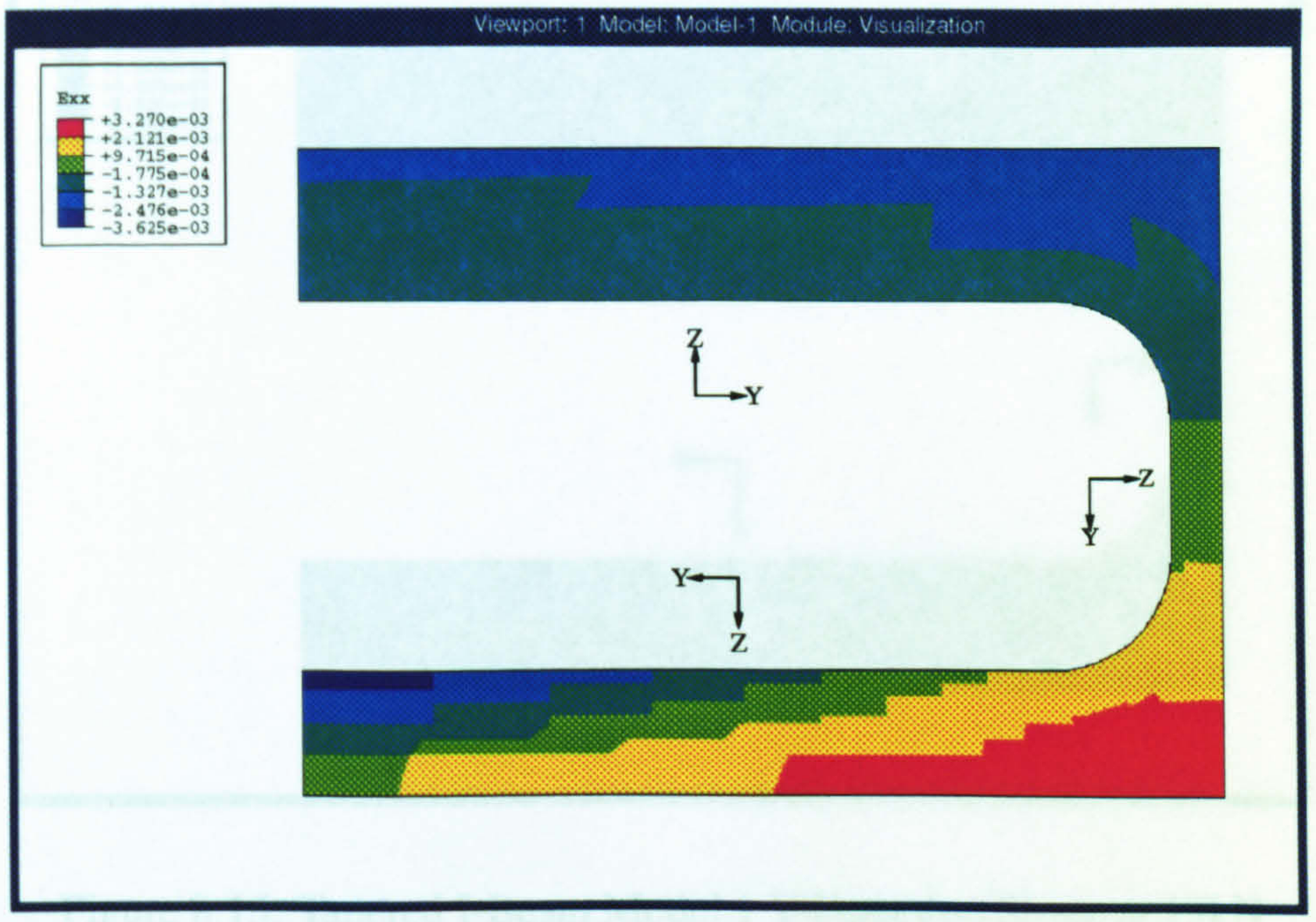

Figure 8.13: Tapered I-Beam Model 1 Longitudinal Strain at 15kN

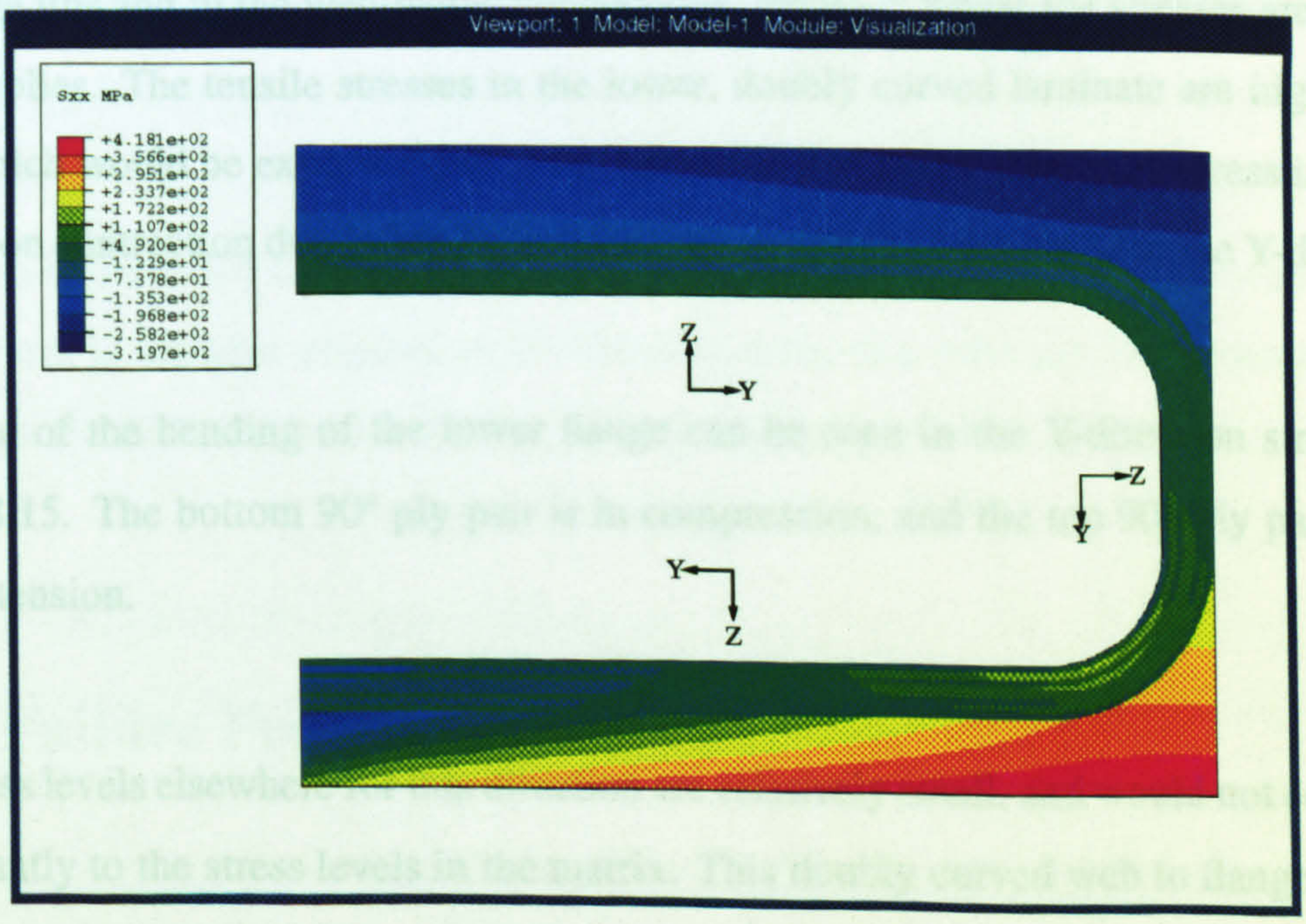

Figure 8.14: Tapered I-Beam Model 1 Longitudinal Stress at 15kN

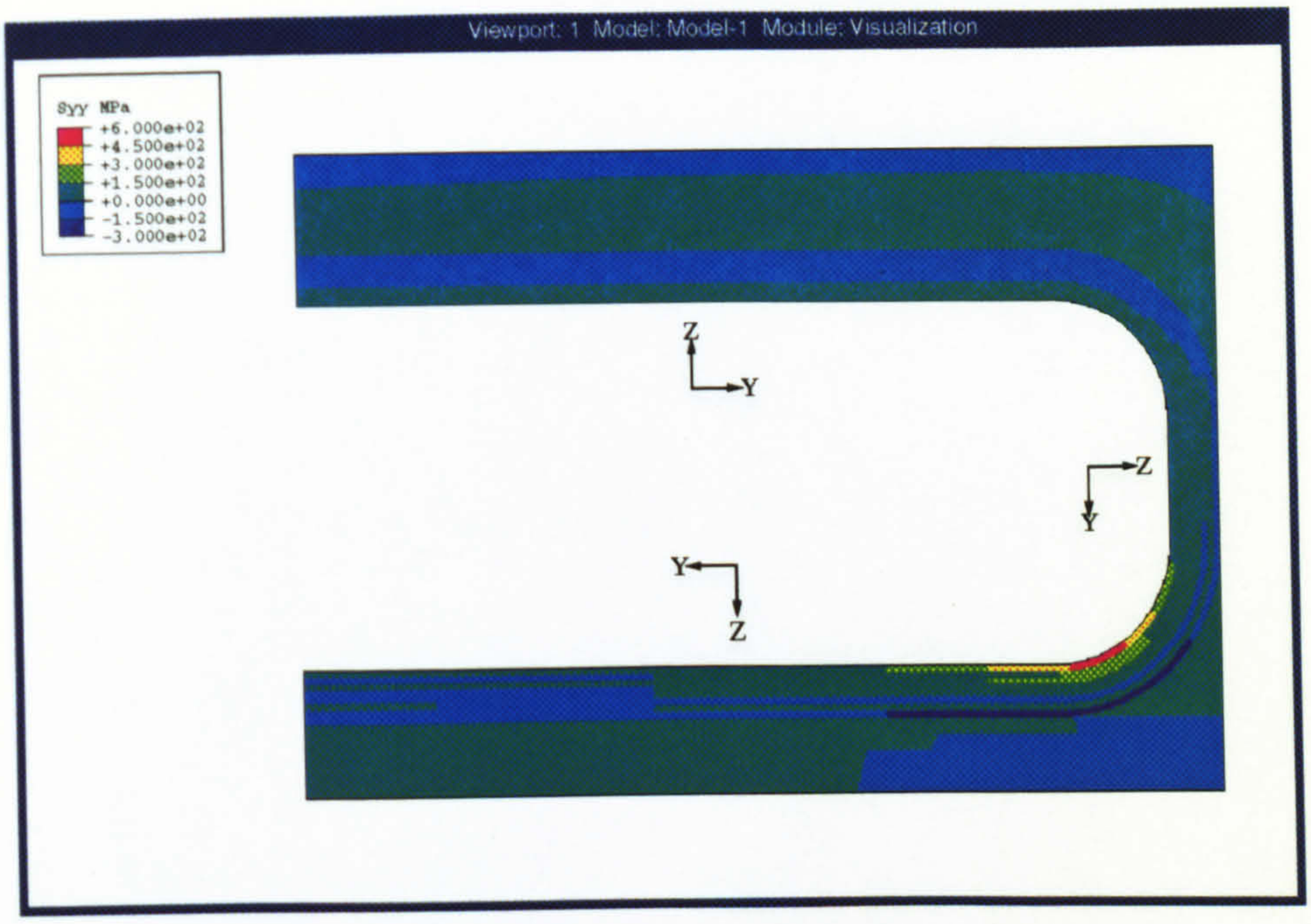

Figure 8.15: Tapered I-Beam Model 1 Y-Direction Stress at 15kN

The same effect can be seen on the longitudinal stresses seen in Figure 8.14. The flange caps and fill-in regions had much higher stresses because they were composed of 0^o plies and were also at the longitudinal strain maxima. The 45^o plies can also be picked out at the flange tips and in the web/flange connections, which is where the stresses are highest in these plies. The tensile stresses in the lower, doubly curved laminate are higher than those which would be expected due to the strains at that point. The extra stress is caused by Poisson contraction due to bending strains running around the curve in the Y-direction.

Evidence of the bending of the lower flange can be seen in the Y-direction stress plot, Figure 8.15. The bottom 90^o ply pair is in compression, and the top 90^o ply pair is in a state of tension.

The stress levels elsewhere for this direction are relatively small, and would not contribute significantly to the stress levels in the matrix. This doubly curved web to flange connection is also the area where there are any significant interlaminar stresses. The interlaminar direct stress levels are shown in Figure 8.16.

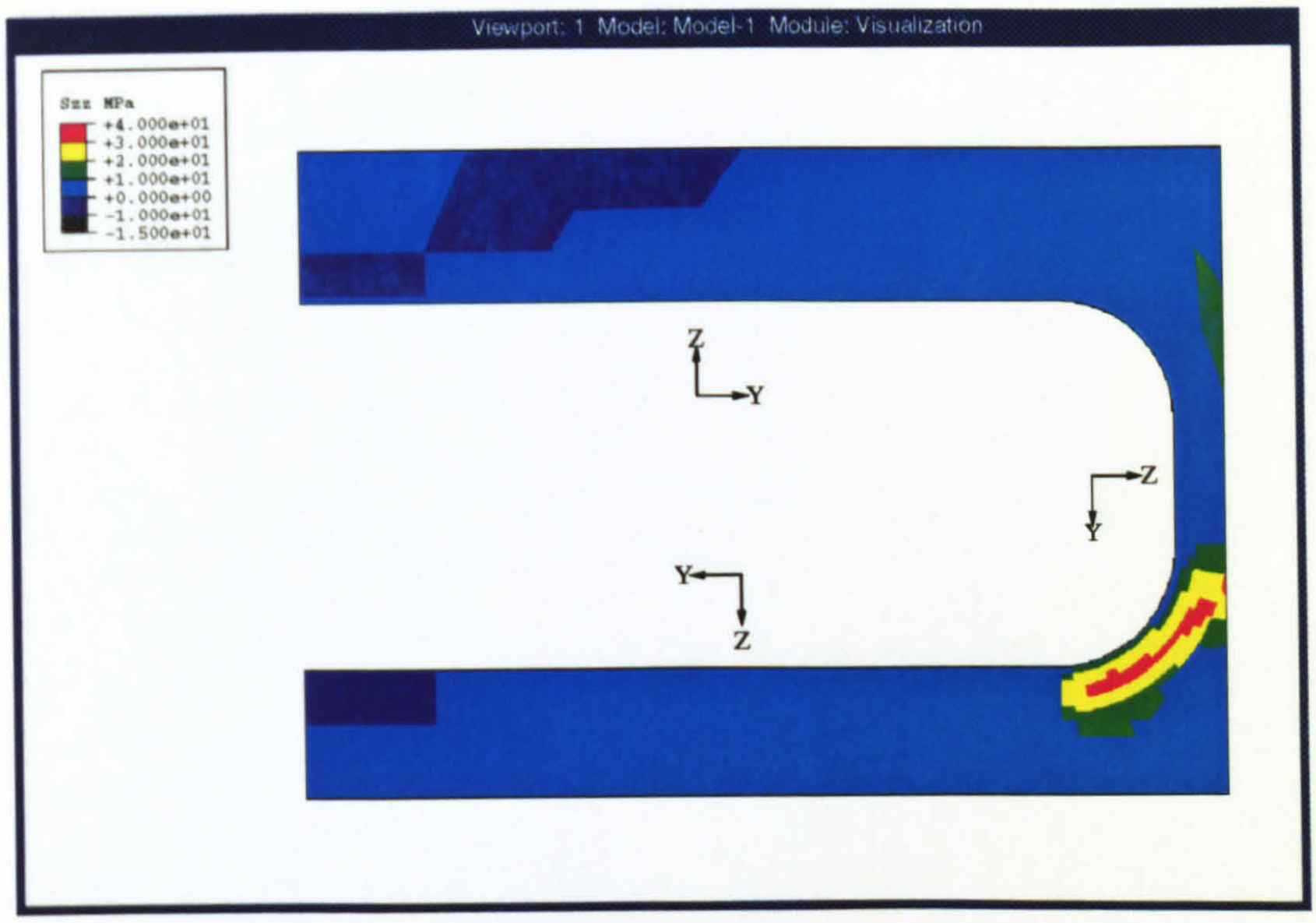

Figure 8.16: Tapered I-Beam Model 1 Interlaminar Tensile Stress at 15kN

The highest interlaminar tensile stresses are in the centre of the doubly-curved laminate. These stresses are as a direct result of the bending moment applied by the opening flange forces. The 0^o plies in the flange cap and fill-in region do not have significant inter-fibre stresses in this direction. The interlaminar shear stresses (Figure 8.17) go hand-in-hand with bending in a curved composite laminate.

The stress maxima are once again in the doubly-curved laminate. The highest magnitude of the stress is the blue negative peak which is coincident with the interlaminar tensile stresses, and will hence be the most important in making a failure prediction.

8.5 Failure Predictions

Each beam required a different analysis to be carried out because of the difference in the thickness of the lower flange which is critical in establishing the interlaminar stresses. This is because the overall deformation of the beam is reduced by having a thicker

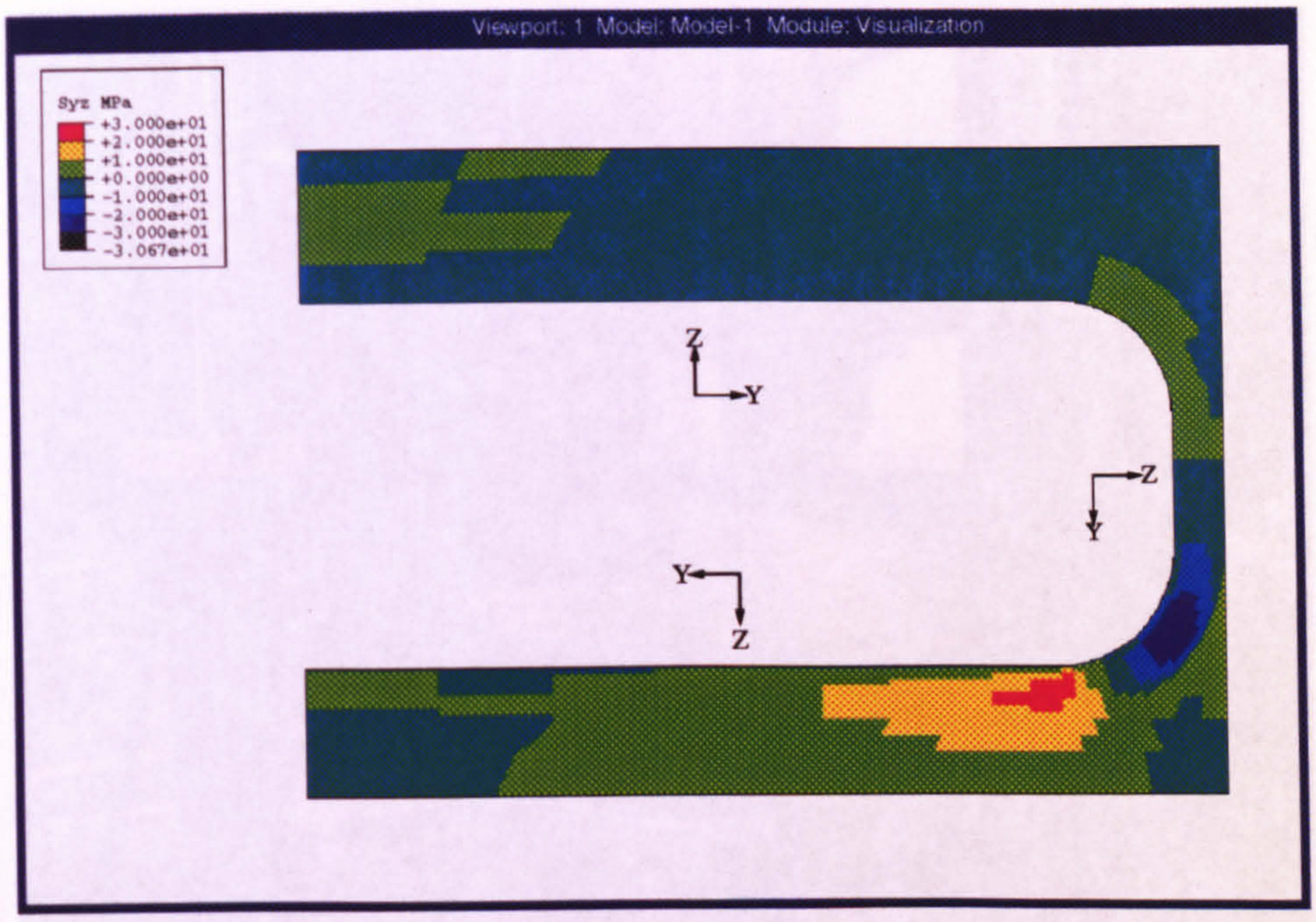

Figure 8.17: Tapered I-Beam Model 1 Interlaminar Shear Stress at 15kN

flange. As the overall amount of bending is reduced for the thicker-flanged beam, then the amount of secondary bending (flange opening) is reduced. This leads to lower interlaminar stresses in the curve and a higher delamination load for beam 1.

The proposed method takes stress results from the elements likely to contribute to the failure, so in this case, all the elements from the doubly curved laminate and the associated fill-in region were used. The output from these elements was post-processed using the UVES code, and the failure load for beam 1 was predicted at 25.2kN. The second beam had a predicted failure load of 18.4kN.

Further investigation of the individual element UVES results showed that the delaminations were expected to occur in the doubly-curved laminate at the longitudinal centre-line because this is where the stresses were highest. The failure was expected in plies 5 and 6 as the highest stresses were in the third row of elements starting at the free surface. This was at approximately 45° around the curve in the cross-section plane.

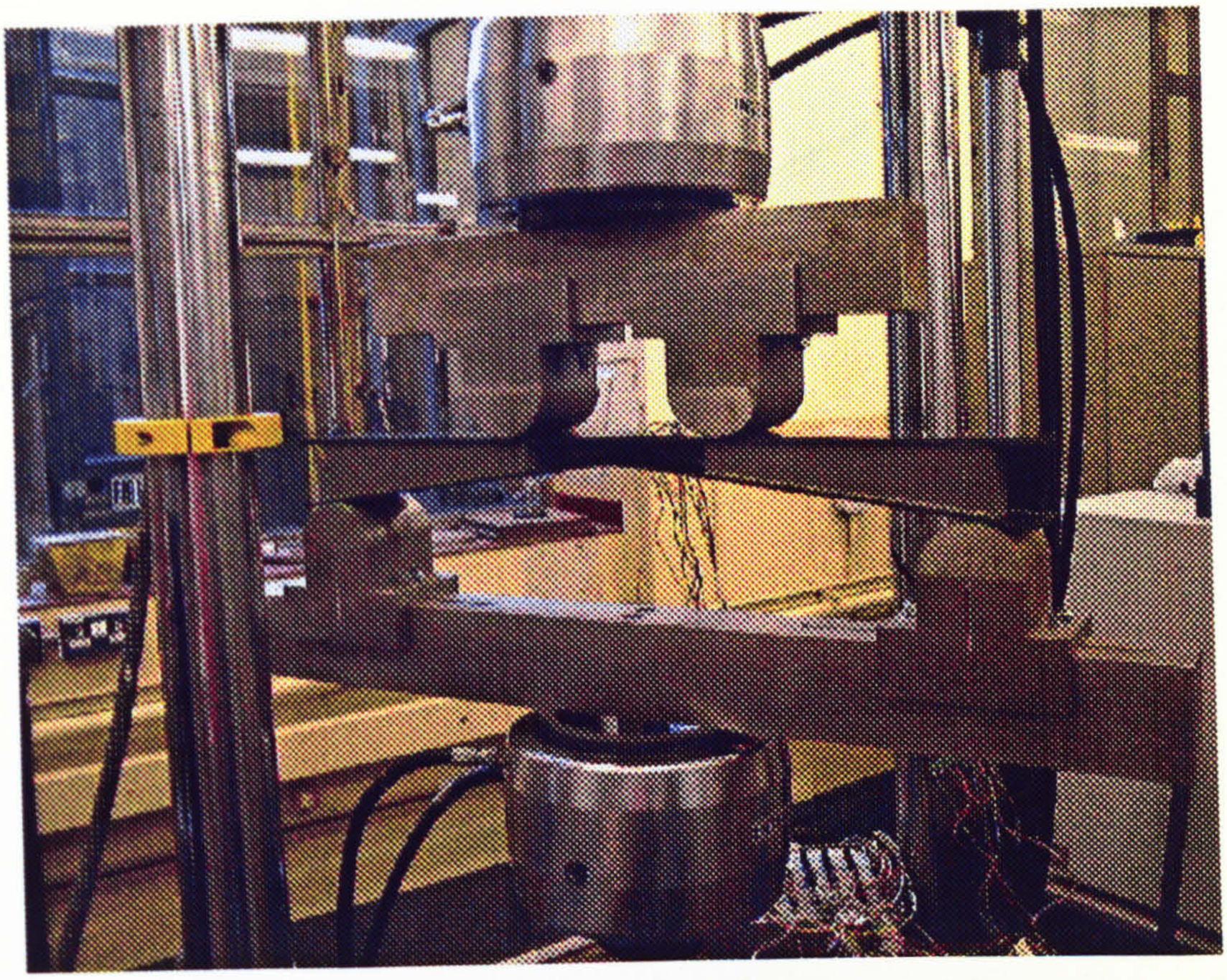

Figure 8.18: Tapered I-Beam Under Test

8.6 Testing and Results

8.6.1 Beam 1

The tapered I-beam specimens were large and required a new four-point bend test rig to be built. This rig can be seen in a picture of the first beam under test in Figure 8.18.

The load was applied downwards at the middle two noses and reacted upwards at the outer noses. This produced bending so that the lower flanges were in tension and the straight upper flanges were in compression. The first loading cycle took beam 1 to 27.7kN, 5 audible events were detected, starting at 22.4kN. The second loading took it to 37kN where the beam failed catastrophically.

Prior to testing, strain gauges were attached to the central portion of the beam at various

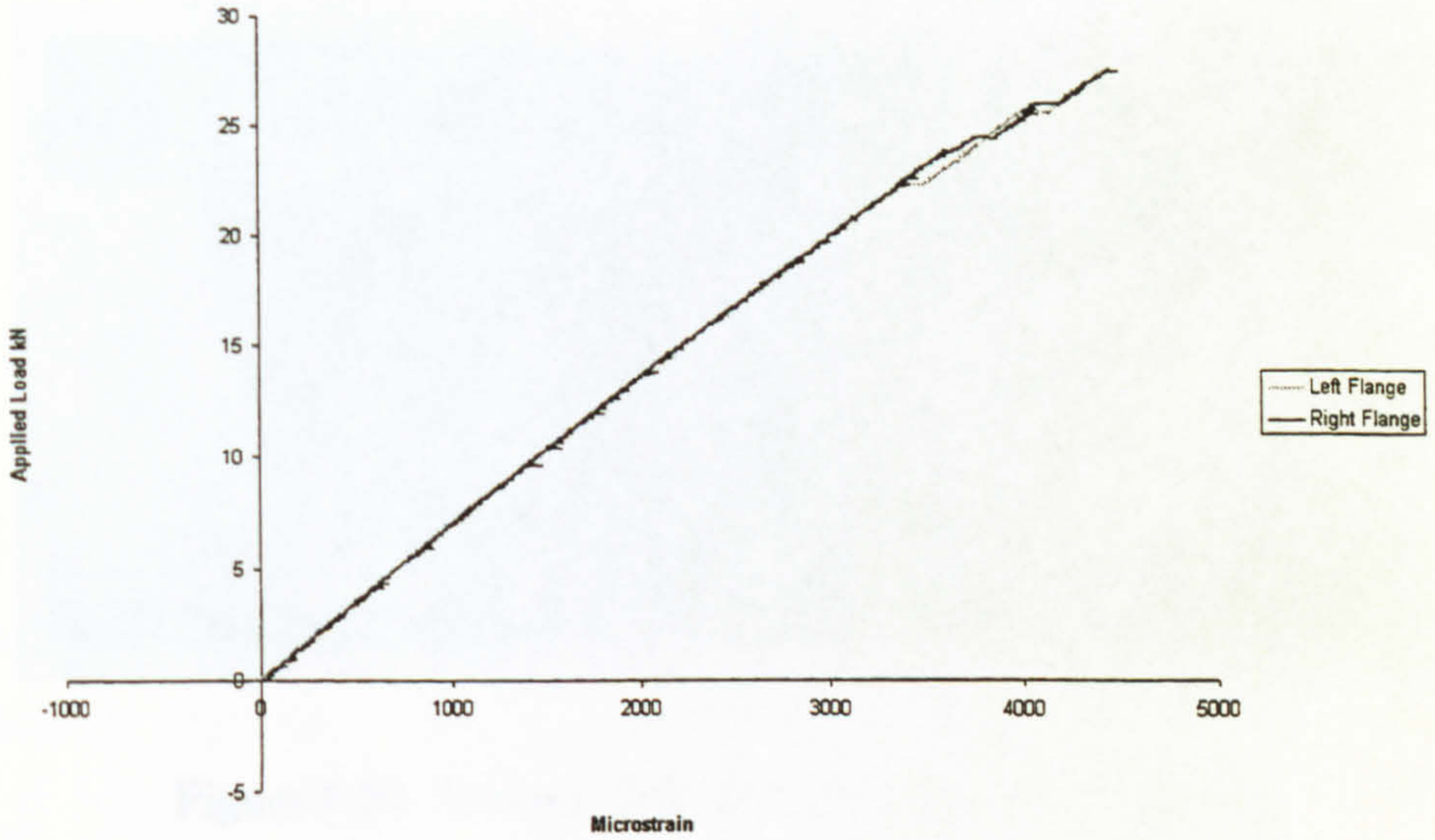

Figure 8.19: Tapered I-Beam Strain Readings

locations. The strain levels were measured during the tests, and the strains on the lower surface of the lower flanges are shown in Figure 8.19. Each audible emission coincided with a change in the strain levels for one side or the other. This indicates that localised damage was occurring at each emission, the causes were established by dissecting the beam.

The beam was inspected after catastrophic failure. The lower flange cap was not in contact with the rest of the specimen for most of the length of the beam. There was evidence of discrete delaminations in each of the doubly-curved laminates. It is believed that the relatively small delaminations were indicated by the small changes in the strain gauge readings at each audible emission. The delaminations occurred at 90°/45° interfaces at different locations in both laminates, and so it is not possible to establish which delamination would have occurred first.

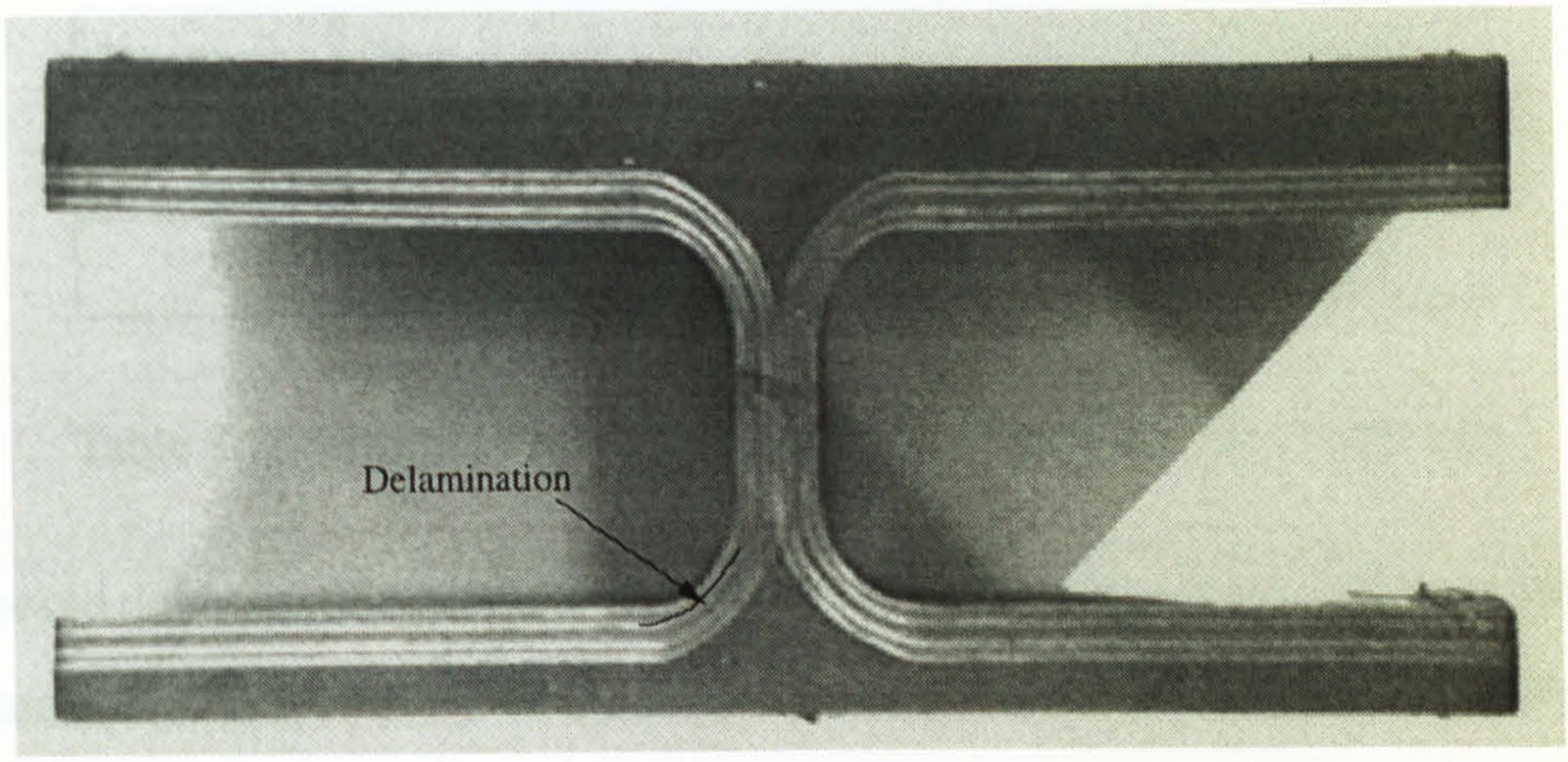

Figure 8.20: Tapered I-Beam 2 Delamination Location

8.6.2 Beam 2

The second beam was only tested to the first strain jump and was then dissected. After the central section was cut and polished, dye penetrant clearly indicated a delamination, 8mm long in between plies 4 and 5 (a 0^o and a 45^o ply) in the laminate on the side of the strain gauge which showed a discontinuity in its readings. The location of the delamination is shown in Figure 8.20.

There was no other damage visible within the central section, and no voidage was visible in any of the composite material.

8.7 Conclusions

The tapered I-beam specimens were designed to fail by delamination in the doubly-curved laminates making up the central portion of the 'C'-sections. The failure of the specimens during testing was localised in this region, a number of delaminations occurring prior to catastrophic failure which led to the lower flange cap becoming separated from the rest of the specimen due to the energy released.

Beam no.	Test Result kN	Predicted Load kN	Difference
1	22.4	25.2	+13%
2	17.1	18.4	+8%

Table 8.2: Summary of Tapered I-Beam Delamination Prediction

The proposed delamination prediction method accurately located the failure in the doubly-curved laminates. A summary of the predicted and test failure loads are shown in Table 8.2. Both of the predictions were only slightly unconservative, with the largest error being 13%.

The models showed large deflections, and the deflection of the lower flange was important in establishing the interlaminar stresses in the doubly curved laminate. It was not possible to analyse the models with non-linear geometry to account for a large deflection effect due to their size and a lack of computer resources. If this had been carried out, and if the non-linear geometry was important, then the stress levels in the delamination region could have reduced, affecting the failure prediction adversely.

The models of the I-beam specimens were 3-D and it was not feasible to produce a model which was as accurate to the specimens in terms of geometry as it was for the sandwich panels and the 'T'-pieces. The author is confident that a more conservative delamination prediction could be gained if the specimens were modelled accurately because the stress field would be more accurate to the specimens. The actual curvatures of the I-beam specimens in the central section were not perfectly circular, but flattened. The shape of the specimens locally has a significant effect on the stress levels, as shown in Chapters 6&7. Experience also shows that a tighter curvature in the laminates is likely to have led to higher interlaminar stress levels than those seen in a radial specimen.

Chapter 9

Conclusions

9.1 Main Achievements

A review of the currently available literature showed some shortcomings in the area of delamination prediction using stress-based methods. The most critical aspect was the lack of accuracy for most of the criteria already published (see Chapter 2 and Appendix B for further details).

A number of matrix dominated strength issues for laminated composite materials were identified. These were the stress in all directions in the matrix influencing delamination, the effect of volume on the strength of the material, the hydrostatic pressure influencing strength of polymers and the significance of thermal residual stresses in delamination prediction.

These factors were pulled into an integrated delamination failure prediction method. It is capable of predicting delamination in uni-directional and general laminates. This was achieved by creating the method so that it works internally at each ply in the compos-

ite. The method was coded using Fortran77 and interfaced with ABAQUS as a 'User Material', replacing the internal material behaviour routines.

The results from a series of scaled interlaminar tensile strength specimens were used to provide the interlaminar strength data for the method. The magnitude of the volume effect in the HTA/913C material was found to be equivalent to a 12% loss in strength for a doubling of the scale of the specimens. The equivalent strength of the matrix material for a unit volume of the composite was calculated to be 130.5MPa.

The method was then used to predict the inter-fibre failure of 'T'-piece specimens. The failure location was predicted accurately within the fill-in region for both the 5 and 10mm radius specimen designs. The predicted failure loads were both within 13% of the mean loads found in testing.

The delamination failure of three different designs of sandwich panel edge closure sections were analysed. The local geometry of the delamination region was found to be important in producing accurate failure load predictions. The difference in magnitude of some stress components in the 90° design was as much as 22% between the nominal geometry and a model based on the actual specimen geometry. Any discrepancy in the stress levels is of great concern to an engineer, the accurate modelling of geometry is therefore important in reliable failure prediction. The delamination prediction was only 1% out from the mean failure load in testing using the proposed method with an accurately modelled geometry.

The 30° specimens were made using two different manufacturing methods, precuring and cocuring the edge closure sections. The geometries of the designs were nominally the same, but stress levels once again were significantly different. The precured specimen geometry model showed approximately 20% lower stresses than the cocured model. Testing of the specimens did not reveal such a large difference in the strength of these specimens. The precured specimens suffered from a manufacturing problem due to slight dimensional mismatch between the precured edge closure and the aluminium honeycomb. This mis-

match caused a gap between the honeycomb and the edge closure which meant that the edge closure was not supported as much as was expected. This led to much higher stress levels in the delamination region, which were realised by altering the model to include this debonded region. The delamination predictions of these sandwich panel specimens were within 16% using the proposed method after correlation.

The final specimen design analysed using the proposed delamination prediction method was that of a tapered I-beam. These specimens delaminated in the doubly-curved laminates and provided a stern test for the accuracy of the method. Two specimens were manufactured, and because of a problem with the tooling, one beam had a thicker lower flange. This meant that each specimen required a separate model because of the difference in the stress levels at the same load case. The method predicted the delamination of the doubly-curved laminates accurately, with both predictions being within 13% of the failure loads.

The difference in geometry due to manufacturing variation is of great concern for engineering designers as it indicates the possible variation that can occur in manufacture. In any situation where components are made in large numbers, it would be prudent for the designer to make failure predictions based on the worst case scenario. This means using the geometry from a specimen which has the highest stress concentrations caused by manufacturing variation.

In conclusion, a stress-based method for predicting delamination in composite materials with general lay-ups has been developed. It takes into account factors which have been shown to be significant in delamination of composite materials, including the volume effect, in-plane stresses, thermal residual stresses and the hydrostatic pressure. It has been applied to a number of different specimen designs including dropped plies and curved geometry. In all cases it was shown to be accurate to within 16% of the failure load.

9.2 Further Work

The proposed method for predicting delamination has been shown to be accurate in predicting the delamination of structures made from HTA/913C carbon-fibre reinforced material. For the method to be widely accepted, it needs to be shown to be accurate in other materials. It is therefore suggested that structures made from other material systems be analysed and the delaminations predicted.

The issue of manufacturing variation has been highlighted within this thesis, and has been shown to be important in predicting the delamination of composite structures. This problem should be investigated further because delamination will be become more critical in composite structures as they are used closer to the limits of the material.

Bibliography

[1] Larsson, F. (1997): Damage Tolerance of a Stitched Carbon/Epoxy Laminate. Composites - Part A, Vol.28A, pp.923-934.

[2] Sun, C.T., Norman, T.L. (1990): Design of a Laminated Composite With Controlled-Damage Concept. Composites Science and Technology, Vol.39, pp.327-340.

[3] Wooh, S.C., Wei, C. (1999): High-Fidelity Ultrasonic Pulse-Echo Scheme for Detecting Delaminations in Composite Laminates. Composites - Part B, Vol.30, pp.433-441.

[4] Ball, R.J., Almond, D.P. (1998): Detection and Measurement of Impact Damage in Thick Carbon Fibre Reinforced Laminates by Transient Thermography. NDT&E International, Vol.31, pp.165-173.

[5] Hill, G.F.J., Wisnom, M.R., Jones, M.I. : Failure Prediction of Composite T-Piece Specimens. Proceedings of the 5th International Conference on Deformation and Fracture of Composites, March 1999, London, UK, pp.169-178.

[6] Hill, G.F.J., Wisnom, M.R., Jones, M.I. : The Design, Manufacture and Test of a Tapered Composite I-Beam. Proceedings of ICCM-12: The 12th International Conference on Composite Materials. July 1999, Paris, France.

[7] Hinton, M.J, Soden, P.D. (1998): Predicting Failure in Composite Laminates - The Background to the Exercise. Composites Science and Technology. Vol.58, pp.1001-1010.

[8] Soden, P.D., Hinton, M.J., Kaddour, A.S. (1998): A Comparison of the Predictive Capabilities of Current Failure Theories for Composite Laminates. Composites Science and Technology, Vol.58, pp.1225-1254.

[9] Qiaoa Yan, X., Du, S., Wang, D. (1991): J-Integral Criterion of Delamination Onset in Toughened Matrix Composite Laminates. Engineering Fracture Mechanics, VOl.40, pp.67-74.

[10] Sheinman, I., Kardomateas, G.A. (1997): Energy Release Rate and Stress Intensity Factors for Delaminated Composite Laminates. International Journal of Solids and Structures, Vol.34, pp.451-459.

[11] Shivakumar, K.N., Allen, H.G., Avva, V.S. (1994): Interlaminar Tension Strength of Graphite/Epoxy Composite Laminates. AIAA Journal Vol.32, pp.1478-1484.

[12] Bullock, R.E. (1974): Strength Ratios of Composite Materials in Flexure and in Tension. Journal of Composite Materials Vol.8, pp.200-206.

[13] O'Brien, T.K., Salpekar, S.A. (1993): Scale Effects on the Transverse Tensile Strength of Graphite/Epoxy Composites. ASTM STP 1206, pp.23-52.

[14] Wisnom, M.R., Jones, M.I. (1996): Size Effects in Interlaminar Tensile and Shear Strength of Unidirectional Glass Fibre/Epoxy. Journal of Reinforced Plastics and Composites Vol.15, pp.2-15.

[15] Sutherland, L.S., Shenoi, R.A., Lewis, S.M. (1999): Size and Scale Effects in Composites: I. Literature Review. Composite Science and Technology, Vol. 59, pp. 209-220.

[16] Zweben, C. (1994): Is There a Size Effect in Composites? Composites Vol.25, pp.451-.

[17] Weibull, W. (1951): A Statistical Distribution Function of Wide Applicability. Journal of Applied Mechanics 18, pp.293-297.

[18] Cui, G. Y., Ruiz, C. (1995): Through-thickness failure of laminated carbon/epoxy composites under combined stress. Composites Science and Technology, Vol.53, pp. 253-258.

[19] Cui, W.C., Wisnom, M.R., Jones, M. (1992): A Comparison of Failure Criteria to Predict Delamination of Unidirectional Glass/Epoxy Specimens Waisted Through the Thickness. Composites Vol.23, pp.158-166.

[20] Fenske, M.T., Vizzini, A.J. (1998): The Inclusion of In-Plane Stresses in Delamination Criteria. Collection of Technical Papers - AIAA/ASME/ASCE/AHS/ASC Structures, Structural Dynamics & Materials Conference, Vol1, pp.372-382. Paper no. AIAA-98-1743.

[21] Rotem, A. (1998): Prediction of Laminate Failure with the Rotem Failure Criterion. Composites Science and Technology, Vol.58, pp.1083-1094.

[22] Whitney, W., Andrews, R.D. (1967): . Journal of Polymer Science (C), Vol.16, p.2981.

[23] Bauwens, J.C. (1970): . Journal of Polymer Science (A-2), Vol.8, p.893.

[24] Rhee, K.Y., Pae, K.D. (1995): Effects of Hydrostatic Pressure on the Compressive Properties of Laminated 0 Unidirectional, Graphite Fiber/Epoxy Matrix Thick- Composite. Journal of Composite Materials Vol.29, pp.1295-1307.

[25] Shin, E.S., Pae, K.D., (1992): Effects of Hydrostatic Pressure on the Torsional Shear Behaviour of Graphite/Epoxy Composites. Journal of Composite Materials Vol.26, pp.462-485.

[26] Shin, E.S., Pae, K.D. (1992): Effects of Hydrostatic Pressure on In-Plane Shear Properties of Graphite/Epoxy Composites. Journal of Composite Materials Vol.26, pp.828-868.

[27] Hoppel, C.P.R., Bogetti, T.A, Gillespie, J.W. (1995): Literature Review - Effects of Hydrostatic Pressure on the Mechanical Behavior of Composite Materials. Journal of Thermoplastic Composite Materials, Vol.8, pp.375-409.

[28] de Kok, J.M.M., Meijer, H.E.H. (1999): Deformation, Yield and Fracture of Unidirectional Composites in Transverse Loading 1. Influence of Fibre Volume Fraction and Test-Temperature. Composites: Part A, Vol.30, pp.905-916.

[29] Wisnom, M.R., Reynolds, T., Gwilliam, N. (1996): Reduction in Interlaminar Shear Strength by Discrete and Distributed Voids. Composites Science and Technology, Vol.56, pp.93-101.

[30] Puppo, A.H., Evenson, H.A. (1970): Interlaminar Shear in Laminated Composites Under Generalized Plane Stress. Journal of Composite Materials, Vol.4, pp.204-220.

[31] Azzi, V.D., Tsai, S.W. (1965): Anisotropic Strength of Composites. Proceedings of the Society for Experimental Stress Analysis, Vol.22, pp.283-288.

[32] Tsai, S. W., Wu, E. M. (1971): A General Theory of Strength for Anisotropic Materials. Journal of Composite Materials, Vol.5, pp. 58-80.

[33] Vizzini, A. J., Lee, S. W. (1995): Damage Analysis of Composite Tapered Beams. Journal of the American Helicopter Society, Vol.40, pp. 43-49.

[34] Waddoups, M.E. (1968): Characterization and Design of Composite Materials, Composite Materials Workshop, S.W. Tsai, J.C. Halpin and N.J. Pagano, Eds., Technomic, p.254.

[35] Hashin, Z. (1980): Failure Criteria for Unidirectional Fiber Composites. Journal of Applied Mechanics, Vol.47, pp. 329-334.

[36] Altus, E., Dorogoy, A. (1989): A Three-Dimensional Study of Delamination. Eng. Frac. Mech., Vol.33, pp. 1-19.

[37] Brewer, J.C., Legace, P.A. (1988): Quadratic Stress Criterion for Initiation of Delamination. Journal of Composite Materials, Vol.22, pp.1141-1155.

[38] Christensen, R.M. (1996): Stress-Based Yield/Failure Criteria for Fibre Composites. International Journal of Solids and Structures, Vol.34, pp.529-543.

[39] Hashin, Z., Rotem, A. (1973): A Fatigue Failure Criterion for Fiber Reinforced Materials. Journal of Composite Materials, Vol.7, pp.448-464.

[40] Puck, A., Schürmann, H. (1998): Failure Analysis of FRP Laminates by Means of Physically Based Phenomenological Models. Composites Science and Technology, Vol.58, pp.1045-1067.

[41] Wisnom, M.R., Petrossian, Z.J., Jones, M.I. (1996): Interlaminar Failure of Unidirectional Glass/Epoxy Due to Combined Through Thickness Shear and Tension. Composites - Part A: Applied Science and Manufacturing, Vol.27, pp.921-929.

[42] Whitney, J. M., Nuismer, R. J. (1974): Stress Fracture Criteria for Laminated Composites Containing Stress Concentrations. Journal of Composite Materials, Vol.8, pp. 253-365.

[43] Kim, R. Y., Soni, S. R. (1984): Experimental and Analytical Studies on the Onset of Delamination in Laminated Composites. Journal of Composite Materials, Vol.18, pp. 70-80.

[44] Fish, J. C., Lee, S. W. (1989): Delamination of Tapered Composite Structures. Eng. Frac. Mech., Vol.34, pp. 43-54.

[45] Griffith, A. A. (1920): The Phenomena of Rupture and Flaw in Solids. Transactions, Royal Society of London, Series A, Vol. 221, pp. 163-198.

[46] Irwin, G. R. (1958): Fracture. Handbuch der Physik, Vol.6, p. 551.

[47] Rybicki, E. F., Kanninen, M. F. (1977): A Finite Element Calculation of Stress Intensity Factors by a Modified Crack Closure Integral. Eng. Frac. Mech., Vol.9, pp. 931- 938.

[48] Johnson, W. S. (1987): Stress Analysis of the Cracked-Lap-Shear Specimen: An ASTM Round-Robin. J. of Test and Eval., Vol.15, pp. 303-324.

[49] Rybicki, E. F., Schmueser, D. W., Fox, J. (1977): An Energy Release Rate Approach for Stable Crack Growth in the Free-Edge Delamination Problem. Journal of Composite Materials, Vol.11, pp. 470-487.

[50] O'Brien, T. K. (1982): Characterization of Delamination Onset and Growth in a Composite Laminate. ASTM STP 775, pp. 140-167.

[51] Nicholls, D. J., Gallagher, J. P. (1983): Determination of G_{IC} in Angle Ply Composites Using a Cantilever Beam Test Method, Journal of Reinforced Plastics and Composites, Vol.2, pp.2-17.

[52] Robinson, P., Song, D. Q. (1992): A Modified DCB Specimen for Mode I Testing of Multidirectional Laminates. Journal of Composite Materials, Vol.26, pp.1554-1577.

[53] Jurf, R. A., Pipes, R. B. (1982): Interlaminar Fracture of Composite Materials. Journal of Composite Materials, Vol.16, pp. 386-394.

[54] Rhee, K. Y. (1994): Characterization of Delamination Behaviour of Unidirectional Graphite/PEEK Laminates Using Cracked Lap Shear (CLS) Specimens. Composite Structures, Vol.29, pp. 379-382.

[55] Law, G. E. (1984): Mixed-Mode Fracture Analysis of (?25/90n)s Graphite/Epoxy Composite Laminates. ASTM STP 836, pp. 143-160.

[56] Hwu, C., Kao, C. J., Chang, L. E. (1995): Delamination Fracture Criteria for Composite Laminates. Journal of Composite Materials, Vol.15, pp. 1962-1987.

[57] Greenhalgh, E., Asp, L., Singh, S. (1999): Delamination Resistance, Failure Criteria and Fracture Morphology of 0/0, 0/5 and 0/90 Ply Interfaces in CFRP. Proceedings of the 5th International Conference on Deformation and Fracture of Composites, March 1999, London, UK.

[58] Zhou, S. G., Sun, C. T. (1990): Failure Analysis of Composite Laminates with Free Edge. Journal of Composite Technology and Research, Vol.12, pp. 91-97.

[59] Minguet, P.J., O'Brien, T.K. (1995): Analysis of Composite Skin/Stringer Bond Failure Using a Strain Energy Release Rate Approach. Proceedings of ICCM-10, Whistler, Canada.

[60] Theotokoglou, E.E., Moan, T. (1996): Experimental and Numerical Study of Composite T-Joints. Journal of Composite Materials, Vol.30, pp.190-209.

[61] Li, J., O'Brien, T.K., Rousseau, C.Q. (1997): Test and Analysis of Composite Hat Stringer Pull-Off Test Specimens. American Helicopter Society Journal, Vol.42, pp.350-357.

[62] Wisnom, M.R., Petrossian, Z.J., Jones, M.I. (1996): Interlaminar Failure of Unidirectional Glass/Epoxy due to Combined Through Thickness Shear and Tension. Composites Part A Vol.27A, pp.921-929.

[63] Raghava, R. S., Caddell, R. M. (1973): The Macroscopic Yield Behaviour of Polymers. Journal of Materials Science, Vol.8, pp. 225-232.

[64] Young, W. C. (1989): Roark's Formulas for Stress and Strain, 6^{th} Edition. McGraw-Hill Publishing Company. ISBN 0071003738.

[65] Hexcel Composites, Duxford, Cambridge, CB2 4QD, UK.

[66] Adams, R. D. (1989): Strength Predictions for Lap Joints, Especially with Composite Adherends: A Review. Journal of Adhesion Vol.30, pp.219-242.

[67] Wisnom, M.R. (1996): 3-D Finite Element Analysis of Curved Beams in Bending. Journal of Composite Materials Vol.30, pp.1178-1190.

[68] Yoshida, H., Ogasa T., Hayashi, R. (1986): Statistical Approach to the Relationship Between ILSS and Void Content of CFRP. Composites Science and Technology, Vol.25, pp3-18.

[69] Tang, J.M., Lee, W.I., Springer, G.S. (1987): Effects of Cure Pressure on Resin Flow, Voids and Mechanical Properties. Journal of Composite Materials, Vol21, pp.421-440.

[70] Hibbit, Karlsson and Sorenson, Inc., 1080 Main Street, Pawtucket, RI 02860, U.S.A.

[71] Microsoft Excel97, Microsoft Corporation, One Microsoft Way, Redmond, WA 98052-6399, U.S.A.

[72] Fortran77, MIPSpro F77 Compiler for IRIX Systems.

[73] Vinson, J.R., Sierakowski, R.L. (1986): The Behaviour of Structures Composed of Composite Materials. Martinus Nijhoff Publishers, Dordrecht. pp.43-49.

[74] British Aerospace Airbus Ltd, Carbon T300 Fibre with 924 Resin System: BAER 3212, Ref.: GEN/B0500/04086, February 1993, pp.1.2.2.1-2.

[75] Shenoi, R.A., Hawkins, G.L. (1992): Influence of Material and Geometry Variations on the Behaviour of Bonded Tee Connections in FRP Ships. Composites, Vol.23, pp.335-345.

[76] Rispler, A.R., Steven, G.P., Tong, L. (1997): Failure Analysis of Composite T-Joints Including Inserts. Journal of Reinforced Plastics and Composites, Vol.16, pp.1642-1658.

[77] Cope, R.D., Pipes, R.B. (19): Design of the Composite Spar-Wingskin Joint. Journal of Composites, Vol.13, pp.47-53.

[78] 3M United Kingdom plc, 3M House 28, Great Jackson Street, Manchester, Lancashire, M15 4PA.

[79] I-DEAS Master Series, Structural Dynamics Research Corporation, 2000Eastman Drive, Milford, Ohio 45150, U.S.A.

[80] Allen, H.G. (1969): Analysis and Design of Structural Sandwich Panels. Pergamon Press, Oxford, UK.

[81] Teti, G.C.R (1989): Sandwich Structures Handbook. Il Prato, Padua, Italy.

[82] Kim, C.G., Jun, E.J., (1992): Impact Resistance of Composite Laminated Sandwich Plates. Journal of Composite Materials, Vol.26, pp.2247-2262.

[83] Lin, C.C., Cheng, S.H., Wang, J.T.S. (1996): Local Buckling of Delaminated Composite Sandwich Plates. AIAA Journal, Vol.34, pp.2176-2183.

[84] Kim, W.C., Miller, T.C., Dharan, C.K.H. (1993): Strength of Composite Sandwich Panels Containing Debonds. International Journal of Solids and Structures, Vol.30, pp.211-223.

[85] Frostig, Y. (1993): On Stress Concentration in the Bending of Sandwich Beams With Transversely Flexible Core. Composite Structures, Vol.24, pp.161-169.

[86] Gürdal, Z., Tomasino, A.P., Biggers, S.B. (1991): Effects of Processing Induced Defects on Laminate Response: Interlaminar Tensile Strength. SAMPE Journal, Vol.27, pp.39-49.

Appendix A

Humpback Bridge Specimen Data and Test Results

This Appendix contains humpback bridge specimen dimension and test result data in a series of tables. These are labelled as follows:

APPENDIX A. HUMPBACK BRIDGE SPECIMEN DATA AND TEST RESULTS

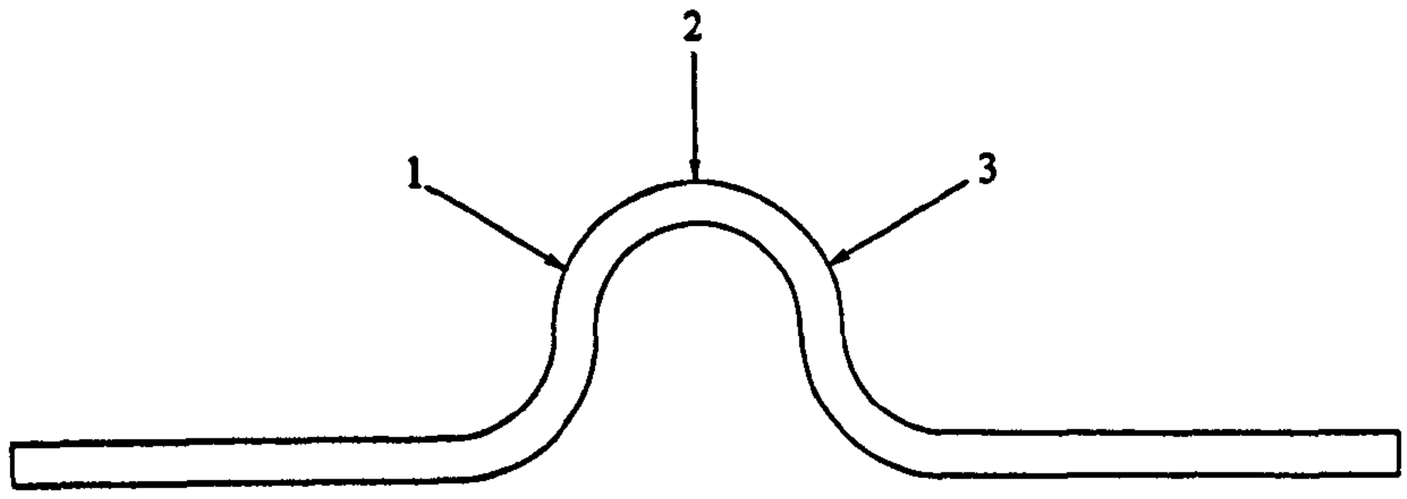

Figure A.1: Humpback Bridge Specimen Measurement Positions

Specimen no.	Position 1	Position 2	Position 3
1	1.96	1.98	1.99
2	2.02	2.03	2.07
3	1.97	1.97	1.98
4	2.03	2.02	2.06
5	2.01	1.99	2.03
6	2.03	2.01	2.08
7	1.97	2.01	2.01
8	1.98	1.98	2.02
9	2.03	2.06	2.06
10	2.02	2.03	2.06

Table A.1: 16-Ply Humpback Bridge Specimen Thickness Data (mm)

Specimen no.	Position 1	Position 2	Position 3
1	5.085	5.10	5.10
2	5.06	5.065	5.065
3	5.02	5.005	5.025
4	5.09	5.09	5.085
5	5.005	5.005	4.995
6	4.975	4.975	4.975
7	5.00	5.00	5.015
8	5.09	5.09	5.09
9	5.07	5.075	5.07
10	5.01	5.005	5.015

Table A.2: 16-Ply Humpback Bridge Specimen Width Data (mm)

Test no.	Max. Load(N)
1	511
2	450
3	482
4	443
5	476
6	486
7	487
8	503
9	518
10	515
Mean	487 c.v. 5.31%

Table A.3: 16-Ply Humpback Bridge Specimen Test Data

Specimen no.	Position 1	Position 2	Position 3
1	4.15	4.22	4.13
2	4.18	4.29	4.20
3	4.22	4.29	4.24
4	4.27	4.33	4.22
5	4.19	4.25	4.19
6	4.25	4.33	4.24
7	4.05	4.09	4.08
8	4.15	4.15	4.09
9	4.23	4.28	4.18
10	4.19	4.20	4.19

Table A.4: 32-Ply Humpback Bridge Specimen Thickness Data (mm)

Specimen no.	Position 1	Position 2	Position 3
1	10.075	10.085	10.07
2	10.025	10.035	10.025
3	10.055	10.06	10.05
4	10.06	10.055	10.05
5	10.11	10.115	10.11
6	10.03	10.04	10.03
7	10.085	10.09	10.08
8	10.05	10.06	10.065
9	9.97	9.985	9.985
10	10.03	10.03	10.03

Table A.5: 32-Ply Humpback Bridge Specimen Width Data (mm)

Test no.	Max. Load(N)
1	1809
2	1851
3	2053
4	2166
5	1458
6	2161
7	1721
8	1912
9	2083
10	1902
Mean	1912 c.v.11.5%

Table A.6: 32-Ply Humpback Bridge Specimen Test Data

Specimen no.	Position 1	Position 2	Position 3
1	8.503	8.420	8.477
2	8.877	8.884	8.858
3	8.700	8.687	8.700
4	8.852	8.814	8.858
5	8.858	8.839	8.839

Table A.7: 64-Ply Humpback Bridge Specimen Thickness Data (mm)

Specimen no.	Position 1	Position 2	Position 3
1	20.015	20.015	20.02
2	20.07	20.085	20.09
3	20.07	20.07	20.075
4	20.015	20.015	20.02
5	20.065	20.075	20.07

Table A.8: 64-Ply Humpback Bridge Specimen Width Data (mm)

Test no.	Max. Load(N)
1	6592
2	6439
3	6439
4	7501
5	7269
Mean	6848 c.v. 7.32%

Table A.9: 64-Ply Humpback Bridge Specimen Test Data

Specimen no.	Position 1	Position 2	Position 3
1	4.23	4.28	4.22
2	4.22	4.30	4.20
3	4.19	4.22	4.16
4	4.23	4.28	4.23
5	4.21	4.24	4.22
6	4.14	4.19	4.14

Table A.10: Non-UD Humpback Bridge Specimen Thickness Data (mm)

Specimen no.	Position 1	Position 2	Position 3
1	20.08	20.10	20.09
2	20.08	20.095	20.085
3	18.735	18.735	18.73
4	20.07	20.09	20.07
5	20.09	20.10	20.08
6	20.065	20.095	20.075

Table A.11: Non-UD Humpback Bridge Specimen Width Data (mm)

Test no.	Max. Load(N)
1	3513
2	3621
3	2871
4	3816
5	3611
6	3716
Mean	3525 c.v. 9.54%

Table A.12: Non-UD Humpback Bridge Specimen Test Data

Appendix B

Failure Criteria Comparison

A comparison of this method with other failure criteria is presented in Table B. The Puck inter-fibre failure criterion [40] and a modified and degraded form of the Tsai failure criterion were used and are shown in Equations (B.1&B.2). The Puck criterion used here utilises only 2 stress components for the prediction, the interlaminar tension and either of the interlaminar shear values. The version of the Tsai criterion used here can utilise three stress components to predict failure, and can be extended to employ more quite simply. The strength values were based on the largest of the interlaminar strength specimens. Therefore the interlaminar tensile strength was 88MPa and the interlaminar shear strength was 90MPa. The transverse tensile strength was taken to be the same as the interlaminar tensile strength by assuming transverse isotropy. The two published criteria were applied to the elements with the highest individual interlaminar stress values, the highest overall result is quoted in the table. The thermal residual stress values from FE analysis were also included for a fair comparison.

$$\sqrt{\left(\frac{\tau_{13}}{S_{13}}\right)^2 + \left(1 - P_F\left(\frac{Z}{S_{13}}\right)\right)^2 \left(\frac{\sigma_{33}}{Z}\right)} + P_F\left(\frac{\sigma_{33}}{S_{13}}\right) = 1 \qquad \text{(B.1)}$$

$$\left(\frac{\sigma_{22}}{Y}\right)^2 - \left(\frac{\sigma_{22}\sigma_{33}}{Y^2}\right) + \left(\frac{\sigma_{33}}{Z}\right)^2 + \left(\frac{\tau_{23}}{S_{23}}\right)^2 = 1 \qquad \text{(B.2)}$$

Where : τ = Shear stress component

σ = Direct stress component

S = Shear strength of material

Y = Transverse in-plane tensile strength of material

Z = Interlaminar tensile strength of material

P_F = Stress interaction factor taken from failure envelope in the relevant plane. Calculated as the negative slope of the envelope at $\sigma_{22} = 0$. In this case it was assumed to be 0.1, the result was not particularly sensitive to this value. When the value was varied from 0.3 to 0.1, the failure values varied by less than 2% from those given.

The Tsai criterion was seen to be very conservative on the first four specimens, so the final comparison was not made. This sort of result was expected as it was created with conservative design in mind. The Puck Inter-Fibre Failure criterion produced some good predictions of the failure load. The pre-cured 30° sandwich panel showed a limitation in its formulation, however. It predicted failure at a very small region of high shear stress, whereas the proposed method took into account the small affected volume and the impact of the high stress was reduced, improving the prediction.

Overall, the proposed method is more consistent than Puck's method because it can take account of the effect of small stressed volumes of material. This makes it more reliable in its application and should be investigated with other material systems than the HTA/913C.

Specimen Type	Tsai	Puck	Proposed Method	Test Result (N/mm)
10mm T-Piece	144	174	167	193
5mm T-Piece	90	105	102	113
90° Sandwich Panel	45	54	59	58
Pre-Cured 30° Sandwich Panel with 14mm debond	95	116	146	158
0±45 Humpback Bridge	N/A	161	156	177

Table B.1: A Comparison of the Proposed Delamination Prediction Method with Other Published Criteria

Appendix C

User Material Code

The Fortran77 code included in this section is that which is used in 2-dimensional plane strain analysis of composite structures.

```
*USER SUBROUTINE
      SUBROUTINE UMAT(STRESS,STATEV,DDSDDE,SSE,SPD,SCD,
     1 RPL,DDSDDT,DRPLDE,DRPLDT,
     2 STRAN,DSTRAN,TIME,DTIME,TEMP,DTEMP,PREDEF,DPRED,MATERL,
     3 NDI,NSHR,NTENS,NSTATV,PROPS,NPROPS,COORDS,DROT,PNEWDT,
     4 CELENT,DFGRD0,DFGRD1,NOEL,NPT,LAYER,KSPT,KSTEP,KINC)
C
      INCLUDE 'ABA\_PARAM.INC'
C
      CHARACTER*8 MATERL
C
      DIMENSION STRESS(NTENS),STATEV(NSTATV),
     1 DDSDDE(NTENS,NTENS),DDSDDT(NTENS),DRPLDE(NTENS),
     2 STRAN(NTENS),DSTRAN(NTENS),TIME(2),PREDEF(1),DPRED(1),
     3 PROPS(NPROPS),COORDS(3),DROT(3,3),DFGRD0(3,3),DFGRD1(3,3)
C
C MY CODE HERE
C
      DIMENSION DS(6),EFFSTR(6),STRSOLD(6),PS(3),RAGSTR(2),LOCSTRN(6),
     1 LOCSTRS(6),GSTRAN(6),JACOB(6,6),LOCSTRN2(6),LOCSTRS2(6)
C
      DOUBLE PRECISION DS,STRSOLD,PS,VAL,A,B,C,RAGSTR,EFFSTR,PROPS,
     1 E1,E2,E3,G12,G13,G23,V12,V21,V13,V31,V23,V32,V,SCALE,FIBREANG,
     2 LOCSTRN,LOCSTRS,GSTRAN,JACOB,Q11,Q12,Q13,Q22,Q23,Q33,Q44,Q55,Q66,
     3 QBAR11,QBAR12,QBAR13,QBAR16,QBAR22,QBAR23,QBAR26,QBAR33,QBAR36,
     4 QBAR44,QBAR45,QBAR55,QBAR66,M,N,LOCSTRN2,LOCSTRS2,SWAPVAL
C
C PROPS VALUES ARE AS FOLLOWS
C
C 1 E1
C 2 E2,E3
C 3  V12,V13
C 4 V23
C 5 G12,G13
C 6 G23
C 7 ANGLE
C 8 SCALE VALUE
```

```
C
C PULL IN OLD STRESS VALUES
C
      DO M=1,6
        STRSOLD(M)=STRESS(M)
      END DO
C
C PULL IN LOCAL PROPERTIES AND ANGLE/SCALE
C
      E1=PROPS(1)*1.
      E2=PROPS(2)*1.
      V12=PROPS(3)*1.
      V23=PROPS(4)*1.
      G12=PROPS(5)*1.
      G23=PROPS(6)*1.
      FIBREANG=-PROPS(7)*3.14159265359/180.
      SCALE=PROPS(8)*1.
C
C CALCULATE OTHER VALUES FOR ELASTIC JACOBIAN GLOBAL
C
      E3=E2
      V13=V12
      G13=G12
      V21=1.*V12*E2/E1
      V31=1.*V13*E3/E1
      V32=1.*V23*E3/E2
      V=(1.-V12*V21-V13*V31-V23*V32-2.*V21*V13*V32)
C
C CALCULATE VALUES INTO DDSDDE/JACOBIAN
C
C USES GENERAL CONSTITUTIVE STIFFNESS MATRIX CONVENTION
C
C QXX VALUES ARE LOCAL PLY PROPERTIES
C
      Q11=E1*(1-V23*V32)/V
      Q12=(V21+V31*V23)*E1/V
      Q13=(V31+V21*V32)*E1/V
      Q22=E2*(1-V31*V13)/V
      Q23=(V32+V12*V31)*E2/V
      Q33=E3*(1-V12*V21)/V
      Q44=G23
      Q55=G13
      Q66=G12
C
C QBARXX VALUES ARE GLOBAL LAMINATE PROPERTIES
C
      M=COS(FIBREANG)
      N=SIN(FIBREANG)
      QBAR11=Q11*M**4.+2.*(Q12+2.*Q66)*M**2.*N**2.+Q22*N**4.
      QBAR12=(Q11+Q22-4.*Q66)*M**2.*N**2.+Q12*(M**4.+N**4.)
      QBAR13=Q13*M**2.+Q23*N**2.
C      QBAR16=-M*N**3.*Q22+M**3.*N*Q11-M*N*(M**2.-N**2.)*(Q12+2.*Q66)
      QBAR22=Q11*N**4.+2.*(Q12+2.*Q66)*M**2.*N**2.+Q22*M**4.
      QBAR23=N**2.*Q13+M**2.*Q23
C      QBAR26=-M**3.*N*Q22+M*N**3.*Q11+M*N*(M**2.-N**2.)*(Q12+2.*Q66)
      QBAR33=Q33
C      QBAR36=(Q13-Q23)*M*N
      QBAR44=Q44*M**2.+Q55*N**2.
      QBAR45=(Q55-Q44)*M*N
      QBAR55=Q55*M**2.+Q44*N**2.
      QBAR66=(Q11+Q22-2.*Q12)*M**2.*N**2.+Q66*(M**2.-N**2.)**2.
C
C PUT ZERO VALUES IN JACOBIAN GLOBAL 4x4 matrix for plane strain
C X Y Z XY
      DO N=1,NTENS
        DO M=1,NTENS
          DDSDDE(M,N) = 0.
        END DO
      END DO
C
C VALUES INTO DDSDDE - USES ABAQUS STIFFNESS CONVENTION
C
      DDSDDE(1,1)=QBAR11
      DDSDDE(1,2)=QBAR13
      DDSDDE(1,3)=QBAR12
      DDSDDE(2,1)=QBAR13
      DDSDDE(2,2)=QBAR33
      DDSDDE(2,3)=QBAR23
      DDSDDE(3,1)=QBAR12
      DDSDDE(3,2)=QBAR23
      DDSDDE(3,3)=QBAR22
```

```
      DDSDDE(4,4)=QBAR55
C
C CALCULATE STRESS INCREMENT calc DDSDDE*dstran
C
      DO N=1,NTENS
        VAL=0.
        DO M=1,NTENS
          VAL=VAL+DDSDDE(M,N)*DSTRAN(M)
        END DO
        DS(N)=VAL
C
C  AND THE TOTAL STRESS VALUE AT END OF THIS INCREMENT
C
        STRESS(N)=DS(N)+STRSOLD(N)
      END DO
C
C CALCULATE TOTAL LOCAL STRAIN VALUES
C
      DO N=1,NTENS
        GSTRAN(N)=STRAN(N)+DSTRAN(N)
      END DO
C
      M=COS(FIBREANG)
      N=SIN(FIBREANG)
      LOCSTRN(1)=M**2.*GSTRAN(1)+N**2.*GSTRAN(3)
      LOCSTRN(2)=N**2.*GSTRAN(1)+M**2.*GSTRAN(3)
      LOCSTRN(3)=GSTRAN(2)
      LOCSTRN(4)=M*GSTRAN(4)
C
C NEED TO DO IT TWICE FOR 45DEG
C
      IF (PROPS(7).EQ.45.) THEN
        M=COS(-FIBREANG)
        N=SIN(-FIBREANG)
        LOCSTRN2(1)=M**2.*GSTRAN(1)+N**2.*GSTRAN(3)
        LOCSTRN2(2)=N**2.*GSTRAN(1)+M**2.*GSTRAN(3)
        LOCSTRN2(3)=GSTRAN(2)
        LOCSTRN2(4)=M*GSTRAN(4)
      END IF
C
C CALCULATE LOCAL STRESS VALUES WITH SCALE FACTOR
C       IN THE FIBRE DIRECTION
C
C PUT ZERO VALUES IN JACOBIAN LOCAL
C
      DO N=1,NTENS
        DO M=1,NTENS
          JACOB(M,N) = 0.
        END DO
      END DO
C
C CALCULATE VALUES INTO JACOB/JACOBIAN
C
      JACOB(1,1)=Q11
      JACOB(1,2)=Q12
      JACOB(1,3)=Q13
      JACOB(2,1)=Q12
      JACOB(2,2)=Q22
      JACOB(2,3)=Q23
      JACOB(3,1)=Q13
      JACOB(3,2)=Q23
      JACOB(3,3)=Q33
      JACOB(4,4)=Q55
C
C CALCULATE LOCAL STRESS TOTAL jacobian*GSTRAN
C
      DO N=1,NTENS
        VAL=0.
        DO M=1,NTENS
          VAL=VAL+JACOB(M,N)*LOCSTRN(M)
        END DO
        LOCSTRS(N)=VAL
      END DO
C
C NEED TO SWAP 2 AND 3 TO GET LOCSTRS(4) SHEAR
C       VALUE IN CORRECT PLANE
C
      SWAPVAL=LOCSTRS(3)
      LOCSTRS(3)=LOCSTRS(2)
      LOCSTRS(2)=SWAPVAL
C
```

```
      LOCSTRS(1)=LOCSTRS(1)*SCALE
      LSTR=1
      CALL SPRINC(LOCSTRS,PS,LSTR,NDI,NSHR)
C
C CALCULATE RAGHAVA STRESS
C
      A=2.6
      B=-0.6*(PS(1)+PS(2)+PS(3))
      C=-((PS(1)-PS(2))**2.+(PS(2)-PS(3))**2.+(PS(3)-PS(1))**2.)
      RAGSTR(1)=(-B+SQRT(B*B-4.*A*C))/(2.*A)
      RAGSTR(2)=(-B-SQRT(B*B-4.*A*C))/(2.*A)
C
C AND AGAIN IF 45deg CALCULATE LOCAL STRESS
C        TOTAL jacobian*GSTRAN
C
      IF (PROPS(7).EQ.45.) THEN
        DO N=1,NTENS
          VAL=0.
          DO M=1,NTENS
            VAL=VAL+JACOB(M,N)*LOCSTRN2(M)
          END DO
          LOCSTRS2(N)=VAL
        END DO
C
C NEED TO SWAP 2 AND 3 TO GET LOCSTRS(4) SHEAR
C       VALUE IN CORRECT PLANE
C
        SWAPVAL=LOCSTRS2(3)
        LOCSTRS2(3)=LOCSTRS2(2)
        LOCSTRS2(2)=SWAPVAL
C
        LOCSTRS2(1)=LOCSTRS2(1)*SCALE
        LSTR=1
        CALL SPRINC(LOCSTRS2,PS,LSTR,NDI,NSHR)
C
C CALCULATE RAGHAVA STRESS
C
        A=2.6
        B=-0.6*(PS(1)+PS(2)+PS(3))
        C=-((PS(1)-PS(2))**2.+(PS(2)-PS(3))**2.+(PS(3)-PS(1))**2.)
        RAGSTR(2)=(-B+SQRT(B*B-4.*A*C))/(2.*A)
      END IF
C
C DUMP OUT STATE VARIABLES
C
      DO N=1,3
        STATEV(N)=PS(N)
      END DO
      STATEV(4)=RAGSTR(1)
      STATEV(5)=RAGSTR(2)
      DO N=1,4
        STATEV(N+5)=LOCSTRN(N)
      END DO
C
C DONE
C
C MY CODE ENDS HERE
C
      RETURN
      END
```

Appendix D

Post-Processing Code

The Fortran77 code for post-processing the Raghava stress output is included here. The output .fil file from abaqus must be renamed RESULTS.fil in order for the code to work.

```
      PROGRAM  Calculate UVES Result
C
      INCLUDE 'aba_param.inc'
      DIMENSION  ARRAY(513), JRRAY(NPRECD,513), RESARRAY(150000,3,15)
      EQUIVALENCE (ARRAY(1), JRRAY(1,1))
C
C
      INTEGER  LRUNIT(2,1),LUNIT(10),ELNO,STEPNO
      CHARACTER  FNAME*80
C
      WRITE(6,*) 'This program pulls in a results file'
      WRITE(6,*) 'MAX ELEMENT NUMBER 150000, MAX STEP NO 10.'
      NRU=1
C
C
      WRITE(6,*) 'and outputs the RAGHAVA stress Weibull total'
      LRUNIT(1,1)=8
   42 CONTINUE
      LRUNIT(2,1)=2
   45 CONTINUE
      LOUTF=0
C
C  Filename of results file is RESULTS.fil
C
      FNAME='RESULTS'
C
      CALL INITPF(FNAME, NRU, LRUNIT, LOUTF)
C
      JUNIT =8
      CALL DBRNU(JUNIT)
C
C  Read up to 10 million records for safety reasons
C
      STEPNO=1
      PNTELE=0
      PNTRAG=0
      PNTEVOL=0
```

```
      DO 80 IXX2 = 1, 100
      DO 80 IXX = 1, 99999
         CALL DBFILE(0,ARRAY,JRCD)
         IF (JRRAY(1,2).EQ.2000) THEN
           STEPNO=JRRAY(1,8)
           PNTELE=0
           PNTRAG=0
           PNTEVOL=0
         ENDIF
         IF (JRRAY(1,2).EQ.1) THEN
           PNTELE=PNTELE+1
           ELNO=JRRAY(1,3)
           RESARRAY(PNTELE,1,STEPNO)=ELNO
         ENDIF
         IF (JRRAY(1,2).EQ.5) THEN
           PNTRAG=PNTRAG+1
           RAG=ARRAY(6)
           RESARRAY(PNTRAG,2,STEPNO)=RAG
         ENDIF
         IF (JRRAY(1,2).EQ.78) THEN
           PNTEVOL=PNTEVOL+1
           EVOL=ARRAY(3)
           RESARRAY(PNTEVOL,3,STEPNO)=EVOL
         ENDIF
         IF (JRCD .NE. 0) THEN
           GOTO 110
         ENDIF
   80    CONTINUE
  100 CONTINUE
  110 CONTINUE
C
C SUM THE WEIBULL VALUES
C
      WRITE(6,*)'Enter volume multiplier'
      READ(5,*) VOL
      DO STEPNO=1,14
        WEIBULLSUM=0.D0
        DO ELNO=0,150000
          WEIBULL=RESARRAY(ELNO,3,STEPNO)*VOL*(RESARRAY(ELNO,2,STEPNO)
     1 **18.1)
          WEIBULLSUM=WEIBULLSUM+WEIBULL
C          WRITE(6,*)' ',RESARRAY(ELNO,1,STEPNO),RESARRAY(ELNO,2,STEPNO)
C     1 ,RESARRAY(ELNO,3,STEPNO)
        END DO
        WEIBULL=WEIBULLSUM**(1/18.1)
        WRITE(6,*) 'STEP ',STEPNO,' WEIBULL ',WEIBULL
      END DO
      STOP
      END
```

Appendix E

Example Input File

This Appendix shows the an example ABAQUS input deck which uses the proposed delamination prediction method. This particular example is taken from the 0/±45° humpback bridge specimens slice model. The critical part is that which defines the MATERIAL for each element.

```
*HEADING
SLICE MODEL OF HUMPBACK BRIDGE SPECIMEN - 0/45 DEGREE 20mm WIDTH
**
** NODES ON AE
**
*NODE
1,8.,0.,0.
101,8.,0.5,0.
201,8.,1.,0.
**
** NODES ON BF
**
*NODE
33,12.2,0.,0.
133,12.2,0.5,0.
233,12.2,1.,0.
**
** NODES ON AB
**
*NGEN,NSET=NODESAB
1,33,1
**
** NODES ON EF
**
*NGEN,NSET=NODESEF
201,233,1
**
** MIDSIDE NODES ON FACE ABFE
**
*NGEN,NSET=MIDABFE
101,133,2
**
```

```
** NODES FOR GENERATING THE REST
**
*NCOPY,OLD SET=NODESAB,SHIFT,NEW SET=NODESCD,CHANGE NUMBER=50000
0.,0.,10.
0.,0.,0.,1.,1.,1.,0.
*NCOPY,OLD SET=NODESEF,SHIFT,NEW SET=NODESGH,CHANGE NUMBER=50000
0.,0.,10.
0.,0.,0.,1.,1.,1.,0.
*NCOPY,OLD SET=MIDABFE,SHIFT,NEW SET=MIDDCGH,CHANGE NUMBER=50000
0.,0.,10.
0.,0.,0.,1.,1.,1.,0.
*NODE
1001,8.,0.,0.2
1201,8.,1.,0.2
1033,12.2,0.,0.2
1233,12.2,1.,0.2
*NGEN,NSET=ABCDCOL1
1001,1033,2
*NGEN,NSET=EFGHCOL1
1201,1233,2
*NCOPY,OLD SET=ABCDCOL1,SHIFT,NEW SET=ABCDCOL2,CHANGE NUMBER=48000
0.,0.,9.6
0.,0.,0.,1.,1.,1.,0.
*NCOPY,OLD SET=EFGHCOL1,SHIFT,NEW SET=EFGHCOL2,CHANGE=48000
0.,0.,9.6
0.,0.,0.,1.,1.,1.,0.
**
** GENERATE THEM NODES
**
*NFILL,NSET=NABCD1
NODESAB,NODESCD,25,2000
*NFILL,NSET=NABCD2
ABCDCOL1,ABCDCOL2,24,2000
*NFILL,NSET=NEFGH1
NODESEF,NODESGH,25,2000
*NFILL,NSET=NEFGH2
EFGHCOL1,EFGHCOL2,24,2000
*NFILL,NSET=MIDSIDE
MIDABFE,MIDDCGH,25,2000
**
** COMBINE NODE SETS
**
*NSET,NSET=NABCD
NABCD1,NABCD2
*NSET,NSET=NEFGH
NEFGH1,NEFGH2
*NSET,NSET=ALLNODES
NABCD,NEFGH,MIDSIDE
**
** MAP NODES TO CYLINDRICAL CO-ORDINATES
**
*NMAP,NSET=ALLNODES,TYPE=CYLINDRICAL
0.,0.,0.,0.,0.,1.
1.,0.,0.
1.,1.,1.
*TRANSFORM,NSET=ALLNODES,TYPE=C
0.,0.,0.,0.,0.,10.
**
** ELEMENTS
**
*ELEMENT,TYPE=C3D20
1,201,2201,2001,1,203,2203,2003,3,1201,2101,1001,101,1203,2103,1003,
103,202,2202,2002,2
*ELGEN,ELSET=ALLELE
1,16,2,1,25,2000,100,1
*ELSET,ELSET=ZERO,GEN
1,2401,100
3,2403,100
5,2405,100
7,2407,100
10,2410,100
12,2412,100
14,2414,100
16,2416,100
*ELSET,ELSET=FOR5,GEN
2,2402,100
4,2404,100
6,2406,100
8,2408,100
9,2409,100
11,2411,100
```

```
13,2413,100
15,2415,100
**
** MATERIALS                    -                    The Critical Part of this code
**
*SOLID SECTION,ELSET=ZERO,MATERIAL=USER0,ORIENTATION=ZERO
*MATERIAL,NAME=USER0
*USER MATERIAL,CONSTANTS=8                                  <-- User Material Command
131500.,9200.,0.3,0.45,4340.,3103.,90.,0.02578              <-- Required Material Data
*DEPVAR                                                     <-- Solution Dependent Variables
5                                                           <-- 5 Outputs, incl Raghava Stress
*EXPANSION,TYPE=ORTHO,ZERO=21.85
 2.700E-05 2.200E-08 2.700E-05
*SOLID SECTION,ELSET=FOR5,MATERIAL=USER45,ORIENTATION=ZERO
*MATERIAL,NAME=USER45
*USER MATERIAL,CONSTANTS=8                                  <-- User Material Command
131500.,9200.,0.3,0.45,4340.,3103.,45.,0.02578              <-- Required Material Data
*DEPVAR                                                     <-- Solution Dependent Variables
5                                                           <-- 5 Outputs, incl Raghava Stress
*EXPANSION,TYPE=ORTHO,ZERO=21.85
 2.240E-06 2.240E-06 2.700E-05
*ORIENTATION,NAME=ZERO,SYSTEM=CYLINDRICAL,DEFINITION=COORDINATES
0.,0.,0.,0.,0.,1.
2,90.
**
** BOUNDARY CONDITIONS
**
*BOUNDARY
1,1,1
NODESAB,2,3
MIDABFE,3,3
NODESEF,3,3
**
** MULTI-POINT CONSTRAINTS
**
** RADIAL DISPLACEMENT - FIRST ROW
**
*EQUATION
4
1001,1,1.,1201,1,-1.,1,1,-1.,201,1,1.
*EQUATION
4
2001,1,1.,2201,1,-1.,1,1,-1.,201,1,1.
*EQUATION
4
.....................................................................
.....................................................................
....    These equations are cut because there 3814 of them! .......
.....................................................................
.....................................................................
*EQUATION
3
218,2,4.2,201,2,-1.96875,233,2,-2.23125
*NSET,NSET=LOAD3,GEN
203,231,2
*NSET,NSET=LOAD23,GEN
202,232,2
*NSET,NSET=LOAD6
201,233
**
** PROCESS THE SLICE WITH APPLIED THERMAL STRESSES
**
*initial conditions, type=temperature
ALLNODES,120.
*user subroutines,input=3dragxyorth.inp                     <-- Calls the USER Material Code
*STEP,AMPLITUDE=STEP
*STATIC
*TEMPERATURE
ALLNODES,20.
*CLOAD
233,2,-6294.643
201,2,6294.643
*NODE PRINT,NSET=LOAD6
U
*EL FILE,POSITION=CENTROIDAL
EVOL
SDV
*EL PRINT,POSITION=CENTROIDAL
EVOL
S
*END STEP
```